REFERENCE ONLY

UNIVERSITY OF LONDON THESIS

Degree P h D   Year 2007   Name of Author SCHADY, Patricia

COPYRIGHT
This is a thesis accepted for a Higher Degree of the University of London. It is an unpublished typescript and the copyright is held by the author. All persons consulting this thesis must read and abide by the Copyright Declaration below.

COPYRIGHT DECLARATION
I recognise that the copyright of the above-described thesis rests with the author and that no quotation from it or information derived from it may be published without the prior written consent of the author.

LOANS
Theses may not be lent to individuals, but the Senate House Library may lend a copy to approved libraries within the United Kingdom, for consultation solely on the premises of those libraries. Application should be made to: Inter-Library Loans, Senate House Library, Senate House, Malet Street, London WC1E 7HU.

REPRODUCTION
University of London theses may not be reproduced without explicit written permission from the Senate House Library. Enquiries should be addressed to the Theses Section of the Library. Regulations concerning reproduction vary according to the date of acceptance of the thesis and are listed below as guidelines.

A.   Before 1962.   Permission granted only upon the prior written consent of the author. (The Senate House Library will provide addresses where possible).

B.   1962-1974.   In many cases the author has agreed to permit copying upon completion of a Copyright Declaration.

C.   1975-1988.   Most theses may be copied upon completion of a Copyright Declaration.

D.   1989 onwards.   Most theses may be copied.

This thesis comes within category D.

☑   This copy has been deposited in the Library of _University College London_

☐   This copy has been deposited in the Senate House Library, Senate House, Malet Street, London WC1E 7HU.

Prompt Observations Of

Gamma-Ray Bursts with *Swift*

Patricia Schady

Mullard Space Science Laboratory

Department of Space and Climate Physics

University College London

A thesis submitted to the University of London

for the degree of Doctor of Philosophy

UMI Number: U592360

UMI

Dissertation Publishing

UMI U592360

ProQuest

I, Patricia Schady, confirm that the work presented in this thesis is may own. Where information has been derived from other sources, I confirm that this has been indicated in the thesis.

Abstract

This thesis uses early-time and simultaneous data from all three instruments on-board *Swift* to explore how the conditions of long Gamma-Ray Bursts (GRBs) and their environment affect their observed prompt and afterglow properties.

I firstly analyse two long GRBs with properties that distinguish them from the more standard class of long GRB; XRF 050406 and GRB 061007. The X-Ray Flash XRF 050406 is a class of GRB with softer prompt emission spectra than is typically observed. At the time, *Swift* UVOT observations of XRF 050406 were the earliest to be taken of an XRF optical counterpart, and the temporal and spectral *Swift* multi-wavelength data indicate that the bursts' softness is due to a geometrical effect where the GRB is observed off-axis. GRB 061007 is the brightest GRB to be detected by *Swift* and is accompanied by an exceptionally luminous afterglow that had a V-band magnitude < 11.1 at 80 s after the prompt emission. Although several properties of GRB 061007 are comparable to that of more standard GRBs, the brightness and the similarity in the decay rate of the X-ray, UV/optical and γ-ray emission from 100 s after the trigger require either an excessively large kinetic energy or highly collimated outflow.

To study GRB local environments, I analyse the X-ray and UV/optical spectral energy distributions of seven GRBs, and determine the column density and dust extinction in the GRB local environment. Using the SMC, LMC and Milky Way extinction curves to model the host galaxy dust, I find the SMC model to provide the best fit to the majority of the sample, indicating that the local environments of long GRBs are characteristic of irregular, low metallicity galaxies. I investigate the factors that contribute to the extinction and absorption in GRB afterglows, and the implications for the host galaxy properties.

3

Contents

List of Figures

List of Tables

Chapter 1

Introduction

Gamma-Ray Bursts (GRBs) are powerful flashes of γ-rays, which, for a few milliseconds to hundreds of seconds are the most luminous electromagnetic phenomena in the Universe. They are unpredictable in nature, are distributed isotropically across the sky, and occur at a rate of ~ 1 day, releasing an isotropic equivalent luminosity of up to 10^{54} erg s^{-1} in γ-rays alone. The initial outburst of high energy emission of GRBs is referred to as the prompt phase, and this is accompanied by a less energetic afterglow.

During the prompt, γ-ray phase the emission is chaotic and highly variable, and produces light curves that frequently show multiple peaks that can have precursors occurring as early as hundreds of seconds before the main event, as well as smooth emission continuing for many tens of seconds after the initial outburst. This is followed by a much longer lasting afterglow that spans a large fraction of the electromagnetic spectrum, from the X-ray band [e.g. Costa et al., 1997] through optical [e.g. van Paradijs et al., 1997] to radio [e.g. Frail et al., 1997] wavelengths. Their high-energy emission is relatively unaffected by intervening absorption systems, which, together with their vast luminosities, allow GRBs to be detected in principle out to redshifts, z, of 10 or more [Lamb & Reichart, 2000]. This would make GRBs the furthest discrete probe available of the high-redshift Universe.

1.1 A Brief History

GRBs were first detected in 1967 by the Vela Satellites that were launched by the US to monitor compliance with the 1963 Partial Test Ban Treaty by the Soviet Union and other nuclear-capable states. GRBs were first identified as such in 1969, and the first publication on these extraterrestrial, high energy explosions was in 1973 [Klebesadel et al., 1973]. For the next couple of decades GRBs were serendipitously detected by a number of astrophysical missions. However, it was not until 1991 that a satellite equipped with the capabilities to study and monitor GRBs in a systematic way was launched. This was the Compton Gamma Ray Observatory (CGRO), which, as part of its payload carried the Burst and Transient Source Experiment (BATSE). In its 9 year lifetime BATSE detected 2704 GRBs in the 20 keV to > 800 keV energy range, and one of the most important outcomes from this was the discovery that GRBs were distributed isotropically across the sky, strongly indicating that they were either a very local phenomenon, or were extragalactic in nature.

The next important milestone in GRB research was in 1997, when GRB afterglows were discovered by the Italian-Dutch satellite *Beppo*SAX, three decades after the first detection of a GRB. The *Beppo*SAX satellite detected GRB 970228 with its all-sky Gamma-Ray Burst Monitor (GRBM) in the 40–700 keV energy range, and observations with its two Wide Field Cameras (WFCs) in the 2–26 keV energy range localised the GRB promptly within a few arcminute accuracy. This allowed follow-up observations of the GRB to be made with the two narrow field instruments on-board, the LECS (0.1–10 keV) and MECS (1.3–10 keV), $\sim$ 8 hours after the initial GRB detection, which led to the discovery of the X-ray afterglow of this burst [Costa et al., 1997]. The fast imaging and arcminute localisation prompted a multiwavelength campaign, and this led to the identification of an afterglow in the optical [Galama et al., 1997] and radio [Frail et al., 1997] consistent with the X-ray source. Following this burst, dedicated campaigns led to the detection of afterglows for a number of GRBs, typically in the X-ray, optical and near infra-red (NIR), but also in the radio, lasting from days to months after the prompt emission. It was

the detection of the optical afterglow of GRB 970508 that finally led to the first redshift measurement of a GRB [z=1.09; Reichart, 1998], confirming the extragalactic nature of GRBs. In the early years of the new millennium, prompt follow-up observations of GRB afterglows were aided by the fast and accurate localisations of GRBs by the HETE-2 [Ricker et al., 2000] and INTEGRAL [Ubertini et al., 2000] missions. However, the time delay between the initial detection of the prompt emission and the start of the afterglow follow-up observations was, still, on the order of several hours, and it was not until the launch of *Swift* that frequent early time afterglow observations were made available.

The *Swift* Gamma-Ray Burst mission [Gehrels et al., 2004] is a multi-wavelength satellite with rapid-response capabilities, which was launched on 20th November, 2004. It is equipped with three telescopes to observe both the prompt emission and the X-ray, UV and optical afterglow. The Burst Alert Telescope [BAT; Barthelmy et al., 2005a] can monitor a quarter of the sky at any one time and detects prompt emission in the 15–150 keV energy range. Afterglow observations are taken with the X-ray Telescope [XRT; Burrows et al., 2005a] which has a 0.2–10 keV energy range, and the UV and Optical Telescope [UVOT; Roming et al., 2005] that covers the wavelength range 1600–6500 Å. When the BAT triggers on a GRB, the *Swift* satellite is designed to slew rapidly to the GRB so that it is in the field of view of the XRT and UVOT, providing panchromatic observations of the burst within the first few hundred second of the BAT trigger. The launch of *Swift* represents a new era in GRB research, where the early time observations of the GRB afterglow are revealing important clues on the nature of the mechanism that powers these huge explosions, as well as the properties of the GRB environment.

1.2 Gamma-Ray Properties

The early-time X-ray and UV/optical observations available with *Swift* are closing the gap between the previously distinct prompt and afterglow GRB emission phases. In a few cases the narrow field instruments have even been on target and taking data whilst the prompt emission has still been ongoing [e.g. GRB 060124; Romano et al. (2006b),

GRB 061121; Page et al. (2007)], revealing the overlap between these two phases. Although the distinction between the prompt emission and the afterglow is no longer trivial, their emission mechanisms are likely to differ, and they are, therefore, typically treated separately.

1.2.1 Prompt Emission

Duration

The GRB prompt emission can be made up of an arbitrary number of pulses that typically overlap, although they can be discrete events. GRBs that have well-resolved pulses frequently show a Fast Rise and Exponential Decay (FRED) profile. Some bursts consist of just a single FRED profile, and in other cases isolated FRED pulses or overlapping pulses may occur a long time before or after the bulk of the chaotic and highly variable emission. This, as well as the usually smaller signal to noise of pulses towards the end of the outburst, make it difficult to define the duration of the prompt emission. The term T_{90} was, therefore, introduced to define the GRB prompt phase, which is the time-interval over which 90% of the radiation in a given energy range is emitted. That is, the time between the emission of the first 5% of the total counts above background and the time that 95% of the total counts above background have been emitted. The widths of individual pulses, δt, can be $\delta t / T_{90} \ll 1$.

Using the term T_{90}, the 2704 GRBs detected by BATSE showed a bimodal distribution in the duration of the prompt, γ-ray emission (see Fig. 1.1), leading to the categorisation of GRBs as either long or short [Kouveliotou et al., 1993]. The short and long populations of GRBs as observed in the BATSE dataset have a mean T_{90} of ~ 0.3 s and ~ 35 s, respectively, with a nominal divider between the two populations at ~ 2 s. As well as the difference in the duration of the prompt emission, short and long GRBs are also distinguished by their spectra, which are typically harder in short GRBs, thus leading to the categorisation of short, hard bursts (SHB) and long, soft bursts (LSB).

---

[1]www.batse.msfc.nasa.gov/batse/grb/duration/
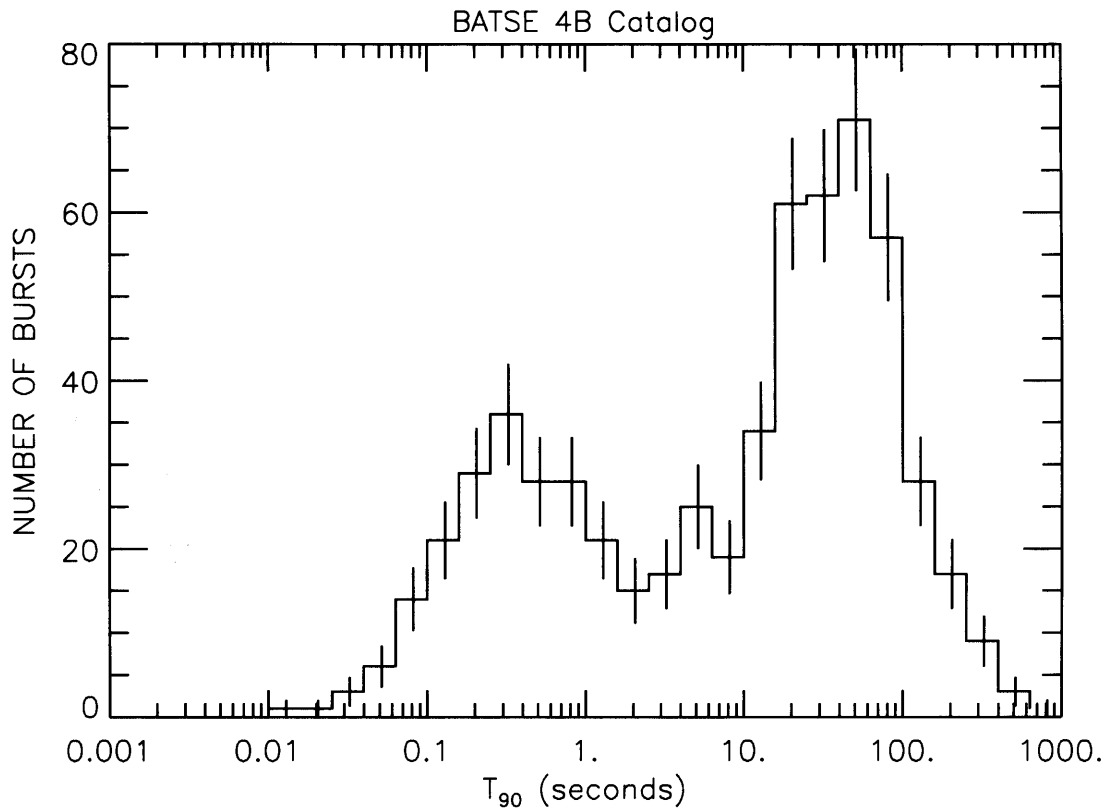
Figure 1.1: Distribution of the prompt emission duration for 2704 GRBs observed by BATSE from the 4B catalogue[1]. The duration, T_{90}, is the time over which a burst emits from 5% to 95% of its background subtracted counts in a given energy band.

However, detailed observations of GRBs using *Swift* and other missions are revealing the ambiguities in the categorisation of GRBs by their prompt emission alone, which uses observer frame properties rather than properties intrinsic to the GRB. Other characteristics that reflect the origin of the observed differences between these two populations of GRBs are, therefore, needed, such as the conditions in the circumburst environment or the nature of the progenitor.

Energy Range

Due to the uncertainty of the jet angle within which the GRB emission is released, the energy of a burst is typically given as an isotropic-equivalent value. That is, the energy that would be produced by the GRB if it were emitted isotropically with the same flux as observed along our line of sight. The isotropic-equivalent energy, E_{iso}, released by a GRB in a given observer frame energy range, $[e_1, e_2]$, is a function of the measured fluence of the burst in that energy range, $S = \int_{e_1}^{e_2} E\Phi(E)dE$, where $\Phi(E)$ is the GRB's observer frame spectral shape, its redshift, z, and the luminosity distance, D_l. It is defined as

$$E_{iso} = \frac{4\pi D_l^2}{1+z}S. \tag{1.1}$$

To compare the isotropic energy between GRBs, E_{iso} has to be shifted into the rest frame, and to a common rest frame energy range [Bloom et al., 2001]. To do this a k-correction is applied to convert the isotropic equivalent energy measured in the observer frame energy range $[e_1, e_2]$ to that measured over a certain rest frame energy band, $[e_1',$ $e_2']$. The k-correction is then the ratio of the measured GRB fluence between the rest frame energies $[e_1'/(1+z), e_2'/(1+z)]$ over the fluence measured in the detector bandpass, $[e_1, e_2]$. This is parametrically defined by

$$k = \frac{\int_{e_1'/(1+z)}^{e_2'/(1+z)} E\Phi(E)dE}{\int_{e_1}^{e_2} E\Phi(E)dE}, \tag{1.2}$$

where z is the redshift of the GRB and $\Phi(E)$ is the observer frame spectral shape. The k-corrected isotropic-equivalent energy released by a GRB is, therefore, given by

$$E_{iso,k} = E_{iso} \times k = \frac{4\pi D_l^2}{1+z}S \times k. \tag{1.3}$$

During the prompt phase, a GRB can release an isotropic-equivalent, rest frame energy ranging from 1.0×10^{48} erg [e.g. GRB 980425] to 2.7×10^{54} erg [e.g. GRB990123] [Amati, 2006]. However, this distribution in energies is not free from selection effects, and is biased towards more luminous and lower redshift GRBs. Furthermore, it is likely that the energy released by GRBs is collimated, which could reduce the energy budget by up to ~ 4 orders of magnitude [e.g. Rhoads, 1997], and decrease the range in prompt emission energetics [e.g Frail et al., 2001, Bloom et al., 2003] (see section 1.7 for further details).

Spectrum

The prompt emission has a non-thermal spectrum that is well modelled by the Band function [Band et al., 1993], which is a smooth broken power law of the form

$$\phi(E) = \begin{cases} E^{-\beta_1} \exp\left(-\frac{E}{E_0}\right) & \text{for}(\beta_2 - \beta_1)E_0 \geq E, \\ [(\beta_2 - \beta_1)E_0]^{\beta_2-\beta_1} \exp(\beta_1 - \beta_2)E & \text{for}(\beta_2 - \beta_1)E_0 \leq E, \end{cases}$$

where β_1 is the low-energy index, β_2 is the high energy index, and E_0 is the spectral break energy. The spectral break, E_0, is related to the peak energy in the νF_ν spectrum by $E_p = E_0(2 - \beta_1)$. When fitting the average prompt emission spectrum, the low and high energy spectral indices of GRBs are narrowly distributed at around $\langle \beta_1 \rangle \approx 1.0$, and a $\langle \beta_2 \rangle \approx 2.3$, respectively [D'Alessio et al., 2006]. The distribution in E_p, on the other hand, is much larger and defines the hardness of the prompt emission spectrum. GRBs typically have peak energies of $E_p \sim 200$ keV [D'Alessio et al., 2006]. However, there are two subclass of GRBs that have a softer prompt emission spectrum known as X-Ray Flashes (XRFs) and X-Ray Rich (XRR) GRBs, where XRR GRBs are intermediate between XRFs and 'classical' GRBs (see section 1.8). These two combined groups of softer GRB are found to have an average peak energy of $E_p \sim 20$ keV [D'Alessio et al., 2006]. The similarity between many aspects of XRFs, XRR GRBs and classical GRBs suggest that they represent the same underlying phenomenon.

For both GRBs and XRFs, the spectra of individual pulses, when well resolved, show strong time evolution, whereby individual pulses evolve from hard to soft [Ryde & Svensson, 1999].

Luminosity

A broad range in the prompt emission luminosity of GRBs is also observed, which spans around 7 orders of magnitude [Li & Paczyński, 2006]. However, due to the lack of spectroscopic or photometric measurements for over 2/3 of the GRBs detected, the luminosity function (LF) of GRBs is still not well determined. Various redshift estimators have been used to try and measure the GRB LF [e.g. spectral lag-luminosity [Norris et al., 2000], variability-peak luminosity [Reichart et al., 2001], $E_p - E_{iso}$ [Amati et al., 2002b] correlations]. However, the level of uncertainty in both the current pseudo-z measurements and in the collimation of GRBs make the LF estimated in this way unreliable.

1.2.2 Afterglow

Temporal Behaviour

The GRB afterglow can last days to months after the prompt emission and has a more generic temporal behaviour than the prompt emission [e.g. Nousek et al., 2006]. The X-ray light curve is typically composed of several components in which the canonical shape has four power law segments, expressed by $F_t \propto t^{-\alpha_i}$ for $i = 1, 2, 3, 4$, with a usually smooth transition from one power law to the next at the break time (see Fig. 1.4). The first power law segment (phase I) is a steep early time decay phase ($3 < \alpha_{X,1} < 5$) lasting for a few hundred seconds. This is followed by a plateau phase with decay index $\alpha_{X,2} \sim 0.5$ up to $10^3 - 10^4$ s after the prompt emission (phase II) that breaks to a steeper phase with $\alpha_{X,3} \sim 1.2$ (phase III), and the fourth power law segment begins at $10^4 - 10^5$ s after the prompt emission (phase IV), where the afterglow steepens to a decay rate of $\alpha_{X,4} \sim 2.2$. Prior to the launch of *Swift*, X-ray observations of GRBs typically sampled the third and fourth power law segment of the canonical light curve described above. Flares may also be superimposed on the smooth decay light-curve, and are observed in around half of the GRBs with early-time X-ray data [Willingale et al., 2007].

The optical afterglow light curve is not, typically, as complex as the X-ray light curve, and is usually well described by a power law. Prior to *Swift* the mean decay index of optical

afterglows was $\alpha_{opt} \sim 1.1$ [Zeh et al., 2006], although current *Swift* observations indicate that at early times $\alpha_{opt} \sim 0.5$ [Oates et al., 2007b], similar to the flat segment of the X-ray light curve. However, there are examples of optical light curves with more complex behaviour that may brighten at late times [e.g. GRB 990123, GRB 990508, GRB 060607], or show signs of variability [e.g. GRB 050319; Mason et al. (2006), GRB 060124; Romano et al. (2006a)]. A break to $\alpha_{opt} \approx 2 - 2.5$ is sometimes also observed in the optical light curve on the order of days [e.g. 990123, 990510, 991216, 000301, 000926, 011121, 050525, 060526, 070311], which before the launch of *Swift* was attributed to the presence of a jet (see section 1.7). However, the lack of well sampled multi-wavelength observations on these timescales makes the cause of such breaks difficult to determine with confidence in many cases.

Energy Range

In the optical band GRBs can be as bright as 9th magnitude [GRB 990123 Akerlof et al., 1999], although their optical afterglow can be severely extinguished by dust along the line of sight, or fully absorbed by neutral hydrogen gas if at large redshifts. The X-ray band is not as greatly affected by the ISM, especially at larger energies (i.e. $\gtrsim 2$ keV), and is, therefore, a more reliable measure of the intrinsic energetics of the GRB afterglow. GRB X-ray afterglow isotropic-equivalent luminosities at 11 hours after the prompt emission range from $\sim 10^{44}$ erg s^{-1} up to 10^{47} erg s^{-1}, although their intrinsic luminosity may be more narrowly clustered when collimation is taken into account [e.g. Frail et al., 2001].

Spectrum

The afterglow spectrum is also non-thermal, and the broadband nature of the GRB afterglow is well described by synchrotron emission (see section 1.4.2), although an inverse Compton (IC) component may also contribute to the X-ray afterglow.

The X-ray afterglow is typically well fit by an absorbed power law with a photon spectral index $\Gamma \sim 2.1$ and a column density of the order of $10^{21} - 10^{22}$ cm^{-2}. Spectral evolution is sometimes observed at early times during the transition from the steep decay

phase to the plateau phase, which could variously be due to the transition from the prompt emission to the afterglow [Barthelmy et al., 2005b], the result of photoionisation of the circumburst material by the GRB emission [e.g. Campana et al., 2007], or the migration of E_p through the X-ray band as the outflow cools adiabatically [e.g. Butler & Kocevski, 2007]. Spectral evolution is also observed during X-ray flares, which evolve from hard to soft, as in the case of the prompt emission phase, suggesting that X-ray flares are produced by the same mechanism as the prompt emission.

1.3 Basic Phenomenological Model

Two essential requirements of any GRB progenitor model are that the internal engine be able to produce an apparent isotropic energy between 10^{48} and 10^{54} erg within a few tens of seconds, and that the emission be highly variable on timescales of seconds, and even milliseconds for short GRBs.

Accretion of stellar material onto a newly formed black hole is about the only known mechanism that can supply enough energy to power the vast explosions observed in both SHBs and long GRBs. In order for the accretion disk to form, rotation must be present in the system such that, during the gravitational collapse to a black hole, infalling material accumulates mostly at the equator, forming a torus around the black hole. Gravitational energy from the accreting disk is then extracted and converted into outflowing kinetic energy by some mechanism, such as neutrino transportation or due to the presence of a strong magnetic field.

In the former model, neutrinos and antineutrinos produced from the increased pressure in the core during stellar collapse annihilate and form a reservoir of electron-positron pairs and photons that exert a pressure against the infalling material [Fryer & Mészáros, 2003]. Neutrino annihilation primarily occurs along the rotation axis of the collapsing star, where there is an under-density of baryonic matter that would otherwise dampen the neutrino energy. When the radiation pressure within the dense, optically thick, electron-positron pair fireball exceeds the gravitational energy, it will expand adiabatically and convert

its internal energy into kinetic energy, accelerating material out along the path of least resistance, which will be the disk rotational axis.

In the latter model, a strong magnetic field can extract energy from the accretion disk through particle acceleration, which can produce an electron-positron pair-fireball. As was the case with neutrino transportation, the radiation pressure exerted by the pair-fireball would drive out the infalling material.

The fireball's kinetic energy is converted back into electron energy and dissipated via shocks, formed both within the fireball from existing inhomogeneities, and as the outflow ploughs into the surrounding interstellar medium. Discrete shells will exist within the fireball due to the inhomogeneous nature of accretion and infalling material onto the black hole.

The small-scale variability observed in the prompt emission light curves necessitates a compact emission region that is close to the source. However, this leads to a compactness problem [Piran, 1996], whereby the optical depth of such a region produces a barrier to the high-energy radiation, causing it to be attenuated through $\gamma\gamma$ interactions and form electron-positron pairs. This situation is avoided if the material is moving at relativistic velocities, with bulk Lorentz factor Γ, such that the photon energies are blue-shifted by a factor of Γ. The observed prompt emission would then be a factor of Γ less energetic in the rest frame, which will increase the fraction of photons below the pair-production threshold and reduce the number of $\gamma\gamma \to e^{\pm}$ interactions. Relativistic motion will also increases the physical scale of the emission region by a factor of Γ^2, thus decreasing the pair production optical depth, $\tau_{\gamma\gamma}$, by a factor of Γ^4. In most GRBs a bulk Lorentz factor of $\Gamma \geq 100$ would reduce the optical depth to $\tau_{\gamma\gamma} < 1$.

1.3.1 GRB Progenitors

The Collapsar Model

In the Collapsar model [Woosley, 1993] a GRB is a consequence of the gravitational collapse of a massive, rapidly rotating star that forms a black hole-accretion disk system.

There is mounting evidence to suggest that long GRBs are the result of the gravitational collapse of a massive star, such as the underlying supernova features in the afterglow of some GRBs (e.g. GRB 980425 [Kulkarni et al., 1998], GRB 030329 [Hjorth et al., 2003] and GRB 060218 [Campana et al., 2006a]), and the association between GRB host galaxies and high-mass star formation [Bloom et al., 2002, Tanvir et al., 2004]. In fact, evidence of an under-luminous supernova component is observed in the majority of nearby GRBs ($z < 0.7$) [Zeh et al., 2004].

The necessary conditions in the collapsar model are that the progenitor star has a massive core of helium and heavier elements ($10 - 15$ $M_\odot$) large enough to collapse into a black hole, that it has lost its hydrogen envelope prior to core collapse so that the relativistic outflow can break through the surface (i.e. it is a Wolf-Rayet star), and that enough angular momentum remains during the core collapse to form a rotating disk that is maintained by its centrifugal force, rather than free falling into the black hole [Woosley, 1993].

These conditions impose constraints on the mass loss rate during the progenitor lifetime, which has to be sufficient to completely strip its hydrogen envelope from the star, but low enough to prevent the simultaneous loss of too much angular momentum. Furthermore, the mass-loss rate of a star is dependent on its metallicity due to the increase in the photon pressure in a metal rich environment. High metallicity stars will, thus, have a larger mass loss rate than lower metallicity ones, resulting in a greater loss of angular momentum. The metallicity is, therefore, also a factor in the collapsar model, which requires the progenitor star to have a low metallicity in order to maintain a sufficient level of angular momentum at the time of collapse and form a fast-rotating accretion disk [e.g. Hirschi et al., 2005, Woosley & Heger, 2006, Langer & Norman, 2006].

To collapse directly into a black hole the mass of the stellar helium core needs to be larger than the Virial mass. For smaller masses than this, the core may still collapse into a black hole, but in a two step process, where the helium core first collapses into a proto-neutron star [MacFadyen et al., 2001]. As it accretes mass from the stellar mantle, the accumulation of mass and the loss of radiation pressure from the emission of neutrinos

will cause the neutron star to collapse into a black hole of several $M_\odot$, which will occur on the order of a few seconds after the initial core collapse [Woosley, 1993, MacFadyen et al., 2001]. Simulations of core collapse into a black hole suggest initial stellar masses of $\sim 35 - 40\ M_\odot$, although this will depend on the metallicity of the star [e.g. Woosley, 1993, Fryer, 1999, Heger et al., 2003]. Stellar material continues to fall onto the black hole, and the angular momentum remaining from the progenitor star creates a rotating accretion disk around the black hole with mass in the range of 0.1 $M_\odot$ to 1 $M_\odot$ [Woosley, 1993].

In the collapsar model a supernova (SN) is also expected to result from the gravitational collapse of the stellar core. This may occur prior to the formation of a black hole, whereby infalling material from the collapse onto a neutron star may gain sufficient energy, possibly via neutrino interactions, to cause the surrounding material to be blasted away in a supernova explosion. The GRB is then produced once the neutron star collapses into a black hole and a rotating accretion disk is formed. Alternatively, the SN explosion may occur simultaneously with the formation of an accretion disk around a black hole, where the GRB jets blow out the infalling stellar material as they push through the outer envelope. It is still not clear whether the SN occurs before or simultaneously with the GRB explosion, although observations of GRBs with supernova components indicate the time delay, ΔT, to range from a few seconds to 1–2 days [Norris & Bonnell, 2004]. The time delay will depend on the size of the progenitor, the length of time between the collapse into a neutron star and the final collapse to a black hole, and on the accretion rate onto the black hole.

The model described above assumes the core collapse of a single star. However, a collapsar model in which the GRB progenitor is part of a binary system removes the need for high angular rotation of an individual star. This is compensated by the angular momentum of the binary system, and the angular momentum of the progenitor can be maintained despite high mass loss rate.

Binary Mergers

In the collapsar model the duration of the prompt γ-ray emission produced is proportional to the free-fall timescale, which is on the order of a few to tens of seconds, and this model thus cannot produce a SHB. A likely progenitor for SHBs is a compact neutron star-neutron star (NS-NS) [Paczynski, 1986] or neutron star-black hole (NS-BH) binary system [Eichler et al., 1989], where a black hole is formed by the merger of the binary components.

Observations of those SHBs with identified host galaxies have shown large offsets from the galaxy centre (see section 1.10.1), which is expected in compact binary mergers as a result of the kick that the binary system receives at the time of the supernova explosions that formed the compact stars, and because of the long evolutionary timescale of such a binary, which allows it to travel far from its birth place. This thus strengthens the evidence for such a progenitor model.

1.4 Emission Mechanisms

1.4.1 Prompt Emission

The prompt emission is believed to be generated by internal shocks within the fireball that arise above the pair production photosphere, at $\sim 10^{12} - 10^{14}$ cm. These shocks stem from mini-shells within the jet produced by the unsteady accretion of material onto a black hole as well as the generation of Kelvin-Helmholtz instabilities, where velocity shears and density differences result in a turbulent outflow.

The shells have a distribution in Lorentz factor, γ, of several, whereby $\Delta\gamma \propto \Gamma$, where Γ is the bulk Lorentz factor. As faster shells catch up with slower ones, they form strong internal shocks that propagate into both shells, generating a magnetic field and dissipating kinetic energy into the internal energy of the electrons. Once above the photosphere, the heated and accelerated electrons cool by synchrotron emission and Inverse Compton (IC) scattering and are observed in the γ-ray band. Each such collision that occurs above the

R ~ 10⁶ cm

γ, X

R ~ 10¹²⁻¹⁴ cm

R ~ 10¹⁶⁻¹⁸ cm

X-ray, optical radio
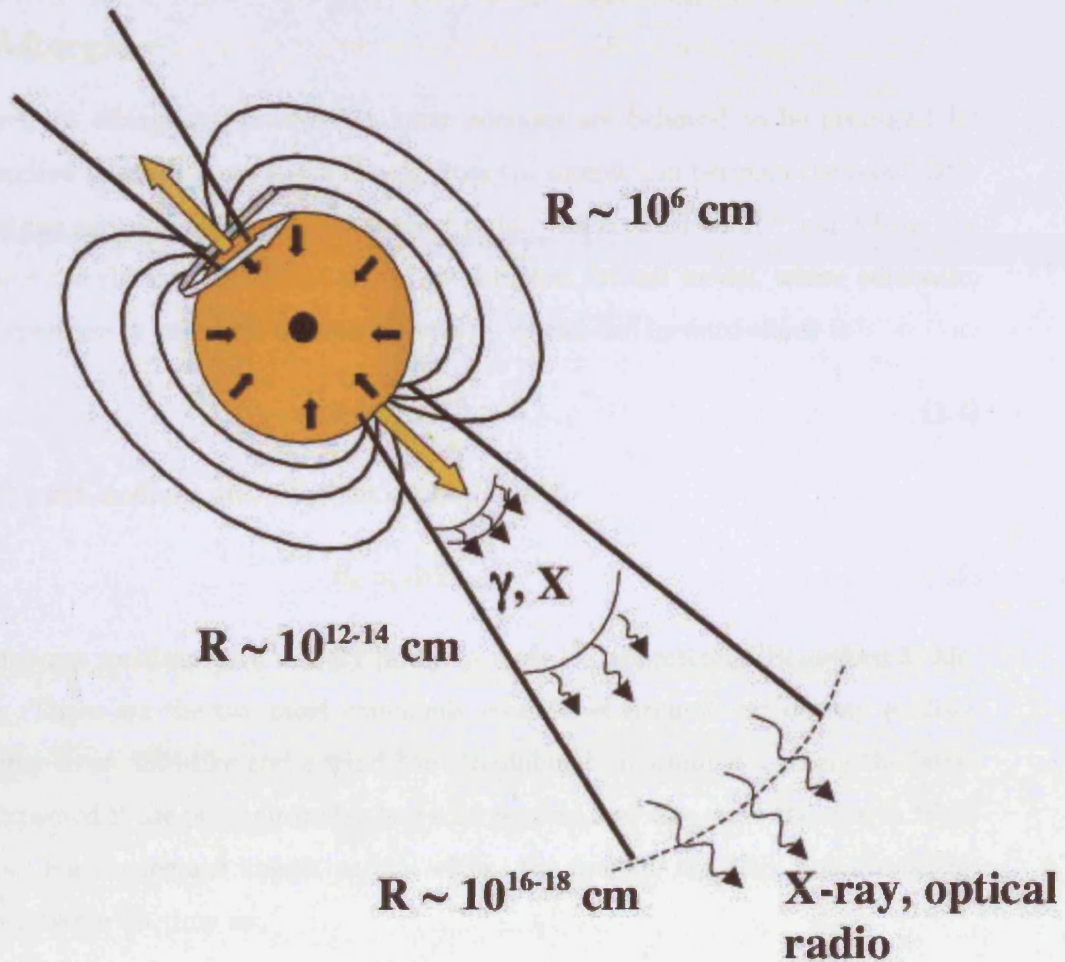
Figure 1.2: Collapsar model for long GRBs. A massive star that collapses under it's own gravitational strength forms a black hole with an accretion disk system. Angular momentum and gravitational energy are converted into an electron-positron fireball that expands adiabatically and drives out the infalling and accreting material in the form of jets. Internal shocks within the fireball dissipate kinetic energy into the internal energy of the electrons, producing the GRB, and the afterglow is produced in a forward shock as the front of the jet ploughs into the surrounding, interstellar medium.

pair photosphere produces a pulse in the burst's light curve.

1.4.2 Afterglow

The longer lived afterglows observed at lower energies are believed to be produced by electrons excited in an external shock arising from the interaction between the relativistic outflow and the surrounding, colder medium at radii $r = \Gamma c t \approx 10^{16} - 10^{18}$ cm^{-2} from the source, where t is the age of the fireball. In the simplest fireball model, where adiabatic, spherical expansion is assumed, the kinetic energy within the forward shock is

$$E_k \propto n r^3 \Gamma^2, \tag{1.4}$$

for a circumburst medium with constant density n, and

$$E_k \propto A r \Gamma^2, \tag{1.5}$$

for a circumburst medium with density profile $\rho = A r^{-2}$, respectively [Blandford & McKee, 1976]. These are the two most commonly considered circumburst density profiles, corresponding to an ISM-like and a wind like circumburst environment, where the latter would be expected if the progenitor star had a large mass loss rate, as is the case in Wolf-Rayet stars. For a constant kinetic energy within the fireball, the bulk Lorentz factor, therefore, evolves with time as

$$\Gamma \propto t^{-3/8}, \tag{1.6}$$

$$\Gamma \propto t^{-1/4}, \tag{1.7}$$

for an ISM and wind density profile, respectively, which would cause the afterglow to decay as a power law.

Synchrotron Spectrum

As the relativistic jet ploughs into the circumburst medium, it produces a forward shock that compresses and intensifies the magnetic field within the outflow. Inhomogeneities

that develop within the magnetic field reflect charged particles within the shock, causing them to accelerate with a power law distribution of Lorentz factors γ_e and minimum Lorentz factor γ_m, which can be expressed as $N(\gamma_e) \propto \gamma_e^{-p} \, d\gamma_e$ for $\gamma_e \geq \gamma_m$.

The synchrotron spectrum produced by this distribution of electrons is a four-segment broken power law, where each segment is defined by $F_\nu \propto \nu^{-\beta_i}$ for $i = 1, 2, 3, 4$, and the spectral breaks are determined by three critical frequencies; the cooling frequency, ν_c, which defines the frequency above which electrons have already lost a significant fraction of their energy to radiation, the minimum characteristic frequency, ν_m, and the self-absorption frequency, ν_a. Relativistic particles accelerated in a magnetic fields will radiate at a characteristic frequency that is dependent on their Lorentz factor, γ_e, and in the observer frame is defined by

$$\nu(\gamma_e) = \nu_e = \Gamma \gamma_e^2 \frac{q_e B}{2\pi m_e c}, \tag{1.8}$$

where q_e and m_e are the charge and mass of the electron, and B is the magnetic field strength [Sari et al., 1998]. ν_m is, therefore, the characteristic synchrotron frequency corresponding to electrons with minimum Lorentz factor γ_m (i.e. $\nu_m = \nu(\gamma_m)$).

Electrons with larger Lorentz factors cool more rapidly, and this causes a break in the synchrotron spectrum at a critical cooling frequency, $\nu_c = \nu(\gamma_c)$, where electrons with characteristic frequency $\nu_e > \nu_c$ have already radiated away the bulk of their energy. Due to the dynamics of the system, the cooling frequency is, therefore, time dependent, and at any one time corresponds to the characteristic frequency of electrons that cool within the fireball expansion time. The observer frame cooling timescale of an electron with energy E_e is given by

$$t_c = \frac{E_e}{P_e} = \frac{6\pi m_e c^2}{\Gamma \sigma_T c \gamma_e^2 B^2} = \frac{6\pi m_e c}{\Gamma \sigma_T \gamma_e B^2}, \tag{1.9}$$

where P_e is the power radiated by an electron with Lorentz factor γ_e, and σ_T is the Thomson scattering cross-section. The cooling frequency, ν_c, is, therefore, the characteristic frequency of an electron that has an observer frame Lorentz factor

$$\gamma_c = \frac{6\pi m_e c}{\Gamma \sigma_T t_c B^2}. \tag{1.10}$$

The location of the critical frequencies ν_m, ν_c and ν_a, as well as the normalisation, F_{max,ν_c}, which is the peak flux density of the afterglow, are dependent on the burst and circumburst properties, such as the kinetic energy within the fireball, E_k, and the circumburst density and density profile, as well as the forward shock microphysical parameters. These are the fraction of energy in the electrons within the shock, ϵ_e, the fraction of energy in the magnetic field, ϵ_B, and the electron energy distribution index, p. The critical frequencies and afterglow peak flux density are as follows for an ISM circumburst medium:

$$
\begin{aligned}
\nu_m &= 3.3 \times 10^{15} \left(\tfrac{p-2}{p-1}\right)^2 (1+z)^{1/2} \epsilon_B^{1/2} \epsilon_e^2 E_{k,52}^{1/2} t_d^{-3/2} \text{ Hz} \\
\nu_c &= 6.3 \times 10^{12} (1+z)^{-1/2} (1+Y)^{-2} \epsilon_B^{-3/2} E_{k,52}^{-1/2} n^{-1} t_d^{-1/2} \text{ Hz} \\
\nu_a &= 1.05 \times 10^9 \left(\tfrac{(p+2)(p-1)}{(3p+2)}\right)^{3/5} \left(\tfrac{p-1}{p-2}\right)(1+z)^{-1} \epsilon_e^{-1} \epsilon_B^{1/5} E_{k,52}^{1/5} n^{3/5} \text{ Hz} \\
F_{\nu,\text{max}} &= 16(1+z) D_{28}^{-2} \epsilon_B^{1/2} E_{k,52} n^{1/2} \text{ mJy}
\end{aligned}
\tag{1.11}
$$

[Zhang et al., 2007], and for a wind environment

$$
\begin{aligned}
\nu_m &= 4.0 \times 10^{15} \left(\tfrac{p-2}{p-1}\right)^2 (p - 0.69)(1+z)^{1/2} \epsilon_B^{1/2} \epsilon_e^2 E_{K,52}^{1/2} t_d^{-3/2} \text{ Hz} \\
\nu_c &= 4.4 \times 10^{10} (3.45 - p) e^{0.45p} (1+z)^{-3/2} (1+Y)^{-2} \epsilon_B^{-3/2} E_{K,52}^{1/2} A_*^{-2} t_d^{1/2} \text{ Hz} \\
\nu_a &= 8.3 \times 10^9 \left(\tfrac{p-1}{3p+2}\right)^{3/5} \left(\tfrac{p-1}{p-2}\right)(1+z)^{-2/5} \epsilon_e^{-1} \epsilon_B^{1/5} E_{k,52}^{-2/5} A_*^{6/5} t_d^{-3/2} \text{ Hz} \\
F_{\nu,\text{max}} &= 77(p + 0.12)(1+z)^{3/2} D_{28}^{-2} \epsilon_B^{1/2} E_{K,52}^{1/2} A_* t_d^{-1/2} \text{ mJy}
\end{aligned}
\tag{1.12}
$$

[Chevalier & Li, 2000], where $E_{k,52}$ is the kinetic energy in the GRB in units of 10^{52}, t_d is the time since the prompt emission in units of days, Y is the Compton parameter, D_{28} is the luminosity distance in units of 10^{28} cm, and $A_* = A/(5 \times 10^{11})$ g cm^{-1} is the density scaling such that $\rho = Ar^{-2}$. Both the GRB properties and the forward shock microphysical parameters are typically assumed to remain constant throughout the afterglow. In this case the evolution of the minimum characteristic synchrotron frequency is only dependent on time, and goes as $t^{-3/2}$ for any circumburst medium. However, the time dependency of the cooling frequency is $t^{-1/2}$ for a constant density profile [Sari et al., 1998], and $t^{1/2}$ for a wind-like circumburst medium [Chevalier & Li, 2000]. The reason for this is that for a wind-like circumburst medium the circumburst environment will present less of an obstacle to the forward shock at larger radii, where the density is smaller. Electrons within the forward blastwave will, therefore, be excited by continual

shocks within the forward blastwave at a faster rate than they cool, providing an overall gain in energy per particle. The self-absorption frequency is independent of time in an ISM constant density medium, but goes as $t^{-3/2}$ in a wind circumburst environment.

An electron with a characteristic frequency $\nu_e > \nu_c$ cools rapidly, losing a significant fraction of its energy in radiation at a rate proportional to $\nu^{-1/2}$, whereas electrons with $\nu_e < \nu_c$ radiate as $\nu^{1/3}$ [Sari et al., 1998]. At frequencies below the self-absorption frequency, ν_a, radiation is re-absorbed by the same population of electrons that released the photons, and this absorption produces a sharp drop in the synchrotron spectrum below ν_a. The flux from electrons with a characteristic frequency $\nu < \nu_a$ is proportional to ν^2. This process is known as synchrotron self-absorption (SSA).

Due to the change in the cooling rate for electrons with characteristic frequencies above and below the cooling frequency, the location of ν_m and ν_c with respect to each other, and with respect to the observing frequency, ν, is, of importance when considering the shape of the synchrotron spectrum produced, which will differ for $\gamma_m < \gamma_c$ and $\gamma_m > \gamma_c$. Both ν_m and ν_c evolve with time and, initially, when ν_m is expected to be large, it is likely that $\gamma_m > \gamma_c$. In this case all electrons will emit at characteristic frequencies $\nu_e > \nu_c$ and will thus cool rapidly down to frequencies ν_c. This is referred to as the fast cooling regime. At later times, the difference in the rate at which ν_m and ν_c evolve will lead to a distribution in Lorentz factors such that $\gamma_m < \gamma_c$, which is known as the slow cooling regime. In this case only a certain fraction of the electron population will have Lorentz factors $\gamma_e > \gamma_c$ and radiate as $\nu_e^{-1/2}$.

The spectra produced for populations of electrons in the slow and fast cooling regimes, are shown in Fig. 1.3, where ν_a is below the minimum characteristic frequency and the cooling frequency in both cases. The time dependencies of ν_m and ν_c are indicated in the figure for both an ISM (above the arrow) and a wind-like circumburst medium (below the arrow). In both situations there is a change in the spectrum below ν_a to a power law distribution that varies as ν^2, due to SSA.
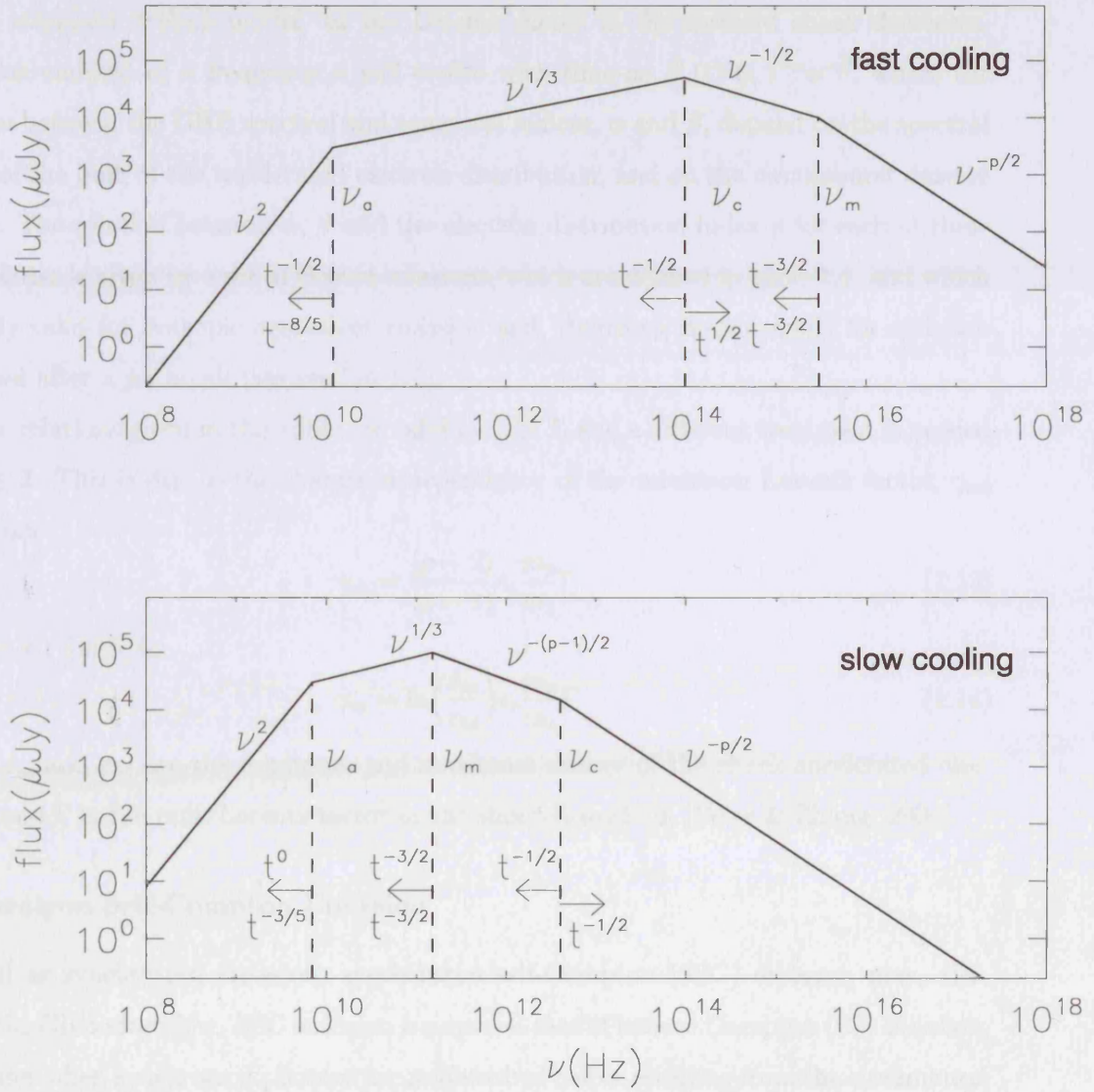
Figure 1.3: Synchrotron spectrum for a relativistic shock that accelerates electrons to a power law electron distribution with an index p and minimum frequency ν_m. The break frequencies are determined by the synchrotron self-absorption, ν_a, and the cooling frequency, ν_c. The top panel corresponds to the spectrum produced in the fast cooling regime ($\nu_m > \nu_c$), and the bottom panel corresponds to the slow cooling regime ($\nu_m < \nu_c$). The time dependencies on the spectral break frequencies are indicated for an ISM and wind density circumburst medium above and below the arrows, respectively

Closure Relations

In the standard fireball model, as the Lorentz factor in the forward shock decreases, radiation emitted at a frequency ν will evolve with time as $F_\nu(t) \propto t^{-\alpha}\nu^{-\beta}$, where the relation between the GRB spectral and temporal indices, α and β, depend on the spectral phase of the bulk of the accelerated electron distribution, and on the circumburst density profile. The relation between α, β and the electron distribution index p for each of these possibilities is given by a set of closure relations, which are defined in table 1.1, and which are only valid for isotropic equivalent emission and, therefore, do not apply for emission observed after a jet break (see section 1.7).

The relations given in this table are valid for $p > 2$, and a different treatment is needed for $p \leq 2$. This is due to the change in dependency of the minimum Lorentz factor, γ_m, on p from

$$\gamma_m = \frac{(p-2)}{(p-1)}\epsilon_e\frac{m_p}{m_e}\Gamma \tag{1.13}$$

[Sari et al., 1998] to

$$\gamma_m = \ln\left(\frac{\varepsilon_m}{\varepsilon_M}\right)\epsilon_e\frac{m_p}{m_e}\Gamma \tag{1.14}$$

where ε_m and ε_M are the minimum and maximum energy of the shock accelerated electrons, and Γ is the bulk Lorentz factor in the shocked medium [Pe'er & Zhang, 2006].

Synchrotron Self-Compton Emission

As well as synchrotron emission, synchrotron self-Compton (SSC) emission may, also, affect the GRB afterglow. SSC emission is a special case of Inverse Compton (IC) emission, and arises when synchrotron photons are re-absorbed before escaping from the circumburst environment of the GRB. In IC emission an electron that collides with a photon transfers some of its energy to the photon, giving rise to a harder spectrum. In SSC emission, the same electrons excited in a magnetic field and producing synchrotron radiation are also upscattering the photons they released through the IC process. The energy gained by the radiation field from the electron is proportional to γ^2, which, for a typical afterglow spectrum, corresponds to $\gtrsim 5$ keV. GRB afterglows have not generally been observed at

Table 1.1: Temporal index α and spectral index β in various afterglow models.[1]

	$p > 2$			$1 < p < 2$	
	β	α	$\alpha(\beta)$	α	$\alpha(\beta)$
ISM, slow cooling					
$\nu < \nu_m$	$-\frac{1}{3}$	$-\frac{1}{2}$	$\frac{3\beta}{2}$	$-\frac{p+2}{8(p-1)}$	
$\nu_m < \nu < \nu_c$	$\frac{p-1}{2}$	$\frac{3(p-1)}{4}$	$\frac{3\beta}{2}$	$\frac{3(p+2)}{16}$	$\frac{3(2\beta+3)}{16}$
$\nu > \nu_c$	$\frac{p}{2}$	$\frac{3p-2}{4}$	$\frac{3\beta-1}{2}$	$\frac{3p+10}{16}$	$\frac{3\beta+5}{8}$
ISM, fast cooling					
$\nu < \nu_c$	$-\frac{1}{3}$	$-\frac{1}{6}$	$\frac{\beta}{2}$	$-\frac{1}{6}$	$\frac{\beta}{2}$
$\nu_c < \nu < \nu_m$	$\frac{1}{2}$	$\frac{1}{4}$	$\frac{\beta}{2}$	$\frac{1}{4}$	$\frac{\beta}{2}$
$\nu > \nu_m$	$\frac{p}{2}$	$\frac{3p-2}{4}$	$\frac{3\beta-1}{2}$	$\frac{3p+10}{16}$	$\frac{3\beta+5}{8}$
Wind, slow cooling					
$\nu < \nu_m$	$-\frac{1}{3}$	0	$\frac{3\beta+1}{2}$	$\frac{5(p-2)}{12(p-1)}$	
$\nu_m < \nu < \nu_c$	$\frac{p-1}{2}$	$\frac{3p-1}{4}$	$\frac{3\beta+1}{2}$	$\frac{p+8}{8}$	$\frac{2\beta+9}{8}$
$\nu > \nu_c$	$\frac{p}{2}$	$\frac{3p-2}{4}$	$\frac{3\beta-1}{2}$	$\frac{p+6}{8}$	$\frac{\beta+3}{4}$
Wind, fast cooling					
$\nu < \nu_c$	$-\frac{1}{3}$	$\frac{2}{3}$	$\frac{1-\beta}{2}$	$\frac{2}{3}$	$\frac{1-\beta}{2}$
$\nu_c < \nu < \nu_m$	$\frac{1}{2}$	$\frac{1}{4}$	$\frac{1-\beta}{2}$	$\frac{1}{4}$	$\frac{1-\beta}{2}$
$\nu > \nu_m$	$\frac{p}{2}$	$\frac{3p-2}{4}$	$\frac{3\beta-1}{2}$	$\frac{p+6}{8}$	$\frac{\beta+3}{4}$

[1] Taken from Zhang & Mészáros [2004]

energies higher than ~ 10 keV, and any SSC component can, therefore, only be observed in the $\sim$5–10 keV range. Such a component would cause a flattening of the X-ray light curve relative to that produced by synchrotron emission alone, due to the increase in X-ray photons.

The SSC emission spectrum is made up or four power law segments with the same corresponding spectral indices for each segment as for the synchrotron spectrum, but the location of the three break frequencies ν_a^{IC}, ν_m^{IC}, and ν_c^{IC}, will be a factor of γ_a^2, γ_m^2 and γ_c^2 larger, respectively, than the break frequencies in the synchrotron spectrum.

The X-ray Light Curves

Spectral evolution is frequently observed between phase I and phase II of the X-ray light curve (see section 1.2.2 and fig 1.4), suggesting that these two phases stem from different emission mechanisms, which could mark the transition from internal shock to external shock dominated emission [e.g Burrows et al., 2005b, Zhang et al., 2006].

The initially steep decay phase observed in a large fraction of GRB X-ray light curves could be interpreted as the low-energy tail of the prompt emission. This tail emission results from the 'curvature' effect [e.g. Kumar & Panaitescu, 2000, Dermer, 2004], and is due to the reduced effect of the Doppler boosting at larger angles, θ, which is approximately proportional to $\propto \theta^{-2}$. This emission, also termed as high-latitude emission, is observed at later times than the prompt emission due to the increase in distance that photons have to travel from regions at larger angles to the line of sight. A high-latitude emission model for the steep X-ray decay phase is supported by the smooth transition observed in many cases between the prompt γ-ray emission with the spectral extrapolation of the early-time X-ray light curve [O'Brien et al., 2006]. However, assuming that the internal engine switches off abruptly, the relation between the temporal (α) and spectral (β) indices resulting from the curvature effect is $\alpha = 2 + \beta$, and this is not typically observed to be the case [e.g. Willingale et al., 2007]. GRBs with an initially steep decay phase in the X-ray band (phase I) usually have decay indices $\alpha > \beta + 2$.

The break into the second phase of the X-ray light curve to a shallower decay phase
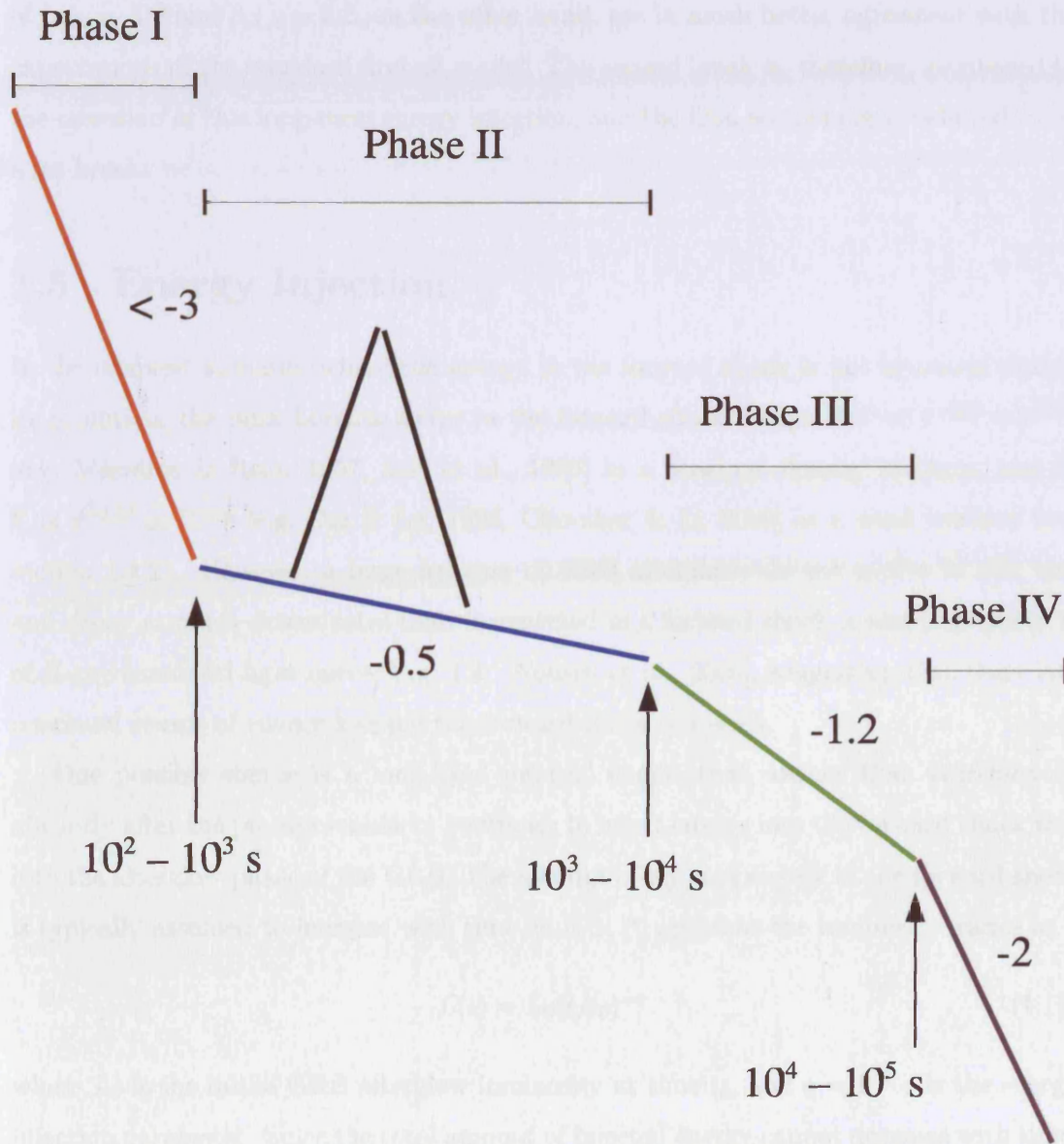
Figure 1.4: Schematic illustration of canonical X-ray light curve. The light curve is composed of four power law segments with flares overlaid. [Nousek et al., 2006]

with $\alpha_{X,2} \sim 0.5$ (see Fig. 1.4), may define the time when the external shock becomes dominant over the internal shock emission. However, the X-ray energy spectral indices during this phase are around $\beta_X \sim 1$, which, given the decay phase, is inconsistent with the standard fireball model, and energy injection is required to maintain this near-constant X-ray emission (see section 1.5). The second and third breaks to steeper decays of $\alpha_{X,3} \sim 1.2$ and $\alpha_{X,4} \sim 2.2$, on the other hand, are in much better agreement with the expectations of the standard fireball model. The second break is, therefore, attributed to the cessation of this long-term energy injection, and the final steepening is believed to be a jet break.

1.5 Energy Injection

In the simplest scenario, where the energy in the forward shock is not increased during its evolution, the bulk Lorentz factor in the forward shock decays as $\Gamma \propto r^{-3/2} \propto t^{-3/8}$ [e.g. Mészáros & Rees, 1997, Sari et al., 1998] in a constant density medium, and as $\Gamma \propto r^{-1/2} \propto t^{-1/4}$ [e.g. Dai & Lu, 1998, Chevalier & Li, 2000] in a wind medium (see section 1.4.2). However, a large fraction of GRB afterglows do not evolve in this way and decay at much slower rates than is expected in a forward shock model [e.g. phase II of X-ray canonical light curve, Fig. 1.4; Nousek et al., 2006], suggesting that there is a continual source of energy keeping the forward shock refreshed.

One possible source is a long-lived internal engine that, rather than switching-off abruptly after the prompt emission, continues to inject energy into the forward shock well into the afterglow phase of the GRB. The amount of injected energy in the forward shock is typically assumed to increase with time as $\dot{E} \propto t^e$, and thus the luminosity varies as

$$L(t) = L_0(t/t_0)^{-q}, \tag{1.15}$$

where L_0 is the initial GRB afterglow luminosity at time t_0, and $q = 1 - e$ is the energy injection parameter. Since the total amount of injected energy cannot decrease with time, $e > 0$, and, therefore, $q < 1$, where $q = 1$ corresponds to there being no energy injection.

Taking energy injection into account the dependence of Γ on distance from the source, r, and time, t, is then

$$\Gamma \propto r^{-(2+q)/2(2-q)} \propto t^{-(2+q)/8}, \quad r \propto t(2-q)/4, \tag{1.16}$$

$$\Gamma \propto r^{-q/2(2-q)} \propto t^{-q/4}, \quad r \propto t(2-q)/2, \tag{1.17}$$

for an ISM and wind density profile, respectively.

However, energy may be injected into the forward shock without the need for the internal engine to be active for the duration of the energy injection phase, which can continue for up to 10^6 s [e.g. Romano et al., 2006a]. Instead, slower moving material can continue to replenish the energy in the forward blast wave a long time after the internal engine has become inactive [e.g. Rees & Mészáros, 1998, Sari & Mészáros, 2000, Granot & Kumar, 2006].

Ejecta are likely to be released from the GRB internal engine in clumps, producing shells with a range in Lorentz factors. As leading shells are slowed down by the cir-cumburst medium, slower, trailing shells will plough into the forward shock and produce late-time shocks, which re-energise and refresh the forward shock.

In order for the injection to be smooth, the distribution in Lorentz factor amongst the shells should approximate a power law, where the amount of ejected mass moving with Lorentz factor greater than γ is

$$M(> \gamma) \propto \gamma^{-s}. \tag{1.18}$$

The resulting energy injected into the fireball is then proportional to the bulk Lorentz factor such that $\dot{E} \propto \Gamma^{1-s}$. A density profile index of $s = 1$, therefore, corresponds to zero energy injection in the afterglow, and $s > 1$ is needed in order for refreshed shocks to occur. Energy injection through refreshed shocks then modifies the evolution of the bulk Lorentz factor to

$$\Gamma \propto R^{-3/(1+s)} \propto t^{-3/(7+s)}, \quad R \propto t^{(1+s)/(7+s)}, \tag{1.19}$$

$$\Gamma \propto R^{-1/(1+s)} \propto t^{-1/(3+s)}, \quad R \propto t^{(1+s)/(3+s)}, \tag{1.20}$$

for an ISM and wind circumburst density profile, respectively.

The effect that the two energy injection mechanisms described above have on the observed afterglow decay rate are essentially indistinguishable without other contextual factors, and both mechanisms can be inter-changed whereby

$$s = \frac{10 - 7q}{2 + q}, q = \frac{10 - 2s}{7 + s}, \tag{1.21}$$

$$s = \frac{4 - 3q}{q}, q = \frac{4}{3 + s}, \tag{1.22}$$

for an ISM and wind circumburst density profile respectively

1.6 GRB Efficiency

An important GRB parameter is the efficiency of the burst, which is a measure of how effectively kinetic energy is converted into electromagnetic radiation during its prompt phase. This is defined by

$$\eta \equiv E_\gamma / (E_k + E_\gamma), \tag{1.23}$$

where E_γ is the energy emitted during the GRB prompt emission in a given energy band, and E_k is the kinetic energy remaining at the onset of the afterglow. This definition of GRB efficiency assumes that by the end of the prompt phase no further energy is injected into the jet by the internal engine.

1.7 GRB Outflow in Jets

Prompt isotropic-equivalent luminosities on the order of $L_{iso} \sim 10^{54}$ erg s^{-1}, such as was observed in GRB 990123, are around two orders of magnitude larger than expected from the collapsar model [e.g. MacFadyen & Woosley, 1999], and such energies would require a highly efficient GRB with an implausibly large progenitor.

The large energies observed in GRBs are more easily explained by including the possibility of collimation, as is observed in a number of compact astrophysical sources (e.g. AGN, micro-quasars). Material ejected by the black hole will take the easiest exit path,

Table 1.2: Temporal index α and spectral index β in various afterglow models with energy injection taken into account, where q is the energy injection parameter.[1]

	β	$\alpha(\beta)$
ISM, slow cooling		
$\nu < \nu_m$	$\frac{5q-8}{6}$	$(q-1) + \frac{(2+q)\beta}{2}$
$\nu_m < \nu < \nu_c$	$\frac{(2p-6)+(p+3)q}{4}$	$(q-1) + \frac{(2+q)\beta}{2}$
$\nu > \nu_c$	$\frac{(2p-4)+(p+2)q}{4}$	$\frac{q-2}{2} + \frac{(2+q)\beta}{2}$
ISM, fast cooling		
$\nu < \nu_c$	$\frac{7q-8}{6}$	$(q-1) + \frac{(2-q)\beta}{2}$
$\nu_c < \nu < \nu_m$	$\frac{3q-2}{4}$	$(q-1) + \frac{(2-q)\beta}{2}$
$\nu > \nu_m$	$\frac{(2p-4)+(p+2)q}{4}$	$\frac{q-2}{2} + \frac{(2+q)\beta}{2}$
Wind, slow cooling		
$\nu < \nu_m$	$\frac{q-1}{3}$	$\frac{q}{2} + \frac{(2+q)\beta}{2}$
$\nu_m < \nu < \nu_c$	$\frac{(2p-2)+(p+1)q}{4}$	$\frac{q}{2} + \frac{(2+q)\beta}{2}$
$\nu > \nu_c$	$\frac{(2p-4)+(p+2)q}{4}$	$\frac{q-2}{2} + \frac{(2+q)\beta}{2}$
Wind, fast cooling		
$\nu < \nu_c$	$\frac{1+q}{3}$	$\frac{q}{2} - \frac{(2-q)\beta}{2}$
$\nu_c < \nu < \nu_m$	$\frac{3q-2}{4}$	$\frac{q}{2} - \frac{(2-q)\beta}{2}$
$\nu > \nu_m$	$\frac{(2p-4)+(p+2)q}{4}$	$\frac{q-2}{2} + \frac{(2+q)\beta}{2}$

[1] Taken from Zhang et al. [2006]

which is along the rotational axis of the accretion disk, and can be collimated by either a large magnetic field or by pressure from the medium surrounding the jet. The collimated energy is a factor f_b of the isotropic equivalent energy, E_{iso}, where $f_b = 1 - \cos\theta_j$, and θ_j is the jet half-opening angle [Rhoads, 1997, Sari et al., 1999], and this correction can reduce the energy budget by several orders of magnitude [Rhoads, 1997]. This has led to speculation that there is a single GRB energy reservoir, such that the observed spread in isotropic luminosities is the result of a range in jet-opening angles [Frail et al., 2001, Bloom et al., 2003].

One of the consequences of collimation is a break in the afterglow light curve, which occurs when the observer can see the edge of the jet. Although in the co-moving frame radiation is emitted isotropically, relativistic effects cause a significant fraction of radiation to be beamed into a cone with half-opening angle Γ^{-1}, where Γ is the bulk Lorentz factor of the ejecta. To produce the highly variable prompt emission observed in GRBs, the initial bulk Lorentz factor must be large, such that it is typically the case that $\Gamma > 1/\theta_j$. The radiation is, thus, beamed into a cone that has a smaller opening angle than the jet itself. As the jet is slowed down through interactions with the circumburst material, the Lorentz factor becomes smaller, and the beaming angle increases. At $\Gamma \sim \theta_j^{-1}$, the whole of the jet can be seen, and as the Lorentz factor continues to fall, the beaming cone expands further and covers areas beyond the emission region. The result is that the observed emission from the jet decreases more rapidly than before, producing a break in the afterglow light curve across the spectrum. This is known as a jet break.

The change in decay index at the jet break will depend on the specifics of the jet model, such as the sharpness of the edge of the jet and whether or not the causal connection between the axis and edge of the jet when $\Gamma \sim \theta^{-1}$ leads to lateral expansion. However, in the simplest model where the jet is assumed to have a constant energy density profile with a sharp cutoff at the edges and no lateral expansion, the decay index will decrease by $\Delta\alpha = 3/4$ at the time of jet break. The variations in the change in decay rate with jet model are discussed further in chapter 3.

1.7.1 Time of Jet Break

The well-sampled X-ray and optical light curves provided by the simultaneous observations of GRB afterglows available with the *Swift* satellite have resulted in far fewer achromatic breaks than had been expected prior to launch, and this result is presenting a challenge for GRB jet models.

For spherical adiabatic evolution into an ISM-like circumburst medium, the bulk Lorentz factor decreases with time as $\Gamma(t) = 6(E_{k,52}/n)^{1/8}t^{-3/8}(1 + z)^{3/8}$, where n is the mean circumburst environment density, $E_{k,52}$ is the kinetic isotropic-equivalent energy in the fireball in units of 10^{52} erg, and t is the time in units of days [Sari et al., 1999]. The time of jet break, when $\Gamma \propto \theta_j^{-1}$, will, therefore, depend on both the density of the circumburst environment and the kinetic energy within the jet, where a denser circumburst environment will slow down the jet more rapidly, and a more energetic jet will need to accumulate a greater amount of mass to slow it down. For a constant density circumburst environment, the time of the jet break, t_j, is related to the jet-opening angle, θ_j, by

$$t_j = 119(1 + z)(E_{k,52}/n)^{1/3}\theta_j^{8/3} \tag{1.24}$$

The time of the jet break, t_j, is, therefore, most strongly dependent on the jet-opening angle, θ_j, and the lack of an observed jet break in the *Swift* sample may, therefore, be the result of either larger or smaller average jet-opening angles than had previously been proposed. In this case the GRB jet break will occur outside the observing window, either before the first UV/optical and X-ray observations or at a time when the afterglow flux is below the detectability threshold,

1.8 X-Ray Flashes (XRFs), X-Ray Rich (XRR) and *Classical* Gamma-Ray Bursts

X-Ray Flashes and X-Ray Rich GRBs are a category of GRBs that have a softer prompt emission spectrum. The first indication of this subclass of GRB came with the detection

of X-ray transients by the Wide Field Cameras (WFC), on-board the Italian-Dutch X-ray satellite *Beppo*SAX, which showed similar properties to GRBs, but lacked a counterpart detection in the γ-ray monitor (40-700 keV). The connection between these WFC sources and GRBs was made by the simultaneous observations of ten of the WFC XRFs by BATSE. However, it was not until the launch of HETE-2 that systematic and simultaneous observations of XRFs in the 2–30 keV and 30–400 keV energy bands were possible, which led to the categorisation of GRBs into three spectral classes. This was based on the hardness ratio between the 2 – 30 keV (S_X) and 30 – 400 keV (S_γ) energy range, where $\log[S_X/S_\gamma] > 0$, $-0.5 < \log[S_X/S_\gamma] < 0$, $\log[S_X/S_\gamma] < -0.5$ provided the thresholds between X-Ray Flashes, X-Ray Rich GRBs and classical GRBs.

1.9   Optically *Dark* GRBs

The lack of an optical afterglow detection in $\sim 50\%$ of GRBs detected by *Beppo*SAX prompted a new classification of GRBs based on their optical afterglow properties; those bursts with no optical afterglow detection were referred to as 'dark'. This definition is rather ambiguous given the observational inhomogeneities that exist within GRB samples, including differences in the number of observations and in the wavebands used, and the promptness and depth of these observations. The rapid follow up observations made possible by the arcsecond localisations available with the HETE-2 mission reduced the fraction of dark bursts to 10%, with 12/13 of those observed in the first year having an optical counterpart [Ricker et al., 2003]. These observations led to the belief that the prime cause of dark bursts was that they had dim afterglows that had decayed below the sensitivity levels, and that, therefore, prompt optical and IR observations of GRB afterglows would further reduce the fraction of dark GRBs. However, in the *Swift* era, UVOT observations have found the fraction of GRBs with no afterglow detection blueward of ~ 5500 Å to have risen to $\sim 2/3$.

There are several possible explanations for the lack of an optical counterpart, including: extinction of the afterglow by dust [e.g. Taylor et al., 1998], Ly-α blanketing and

absorption due to high redshift [e.g. Groot et al., 1998a], low-density environments [e.g. Frail et al., 1999, Groot et al., 1998b, Taylor et al., 2000], steep optical decays [e.g. Groot et al., 1998b], and intrinsic faintness of the afterglow [e.g. Lazzati et al., 2002]. It is likely that dark GRBs stem from a combination of these explanations.

1.10 GRB Local Environments

1.10.1 GRB Host Galaxies

Short GRBs

Since the launch of *Swift* the afterglows of a number of short GRB have been detected, leading to the identification of their host galaxies [e.g. GRB 050709; Fox et al (2005), Villasenor et al. (2005), Hjorth et al. (2005), Covino et al. (2006), GRB 050724; Berger et al. (2005c), Gorosabel et al (2006), Soderberg et al. (2006)], which have been identified as both late-time, red ellipticals and as well as star forming galaxies. The star formation rate (SFR) of short GRB hosts are typically $0.1 - 0.2$ $M_\odot \mathrm{yr}^{-1}$ [e.g. GRB 050509b; Gehrels et al., 2005, GRB 050709; Hjorth et al., 2005], in contrast to long GRB host galaxies, which are observed to have SFRs at least an order of magnitude larger than this, lying in the range $1 - 10$ $M_\odot \mathrm{yr}^{-1}$. The well-studied host-galaxy of the short GRB 051221a, however, has a SFR more typical of long GRB hosts, with 1.6 ± 0.4 $M_\odot \mathrm{yr}^{-1}$ [Soderberg et al., 2006], although the specific SFR is around 2.5 times less than that which is typical for long GRBs [Christensen et al., 2004]. Short GRBs also have large offsets, in comparison with long GRBs, between the burst location and the centre of the host galaxy. The measured offsets for short GRBs currently range from 760 ± 30 pc for GRB 051221a [Soderberg et al., 2006] to 40 ± 13 kpc for GRB 060502b [Bloom et al., 2007]. Both these large offsets and the small amount of star formation that is detected in short GRB hosts suggests that short GRBs are not due to collapsars, whose progenitors have short lifetimes ($\sim$ a few Myrs). These observations are more consistent with binary merger progenitors, which will have received a large velocity kick during the supernova explosions that formed

the compact components. The range observed in the offsets between short GRBs and their host galaxies, as well as the galaxy types suggests that the progenitor lifetimes span a wide distribution of delay times between formation and explosion, and this can be accounted for by the expected distribution in the properties of the binary system, such as the kick velocities the system receives, the mass of the host, and the timescale for the compact binary system to form, and orbiting objects to merge.

Long GRBs

Observations of long GRB host galaxies suggest that they are sub-luminous, blue compact, irregular or merging systems [Le Floc'h et al., 2003, Fruchter et al., 2006]. Blue compact dwarf galaxies have low metallicities [e.g. Wu et al., 2006], and assuming the luminosity-metallicity correlation holds [Shi et al., 2005], a sub-luminous host would be consistent with the collapsar model, which requires a low metallicity environment, at least in the local surroundings of the GRB. However, the collapsar model also predicts the progenitor star to be found deep in the galaxy, in stellar nurseries, where the environment is dense and enshrouded in dust. In this case the host galaxies of GRBs would be expected to be luminous starbursts. HST observations of 40 GRB revealed this not to be the case, where none of the host galaxies observed were bright red, sub-millimetre bright galaxies [Fruchter et al., 2006]. Similarly, observations of 16 GRB host galaxies with the *Spitzer Space Telescope* found few detections in the IR, suggesting that the hosts are not dusty [Le Floc'h et al., 2006].

However, red, dusty galaxies have substantial metallicities at all redshifts, and the typically blue galaxies observed to host long GRBs could indicate a preference for GRB progenitors to reside in low metallicity environments that are experiencing a first episode of very massive star formation with a weak underlying stellar population [Fruchter et al., 2006]. Alternatively, the sample of detected host galaxies for long GRBs could suffer from selection effects. As already mentioned in section 1.9, one cause for the lack of an optical afterglow detection in some GRBs could be due to them having dusty hosts, which extinguish the optical afterglow. It is possible that the host galaxies of GRBs with

no optical afterglow detection are dustier than those galaxies that host optically bright GRBs. However, the lack of arcsecond positions provided by optical afterglows make it harder to identify these hosts, and they may, therefore, be under-represented in the sample of long GRB host galaxies.

1.10.2 Absorption and Extinction of GRB Afterglows

Due to the power law spectral appearance of GRB afterglows, the effect of absorbing dust and gas in the local environment on the GRB spectral energy distribution (SED) can be identified well, providing a measure of the dust and gas column densities along the line of sight.

The gas column density is estimated from the amount of absorption observed in the soft X-rays, which is primarily due to K-shell photoionisation of medium-weight elements in the GRB surrounding environment. Metal abundances typically decrease with increasing atomic number, Z, and most of the observed X-ray absorption is, therefore, primarily caused by elements with binding energies in the 0.2–2.0 keV energy range, such as oxygen and carbon [Morrison & McCammon, 1983]. Above the ionising threshold, the absorption cross-section of an element decreases as ν^{-3}, and above ~ 7 keV the cross-section is, therefore, so small that absorption becomes negligible.

Most radiation in the rest frame UV energy band is absorbed by neutral hydrogen in the intergalactic medium, which has a binding energy of 13.6 eV. This corresponds to a wavelength of $\lambda = 912.5$ Å and the sharp cutoff that results at rest frame wavelengths blueward of this is known as the Lyman-edge. At energies below the neutral hydrogen edge Ly-α transitions of neutral hydrogen, referred to as the Ly-α forest, cause absorption in the 912–1215 Å wavelength range. The amount of absorption caused by the Ly-α forest is highly dependent on redshift, and will be larger for objects at higher redshifts due to the increase in the likely number of intervening Ly-α forest absorption systems. At redshift $z = 2.5$ Ly-α absorption is of the order of ~ 50 %, and this increases to ~ 98 % for sources at $z = 4.5$ [Madau, 1995].

A further source of optical to NIR absorption is dust, which may dominate over neutral hydrogen absorption at wavelengths redward of 912 Å. Dust may either absorb or scatter UV to NIR radiation out of the line of sight, although typically it is difficult to make a distinction between the two processes from observations. The term extinction is, therefore, used to refer to the combined effect of both absorption and scattering.

Mathis et al. [1977] found the average extinction observed in the Milky Way to be well fit by a population of dust grains composed of a mixture of only silicates and graphites, with a power law dust grain size distribution for each component given by $n(a)da \propto a^{-q}da$ for $q = 3.5$ and $a_{min} < a < a_{max}$, where a is the dust grain radius. They found the size range in graphite to be about $a = 0.005 - 1$ μm and $a = 0.025 - 0.25$ μm for silicates. This model is now referred to as the MRN model of the interstellar grain population, named after its authors, and continues to be in good agreement with current observations of the Milky Way ISM, which over the last few decades have extended further into the NIR and the UV. A silicate/graphite model has also been found to fit other environments well, such as the Small and Large Magellanic Clouds (SMC and LMC, respectively) [Pei, 1992], where the differences in the extinction law can be explain by variations in the grain size distribution and in the relative silicate to graphite abundances.

1.10.3 Effect of GRB Emission on its Environment

It is likely that the intense X-ray and UV radiation emitted by a GRB during the early stages of its evolution will alter the dust grain size distribution and gas ionisation state in the circumburst environment through dust destruction and photoionisation. The amount of photoionisation and dust destruction that occurs will depend on the properties of both the local environment and the GRB itself. Simulations suggest that a typical GRB with 1 eV–100 keV luminosity $L = 10^{50}$ erg s^{-1} will destroy all dust and fully photoionise gas within a radius of a few parsecs [Perna & Lazzati, 2002], and analysis of the spectroscopic properties of the gas suggests that GRBs are capable of photoionising the gas out to radii of a few tens of parsecs [e.g. Prochaska et al., 200].

The photoionisation of gas is caused by the absorption of photons with energies at least as large as the elements' binding energy, as described in section 1.10.2. The destruction of dust is also caused by the absorption of radiation, which will lead to either the heating and sublimation of the grain, or to the shattering of the dust, due to an increase in the Coulomb forces within the grain. Which of these two destruction processes is dominant depends on the intensity of the radiation field and its spectrum.

1.11 Layout Of This Thesis

In this thesis I use early time, simultaneous UV/optical, X-ray and γ-ray data of GRBs, taken with *Swift*, to address some of the still poorly understood GRB phenomenology. In particular I investigate the extrinsic and intrinsic properties that distinguish two particularly interesting bursts from the class of long GRB, and study the local environment of optically bright GRBs to understand better the effect the GRB has on its surrounding environment and vice versa.

In chapter 2 I provide a description of *Swift* and of the three telescopes on-board. I explain the observing strategy followed to maximise the early and late time data return from GRBs and the data reduction techniques that are used for all three instruments. Chapter 3 is an extension on the work of Schady et al. [2006], in which I provide a detailed analysis of *Swift* observations of XRF 050406, which at the time were the earliest to be taken of an XRF optical counterpart, and covers an important time interval during which the predictions from various models of XRFs differ. To better understand the effect that extrinsic properties have on the observed afterglows of GRBs, I investigate their circumburst media in chapter 4 by modelling the combined X-ray and UV/optical spectral energy distributions (SEDs) for a sample of seven GRBs, and use the SMC, LMC and Galactic dust extinction curves to model the dust in the GRB host galaxies. This chapter is based on the work of Schady et al. [2007a]. Chapter 5 builds on the work of Schady et al. [2007b], and provides a detailed analysis of an exceptionally bright burst, GRB 061007, to understand the distinguishing properties that provide such a large isotropic equivalent

luminosity. Finally, in chapter 6 I present a summary of the implications that the findings of this thesis have for our understanding of GRBs, with particular focus on the population of dark GRBs, and use the results from chapter 4 to investigate the implications of dust extinction on the population of dark GRBs. All errors quoted in this thesis are at the 1σ level, unless stated otherwise and temporal and spectral indices, α and β, are given using the standard GRB convention of $F(t) \propto t^{-\alpha}$ and $F(\nu) \propto \nu^{-\beta}$. Luminosities and the energy release are calculated assuming a standard cosmology model with $H_0 = 70$ km s^{-1} Mpc^{-1}, $\Omega_M = 0.3$ and $\Omega_\lambda = 0.7$.

Chapter 2

The *Swift* Mission

The *Swift* satellite was launched on November 20th 2004, and was designed with the specific aim of observing GRBs during the prompt and afterglow phases. To maximise its scientific potential it has rapid-response capabilities and is equipped with three telescopes that cover the γ-ray, X-ray and UV/optical energy range. These are the Burst Alert Telescope [BAT; Barthelmy et al., 2005a], which is wide-field instrument designed to detect the prompt GRB emission, the X-Ray Telescope [XRT; Burrows et al., 2005a] Burrows et al. 2005) and the Ultra-Violet and Optical Telescope [UVOT; Roming et al., 2005]. The XRT and UVOT are narrow field instruments that observe the GRB in the X-ray, UV and optical energy ranges.

Before the launch of *Swift*, optical observations of GRB afterglows typically started 30 minutes or so after the prompt emission, and even later than this in the X-ray band. *Swift* is engineered to rapidly slew to a burst as soon as a GRB is detected by the BAT, and can place the GRB in the field of view (FOV) of the XRT and UVOT within 100 s. *Swift* is, therefore, probing a previously unexplored time-domain, which is crucial for studying the internal engine of GRB and the overlap between the prompt and afterglow emission.

2.1   *Swift* Observing Strategy

Swift was launched into a low circular Earth orbit, inclined at about 20.5° to the equatorial

plane and with an orbital period of $\sim$ 90 minutes. A Pre-Planned Science Timeline (PPST) is uploaded to the spacecraft every weekday or at the beginning of the weekend, providing an observing schedule with a list of targets that *Swift* observes during its orbit. Each target has a figure-of-merit (FoM) assigned to it. When a transient is detected by BAT it is also assigned an FoM, and it is this value that determines whether a slew manoeuvre is requested of the spacecraft. If the detected transient has a larger FoM than that of the pre-planned target currently being observed, the BAT software will request a slew. A transient that fulfils the requirements expected from a GRB is assigned a top-level FoM, and will thus automatically override the pre-scheduled observing target. The BAT software localise the GRB in its image plane, and, providing there are no observing constraints, the spacecraft will automatically slew to the position of the GRB. The GRB will become the new, automated target (AT). Once the GRB is within the narrow field instruments' FOV, both the XRT and UVOT begin an automated sequence of observations.

Over 76% of BAT triggers have led to an immediate slew, in which case the XRT and UVOT are on-target within a minute or two, where the time taken depends on the time taken for the BAT to localise the GRB, and (primarily) on the length of the slew performed. However, there are times when the spacecraft cannot slew immediately as a result of an observing constraint (e.g. Sun, Moon, Earth), which can delay an XRT and UV/optical observation from minutes to as long as months after the trigger. In such a case the spacecraft is programmed to signal to the BAT when a GRB comes out of an observing constraint, at which point the command to slew to the source is resent. Delays deemed too long to credit a late-time slew can be aborted from the ground.

When a GRB triggers the BAT, the astrophysics community is alerted by GRB Coordinate Network Notices (GCN Notices) [1], which provide first level data products. These are sent down to the ground via the Tracking and Data Relay Satellite System (TDRSS). These notices provide the GRB position determined by the BAT, as well as the XRT and UVOT position when available, BAT and XRT early time light curves and spectra, and

---

[1]http://gcn.gsfc.nasa.gov/

UVOT finding charts. The full, high-resolution data sets are sent down to the Malindi Ground Station, located in Kenya. This occurs during Malindi passes, when the satellite is in view of the station, and takes place around 10–11 times a day, lasting for ~ 10 minutes at a time. From here it is forwarded to the Missions Operation Centre (MOC) in Pennsylvania, USA, and then to the *Swift* Data Centre (SDC) in Goddard Space Flight Center (GSFC), where the raw spacecraft telemetry is converted into calibrated and reduced data products and distributed to the community via the Quick-Look web site on timescales of 2–3 hrs. There is also a *Swift* science data centre at Leicester University in the UK, and at the ASI data centre in Italy, where the reduced data can also be accessed.

2.1.1 Burst Alert Telescope (BAT)

The Burst Alert Telescope is a coded aperture imaging, photon-counting instrument with a coded response in the energy range 15–150 keV, and an uncoded response up to 500 keV. The mask has as area of 2.7 m^2, which gives a large FOV that covers 1.4 steradians of the sky at any one time and is sensitive down to a count rate threshold of ~ 0.3 cts s^{-1}cm^{-2}. The detection rate for GRBs is at around 100 per year, and the average positional accuracy during 2006 and mid-way into 2007 is $\sim 1.7'$. The instrument properties are summarised in table 2.1.

The BAT is programmed to bin up data into time bins ranging from 4 ms to 16 s, which are monitored frequently for any significant increase in flux above an expected background rate, which is typically set to a $5 - 7\sigma$ rate increase. The background rate is continuously monitored for this purpose, and the BAT trigger threshold can be adjusted within the range of 4 to 11 σ above background.

When an event trigger occurs a background subtracted image is produced which is used to check for any uncatalogued point sources with brightness above a given significance. This minimises the number of false triggers caused by particle events or flickering in bright galactic sources. The BAT can also trigger on images, which are continually made on timescales ranging from 60 s to the duration of a pointing, and any significant point

Table 2.1: BAT Instrumental Properties

Property	Description
Aperture	Coded mask
Detecting Area	5240 cm^2
Detector	CdZnTe
Detector Operation	Photon counting
Field of View	1.4 sr (partially-coded)
Detection Elements	256 modules of 128 elements/modules
Detector Size	4 mm×4 mm×2 mm
Telescope PSF	17'
Energy Range	15–150 keV
Sensitivity	~ 0.3 cts s^{-1}cm^{-2}

sources within the image will generate a trigger. When an event or image trigger is generated the detection is assigned an FoM and a burst response is initiated. The BAT position and light curves are then sent to the ground through TDRSS for immediate inspection.

2.1.2   X-Ray Telescope (XRT)

Technical Description

The XRT is a focusing X-ray telescope with 12 nested mirrors that focus onto a CCD detector of the same kind as that used in XMM-*Newton*/EPIC MOS [Turner et al., 2001]. XRT has an effective area of 110 cm^2 at 1.5 keV, a 23.6 × 23.6' FOV, and an 18" spatial resolution (half power diameter; HPD) in the 0.2–10 keV energy range. It can reach a flux sensitivity limit of 2×10^{-14} erg cm^{-2} s^{-1} in 10^4 s. The instrument properties are summarised in table 2.2.

Table 2.2: XRT Instrumental Properties

Property	Description
Telescope	JET-X Wolter 1
Focal Length	3.5 m
Effective Area	110 cm^2 at 1.5 keV
Detector	EEV CCD-22,600 × 600 pixels
Detector Operation	Imaging, Timing and Photon-counting
Field of View	23.6 × 23.6'
Detection Element	40 × 40 micron pixels
Pixel Scale	2.36"/pixel
Telescope PSF	18" HPD at 1.5 keV
Energy Range	0.2–10 keV
Sensitivity	2×10^{-14} erg cm^{-2} s^{-1} in 10^4 s

Sequence of Observations

In the event of a BAT trigger, the XRT has an inbuilt automated operating sequence with an option of four read-out modes to maximise the instrument's capability to rapidly locate the source and acquire good quality data [Hill et al., 2004]. During the settling phase the XRT takes three images in image mode in order to centroid on the source. The three images have an exposure time of 0.1 s or 2.5 s, whereby a failure to centroid results in the longer exposure being used. When observing in image mode, the CCD operates like a normal optical CCD. The XRT then begins to also take time-resolved data in order to allow accurate measurements of bright sources that would otherwise suffer from pile-up if observed in imaging photon counting mode. Pile-up arises when the source photon flux is higher than the instrument readout rate such that two lower energy photons may be confused for a single high energy photon (see section 2.3.2). As the source flux decreases XRT automatically switches between read-out modes to optimise the time and spectral resolution of the data acquired.

Table 2.3: Summary of XRT mode characteristics

Mode	Image Capability	Spectra Capability	Time Resolution	Flux Level Mode Switch
Image	2D	No	0.1 s (short)	> 140 mCrab
		No	2.5 s (long)	5.6 mCrab
PD	no	Yes	0.14 ms	0.6–60 Crab
WT	1D	Yes	1.7 ms	1–600 mCrab
PC	2D	Yes	2.5 s	< 1 mCrab

At very high fluxes the Photo-Diode mode (PD) is available, which is a fast timing mode (0.14 ms) that integrates the count rate over the entire CCD and, therefore, loses all spatial information. The fast read-out time of the mode is important to avoid loss of spectral information from pile-up. However, the PD mode has not been in use since a micrometeorite event in late May of 2005 damaged a few columns on the XRT CCD, resulting in very high background rates in PD mode.

The Window Timing mode (WT), which has a 1.7 ms time resolution and 1-dimensional imaging, is estimated to be unaffected by pile-up for fluxes below 600 mCrabs. At least one WT frame is taken after the centroiding image, and if the source flux rate in the central 200 × 200 pixels is below 1 mCrab, a switch is made into the fourth available operating mode, which is Photon-Counting (PC). This has the lowest time resolution (2.5 s) but full imaging and spectroscopic resolution. A summary of the mode characteristics is provided in table 2.3.

2.1.3 Ultra-Violet and Optical Telescope (UVOT)

Technical Description

The UVOT is a 30 cm modified Ritchey-Chrétien reflector with two micro-channel plate intensified CCD detectors that are modelled on the Optical Monitor on-board XMM-*Newton* [Mason et al., 2001]. They are photon counting devices that are capable of detecting very low signal levels, unaffected by CCD read-out noise and cosmic ray events.

The UVOT contains three optical and three ultra-violet (UV) lenticular filters that cover the wavelength range 1600 − 6000 Å, a white band filter that has a good response ranging from 1600–8000 Å, and a blocked filter. The central wavelengths for the narrow band filters are given in table 2.4, and the corresponding responses are shown in Fig. 2.1.

The instrument also has a visible grism and a *UV* grism, which provide low resolution spectra ($\lambda/d\lambda \sim 75$) in the 2800–5200Å and 1600–2900Å energy range, respectively, for sources that are brighter than 17 mag for the optical and 15 mag for the UV. The instrument properties are summarised in table 2.5.

UVOT can record data in three modes, and these are image mode, event mode or image-event mode. Image mode provides a two-dimensional sky map with the start and stop time of the exposure recorded, although no timing information on the individual events is stored. In event mode both the position and time of each recorded event is registered with a time-resolution of 11 ms when the full frame is read out. The third UVOT mode provides both image and event mode data from the same exposure, and does not require the two windows to be of the same size, location or binning.

Sequence of Observations

During a slew UVOT is in blocked, and once UVOT is on-target it goes through a pre-defined set of observations. Since the launch of *Swift* the UVOT automated sequence has gone through a number of changes as the early time optical properties of GRBs have become better understood. A settling exposure of $\sim$ 9 s has always been taken, although this used to be in the *UVW*2 filter, and was changed to the *V*-band filter at the beginning

Table 2.4: UVOT filter central wavelengths

Filter	Central Wavelength (Å) (Å)	FWHM (Å)
V	5440	750
B	4390	980
U	3450	875
$UVW1$	2510	700
$UVM2$	2170	510
$UVW2$	1880	760

Table 2.5: UVOT Instrumental Properties

Property	Description
Telescope	Modified Ritchey-Chrétien
Focal Ratio	12.7
Detector	Intensified CCD
Detector Operation	Photon counting
Field of View	$17 \times 17'$
Detection Element	2048×2048 pixels
Pixel Scale	0.496"
Telescope PSF	2" FWHM at 3500 Å
Wavelength Range	1600–8000 Å
Colour Filters	6 + white filter
Sensitivity	$B = 20.7$ in white light in 1000 s
$\lambda/d\lambda$ (grism)	~ 75
Brightness limit	$V = 7.4$ mag
Camera Speed	11 ms
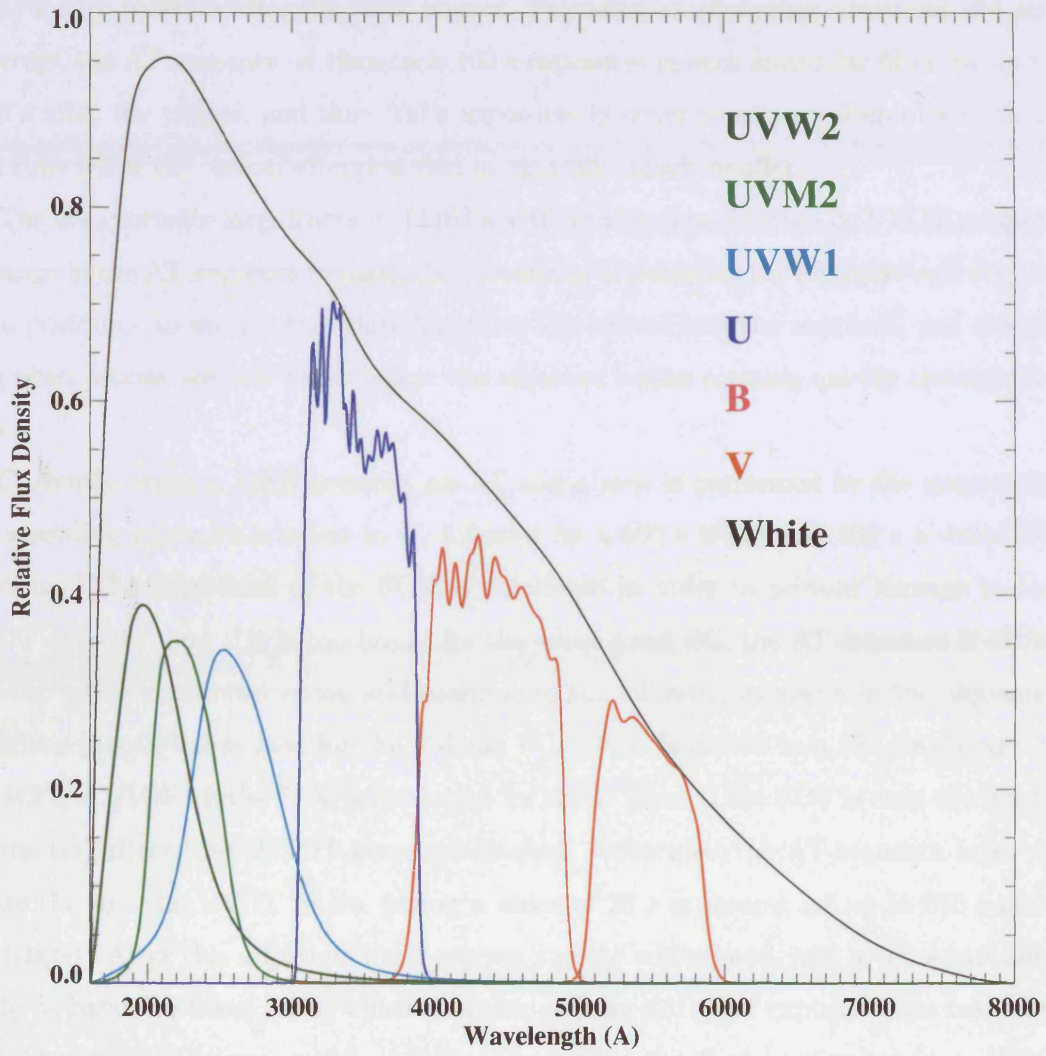
Figure 2.1: Ground based effective area curves for all seven UVOT lenticular filters [Roming et al., 2005].

of April, 2005. To maximise the colour information taken during the early stages of a GRB, the AT sequence prior to October of 2005 consisted of a V-band finding chart (FC) 100 s exposure, followed by a series of short 10 s exposures taken in each of the lenticular filters for up to 981 s after the BAT trigger. Providing an observing constraint did not interrupt the AT sequence, it then took 100 s exposures in each lenticular filter for up to 4096 s after the trigger, and then 900 s exposures in order to acquire deep observations at a time when the optical afterglow flux is, typically, much smaller.

The unexpectedly large fraction of GRBs with no afterglow detected by UVOT prompted a change in the AT sequence to maximise the chance of detecting the afterglow and acquiring a position. To do this the white-band was introduced into the sequence, and several long observations are now taken before the sequence begins rotating quickly through the filters.

Currently, when a GRB becomes an AT and a slew is performed by the spacecraft, a 9 s settling exposure is taken in V, followed by a 100 s white and 400 s V-band FC exposure. The brightness of the FOV is monitored in order to prevent damage to the UVOT detector, and if it is too bright for the white band FC, the AT sequence is set to skip the white band observation and continue to the following exposure in the sequence. A similar precaution is used for the V-band FC, which fails-over to a 150 s exposure in $UVM2$ and $UVW1$ if the FOV is too bright for the V filter. If the FOV is even too bright for the UV filters, then UVOT goes into blocked. Otherwise, the AT sequence is set to rotate through the UVOT filters, taking a series of 20 s exposures for up to 850 s after the trigger. After this a further 100 s exposure in the white band, and a 400 s exposure in the V-band are taken, after which a further sequence of short exposures are taken up to 2700 s after the trigger, which are 10 s in length for the B and white bands, and 20 s for the rest. Beyond this point a set of 100 s and then 900 s exposures are taken in each filter. The filter order of the exposures is set to the order in which they are arranged on the filter wheel in order to minimise the number of movements made by the filter wheel. This order is $UVM2$, $UVW1$, U, B, white, $UVW2$ and V.

All data up to 2700 s are taken in event mode with the exception of the second

white-band FC exposure, which is taken in image mode to save on telemetry. Image mode data are also available for the first white and both *V*-band FC exposures, thus providing a smaller image file that can be sent down to the ground quickly via TDRSS for immediate inspection. The high time-resolution event mode data taken at the start of the observation sequence are sent to the ground during the Malindi pass. To further save on TDRSS telemetry, the FCs are also binned 2 × 2. A detailed description of the different UVOT AT sequences used since the launch of *Swift* is given in appendix A.

2.2 Spacecraft Observing Constraints

As a result of *Swift's* low orbit, the Moon, Sun and Earth will always cause observing constraints of varying degrees. The spacecraft is programmed to not slew to a target that is less than 44° from the Sun, 19° from the Moon, or 30° from the Earth limb, which prevents the NFI's from observing some GRBs promptly. Both the Moon and Sun can block a target from the line of sight for weeks or months whereas a target will only ever be constrained by the Earth limb for a continuous period of 1 hr. This causes periodic gaps in the sequence of observations, which are present in every GRB data set.

One of the changes made to the AT sequence was in March 2005 was to take 3×300 *s* exposures in the optical filters rather than single 900 s, in order to minimise the number of image mode exposures contaminated by scattered light from the bright Earth limb.

2.3 Data Analysis

Swift data are processed and made available on the HEASARC quick-look site as they are received by the SDC from Malindi. The quick-look site is, therefore, continually updated as more data are received and processed by the SDC, where each update produces a new version number of the dataset in question. The initial data set does not, therefore, contain the entire observing sequence, which may not yet have been fully telemetered or processed. After one week the complete data set is taken off the quick-look site and stored

in the *Swift* archive, where the BAT, XRT and UVOT raw (level I) and reduced (level II) data products and housekeeping files can be downloaded.

Any further reduction of data used in this thesis is done in accordance with the BAT, XRT and UVOT calibration documentation[2], unless specified otherwise. There are variations in the versions of the *Swift* software tools and calibration products used, due to the continual updates made to these products. The precise version numbers used during the data reduction and analysis process are, therefore, provided separately in each chapter.

2.3.1 BAT

Downloaded BAT event data is further processed using the BAT pipeline, which produces calibrated light curves with time-resolutions varying from 2 ms to 1 s, pre-slew, peak, and time-averaged spectra, images and duration measurements from the level 1 products.

2.3.2 XRT

The XRT level I data are further processed with the XRTDAS software package, written by the ASI Science Data Centre (ASDC) and distributed within FTOOLS to produce the final cleaned event lists. Calibrated and cleaned level II event files are produced with the XRTPIPELINE task. Only time intervals with a CCD temperature below -50 °C and events with grades 0–12 and 0–2 are considered for the PC and the WT data analysis respectively [according to Swift nomenclature; Burrows et al., 2005a].

When reducing WT mode data a rectangular 40×20-pixel region positioned around the source and in a source free region of the FOV are used to extract source and background count rates, respectively. For PC data, source counts are extracted from a circular region centred on the source with an outer radius that is typically $\sim 100''$, which is ~ 92 % of the Point Spread Function (PSF) of the GRB [Moretti et al., 2005]. Source and background light curves and spectra are extracted within XSELECT, and spectral files are binned to at least 20 counts per energy bin in the 0.3–10 keV energy range, which is the recommended

---

[2]http://heasarc.gsfc.nasa.gov/docs/heasarc/caldb/swift/docs/

band to use for compatibility with the current calibration files[3]. Corresponding effective area files are created using the XRTMKARF tool, where the exposure map file is used to take into account any missing columns resulting from the micrometeorite event.

Pile-Up

GRBs that are very bright and have a count rate greater than ~ 250 counts s^{-1} in WT mode or ~ 0.6 counts s^{-1} in PC mode suffer from significant pile-up. This problem arises when two or more photons are collected in the same CCD pixel within the same frame, causing the charge from both photons to be combined and registered as a single event. The result is an overall loss of photons and an artificial excess of hard photons, which flattens the spectral index and causes the X-ray absorption to be over-predicted.

To deal with this problem a source extraction region that excludes the central pixels is used to remove the area on the CCD affected by pile-up. To determine the size of this exclusion region when analysing WT mode data, a source spectrum is obtained where initially a 15 pixel exclusion region is used. Further spectra are obtained where the size of the inner exclusion region is systematically reduced until the spectral parameters from the resulting spectrum begin to deviate. At this point pile-up is affecting the spectrum and the inner exclusion region should, therefore, not be reduced any further.

The overall loss of photons resulting from pile-up will cause the source PSF to have a flatter profile than the PSF for a source unaffected by pile-up. The XRT PSF is well described by the King function, given by:

$$\mathrm{PSF}(r) = [1 + (r/r_c)^2]^{-\beta}, \tag{2.1}$$

with $r_c = 5.8$ and $\beta = 1.55$ [Moretti et al., 2005]. The point at which data points fall below the model fit corresponds to the approximate inner radius that should be used to avoid pile-up. Further details on the procedure when dealing with pile-up in WT mode data are illustrated in Romano et al. [2006a], and the standard correction for pile-up in PC data is described by Vaughan et al. [2006].

---

[3]http://heasarc.gsfc.nasa.gov/does/heasarc/caldb/swift/docs/xrt/

The default settings of XRTMKARF use the PSF to determine the effective areas, and, therefore, account is made for the loss of source counts resulting from an annular extraction region when dealing with piled-up GRBs.

2.3.3 UVOT

Photometry can be applied directly to the level II UVOT data products made available by the SDC, which are calibrated sky images and event lists. These products are corrected for coincidence loss, which is a similar process to pile-up, and since version 3.9.9 of the pipeline, the data have also been corrected for modulo-8 noise, which is an artifact of imperfections in the UVOT onboard centroiding process, and pixel sensitivity variations.

Coincidence Loss

Coincidence loss arises when the incoming photon count rate is larger than the CCD readout rate such that two or more photons arriving at the same location of the detector are recorded as a single event, and photons are thus lost. A high coincidence loss can also reposition photons, since overlapping photon splashes within a frame may cause the centroiding algorithm to centroid on the wrong position. For the full frame readout rate ($\sim$ 11 ms), coincidence loss begins to become significant above $\sim$ 10 counts s^{-1}. Its effect at different count rates has been calibrated and a correction can be applied up to $\sim$ 90 observed counts s^{-1}[Poole et al., 2007], beyond which correcting for coincidence loss becomes increasingly unreliable.

Modulo-8 Noise

Modulo-8 noise is a consequence of the onboard centroiding algorithm and is a repeating fixed pattern on the UVOT raw images. A real-time algorithm centroids the photon splash produced on the CCD after signal amplification on a sub-pixel that is $1/8^{th}$ of a CCD pixel. However, due to small gain changes over the face of the detector, the effective size of the sub-pixels is dependant on the position within the CCD pixel. This redistribution

of photons produces a repeating pattern on an 8 × 8 sub-pixel scale that becomes more apparent in longer exposures. Since photons are not lost, but only re-distributed it is possible to correct for this effect by ground processing.

Source Aperture Radius

Photometry on UVOT Level II products is typically done using a circular source extraction region with a 6" radius for the V, B and U optical filters and a 12" radius for the three UVOT UV filters and the white-filter, in order to remain compatible with the current effective area calibrations[4].

In the case where the source is close to another object in the field, the photometry has to be performed with a smaller aperture to avoid contamination. A smaller aperture is also used when the source is faint, in order to minimise the background contribution to the noise. However, the conversion from the measured count rates to a universal astrophysical parameter is based on a calibration of the count rates of standard stars measured in 6" and 12" apertures for optical and UV observations, respectively. An aperture correction is, therefore, needed when smaller extraction regions than the standard 6" and 12" radii are used for optical and UV filters respectively. This aperture correction, C_{apt}, compensates for the loss of source photons that lie in the outer parts of the standard extraction regions.

If $CR_{src}(a_{red})$ is the source count rate measured in an aperture of size a_{red}, the aperture corrected source count rate is then $C_{apt}CR_{src}(a_{red})$. To compute C_{apt} several point sources in the FOV are used to measure the difference between the source counts in an aperture of the chosen size and an aperture of the standard size. The sources selected should be bright enough to have a good signal-to-noise ratio, but not so bright that coincidence loss becomes a problem. If a_{cal} is the standard UVOT aperture size used for calibration, and a_{red} is a reduced aperture size, then the aperture correction that needs to be applied to the computed photometry is given by

$$C_{apt} = \frac{1}{N} \sum_{i=1}^{N} \frac{CR_i(a_{cal})}{CR_i(a_{red})}, \qquad (2.2)$$

[4]http://heasarc.gsfc.nasa.gov/docs/heasarc/caldb/swift/docs/uvot/

where $CR_i(a_{cal})$ and $CR_i(a_{red})$ are the count rates measured in an aperture of size a_{cal} and a_{red}, respectively, for point sources $i = 1 \cdots N$ in the FOV. The PSF of objects in the UVOT FOV varies slightly with time as a result of changes in temperature with orbit and background fluctuations. The size of the aperture correction needed will, therefore, vary slightly from one exposure to the next, and so C_{apt} is re-computed for every exposure in which an aperture correction is applied.

Where possible the background rate is taken from an annulus with 12" inner radius and 20" outer radius centred on the source. In the cases where there are nearby sources that contaminate this region, the background is taken from a circular source-free region, close to the target with a radius ranging between 10" and 20". For spectral analysis the tool UVOT2PHA is used to obtain a spectral file from the UVOT count rates that is compatible with XSPEC [Arnaud, 1996].

Chapter 3

Swift Observations of the X-Ray Flash 050406

X-ray flashes (XRFs) and X-ray rich (XRR) GRBs are types of GRB that have a softer spectrum than the norm, with a νF_ν spectrum that peaks at energies $E_p < 30$ keV [Heise et al., 2001]. Their formal definition is purely instrument-based and is given in section 1.8. It is, therefore, not clear whether the observed differences between XRFs, XRR bursts and 'normal' GRBs are extrinsic or intrinsic, which has important implications for the radiation mechanisms involved in GRBs and consequently, also, for the internal engine and progenitor models.

XRFs and XRR GRBs share a number of properties with GRBs, supporting the notion that all three classes are due to the same underlying phenomenon. This includes an isotropic distribution on the sky, variable and chaotic prompt emission light curves with comparable duration and structure, and similar afterglow temporal and spectral properties. Furthermore, although XRFs and XRR GRBs are distinguished from GRBs by their softer prompt emission, all three populations have prompt emission spectra that are well fit by the Band function, and have mean low and high-energy spectral indices, β_1 and β_2, consistent within 3σ and 1σ, respectively [D'Alessio et al., 2006].

Further evidence to support the common nature for these observationally distinct

populations of GRBs is the similarity in the dependencies between some of the prompt emission parameters observed in all three classes of burst. Observations suggest that XRFs, XRR and standard GRBs form a continuum in the $[S(2 - 400 \text{ keV}), E_p]$-plane [Sakamoto et al., 2003], and that they also all satisfy the Amati relation [Amati et al., 2002b]. The Amati relation relates a GRB's rest frame peak energy E_p to its isotropic equivalent energy E_{iso} such that $E_p \propto E_{iso}^{1/2}$ [Lamb et al., 2005]. It currently spans 5 decades in E_{iso}, and is satisfied by at least three XRFs [Lamb et al., 2005, Sakamoto et al., 2006].

The consistency in the spectral parameters β_1 and β_2 between all three populations of bursts indicates that the primary cause for the softer emission observed in XRFs and XRR GRBs is a lower peak energy in the νF_ν spectrum (see section 1.2.1). Observations of XRFs and XRR GRBs also indicate that they have dimmer afterglows when compared to GRBs [e.g. Lamb et al., 2005, Gendre et al., 2007, Sakamoto et al., 2007].

There are a number of theoretical models that aim to explain the origins of XRFs through either intrinsic or extrinsic effects, with the more standard ones being (1) GRBs at high redshift [Heise, 2003], which in this context means redshifts $z > 5$, (2) a baryon loaded fireball (dirty fireball model) [Dermer et al., 1999], (3) a clean fireball ($\Gamma \gg 300$) with a small distribution in the Lorentz factor amongst colliding shells [Zhang & Mészáros, 2002, Barraud et al., 2005], (4) a photosphere-dominated model [Mészáros et al., 2002], and (5) classical GRBs seen off-axis.

Afterglows have now been detected for a number of XRFs from the X-ray up to radio wavebands [Lamb & Graziani, 2003]. The first X-ray and radio afterglows were discovered in 2001 (XRF 011030; Taylor et al. 2001; Harrison et al. 2001), and in 2002 the first XRF optical afterglow was observed (XRF 020903; Soderberg et al. 2004). The increase in the sample size for each of these classes of burst and the improvement in the quality of the afterglow data and energy range of coverage is providing tighter constraints on the viability of models to explain their origins. Consequently, some of the models listed above are no longer able to account for the full population of XRFs and XRR GRBs observed.

The lack of evidence for systematic time-dilation in the γ-ray light curves of XRFs,

and their current redshift distribution rules out a high redshift origin as the sole cause for their soft prompt emission spectra, and neither can the population of XRFs be fully explained by a photosphere-dominated outflow. This latter model fails to cover the softest of XRFs with peak energy values as low as $E_p = 3\text{--}5$ keV, such as XRF 020427 [Amati et al., 2002a], XRF 020903 [Soderberg et al., 2004] and XRF 010213 [Sakamoto et al., 2004].

XRF models that account for the softness of the spectrum due to lines-of-sight off-axis to the GRB jet had been particularly successful at accounting for observations of XRFs [e.g. Fynbo et al., 2004, Soderberg et al., 2005], and their ability to describe both GRBs and XRFs in a unified way has made them increasingly popular. However, within this model there are several subcategories relating to the morphology of the jet, which have implications for the expected temporal behaviour of XRFs at early times and the observed distribution of XRFs, XRR GRBs and standard GRBs. The simplest and most distinct prescriptions for jets are the uniform jet [Yamazaki et al., 2002] and the universal structured jet [Zhang et al., 2004a].

In most XRF models the distinctive signatures are present during the early stages of the afterglow, making early time, broadband data crucial for a conclusive determination of the origins of XRFs, and whether the observed differences are intrinsic or extrinsic. In this chapter I present the *Swift* observations of XRF 050406, which was the first XRF to have its optical afterglow observed within 100 s of the flash, and I use these data to investigate the XRF models that may apply to this particular XRF. Most of the work in this chapter is reported in Schady et al. [2006].

In section 3.2 I review the observations made by all three instruments on-board *Swift* followed by an analysis of the temporal and spectral behaviour of the XRF and its afterglow in the optical, UV and X-ray energy bands in sections 3.3. In section 3.4 I discuss the results and investigate their implications for the fireball model and for XRF theoretical models, and my conclusions are summarised in section 3.5.

3.1   XRF 050406

The UVOT on-board *Swift* detected the optical afterglow to XRF 050406 beginning 88 s after the prompt emission. Prior to this event only a handful of XRFs with an associated optical counterpart had been detected (e.g.XRF 030429, XRF 030528, XRF 030723, XRF 040916, XRF 050315), with the fastest previous detection of an optical afterglow taking place 31.3 minutes after the initial burst (XRF 030723; Smith et al. 2003). At the time, the UVOT observations of XRF 050406 in the *V*, *B* and *U* bands were, therefore, the earliest taken of an XRF optical counterpart, making XRF 050406 an important burst with which to investigate the cause of its soft spectrum.

3.2   Observations

On 2005 April 6 the BAT triggered and located on-board XRF 050406, at 15:58:48 UT [Parsons et al., 2005]. The BAT location calculated on-board was RA $=02^h17^m42.7^s$, Dec$=-50°10'40.8''$ (J2000) [Parsons et al., 2005]. This was later refined to RA$=02^h17^m53^s$, Dec$=-50°10'51.6''$ with an uncertainty of 3' (95% containment) using the full dataset downloaded through the Malindi ground-station $\sim$ 1 hour after the burst [Krimm et al., 2005]. This corresponds to a Galactic latitude of $-61.7°$ with a local reddening of $E(B-V)$ $= 0.022$ mag [Schlegel et al., 1998] and a Galactic column density of $N_H = 2.8 \times 10^{20}$ cm^{-2} [Dickey & Lockman, 1990].

The light curve comprised of a single peak with a FRED profile and a T_{90} burst duration of 5.7 ± 0.2 s in the 15-350 keV band [Krimm et al., 2005]. The burst was very soft, with most flux emitted below 50 keV. The time-averaged spectrum could be well fitted by a simple power law model ($\chi^2 = 94$ for 73 dof), a cutoff power law model ($\chi^2 = 88$ for 72 dof), and the Band spectral model ($\chi^2 = 89$ for 71 dof). The best-fit E_p value in the latter two models was $E_{p,cutoff} = 11.9^{+5.1}_{-4.1}$ keV and $E_{p,Band} = 12.2^{+11.7}_{-1.5}$ keV, and an upper limit of $E_{p,pl} < 15$ keV could be set to E_p when a power law model was fitted to the data.

The spacecraft executed an automated slew to the BAT position, and within 72 s the XRT was on target and imaging the field. Ground analysis of the data revealed a fading X-ray source within the BAT error circle, 28" from the BAT position [Capalbi et al., 2005].

The UVOT began settled observations of the field of XRF 050406 88 s after the BAT trigger, and carried out an automated series of observations corresponding to the first UVOT AT sequence described in section 2.1.3. This amounted to 89 exposures in all three optical and UV filters, the first 1200 s of which were in event-mode.

3.3 Results

Initial analysis of the V band early time data processed on-board revealed no new source in the field down to a 3σ background limit of $V > 18.8$ [Landsman et al., 2005]. However, analysis of the V band image data processed on the ground, revealed a faint source 3.3σ above background within the reported 5" radius XRT error circle, with $V = 19.44 \pm 0.32$. The position of the uncatalogued source is RA $= 02^h17^m52.2^s$, Dec $= -50°11'15.5''$ (J2000) with an estimated uncertainty of 0.5", consistent with the position reported by Berger et al. [2005b], who detected a faint source in r and i band observations taken with the Magellan/Clay telescope 7.8 hrs after the BAT trigger. The afterglow was not observed above background in any of the subsequent V-band images, either in the individual or co-added exposures.

The afterglow was also detected in the UVOT B and U bands, with $B = 19.30 \pm 0.66$ and $U = 18.55 \pm 0.59$ at 423 s and 226 s after the prompt emission, respectively. At 1000 s after the burst trigger the source was no longer detected above background in any of the V, B or U bands, confirming this source to be the fading afterglow of XRF 050406. A co-added image constructed from all exposures in the V, B and U bands up to 1000 s after the burst is shown in Fig. 3.1, which provided a 8.7σ level detection.

3.3.1   The Optical Light Curve

Due to the faintness of the optical afterglow, a source extraction region smaller than is standard in the UVOT data analysis was used (see section 2.3.3). Photometry of the images was carried out using a 2" radius aperture, which was found to maximise the signal-to-noise (S/N) ratio of the source detection, and an appropriate aperture correction was applied to the photometry for all exposures analysed. The V band light curve consists of a 100 s exposure, 8×10 s exposures and a 900 s exposure, and the B and U light curves contain nine 10 s exposures and a single 900 s exposure each, covering the period up to 12000 s after the BAT trigger. There are low significance detections in individual 10 s B and U band exposures. The separate B and U light curves were best fit by a power law with decay indices $\alpha_B = 0.76^{+0.33}_{-0.56}$ and $\alpha_U = 1.20^{+0.37}_{-0.60}$ respectively, and a simultaneous fit with a common decay rate but different normalisations to the B and U light curve yielded a best-fit decay index $\alpha_{B,U} = 0.74^{+0.34}_{-0.48}$.

To obtain a higher S/N light curve the neighbouring pairs of B and U exposures were co-added, on the assumption that there was no colour evolution during this time period. It is possible that the cooling break could have passed through the optical bands at this time, causing a spectral break between the bands and a difference in their temporal decay rate. The quality of the data does not allow this to be verified. However, such a migration of the cooling frequency is typically observed at later times, on the order of $\sim 10^4$ s [e.g. Blustin et al., 2006], thus making the assumption of no colour evolution a reasonable one. The U and B filters are adjacent in the automated observing sequence, and therefore the time delay between the co-added exposures is small.

The co-added UB exposures provided a total of ten images, with the first nine having effective exposures of 2×10 s and the last image having an exposure of 2×900 s. A power law fit to the co-added UB light curve gave a best-fit decay index of $\alpha_{UB} = 0.75^{+0.16}_{-0.20}$ over the time interval $\sim$T+200 to $\sim$T+6000 s. This is consistent with the V band observations, where the afterglow must have decayed at a rate of at least $\alpha_V \sim 0.4$ to account for the drop in count rate from 0.25 ± 0.08 counts s^{-1} down to below the background level
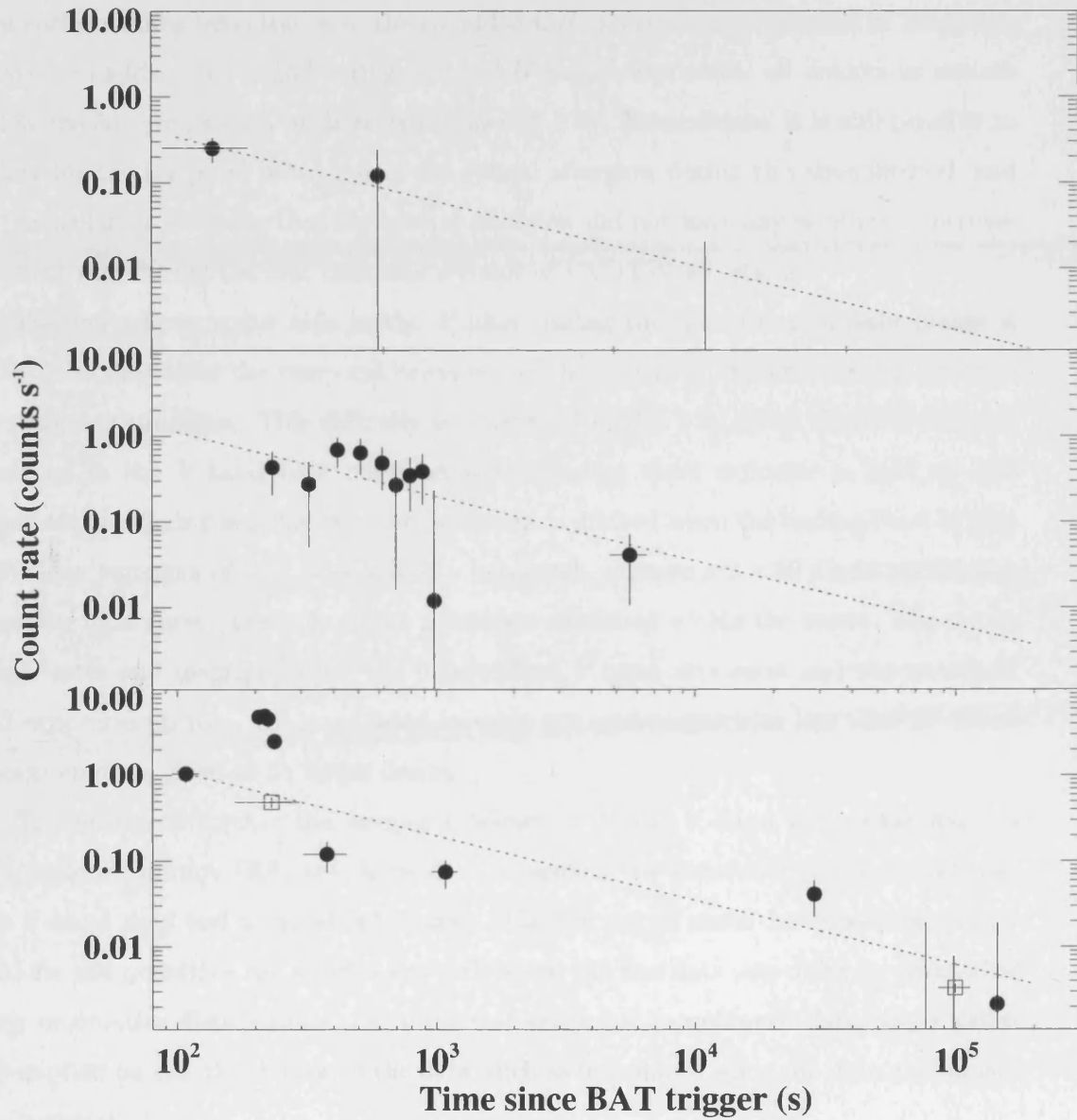
Figure 3.2: V light curve (top), co-added U and B light curve (middle), and X-ray light curve in 0.2-10 keV energy band (bottom) for XRF 050406. All optical data points are listed in table 3.1 and the combined UB data points are plotted at the mid-time of the co-added exposure. The X-ray light curve contains windowed timing (WT) and photon-counting (PC) mode data, shown as filled circles and empty squares respectively. The best power law fit to the UB co-added data points is shown in each panel, and this has a decay index α = 0.75. The power law decay curve is renormalised in the top panel to pass through the first V data point.

in $\sim$ 460 s. The V and UB light curves are shown in Figure 3.2, and the count rate and corresponding magnitudes to the co-added UB exposures are provided in Table 3.1. Despite co-adding the neighbouring pairs of B and U exposures, all detections remain below the 3σ level, with a median significance of 1.7σ. Nevertheless, it is still possible to determine the temporal behaviour of the optical afterglow during this time interval, and in particular, to decipher that the optical afterglow did not have any significant increase in count rate during the first thousand seconds of UVOT observations.

The low source count rate in the V filter during the first 100 s of data makes it difficult to determine the temporal behaviour of the optical afterglow during this period on a shorter timescale. This difficulty is illustrated in Fig. 3.3, which shows the change observed in the V band light curve when the finding chart exposure is split up into segments of differing lengths. A rising behaviour is derived when the finding chart is split into three segments of 35 s, 35 s and 30 s exposures, whereas a 2×50 s split produces a decaying light curve, although all the points are consistent within the errors. The source count rates and magnitudes for the independent V band exposures and the combined UB exposures up to $\sim 10^4$ s are listed in table 3.1, and magnitudes less than 1σ above background are given as 3σ upper limits.

To investigate further the temporal behaviour of the V-band early time data, a Kolmogorov-Smirnov (KS) test is used to determine the statistical similarity between the V-band data and a model light curve. The KS test is useful for continuous distributions and quantifies the significance with which the two data sets differ by comparing their cumulative distributions. Since the test is applied to unbinned data, any a priori assumption on the distribution of the data, such as introduced when the data are binned, are removed.

The KS statistic is the maximum difference between the two samples

$$D = \max_{-\infty < x < \infty} |S_1(x) - S_2(x)| \qquad (3.1)$$

where S is the cumulative distribution of a variable x, which in this case is the number of source counts. The KS null-hypothesis probability, P, is a function of the value D and
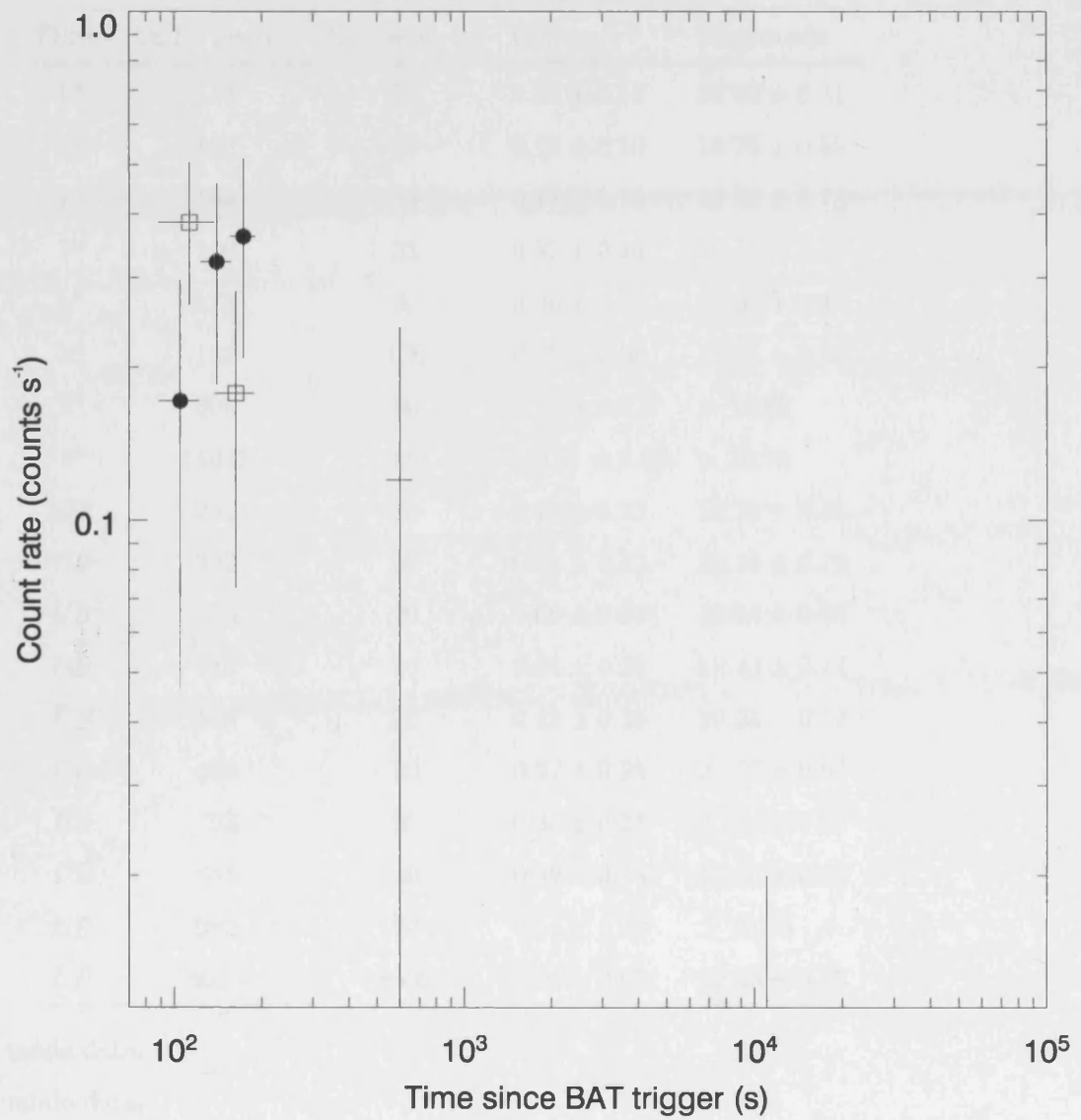
Figure 3.3: *V* filter light curve where the first 100 s observation has been split up into 2 × 50 s segments (open squares), and 3 segments made up of 35 s, 35 s and 30 s (filled circles). The light curve decays for a split into 2 × 50 s and rises when split into three intervals of similar length.

Table 3.1: UVOT Time Resolved Photometry

Filter	Mid Time (s)	Exposure (s)	Counts/s	Magnitude
V^a	113	50	0.38 ± 0.12	18.92 ± 0.31
V^a	163	50	0.18 ± 0.10	19.76 ± 0.59
V^a	105	35	0.17 ± 0.13	19.79 ± 0.73
V^a	140	35	0.32 ± 0.14	19.11 ± 0.43
V^a	173	30	0.36 ± 0.15	18.99 ± 0.42
V^b	138	100	0.25 ± 0.08	19.44 ± 0.32
V^b	598	90	0.12 ± 0.12	> 19.69
V^b	11011	900	-0.01 ± 0.03	> 20.75
UB^c	233	20	0.43 ± 0.23	19.75 ± 0.53
UB	322	20	0.28 ± 0.22	20.24 ± 0.79
UB	415	20	0.69 ± 0.26	19.24 ± 0.38
UB	510	20	0.64 ± 0.28	19.33 ± 0.44
UB	618	20	0.48 ± 0.25	19.63 ± 0.52
UB	699	20	0.27 ± 0.25	20.27 ± 0.93
UB	793	20	0.35 ± 0.21	20.00 ± 0.60
UB	885	20	0.39 ± 0.23	19.88 ± 0.59
UB	982	20	0.01 ± 0.22	> 19.86
UB	5625	1800	0.04 ± 0.03	22.33 ± 0.75

[a] Event mode data.

[b] Image mode data.

[c] A UB filter zero-point of 18.84 is assumed. This is derived using the fact a zero magnitude object with B and U band count rates $CR_{B,0}$ and $CR_{U,0}$ will have a UB combined count rate of $(CR_{B,0} + CR_{U,0})/2$.

the number of data points in the measured sample, and provides the probability that the observed and expected values represent two independent samples that are generated from the same distribution. Two distributions are considered to be statistically different when the null-hypothesis probability is $\ll 1\%$.

A KS test was first applied to compare the observed distribution of source counts in the first 100 s V-band exposure (T+88 to T+188 sec) with the distribution acquired from a simulation of a source decaying as a power law with decay index $\alpha = 0.75$, corresponding to the UB light curve decay rate. This gave a KS probability $P_{\mathrm{KS}} = 0.27$. For comparison, the KS test performed on the observed data set and a data set simulating constant emission was $P_{\mathrm{KS}} = 0.45$, and when compared to a distribution simulated from a source brightening as a power law with decay index $\alpha = -0.75$, the KS probability was $P_{\mathrm{KS}} = 0.68$. The probability for each of the KS tests performed was $P \gg 0.01$ and it is, therefore, not possible to claim with any statistical certainty that any of the simulated distributions differ from the observed data set. The time evolution of the optical light curve before T+200 s cannot, therefore, be determined.

3.3.2 The X-ray Light Curve

During the time of the first 100 s V band exposure, a bright flare was observed in the X-ray afterglow (Fig. 3.2, bottom panel), which increased the light curve flux by a factor of 6 between 150 and 213 s post-burst. Given the rise and fall time-scale of this flare $(\delta t/t_{peak} \ll 1)$, it is likely to be emission from internal shocks occurring several hundred seconds after the end of the γ-ray emission [Romano et al., 2006b, Burrows et al., 2005b]. Other early observations made of GRB optical counterparts have shown evidence for both uncorrelated (e.g. GRB 990123; Akerlof et al. 1999, GRB 050401; Rykoff et al. 2005, GRB 060111B; Klotz et al. 2006, GRB 060124; Romano et al. 2006b) and correlated (e.g. GRB 041219a; Vestrand et al. 2005, Blake et al. 2005, GRB 050904 Boër et al. 2006, GRB 060206; Monfardini et al. 2006, GRB 061126, Page et al. 2007) X-ray and/or γ-ray and optical behaviour. In the case of XRF 050406, the best-fit decay slope to the

co-added UB filters predicts a flux of ~ 0.63 counts s^{-1} at 213 s. An equivalent re-brightening in the optical band to that observed in the X-ray band during the flare would have caused the flux to be 3.78 counts s^{-1}, more than 8 times that observed in the first UB bin. The lack of such a flare in the optical/UV flux, therefore, suggests that there is little contribution to the optical emission from internal shocks in this burst.

Excluding the flare, the X-ray light curve is well fit by a broken power law with a best-fit early time index $\alpha_{X,1} = 1.58 \pm 0.17$, flattening out to a decay rate of $\alpha_{X,2} = 0.50^{+0.14}_{-0.13}$ at ~ 4400 s [Romano et al., 2006b].

3.3.3 Spectrum

Spectral analysis was performed on the UVOT data from 220–950 s after the BAT trigger, which is when the AT sequence is cycling rapidly through the filter wheel, ensuring that each band is sampling the same average in the decay curve. The UVOT exposures taken during this time period were co-added according to filter, producing an 8×10 s exposure for the V-band, and 9×10 s exposures in all other filters. To produce a UVOT spectrum each of these optical and UV exposures were used as an energy bin, generating six source and background spectral files. One of the input parameters required when running the tool UVOT2PHA is the source extraction region, and for this I used a radius that optimised the S/N ratio. To maintain consistency throughout the filters this was defined as being the radius containing $\sim 75\%$ of the counts emitted by the afterglow. This varied between 2.0" and 2.9", and, thus, an aperture size correction was applied to account for the loss of source counts. The background was determined from an annular region around the source. The count rates and corresponding fluxes for each of the UVOT exposures used in the spectrum are listed in table 3.2. Note that the fluxes measured in all three UV filters are barely at the 1σ level. However, the lack of a detection in these filters is still valid information, and these data are therefore included in the spectral analysis.

A fit to the UVOT data using a simple power law model that took into account Galactic reddening provided a statistically unacceptable fit ($\chi^2 = 17.8$ for 4 degrees of

Table 3.2: UVOT Spectral Photometry

Filter	Effective Wavelength (Å)	Exposure (s)	Counts/s	Flux (10^{-16} erg cm^{-2} s^{-1} Å^{-1})
V	5430	64	0.119 ± 0.108	0.266 ± 0.241
B	4340	76	0.405 ± 0.126	0.532 ± 0.165
U	3440	73	0.505 ± 0.114	0.751 ± 0.170
$UVW1$	2600	73	0.003 ± 0.024	0.009 ± 0.084
$UVM2$	2200	71	0.011 ± 0.014	0.075 ± 0.097
$UVW2$	1930	63	0.035 ± 0.028	0.214 ± 0.166

freedom (dof)), with best-fit photon index $\beta_{\mathrm{UVOT}} = 3.46^{+2.23}_{-0.42}$. The addition of a Lyman absorption edge at a free floating redshift significantly improved the fit ($\chi^2 = 2.3$ for 2 dof), and yielded a spectral index of $\beta_{\mathrm{UVOT}} = 0.82^{+3.58}_{-2.18}$ and $z = 2.70^{+0.29}_{-0.41}$. All quoted errors on the best-fit spectral parameters are at the 90% confidence level.

The analysis was repeated employing Cash statistics [Cash, 1979], which uses a likelihood function to fit a model to the data. The likelihood function employs Poisson statistics to assess the quality of a model and, given that counts are sampled from the Poisson distribution, it is a more appropriate statistic to use when working with low source photon count rates, and provides more rigorous confidence intervals.

The likelihood function, L, is the product of the individual Poisson probabilities computed in each bin, i.

$$L = \prod_i \frac{c_i^{n_i}}{n_i!} \exp(-c_i), \qquad (3.2)$$

where c_i and n_i are the number of expected and observed counts (source and background) in bin i. The Cash statistic is determined from L by

$$C = -2 \log L = -2 \sum_i [n_i \log c_i - c_i - \log n_i!] \qquad (3.3)$$

The factorial term in the likelihood function remains constant during fits to the same

dataset and can, therefore, be dropped, so that the Cash statistic reduces to

$$C = 2 \sum_i [c_i - n_i \log c_i] \qquad (3.4)$$

The value of the Cash statistic, C, depends on the number of bins included in the fit and on the value of each bin, and a goodness-of-fit measure can, therefore, not be assigned analytically to C.

Using Cash statistics the spectrum was re-fit with a power law model that took into account Galactic absorption with extinction, and a Lyman absorption edge at a free floating redshift, as before. This produced best-fit parameters consistent with those found with a χ^2 minimisation fit. The fit yielded $\beta_{\mathrm{UVOT}} = 0.94 \pm 2.78$ and $z = 2.50^{+0.43}_{-0.42}$.

To provide tighter constraints on the spectral behaviour of the afterglow the UVOT and XRT data were combined to produce a broadband spectrum. A source and background XRT spectrum was extracted from the time interval T+350 to T+950 s after the prompt emission, in order to exclude the X-ray flare. This only provided 27 events, which were therefore binned into one data point. Using the Cash statistic, the best-fit parameters for a power law model with Galactic absorption and reddening and neutral gas incorporated at a free floating redshift were $\beta = 0.84^{+0.11}_{-0.06}$ and $z = 2.44^{+0.30}_{-0.35}$, consistent with the results from a χ^2 statistics fit, which had a reduced $\chi^2 = 0.6$ ($\chi^2 = 2.3$ for 3 dof). The derived redshift is typical of that measured in the *Swift* sample, which has a mean redshift of $z = 2.8$ [Jakobsson et al., 2006d]. The X-ray UV and optical spectrum is shown in Figure 3.4, with the best-fit model overlaid.

The lack of data points in the spectrum did not allow for the inclusion of an extinction component to account for the host galaxy dust extinction, nor is the absorption caused by the Ly-α forest taken into account in the fit. It is, therefore, possible that the lack of a UV afterglow detection is the result of dust extinction or absorption due to the Lyman forest as well as or instead of the redshifting of the Lyman edge into the UV range. In such a case the redshift of XRF 050406 could be smaller than z=2.44, effectively making this value an upper limit.
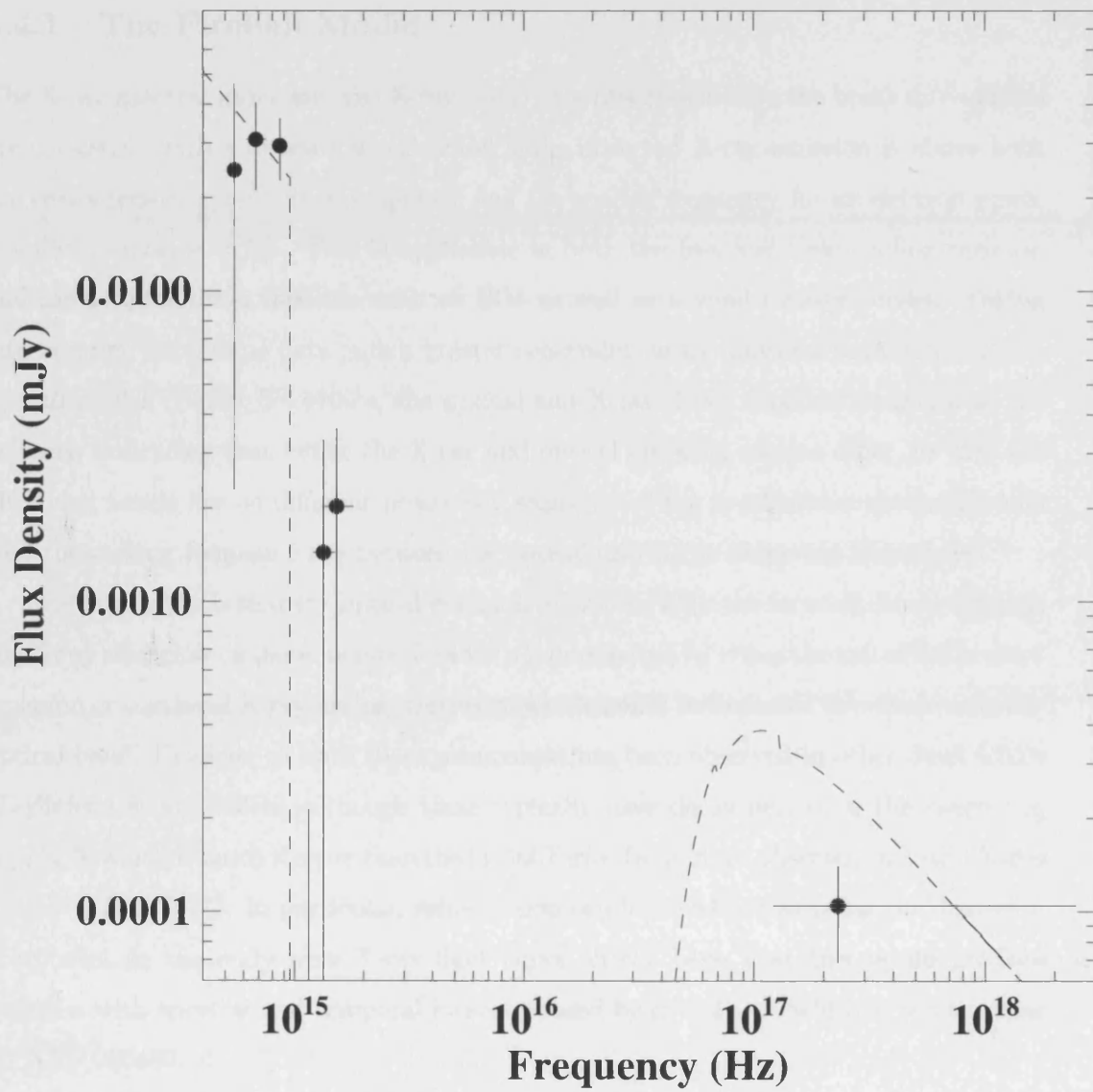
Figure 3.4: Combined UVOT and X-ray spectrum of XRF 050406 between the epochs T+220s and T+950s, when the UVOT filter wheel was cycling rapidly. The dashed line represents the best-fit power law model with Galactic absorption and extinction included, as well as an additional redshifted Lyman absorption edge.

3.4   Discussion

3.4.1   The Fireball Model

The X-ray spectral index and the X-ray decay rate observed before the break at $\sim$ 4400 s are consistent with a forward shock model if the observed X-ray emission is above both the characteristic synchrotron frequency and the cooling frequency for an electron power law distribution $p = 2.5$. This is applicable in both the fast and slow cooling regimes, and for a circumburst medium with an ISM as well as a wind density profile. Taking into account the optical data puts a greater constraint on the physical parameters of the fireball model. Before T+4400 s, the optical and X-ray decay rates only overlap at the 3σ level, indicating that either the X-ray and optical emission regions differ, or that the observing bands are on different power law segments of the synchrotron spectrum, such that the cooling frequency lies between the optical and X-ray observing frequencies.

One possibility is that the optical emission originates from the forward shock, whereas the X-ray afterglow emission before T+4400 s is dominated by either the tail of the prompt emission or continual X-ray flaring, neither of which would be expected to contaminate the optical band. Evidence of both these phenomena has been observed in other *Swift* GRBs [Tagliaferri et al., 2005b], although these typically have decay indices in the range $3 \lesssim \alpha_{X,1} \lesssim 5$, which is much steeper than the initial X-ray decay slope observed in XRF 050406 ($\alpha_{X,1} = 1.58 \pm 0.17$). In particular, tail emission can be ruled out as being the dominant component in the early time X-ray light curve on the basis that this would produce emission with spectral and temporal indices related by $\alpha = 2 + \beta$, which is not the case for XRF 050406.

Instead, both the optical and X-ray are compatible with forward shock emission if, at the time of observations, the fireball is in the slow cooling phase and $\nu_m < \nu_{opt} < \nu_c < \nu_X$, where the circumburst medium has a constant density profile. For an electron power law index $p \sim 2.3$, this model is consistent within 2σ of the data, although further explanation is required for the break observed in the X-ray light curve at T+4400 s.

The flat decay observed in the X-ray after the break could be the result of energy

injection, either through long lasting engine activity or through late time refreshed shocks resulting from a distribution in the Lorentz factor within the ejecta, as described in section 1.5 [Sari & Mészáros, 2000, Zhang & Mészáros, 2001]. Such a mechanism has been invoked to explain the shallow decay observed in many X-ray and optical light curves, including GRB 050319 [Mason et al., 2006] and GRB 050401 [De Pasquale et al., 2006b]. In the case of energy injection, for $\alpha_{X,2} = 0.50^{+0.14}_{-0.13}$, and $\beta = 0.84^{+0.11}_{-0.06}$ the spectral and temporal X-ray properties of XRF 050406 after 4400 s from the prompt emission require an energy injection parameter $q = 0.72 \pm 0.01$ or $q = 0.46^{+0.02}_{-0.01}$, depending on whether $\nu_X > \nu_c$ or $\nu_X < \nu_c$. These values of q are determined from the closure relations given in table 1.2. This assumes that the energy injection results from a long-lasting internal engine, where the continuous luminosity injection of the central engine is denoted by $L \propto t^{-q}$ [Zhang et al., 2006]. If the energy injection were due to refreshed shocks resulting from a power law distribution in the Lorentz factor within the ejecta, then the distribution index would be $s = 1.82 \pm 0.01$ and $s = 2.76^{+0.02}_{-0.01}$, respectively [Zhang et al., 2006] (see Eq.1.21).

The X-ray light curve of XRF 050406 continues to decay at a constant rate with a power law index $\alpha_{X,1} = 0.50^{+0.14}_{-0.13}$, until the source is no longer detected after $\sim 10^6$ s. This plateau phase is much longer than is typically observed in X-ray light curves [e.g. Nousek et al., 2006], and it is hard to reconcile such a prolonged period of shallow decay with a long-lasting internal engine. Collapsar model simulations suggest that there can be ongoing engine activity for up to 10^3 s [MacFadyen et al., 2001], but longer extended periods of engine activity are hard to reproduce. A refreshed shocks model may, therefore, be a more viable mechanism of energy injection in the case of XRF 050406, since this does not require the internal engine to be active throughout the period of shallow decay.

Given the duration and smoothness of the X-ray shallow decay phase, as well as the relatively shallow optical afterglow decay, it is worth considering an alternative model that does not require long-term energy injection. Another explanation that would explain the observations would be a line of sight that is off-axis to the jet axis. Provided that the energy density decreases as a function of the angular distance from the jet axis, θ, (i.e. a

structured jet; see section 1.7),the decay rate will be slowed down by the increased domi-nance of the on-axis component as the relativistic beaming becomes less important. The effects and consequences of an off-axis line-of-sight are discussed further in section 3.4.2.

In such a scenario the X-ray light curve break would no longer be the result of energy injection, and could, instead, be interpreted as the transition from internal shock domi-nated emission to forward shock dominated emission. Furthermore, if the line-of-sight is, indeed, off-axis, then the early steep decay phase in the X-ray afterglow could be inter-preted as X-ray flares, which decay at slower rates than observed in GRBs due to off-axis viewing affects.

3.4.2   Origin Of The Soft Spectrum

The optical observations of XRF 050406 taken with the *Swift*-UVOT telescope were the earliest detection of an X-ray flash optical afterglow at that time. These data probed a previously unexplored time-domain in XRF afterglows, during which the distinguishing features between the various XRF models are greatest. Analysis of the early and simul-taneous multiwavelength temporal and spectral data, therefore, provide some of the most rigorous constraints available on models that explain the origin of XRFs.

In this section I consider each of the principle XRF models and compare the charac-teristic features of these models with the observations of XRF 050406.

Baryon loaded fireball

The GRB prompt emission peak synchrotron energy is proportional to

$$E_p \propto (\Gamma B')\gamma_e^2 \sin \Psi (1 + z)^{-1}, \tag{3.5}$$

where Γ is the bulk Lorentz factor of the ejecta, B' is the co-moving magnetic field, γ_e and Ψ are the mean Lorentz factor and pitch angle of the electrons, and z is the GRB redshift. In the forward shock model, where the prompt emission is caused at the forward shock, the magnetic field producing the synchrotron prompt emission is made in situ at the forward shock, and is directly proportional to Γ. The mean electron Lorentz factor

is also directly proportional to Γ. The peak energy therefore scales with bulk Lorentz factor as $E_p \propto \Gamma^4$. One model that can produce a GRB with a soft prompt emission is, therefore, a forward shock model in which the relativistic ejecta have a small bulk Lorentz factor [Dermer et al., 1999]. A baryon loaded fireball will have a smaller bulk Lorentz factor, and in the forward shock GRB model, will thus reduce the spectral peak energy, E_p [Zhang & Mészáros, 2002]. This does not apply for the internal shock model, for which the Lorentz-boosted magnetic field strength, $\Gamma B'$, is inversely proportional to the internal shock radius, r, where $r \propto \Gamma^2$, and for which γ_e depends only on the relative Lorentz factor between colliding shells and not on the bulk Lorentz factor of the shell. The peak energy, E_p, therefore varies as Γ^{-2} [Zhang & Mészáros, 2002].

In the external shock model the GRB prompt emission is produced at the forward shock, where density inhomogeneities in the surrounding medium on size scales $\ll R/\Gamma_0$ produce the variable γ-ray light curves. Γ_0 is the initial bulk Lorentz factor and R is the distance of the shell from the internal engine. The onset of the afterglow emission occurs once the forward blastwave moves into the smoother surrounding ISM. Due to the strong dependence of the prompt emission spectrum on Γ in the forward shock model (i.e. $E_p \propto \Gamma^4$), a fireball with $\Gamma_0 \ll 300$ [Dermer et al., 1999], which is referred to as a 'dirty' fireball, will result in prompt emission that is most luminous at X-ray energies. For example, a fireball with initial bulk Lorentz factor $\Gamma_0 = 30$ will produce a spectrum that is, on average, ~ 4 orders of magnitude softer than the spectrum produced by a clean fireball with $\Gamma_0 > 300$. A concern with such a model in accounting for the softness of XRF 050406 is that the baryon load also determines the duration of a GRB, such that a dirty fireball should produce a long lasting soft GRB. However, XRF 050406 had a T_{90} of only 5.7 s, which is at the low end of the long GRB distribution.

The difficulty in associating the softness of XRF 050406 to a baryon-loaded fireball can be demonstrated by taking the bulk Lorentz factor of XRF 050406 to be two times smaller than is typical for standard GRBs. The peak energy of XRF 050406 would then be a factor of 16 smaller than that of a standard GRB, which is consistent with the data. In the forward shock model the duration of the prompt emission is the deceleration timescale,

t_d, which has a dependency on the bulk Lorentz factor that scales as $\Gamma^{-8/3}E^{1/3}n^{-1/3}$ [Rees & Mészáros, 1992], where E is the kinetic energy within the fireball, and n is the density of the circumburst medium. Comparing to a typical long GRB, with $T_{90} = 30$ s [Kouveliotou et al., 1993] and a Lorentz factor, say, two times higher than that of a standard GRB, the relative shortness of XRF 050406 requires that either the internal fireball energy is 4.5 orders of magnitude smaller, or that the circumburst medium has a density that is 4.5 orders of magnitude larger. A dirty fireball is, therefore, a rather implausible model for XRF 050406, failing to simultaneously account for the shortness of this burst as well as its softness.

Clean fireball

Simulations of the prompt GRB phase based on the internal shock model indicate that, whereas the dependence of redshift, duration and injected power on the prompt emission spectrum produced is small, the distribution in the Lorentz factor of individual shells has a much more significant effect on the spectrum. A small distribution in the Lorentz factor within the outflow but with a large average Lorentz factor will result in a softer prompt emission spectrum and may, therefore, produce an XRF [Barraud et al., 2005].

The shock radius at which two shells merge, r_s, is proportional to the square of their average Lorentz factor, $\bar{\Gamma} = (\Gamma_1 + \Gamma_2)/2$, where Γ_1 and Γ_2 are the Lorentz factors of shell 1 and shell 2, respectively, where $\Gamma_2 > \Gamma_1$ [Barraud et al., 2005]. Shells with small Lorentz factors will, therefore, collide and merge at smaller radii, r_s. Thus the post shock density of the prompt emission region, $\rho \propto (r_s^2 \bar{\Gamma})^{-1}$, will be greater than in the case of internal shocks that occur at larger radii from the source. For constant equipartition parameters, the prompt emission peak energy, E_p, is proportional to

$$E_p \propto \Gamma_s \rho^{1/2} \epsilon_{diss}^{5/2} \propto \Gamma_s \epsilon_{diss}^{5/2} (r_s \bar{\Gamma}^{1/2})^{-1} \propto \Gamma_s \epsilon_{diss}^{5/2} \bar{\Gamma}^{-5/2}, \qquad (3.6)$$

where $\Gamma_s = \sqrt{\Gamma_1 \Gamma_2}$ is the Lorentz factor of the shocked material in the merged shell, and $\epsilon_{diss} = 1/2(\kappa^{1/2} + \kappa^{-1/2}) - 1)$ is the dissipated energy per unit mass, where $\kappa = \Gamma_2/\Gamma_1$. In terms of the distribution in the Lorentz factor within the outflow, ϵ_{diss} is smallest for $\kappa = 1$

and, therefore, a GRB with large bulk Lorentz factor and small contrast in the Lorentz factor between colliding shells will have a small E_p value and a softer prompt emission spectrum [Barraud et al., 2005]. Furthermore, the smaller the contrast in Lorentz factor between colliding shells, the less efficient the resulting internal shock is at dissipating kinetic energy (i.e. the smaller the value of ϵ_{diss}). A small distribution in Γ will, therefore, cause the prompt emission of the GRB to be both weak and soft. A consequence of this that can be tested is the prediction that XRFs should be systematically less efficient at dissipating kinetic energy (i.e. smaller ϵ_{diss} value) during the prompt emission phase.

The efficiency of a GRB at converting kinetic energy into γ-rays is given in Eq. 1.23, and requires knowledge of the collimation corrected energy in γ-rays, E_γ, and the kinetic energy remaining within the fireball during the afterglow, E_k, neither of which are easily measured. In order to determine both of these the redshift of the GRB has to be known, and to determine the afterglow kinetic energy certain assumptions have to be made on the microphysical parameters of the circumburst medium. Instead, it is possible to estimate a GRB's efficiency using the relative energetics of a GRB's prompt and afterglow phase.

The amount of energy dissipated during the prompt phase is indicated by the fluence of the GRB in γ-rays, S_γ, and the amount of kinetic energy within the fireball affects the X-ray luminosity, which is strongly dependent on E_k. The X-ray flux at a specified epoch, $F_{X,t}$, therefore, provides a good indicator of E_k. The relative efficiency of a GRB can then be estimated by the ratio, $S_\gamma/F_{X,t}$, for which the dependency on the GRB redshift or collimation of the fireball cancels out. A GRB that is not very efficient at converting kinetic energy into γ-ray emission during the prompt phase will have a larger kinetic energy at the onset of the forward shock. A less efficient GRB is, therefore, expected to have a brighter afterglow, and $(S_\gamma/F_{X,t})_{\mathrm{GRB_1}} < (S_\gamma/F_{X,t})_{\mathrm{GRB_2}}$ will suggest that $\mathrm{GRB_1}$ is less efficient than $\mathrm{GRB_2}$, provided that S_γ and $F_{X,t}$ are measured in the same energy range and that the same epoch, t, is used to measure $F_{X,t}$.

In a comparison of the γ-ray fluence in the 15–350 keV energy range and the X-ray flux in the 2–10 keV band at 1 hour after the burst, XRF 050406 lies within 1 σ of the line of best-fit to 23 GRBs in $S_\gamma - F_{X,1}$ parameter space [Roming et al., 2006],

suggesting that the efficiency of XRF 050406 is consistent with that of classical GRBs. In a more detailed investigation on the efficiency of GRBs and XRFs, Zhang et al. [2007] considered the importance of energy injection when selecting the epoch of t to estimate E_k. It is the remaining kinetic energy immediately after the prompt emission that is of interest, and it is important not to include any kinetic energy injected at later times by a long-lasting central engine. The epoch used to measure F_X should, therefore, be late enough that kinetic energy left over after the prompt phase has been transferred into the forward shock, but early enough to avoid additional kinetic energy released at later times reaching the forward shock. The relevant time will depend on whether any late-time energy injection is ongoing in the GRB and, if so, whether this is due to a long-lasting engine or refreshed shocks. Taking this into account Zhang et al. [2007] concluded XRFs to be radiatively as efficient as GRBs and, in particular, they found Log $S_\gamma/F_{X,t}$ ratio of XRF 050406 to be at the more efficient end of the distribution.

Both Roming et al. [2006] and Zhang et al. [2007] find XRF 050406 to be no less efficient than other GRBs, indicating that this burst had a bulk Lorentz factor and a distribution in Γ comparable to standard GRBs. A clear fireball is, therefore, unlikely to be the origin for the softness of XRF 050406.

High-z GRB

At large redshifts the GRB prompt emission peak energy, E_p, is redshifted down to lower energies, and at redshifts $z > 5$ the observer frame peak energy will be a factor of six smaller than the intrinsic peak energy as measured in the rest frame. Such a GRB would, therefore, be observed as an XRF or XRR GRB. Both observations and simulations indicate that GRBs should exist and be detected out to redshifts greater than 5 [e.g. Lamb & Reichart, 2000], and therefore a certain fraction of XRFs should certainly be due to high redshift GRBs.

In the case of XRF 050406, the detection of the optical afterglow in the three optical filters firmly constrains the redshift of this burst to $z < 3.1$, beyond which the Lyman edge would be redshifted past the U-band, and all emission blueward of this would be

absorbed. A model fit to the broadband spectrum that incorporates a Lyman absorption edge provides a best-fit redshift of $z = 2.44^{+0.30}_{-0.35}$. At such a redshift XRF 050406 would have a rest frame peak energy of $E_p^{rest} \sim 50$ keV, around an order of magnitude lower than that of a GRB at $z \sim 1$ with a typical observed peak energy value $E_p \sim 255$ keV. Even at a maximum redshift of $z = 3.1$ the rest frame peak energy would still be a factor of four smaller than that of a more standard GRB. The softer spectrum observed in XRF 050406 cannot, therefore, be solely accounted for by a high-redshift burst.

Off-axis GRB

Another possible model that can account for the observed properties of XRFs is a GRB viewed off-axis. Due to the relativistic motion of the ejecta, radiation emitted at a co-moving frequency ν' will be observed at a frequency $\nu = \nu'\delta$, where $\delta = [\Gamma(1-\beta\cos\theta)]^{-1} \approx 2\Gamma/[1 + \Gamma^2\theta^2]$ is the relativistic Doppler factor [Woods & Loeb, 1999, Yamazaki et al., 2002]. The Doppler boosting will, therefore, be less effective at larger viewing angles, and the bulk of the radiation emitted will be observed at lower frequencies, resulting in a softer GRB.

An off-axis viewing angle will also affect the observed temporal properties of the afterglow, since the dominant emitting region may no longer lie along the line-of-sight, as is the case for a GRB viewed on-axis, and evolving contributions from closer to the jet axis may modify the observed afterglow light curve. The details of how the afterglow light curve varies from that observed on-axis depend on the specifics of the jet morphology and energy distribution.

A number of GRB jet models have been proposed, which may differ in morphology, energy density profile, in the distribution of the Lorentz factor across the jet and in how the structure of the jet evolves with time, and each of these properties will have different consequences for the resultant afterglow observed. The change in decay index at the jet break, for example, will depend on the specifics of the jet model, such as the sharpness of the edge of the jet and on whether there is lateral expansion at the time when $\Gamma \sim \theta^{-1}$. The most commonly used jet models in GRB science, and the type of jet break that

results, are described below, where in all cases it is assumed that there is a constant density circumburst profile, and that there is no energy injection.

- **Uniform Jet** [e.g. Rhoads, 1997, Panaitescu & Mészáros, 1999, Sari et al., 1999]

  This is a homogeneous jet with sharp edges and a constant energy per solid angle, ϵ, and initial Lorentz factor, Γ_0, across the jet. At the time of jet break, a uniform jet with lateral expansion at the jet break time will produce an afterglow light curve that steepens to a decay index $\alpha_2 = p$, where p is the electron energy distribution index. In the case of a non-laterally expanding jet, the afterglow decay index will increase by $\Delta\alpha = 3/4$ at the time of jet break.

- **Universal Structured Jet** [e.g. Lipunov et al., 2001, Rossi et al., 2002]

  The universal structured jet has a narrow central jet at the core with half-opening angle θ_c and an energy and bulk Lorentz factor profile that approximates to a uniform jet. At angles $\theta > \theta_c$, both ϵ and Γ_0 vary smoothly with angle from the jet axis, θ, and are described by $\epsilon = \theta^k$, $\Gamma_0 = \theta^l$. The jet break in this case will arise when $\theta_v = \Gamma_0^{-1/2}$, where θ_v is the viewing angle. At the time of jet break the change in decay index will be $\Delta\alpha = 3/4$.

- **Gaussian Jet** [e.g. Zhang & Mészáros, 2002, Kumar & Granot, 2003]

  The Gaussian jet model lies somewhere between the uniform jet and the universal structured jet model. It has a narrow central uniform jet at the core with half-opening angle θ_c, and an energy profile across the jet at angles $\theta > \theta_c$ described by $\epsilon(\theta) = \exp{-(\theta^2/2\theta_c^2)}$, which, at large angles, is a much steeper energy density drop-off than in the case of a power law energy density profile.

- **Two Component Jet** [e.g Huang et al., 2004]

  This jet model is composed of a narrow jet with a half opening angle θ_{nr} with initial Lorentz factor $\Gamma_{0,nr} \gg 100$ that is embedded inside a wider jet with half opening angle θ_{wd} and $\Gamma_{0,wd} \sim 10 - 30$. In such a model two jet breaks should occur; one when $\theta_{nr} = \Gamma_{nr}^{-1/2}$ and another when $\theta_{wd} = \Gamma_{wd}^{-1/2}$, where Γ_{nr} and Γ_{wd} are the

bulk Lorentz factor of the material within the narrow component jet and the wide component jet, respectively. The change in decay slope and the final decay index after each jet break will depend on the structure of the two jets, and on the details of the distribution of the emission regions for different energy bands within the jet. If the narrow jet produces the bulk of the X-ray emission and the wider jet produces the bulk of the lower energy emission (i.e. optical and NIR), for example, then the jet break will not be achromatic. Since $\theta_{nr} < \theta_{wd}$, the jet break will arise first in the X-ray energy band, when $\theta_{nr} = \Gamma_{nr}^{-1/2}$, and later in the optical and NIR energy bands, when $\theta_{wd} = \Gamma_{wd}^{-1/2}$.

The jet models indicated above are only the more standard examples. However, more complex models exist, such as the Ring Jet model [Granot, 2005], and the Fan jet model [Thompson, 2005], as well as models that take energy injection into account.

The differences in the afterglow produced by different jet models are most marked during the earliest part of the afterglow, and have been most closely studied in the case of a uniform jet model with lateral expansion and a structured jet model. I shall, therefore, use these two jet models to investigate how well the observations of XRF 050406 match an off-axis jet model. The difference in the jet energy density profiles between the uniform and structured jet model are illustrated in Fig. 3.5.

In the case of a uniform jet, an XRF is presumed to be a GRB observed at an angle greater than the half-jet opening-angle, $\theta_v > \theta_j$. During the early phases of the GRB, the bulk of the radiation will be beamed away from the observer, at angles $\theta = 1/\Gamma < \theta_j$, where Γ is the initial bulk Lorentz factor of the relativistic outflow. As the Lorentz factor drops the radiation is beamed into larger angles and a greater portion of the radiation will reach the observer, and produce a flatter, or even rising, early-time light curve relative to that observed from a GRB viewed on-axis [Granot et al., 2002]. Emission received at $\theta_v > \theta_j$ is dominated by the region on the jet surface closest to the observer's line of sight, and the flux received by the observer can, therefore, be approximated to peak when $\Gamma \sim \theta_v^{-1}$, at which time radiation emitted from along the jet axis from the jet core is beamed into the line of sight. After this, the light curve will begin to decay steadily,
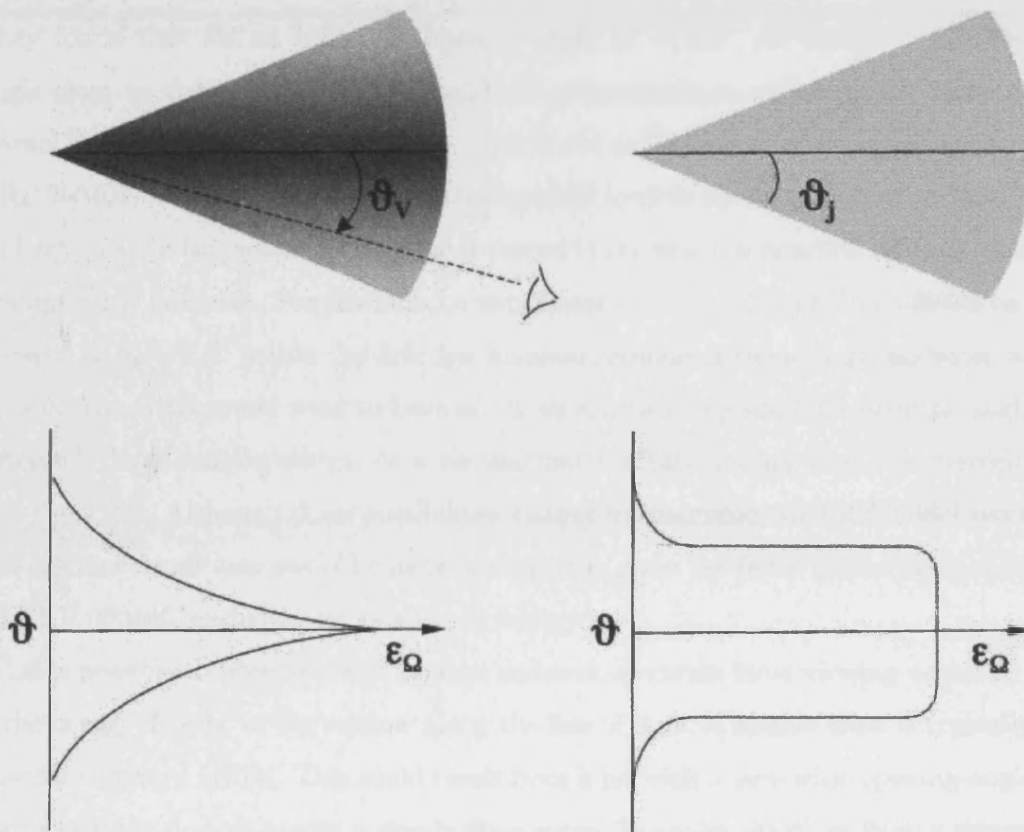
Figure 3.5: Structured and Uniform jet profiles. θ_v and θ_j are the viewing angle and half-jet opening-angle respectively, and ϵ_Ω is the energy density per unit solid angle in the rest-frame.

causing a break at $\Gamma \sim \theta_v^{-1}$.

Assuming a jet opening-angle of $\theta_j = 1°$, Rossi et al. [2002] modelled the resultant afterglow light curve observed from a GRB viewed at various off-axis angles, θ_v. They found that a viewing angle $\theta_v = 1°$, close to the edge of the jet, produced a peak in the light curve at t > 1000 s. Granot et al. [2002] furthered this work by including a two-dimensional hydrodynamics code into their simulations to describe the jet dynamics. They found that for an initial jet opening-angle $\theta_0 = 0.2°$, an observer with viewing angle close to the edge of the jet would see a near-plateau with a break occurring at several days after the prompt emission. This is not consistent with the afterglow decay of XRF 050406, which decayed below the background level in the optical band within 1000 s, and any peak in the optical light curve occurred in the first few hundred seconds after the prompt γ-ray emission. For the bulk Lorentz factor of the outflow of XRT 050406 to have decayed to $\theta_v \sim 1/\Gamma$ within the first few hundred seconds of the prompt emission, where $\theta_v > \theta_j$, the GRB would need to have either an anomalously small jet opening-angle, an extremely large kinetic energy, or a circumburst medium density that is extremely low (see Eq. 1.24). Although these possibilities cannot be discarded, an XRF model requiring less extreme conditions would be more appropriate, given the fairly typical characteristics off XRF 050406, excluding its small peak energy.

It is possible to observe a soft prompt emission spectrum from viewing angles $\theta_\nu < \theta_j$ if the energy density in the outflow along the line of sight is smaller than is typically the case for standard GRBs. This could result from a jet with a very wide opening-angle, θ_j, over which the fireball energy is evenly distributed [Donaghy, 2006], or from a structured jet, provided that the line of sight is close to the edge of the jet. In a structured jet the energy density, ϵ, is a decreasing function of angular distance from the centre, and will therefore be smaller at larger viewing angles from the jet axis.

A GRB with a uniform jet and wide opening-angle will have its energy distributed over a large area, which will, therefore, produce a softer prompt emission spectrum since $E_p \propto \dot{E}^{1/2}$, where $\dot{E}$ is the energy injected into the fireball [Barraud et al., 2005], and since $\theta_v < \theta_j$ in such an XRF model, the afterglow light curve will resemble that of a standard

GRB, i.e. decay as a power law from the onset of observations up until the jet break. The emission from material in the observer's line of sight will dominate over that produced within the core and edges of the jet for the duration of the observations, producing an afterglow light curve primarily composed of a single decaying component dominated by emission regions in the line of sight. Initially this is also true for a structured jet viewed at large angles from the axis. However, in this case, although the contribution from the core is not the dominant source of observed flux, it is not negligible either. This is due to the larger energy density closer to the jet axis, which compensates for the small fraction of the core of the jet that is visible to the observer [Granot, 2007]. The resultant light curve will, therefore, decay from the start, as in the wide jet model, but at a slower rate than if observed on axis. A structured jet model is in good agreement with observations of XRF 050406, which has a shallow optical decay index $\alpha_{opt} = 0.75^{+0.16}_{-0.20}$, and late time shallow X-ray decay index $\alpha_{X,2} = 0.50^{+0.14}_{-0.13}$ and also provides an alternate explanation to long term energy injection, as already indicated in section 3.4.1. This makes a structured jet a more favourable model to a wide jet, which cannot account for the shallowness of the decay rate of XRF 050406 without incorporating further components into the model, such as energy injection.

Another consequence of an off-axis XRF model, independent of the specific jet morphology, is a smoother prompt emission light curve. At large viewing angles θ_v, where $\theta_v > \theta_j$ for a uniform jet, or $\theta_v \gg \theta_0$ for a structured jet, where θ_0 is the jet axis angle, the bulk of observed emission will come from emitting regions within the jet axis, and θ_v. At angles $\theta > \theta_v$ there is either little or no contribution to the observed flux. This is in contrast to a line of sight along the jet axis, where emission is observed from angles $\theta_v - \Gamma^{-1} < \theta < \theta_v + \Gamma^{-1}$, for a bulk Lorentz factor Γ. Fewer pulses should, thus, be observed for off-axis lines of sight, which will produce a smoother prompt emission light curve [Ramirez-Ruiz & Lloyd-Ronning, 2002, Zhang et al., 2004b, Yamazaki et al., 2002]. This is indeed what is observed in the case of XRF 050406.

3.4.3 The Amati Relation E_p vs. E_{iso}

If XRFs do indeed have the same origin as GRBs and XRR GRBs, all three categories would be expected to show similar parametric dependencies, and follow the same empirical laws. One of the tightest correlations observed between the prompt emission properties of GRBs is the Amati relation [Amati et al., 2002b], which relates a GRBs rest-frame peak energy in the νF_ν spectrum, E_p, with its k-corrected, rest-frame isotropic-equivalent energy, E_{iso}, such that $E_p \propto E_{iso}^{1/2}$.

It has been shown that the Amati relation is consistent with the E_p limits for XRF 020903 and XRF 030723 [Sakamoto et al., 2003, Lamb et al., 2005], and recently XRF 050416a has also been shown to satisfy the relation [Sakamoto et al., 2006], extending the correlation over ~ 5 orders of magnitude in E_{iso} and ~ 3 orders of magnitude in E_p.

At the best-fit redshift value of $z = 2.44$, XRF 050406 has an equivalent isotropic energy of $E_{iso} = 1.55 \times 10^{51}$ erg, which, when using the Amati relation, provides an estimated peak energy of $E_{p,Amati} \approx 11.4$ keV in the observer frame. Although the E_p values from spectral fits to the prompt emission are not well constrained, they are consistent within errors to the estimated $E_{p,Amati}$. This provides support to the hypothesis that GRBs and XRFs form a continuum, and that a unified model is therefore necessary to explain the two classes of bursts.

3.5 Summary

I have presented early-time optical data for XRF 050406, beginning 88 s after the burst trigger. This constitutes the first detection of an XRF optical afterglow within 100 s of the GRB, and the properties of the light curve and spectrum constrain the possible models that may explain the soft spectrum of the prompt emission. A fit to the optical light curve provides a decay rate of $\alpha = 0.75_{-0.20}^{+0.16}$, and beyond T+4400 s the X-ray afterglow decays at a rate $\alpha_{X,1} = 0.50_{-0.13}^{+0.14}$, both of which are relatively shallow when compared to other GRBs. The lack of Lyman absorption down to 4000 Å in the UV/optical spectrum provides a firm upper limit of $z \leq 3.1$ on the redshift, and broadband spectral modelling

yields a best-fit redshift $z = 2.44^{+0.30}_{-0.35}$, and spectral index $\beta = 0.84^{+0.11}_{-0.06}$.

Analysis of the prompt γ-ray emission and the X-ray and optical afterglows indicate that the soft spectrum observed in XRF 050406 during the prompt phase is most likely the result of a GRB observed off-axis, in which case a structured jet is the best match to the data. This model is able to account for the lack of a peak in both the X-ray and optical afterglow out to $\sim 10^3$ s or more after the prompt emission, and also provides an explanation for the shallow decay rate observed in both energy bands.

In order to further constrain the possible models that describe the origins of XRFs, further prompt observations of these objects are necessary. It is only during the early stages of emission, when the internal mechanisms that power these bursts are probed, that many of these models can be differentiated, and it is possible that several factors contribute to the soft spectrum observed in XRFs. It is also important to increase the sample of XRFs with spectroscopic redshifts to gain information on their rest-frame properties. The classification of bursts as XRFs is based on observer frame properties. However, only knowledge of the rest-frame properties will reveal the underlying differences between XRFs, XRR bursts and GRBs. At a redshift of $z = 2.44$ XRF 050406 would have a peak energy $E_p \sim 52$ keV, at which stage there begins to be an overlap between the intrinsic properties of XRFs that are at redshifts $z > 2$ and nearby GRBs.

Chapter 4

GRB Environments and Afterglow Observations

There is now a wealth of observational evidence linking long duration gamma-ray bursts (GRBs) with the collapse of a massive star [collapsar model; e.g. Woosley, 1993]. This includes the underlying supernova features in the afterglow of some GRBs (e.g. GRB 980425 [Kulkarni et al., 1998], GRB 030329 [Hjorth et al., 2003] and GRB 060218 [Campana et al., 2006a]), and the association between GRB host galaxies and high-mass star formation [Tanvir et al., 2004]. Whereas in lower energy bands radiation is easily absorbed by dust and gas in the intervening interstellar medium, this material is effectively transparent to γ-rays. The small absorption cross-section at γ-ray frequencies, combined with the vast energy released during the initial explosion, allows GRB prompt emission to be detected out to very high redshifts [e.g. Tagliaferri et al., 2005a]. GRBs are thus potentially very powerful tools with which to trace the star formation history (SFH) of the Universe in an unbiased way. Furthermore, the longer lived, lower energy afterglows light up their host galaxies, albeit for only a brief time (on the order of weeks), providing invaluable insight into the chemical makeup of these galaxies that would otherwise be unattainable in a majority of cases, certainly at high redshifts. To fully maximise the potential that GRBs offer as cosmic probes the selection effects present in GRB studies need to be addressed,

such as the stellar populations that they trace and the environmental conditions necessary for a GRB to occur.

Observations of GRB host galaxies in the optical to IR energy range suggest that they are blue, sub-luminous, irregular systems, which are not particularly dusty or red [Le Floc'h et al., 2003, Fruchter et al., 2006]. Assuming the luminosity-metallicity correlation holds, a sub-luminous host is consistent with the collapsar model, which requires a low metallicity environment, at least in the local surroundings of the GRB. However, the collapsar model also predicts GRB progenitors to be in regions of active star formation, and although UV bright, irregular systems host an abundance of young, massive stars, at larger redshifts, beyond $z = 2$, the majority of active star formation occurs in IR luminous starbursts [Ramirez-Ruiz et al., 2002, Le Floc'h et al., 2006]. The mean redshift for *Swift* GRBs is in the range 2.5–3.0, thus most of these GRBs should reside in bright IR and submm galaxies, which does not appear to be the case (see section 1.10.1).

The small number of GRB host galaxy detections in the IR and submm may signify that other environmental conditions in addition to active star formation may come into play in determining whether GRBs occur and are observable. Red, dusty galaxies have substantial metallicities at all redshifts, which may not be conducive for the formation of a GRB, as suggested by the collapsar model. Instead, GRB progenitors may, preferentially, occur in UV starburst galaxies that are experiencing a first episode of very massive star formation [Fruchter et al., 2006], which will, consequently, have sub-solar metallicities. Although such a hypothesis is certainly valid, it is important not to neglect the observational consequences of selection effects present in GRB host galaxy detections.

Observations of GRB host galaxies are predisposed to selection effects. A GRB position with arcsecond accuracy is realistically needed to confidently identify the host, and these are typically provided by optical and longer wavelength afterglow observations. GRBs that occur in red and dusty galaxies have a large fraction of their UV and optical afterglows absorbed and scattered by the dust, and this will reduce the chance of identifying the host. It may, therefore, be the case that GRBs reside in both UV starbursts and dusty submm galaxies, but that there is a detection bias towards the starbursts. To

address this, further detailed analysis of GRB environments is needed to determine the range of host galaxy properties, and, fundamentally, to provide a better understanding of GRB observations and the limitations that they present. This is the subject of this chapter, which describes the work from Schady et al. [2007a].

4.1 Dust Extinction

Dust extinction is wavelength dependant, where the amount of radiation absorbed and scattered by dust is an inverse function of wavelength, and is described by an extinction law. The cross-section of a dust grain of diameter a to radiation of wavelength λ can be approximated by $\sigma_a \propto a/\lambda$, and since the grain size distribution is mostly skewed towards smaller grains (i.e. $q \sim 3.5$, see section 1.10.2), dust is most efficient at extinguishing radiation in the visual and ultra-violet wavebands, and is an increasing barrier moving from the NIR through to optical and UV. Furthermore, the photoionisation cross-section of medium-weight elements locked up in dust grains is a fraction of that caused by the same number of atoms in the gas phase due to self-shielding, and this fraction falls as the grain size increases [Fireman, 1974].

Dust extinction is typically measured by the visual extinction parameter, A_V, which gives the amount of rest frame V-band flux (~ 5500 Å) extinguished by dust in terms of a magnitude. That is, the V-band magnitude of an object with apparent magnitude m_V has a dust extinction corrected magnitude

$$M_{dustcorr} = m_V - A_V, \tag{4.1}$$

The amount of UV, optical and NIR radiation that is extinguished is dependant on the density of dust in the environment, the grain size distribution, the shape, and the chemical composition, all of which contribute to the dust extinction cross section at varying wavelengths. The extinction law will, therefore, change for different environments.

It is typically not easy to determine the value of A_V when observing extragalactic sources, which require knowledge of the spectral type of the object in order to infer the

absolute flux in each observed band. However, it can be well estimated by the ratio of the total-to-selective extinction, $R_V = \frac{A_V}{E(B-V)}$, where $E(B-V)$ is the colour excess, defined by $E(B-V) = A_B - A_V$. In the presence of dust extinction this term is typically positive, since the dust extinction cross-section is larger at shorter wavelengths, and measurements indicate that for the diffuse ISM $R_V \approx 3.1$. However, the value of R_V also varies with the size of the grain responsible for the extinction and tends to be larger for denser environments [Cardelli et al., 1989].

4.1.1 Variations in Extinction Laws

The proximity of the Milky Way and the Small and Large Magellanic Clouds has made it possible to measure the average extinction caused by dust in these environments over the UV, optical and NIR energy bands at high wavelength resolution. The extinction laws modelled on these three sets of data are shown in Fig. 4.1, which are based on the parameterisation and total-to-selective extinction values from Pei [1992], for which $R_V = A_V/E(B-V) = 3.08$, 2.93 and 3.16 for the Galactic, SMC and LMC extinction laws, respectively. The differences between the extinction laws are apparent at rest frame wavelengths blueward of ~ 2500 Å, with the principle distinguishing characteristics being the amount of far-ultraviolet (FUV) extinction, and the prominence of the absorption feature at ~ 2175 Å. The MW has the strongest extinction at 2175 Å and smallest amount of FUV extinction, whereas the SMC has the greatest amount of FUV extinction, rising faster than $1/\lambda$, and an insignificant 2175 Å feature. A further difference in these three extinction laws is in the amount of reddening per H atom [Draine, 2003], which is observed to be greatest in the MW and least in the SMC.

The Magellanic Clouds are irregular galaxies that are active in star formation and differ from the Milky Way primarily in their gas contents and metallicity. By modelling the Milky Way and Magellanic Clouds empirical dust extinction law using a standard graphite-silicate model (see section 1.10.2), Pei [1992] was able to quantify certain dust properties in these environments. He found the best-fit graphite to silicate abundance
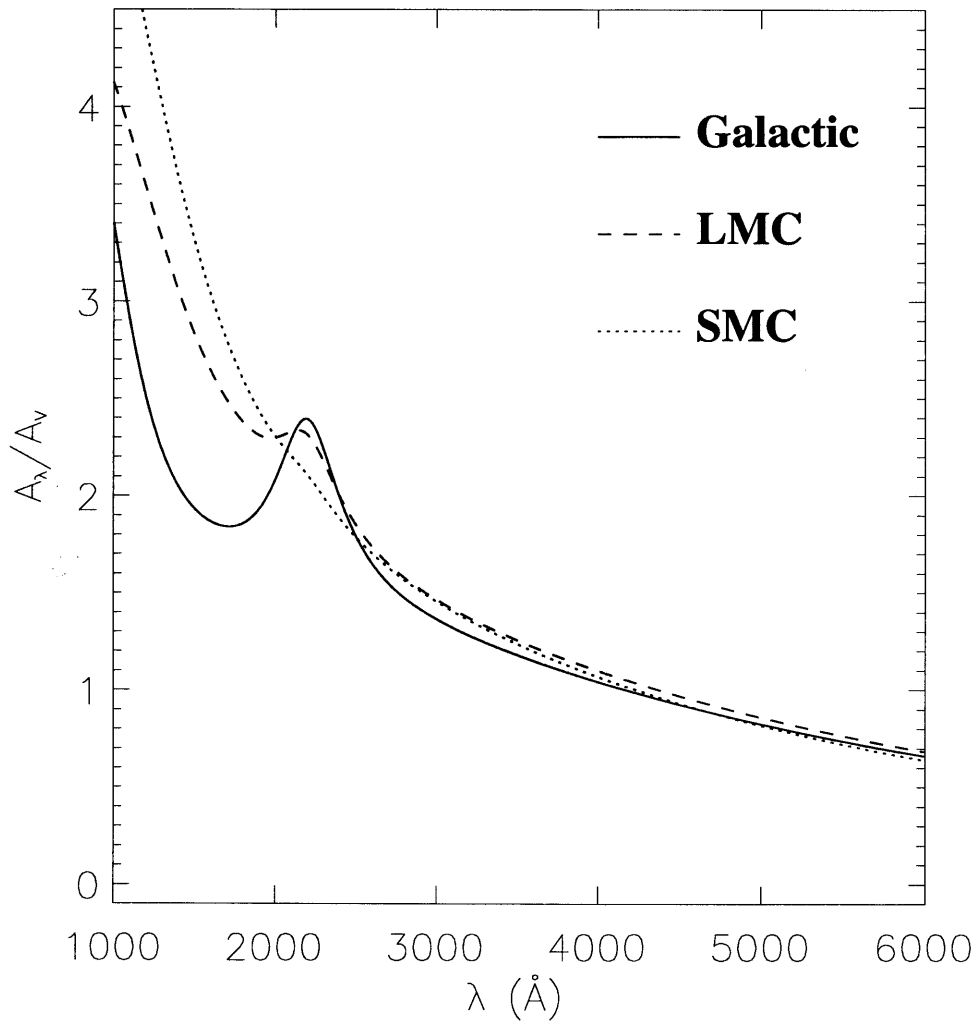
Figure 4.1: Galactic (solid), LMC (dashed) and SMC (dotted) extinction curves. Parameterisations taken from Pei [1992]

ratios, r_C/r_S, for the Milky Way and LMC to be 0.95 and 0.22, respectively, and the SMC extinction curve required no graphites in the extinction law model. Graphite grains are believed to result, primarily, from carbon-rich stars (C>O), suggesting that such populations of stars make up a small fraction of the SMC stellar population. The fits also indicate that the 2175 Å absorption feature is likely to originate from an abundance of carbonaceous material such as small spherical particles of graphite ($a \ll 30$ nm), which have a strong feature at this wavelength and of a similar width [Draine & Lee, 1984]. A lack of graphites in the SMC environment could, therefore, account for the absence of the 2175 Å absorption feature in the SMC extinction law. Pei [1992] also determined the mass ratio of neutral hydrogen to dust in the Milky Way, LMC and SMC to be, on average, 1:2:8, respectively, so that a relatively higher fraction of the mass in the Magellanic Clouds is in hydrogen compared to that of the Milky Way, and the metallicity in the SMC and LMC was determined to be 1/8 and 1/3 that of the Milky Way, respectively.

4.2   Dust and Gas in GRB Host Galaxies

The information provided by dust and gas column densities on the material surrounding the GRB host galaxy is not only useful in absolute terms, but also in relative terms, where the gas-to-dust ratio inferred from the two column densities can be compared with other, better studied environments. Within other galaxies there appears to be a good correlation between the colour excess and the column density of total hydrogen (atomic and molecular), although this correlation varies with metallicity and density of the environment (e.g. Milky Way; Predehl & Schmitt [1995], Small Magellanic Clouds; Woosley [1993]; Large Magellanic Clouds; Koornneef [1982], Fitzpatrick [1985]). With these correlations as a reference, the gas-to-dust ratio measured in the local environment of GRBs can be used as an indicator of the metallicity and relative composition of the matter local to the GRB.

In the analysis of X-ray and optical afterglow spectra for eight GRBs, Galama & Wijers [2001] found evidence for high column densities of gas in the GRB local environment that

were comparable with those observed in Galactic giant molecular clouds. Furthermore, they found the optical extinction to be 10-100 times smaller than expected from Galactic gas-to-dust ratios given the column densities. Stratta et al. [2004] extended this sample and found the ratio of host galaxy column density to visual extinction to be an order of magnitude larger than that observed in the Milky Way (MW), and also greater than that in the SMC. Prompted by theoretical studies that indicate that the intense radiation emitted by a GRB should destroy small dust grains out to radii of around 10 pc [e.g. Fruchter et al., 2001, Perna & Lazzati, 2002, Perna et al., 2003], the large gas-to-dust ratio was taken to be evidence of the destruction of dust in the surrounding vicinity of the burst, thus reducing the visual extinction observed.

Stratta et al. [2004] also found little evidence of the strong 2175 Å Galactic absorption feature in their optical-NIR spectral analysis. Instead they found the SED to be best fit by a model in which the host galaxy has an SMC or starburst galaxy dust extinction law, which has no such absorption feature. More recently Kann et al. [2006] analysed the afterglow spectral energy distributions in the optical and NIR bands on a larger sample of 30 pre-*Swift* GRBs, and also found the SMC extinction curve to provide a better fit to the spectra than the MW or LMC extinction curves.

Prior to the launch of *Swift*, research into the dust and gas column densities in the local environment of GRBs was limited to NIR, optical and X-ray data taken at different times, measurements that were typically made hours after the prompt emission. At these epochs the signal-to-noise (S/N) ratio of the data is significantly less than at the early stages of the afterglow, in particular in the optical bands where the afterglow can decay below the detection threshold within the order of a day. Furthermore, the difference in the time of the observations in the various energy ranges necessitates the extrapolation of the X-ray and/or optical data to a common epoch, introducing an additional level of uncertainty in the analysis.

The simultaneous observations taken with the X-Ray Telescope and the UV/Optical Telescope on-board the *Swift* spacecraft provide GRB afterglow SEDs without the need to extrapolate data to the same epoch. This capability is unique to *Swift* and the accurate

broadband spectral modelling that is possible with these observations provides an important data set in itself, and to compare with previous multi-wavelength GRB samples. In this chapter I present the broadband spectral analysis on a sample of *Swift* GRBs with afterglows detected by both the XRT and UVOT and investigate the rest frame visual extinction and soft X-ray absorption in the GRB host galaxy. This provides an indication of the dust and gas content in the local environment of the GRB, which can be compared to the environment of the MW, the LMC and the SMC.

In section 4.3 I present the GRB sample and describe the X-ray and UV/optical data reduction and analysis, and in section 4.4 I describe the models that were used to fit the data. The results from the spectral modelling are presented in section 4.5, and in section 4.6 I discuss the implications of the results for the local environment of GRBs and the effects of the circumburst medium and of the GRB intense radiation on each other. The conclusions are summarised in section 4.7.

4.3   Data Reduction and Analysis

The GRBs were selected from the sample of *Swift* GRBs up to and including GRB 060512 using the criteria that they had afterglows detected by both the XRT and UVOT instruments and a spectroscopic redshift with $z < 1.75$. Bursts for which the photometry was considered to be too poor to provide useful constraints on the spectral fitting were not used. This included those with UVOT detections in fewer than three filters, or bursts that did not have well enough sampled light curves with which to obtain reliable multi-band photometry at a single epoch.

This provided a sample of seven GRBs, and the SEDs for these were produced at a single-epoch. This epoch was chosen to be 1 hour after the onset of the initial prompt emission (time T) for four of the bursts (GRB 050318, GRB 050525, GRB 050802 and GRB 060512). For the remaining three GRBs (GRB 050824, GRB 051111 and GRB 060418) the SEDs were produced at a time T+2hrs due to a lack of data at T+1hr, resulting from spacecraft observing constraints.

Table 4.1: UVOT Data

GRB	z	Galactic E(B-V) [1]	α_{opt}
050318	1.44 [2]	0.017	0.94 [9]
050525	0.606 [3]	0.095	1.56,0.62 [13]
050802	1.71 [4]	0.021	0.82 [10]
050824	0.83 [5]	0.034	0.55 [11]
051111	1.549 [6]	0.162	0.96 [12]
060418	1.49 [7]	0.224	1.25
060512	0.443 [8]	0.014	0.84

[1] Schlegel et al. [1998]; [2] Berger & Mulchaey [2005]; [3] Foley et al. [2005a]; [4] Fynbo et al. [2005b]; [5] Fynbo et al. [2005a]; [6] Prochaska [2005]; [7] Dupree et al. [2006]; [8] Bloom et al. [2006a]; [9] Still et al. [2005]; [10] Oates et al. [2007a]; [11] Halpern & Mirabal [2005]; [12] Butler et al. [2006]

[13] Light curve best fit by double power law [Blustin et al., 2006]

To avoid any contamination from absorption caused by the Ly-α forest only UVOT data with a rest frame wavelength $\lambda > 1215$ Å were used in the spectral analysis. The redshift limit was, therefore, a necessary requirement to ensure that there were sufficient optical and UV data points in the afterglow SED to constrain the spectral fitting. At the redshift of the sample the afterglow spectra cover the wavelength range in which the redshifted 2175 Å extinction bump is expected to lie, and those GRBs closer to the redshift upper limit also probe the rest frame FUV spectra, where the divergence between extinction curves is greatest.

4.3.1 UVOT Data

Photometric measurements were extracted from the UVOT imaging data using the method described in section 2.3.3. To create a SED at an instantaneous epoch the count rates in

---

[1] http://heasarc.gsfc.nasa.gov/docs/heasarc/caldb/swift/docs/uvot/

Table 4.2: X-Ray Data

GRB	Data Mode	Gal. N_H (10^{20} cm^{-2})	Start Time (s) [1]	Exp. Time (s)
050318	PC	2.8	3280	23431
050525	PC	9.1	7056	3560
050802	PC	1.8	480	4835
050824	PC	3.6	6096	17157
051111	PC	5.0	5552	1583
060418	WT	9.2	448	1841
060512	PC	1.4	3680	58966

[1] Measured from the BAT trigger time.

these files were set to correspond to the count rate of the GRB at the appropriate epoch. These count rates and the associated errors were determined from power law model fits to the light curve in each filter where the GRB afterglow is assumed to decay at the same rate in all the bands. This is justified by the small variations present in the decay rate between filters for the GRBs in the sample, which are all consistent at the 90% confidence level. Furthermore, the colour evolution expected when the cooling break migrates through the optical bands is typically observed at later times than the epochs dealt with in this chapter, on the order of $\sim 10^4$ s [e.g. Blustin et al., 2006].

Where available, the UV/optical decay index was taken from the literature where UVOT data were used in the analysis. This was the case for GRB 050318 [Still et al., 2005], GRB 050525 [Blustin et al., 2006], and GRB 050802 [Oates et al., 2007a]. Otherwise, I carried out a temporal analysis to determine the afterglow decay index, with the exception of GRB 050824 and GRB 051111, for which there was not sufficient UVOT data to constrain the fits to the light curves and, therefore, reported indices from R-band light curve fits were used. When determining the decay index, a combined UVOT light curve was produced by normalising each filter to the V-band light curve. The light curve for each filter was then independently fit using the best-fit decay index to the combined light

curve, and the count rate at an instantaneous epoch was determined from this fit. The light curves were modelled as a power law, with the exception of GRB 050525, which required further components to describe the more complex early time temporal behaviour [Blustin et al., 2006]. The decay rates determined for each burst are listed in Table 4.1, as well as the references used where appropriate.

4.3.2 X-Ray Data

The X-ray data were reduced following the prescription in section 2.3.2. In most cases the data used were taken in PC mode with the exception of GRB 060418, for which the majority of the data taken at the time of interest are in WT mode. For PC data, source counts were extracted from a circular region centred on the source with an outer radius ranging from 50" to 95". In the case of GRB 050802 the data suffered from pile-up and, therefore, an annular extraction region was used to exclude those pixels that were piled-up. The inner radius of this annulus was 9.44" (4 pixels) and the outer radius was 106.2" (45 pixels). The background count rate was estimated from a circular, source-free area in the field of view (FOV) with a radius of 118" (50 pixels). For WT mode data, the extraction regions used for the source and background count rates were 94" slits positioned over the source and in a source free region of the FOV, respectively. Spectral files and the corresponding effective area files were produced and binned following the procedure laid out in section 2.3.2, and the response matrices from version 8 of the XRT calibration files were used for both WT and PC mode data.

All X-ray data were taken from time intervals where spectral evolution was no longer observed, which typically means once any flaring activity is over, which frequently causes spectral evolution [e.g. GRB 050502B Falcone et al., 2006a], and after the transition from phase I to phase II of the X-ray light curve (see section 1.4.2). The X-ray spectra were normalised to the epoch corresponding to the SED by using the best-fit model to the X-ray light curve, in the same way as for the UVOT data. The data mode and time intervals used are listed in Table 4.2.

4.4 The Model

To model the afterglow spectral continuum both a power law and broken power law fit were tried, where in the latter the change in spectral slope was fixed to $\Delta\beta = 0.5$ to correspond to the change in slope caused by a cooling break. In addition to this a constraint was also imposed on the break energy such that it was within the observing window (i.e. 0.002 keV $< E_b < 10.0$ keV). Any fit with a spectral break outside this energy range would be equivalent to a power law fit to the data. In both the power law and broken power law models two dust and gas components were included to correspond to the Galactic and the host galaxy photoelectric absorption and dust extinction. The Galactic column density and reddening in the line of sight were fixed to the values taken from Dickey & Lockman [1990] and Schlegel et al. [1998], respectively. The redshift of the second photoelectric absorption system was set to the redshift of the GRB, and the equivalent neutral hydrogen column density in the host galaxy was determined assuming solar abundances (discussed later). To measure the amount of optical and UV absorption caused by dust in the local environment of the GRB it is necessary to model the dependence of dust extinction on wavelength, which varies with dust composition and grain size distribution, and is described by an extinction law (see section 1.10.2).

Due to the extensive modelling that has been done on the Milky Way, SMC and LMC extinction laws (see section 4.1.1), and the consequently better understood dust properties of these environments, these extinction laws are used to model the dust extinction in the local environment of the GRB as a function of wavelength. Furthermore, their clear differences at rest frame wavelengths > 2500 Å allow the predominant extinction properties of the dust within the GRB local environment to be identified (see Fig. 4.1). From hereon in this chapter I refer to the individual spectral models as the MW, SMC and LMC model, where the name corresponds to the extinction law used to describe the dust extinction properties in the GRB host galaxy. The parameterisation of the dust extinction laws in the MW, LMC and SMC are shown in Fig. 4.1, where $R_V = A_V/E(B-V) = 3.08,\ 2.93$ and 3.16 for the Galactic, SMC and LMC extinction laws, respectively [Pei, 1992].

4.5 Results

The value of N_H determined in the spectral analysis is an equivalent neutral hydrogen column density that results from the amount of soft X-ray absorption in the spectrum, with solar abundances assumed. This is dominated primarily by oxygen K-shell absorption [Morrison & McCammon, 1983]. To distinguish between the equivalent neutral hydrogen column density determined from the X-ray absorption and the true neutral hydrogen column density (which will be a function of abundance), the notation $N_{H,X}$ is used to refer to the former.

The results from the spectral analysis are provided in Table 4.3 and Table 4.4 for a power law and a broken power law fit, respectively. For five GRBs a broken power law provided little improvement to the fit with the significance in improvement being $< 92\%$. For GRB 050802 and GRB 060418 a spectral break at 1–2 keV and ~ 3 keV, respectively, improved the goodness of fit of the model with an F-test probability ranging from 0.003 to 1.7×10^{-5} for GRB 050802 and from 0.02 to 9×10^{-4} for GRB 060418, depending on the model. However, the column density and the dust extinction at the host galaxy do not change significantly between the broken power law and simple power law fits, remaining consistent to 2σ.

For the purpose of this chapter, where the interest is in the properties of the GRB local environment, the factors of importance are the dust extinction law that best fits the GRB afterglows and the relation between the column density and visual extinction in the GRB local environment. The analysis indicates that the best-fit extinction law does not depend on the model used to fit the continuum for any of the GRBs in the sample, and there is no significant dependence in the ratio between the host galaxy column density and rest frame visual extinction. This is illustrated in Fig. 4.2, which plots the value of $N_{H,X}/A_V$ for the best-fit parameters determined from a power law and a broken power law fit as solid and open circles, respectively. Beyond this section I, therefore, refer only to the spectral results from the power law fits. In Figs. 4.3–4.9 the SEDs and best-fit power law models for each GRB are shown. In these figures data points at rest frame

wavelengths $\lambda < 1215$ Å, which were not used in the fits (see section 4.3), are shown as open circles.

The amount of intrinsic absorption and extinction determined in the sample varies by over a factor of five in A_V and by more than an order of magnitude in $N_{H,X}$. Typically the SMC model results in the smallest A_V in the host galaxy and the MW model in the largest. This general trend is to be expected given the difference in FUV extinction observed in the three curves. The MW extinction law is the shallowest of the three extinction curves (see Fig. 4.1) and, in particular, has the least amount of dust-absorption in the FUV for a given A_V. A spectral model with a MW extinction law, therefore, requires a larger A_V to fit the same data.

Although the X-ray column density and UV/optical extinction are independent components in the fit, the fitted value of $N_{H,X}$ depends on the spectral index, which in turn depends on the UV/optical extinction. The best-fit X-ray column density will, therefore, change between extinction models. Typically the MW model requires a steeper spectral index to compensate for the reduced amount of FUV extinction, and this consequently results in larger absorption in the soft X-ray band. Regardless of these differences the hydrogen equivalent column density determined from the spectral modelling is generally consistent at the 1σ level between models. In the case of GRB 050802 the column density is consistent at the 2σ level between dust models.

To further investigate the model dependence between the amount of X-ray absorption and dust extinction in the local environment of the GRB the confidence contours of $E(B-V)$ vs. $N_{H,X}$ for the best-fit power law models to each GRB are shown in Fig. 4.10. For the most part the contours are fairly circular, indicating that there is no significant correlation between $N_{H,X}$ and A_V in the spectral modelling. The X-ray data were also fit alone to make sure that the UV/optical data were not in any way skewing the column densities. The best-fit $N_{H,X}$ value determined from the SED spectral analysis is compatible with the best-fit $N_{H,X}$ value from spectral analysis on the X-ray data alone, as shown in Fig. 4.11. This shows the robustness of the method.

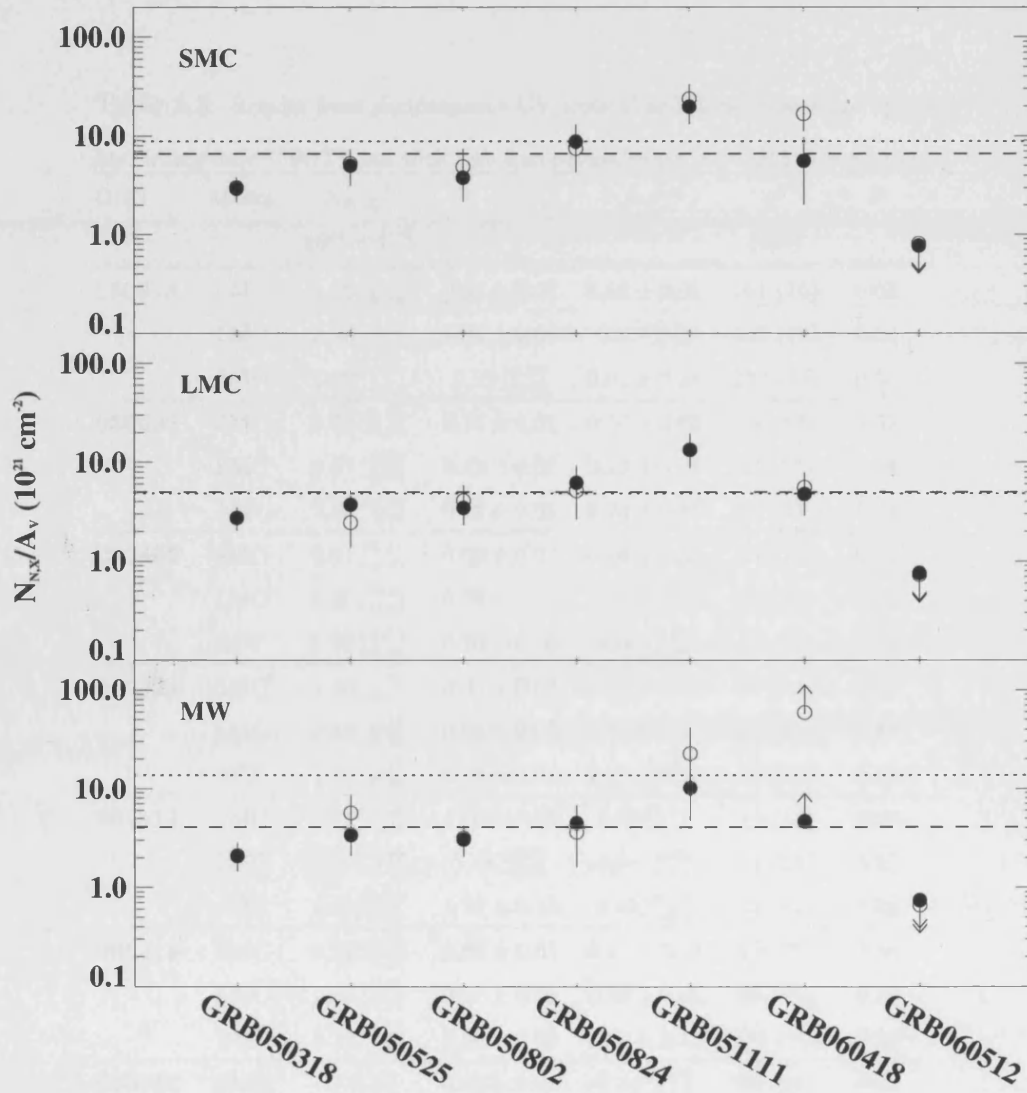Figure 4.2: Ratio of rest frame $N_{H,X}$ to A_V for the three models used in the spectral analysis; SMC model (top panel), LMC model (middle panel) and Milky Way model (bottom panel). Filled circles correspond to power law spectral models and open circles to broken power law fits. Dashed and dotted lines show the mean $N_{H,X}/A_V$ value determined from each spectral model for a power law and broken power law fit, respectively.

Table 4.3: Results from simultaneous UV/optical and X-ray power law spectral fits, where only UVOT data with rest frame wavelength $\lambda > 1215$ Å were used.

GRB	Model	$N_{H,X}$[1] 10^{21} cm^{-2}	β	A_V[1]	χ^2 (dof)	P
050318	SMC	$1.56^{+0.44}_{-0.42}$	0.95 ± 0.03	0.53 ± 0.06	101 (76)	0.03
	LMC	$2.28^{+0.53}_{-0.51}$	1.04 ± 0.04	$0.83^{+0.10}_{-0.09}$	105 (76)	0.02
	MW	$1.90^{+0.60}_{-0.55}$	$0.99^{+0.06}_{-0.05}$	0.91 ± 0.14	154 (76)	0.00
050525	SMC	$0.78^{+0.32}_{-0.29}$	0.76 ± 0.01	0.16 ± 0.03	29 (33)	0.67
	LMC	$0.87^{+0.32}_{-0.29}$	0.79 ± 0.02	0.23 ± 0.04	33 (33)	0.48
	MW	$0.78^{+0.33}_{-0.30}$	0.78 ± 0.03	0.23 ± 0.06	58 (33)	0.01
050802	SMC	$0.91^{+0.41}_{-0.39}$	0.66 ± 0.02	0.24 ± 0.03	106 (81)	0.03
	LMC	$1.30^{+0.44}_{-0.42}$	0.70 ± 0.02	0.38 ± 0.04	98 (81)	0.10
	MW	$1.98^{+0.50}_{-0.48}$	0.76 ± 0.03	$0.65^{+0.08}_{-0.07}$	88 (81)	0.29
050824	SMC	$1.08^{+0.42}_{-0.37}$	0.95 ± 0.02	0.12 ± 0.04	27 (24)	0.33
	LMC	$1.14^{+0.43}_{-0.38}$	0.96 ± 0.03	0.18 ± 0.05	27 (24)	0.29
	MW	$1.20^{+0.45}_{-0.38}$	0.98 ± 0.04	0.27 ± 0.10	31 (24)	0.16
051111	SMC	$7.71^{+1.80}_{-1.55}$	1.10 ± 0.06	$0.39^{+0.11}_{-0.10}$	13 (11)	0.28
	LMC	$8.50^{+1.99}_{-1.73}$	$1.18^{+0.09}_{-0.08}$	$0.64^{+0.19}_{-0.18}$	14 (11)	0.23
	MW	$8.63^{+2.29}_{-2.01}$	1.19 ± 0.13	$0.85^{+0.35}_{-0.34}$	22 (11)	0.03
060418	SMC	$0.97^{+0.69}_{-0.62}$	0.89 ± 0.01	0.17 ± 0.02	79 (75)	0.36
	LMC	$1.83^{+0.76}_{-0.68}$	0.97 ± 0.02	0.38 ± 0.05	68 (75)	0.70
	MW	$0.72^{+0.76}_{-0.71}$	0.88 ± 0.04	0.15 ± 0.10	156 (75)	0.13
060512	SMC	< 0.34	0.99 ± 0.02	$0.44^{+0.04}_{-0.05}$	33 (20)	0.04
	LMC	< 0.33	0.98 ± 0.02	0.44 ± 0.05	37 (20)	0.01
	MW	< 0.27	0.96 ± 0.02	0.37 ± 0.04	44 (20)	0.002

[1] At the redshift of the GRB

Table 4.4: Simultaneous UV/optical and X-ray broken power law spectral fits. Only using UVOT data with rest frame wavelength $\lambda > 1215$ Å.

| GRB	Model	$N_{H,X}^1$ 10^{21} cm^{-2}	β_1	E_b (keV)	β_2	A_V^1	χ^2 (dof)	P
050318	SMC	$1.70^{+0.42}_{-0.34}$	$0.47^{+0.03}_{-0.02}$	0.003 ± 0.0003	$0.97^{+0.04}_{-0.03}$	$0.56^{+0.03}_{-0.04}$	99 (75)	0.03
	LMC	$2.28^{+0.41}_{-0.44}$	0.54 ± 0.04	$0.002^{+0.001}_{-0.0}$	1.04 ± 0.04	$0.83^{+0.09}_{-0.08}$	105 (75)	0.01
	MW	$1.89^{+0.51}_{-0.48}$	0.50 ± 0.05	< 0.0004	1.00 ± 0.05	$0.91^{+0.13}_{-0.14}$	154 (75)	$2e^{-7}$
050525	SMC	$1.39^{+0.48}_{-0.51}$	$0.42^{+0.11}_{-0.10}$	$0.029^{+0.104}_{-0.022}$	$0.92^{+0.11}_{-0.10}$	0.26 ± 0.04	27 (32)	0.73
	LMC	$0.92^{+0.30}_{-0.37}$	$0.30^{+0.01}_{-0.03}$	$0.004^{+0.005}_{-0.001}$	$0.80^{+0.01}_{-0.03}$	$0.38^{+0.03}_{-0.07}$	32 (32)	0.47
	MW	$1.36^{+0.57}_{-0.40}$	$0.67^{+0.03}_{-0.04}$	1.048 ± 0.290	$1.17^{+0.03}_{-0.04}$	0.24 ± 0.07	80 (32)	$5e^{-6}$
050802	SMC	$0.89^{+0.42}_{-0.40}$	0.61 ± 0.02	$2.970^{+0.286}_{-0.348}$	1.11 ± 0.02	0.18 ± 0.03	84 (80)	0.36
	LMC	$1.14^{+0.44}_{-0.43}$	0.64 ± 0.03	$2.990^{+0.516}_{-0.246}$	1.14 ± 0.03	$0.28^{+0.05}_{-0.05}$	81 (80)	0.43
	MW	$1.73^{+0.51}_{-0.49}$	$0.72^{+0.03}_{-0.05}$	$3.960^{+0.538}_{-0.900}$	$1.22^{+0.03}_{-0.05}$	$0.55^{+0.08}_{-0.11}$	79 (80)	0.53
050824	SMC	$1.16^{+0.46}_{-0.37}$	$0.47^{+0.05}_{-0.03}$	0.003 ± 0.001	$0.97^{+0.05}_{-0.03}$	$0.16^{+0.06}_{-0.04}$	26 (23)	0.32
	LMC	$1.27^{+0.45}_{-0.44}$	$0.50^{+0.03}_{-0.04}$	0.003 ± 0.001	$1.00^{+0.03}_{-0.04}$	$0.25^{+0.05}_{-0.08}$	27 (23)	0.28
	MW	$1.36^{+0.48}_{-0.36}$	$0.53^{+0.03}_{-0.04}$	0.003 ± 0.001	$1.03^{+0.03}_{-0.04}$	$0.38^{+0.03}_{-0.18}$	30 (23)	0.14
051111	SMC	$10.04^{+2.70}_{-2.79}$	$0.82^{+0.24}_{-0.20}$	$0.040^{+0.820}_{-0.034}$	$1.32^{+0.24}_{-0.20}$	0.42 ± 0.13	12 (10)	0.25
	LMC	$8.50^{+1.72}_{-1.63}$	$0.68^{+0.42}_{-0.07}$	< 0.772	$1.180^{+0.42}_{-0.07}$	$0.64^{+0.26}_{-0.18}$	14 (10)	0.17
	MW	$11.45^{+2.56}_{-2.83}$	$0.95^{+0.18}_{-0.10}$	< 0.883	$1.45^{+0.18}_{-0.10}$	$0.50^{+0.41}_{-0.34}$	23 (10)	0.01
060418	SMC	$2.80^{+0.97}_{-0.85}$	0.85 ± 0.01	$1.279^{+0.254}_{-0.187}$	1.35 ± 0.01	0.17 ± 0.02	68 (74)	0.68
	LMC	$2.05^{+0.78}_{-0.71}$	0.95 ± 0.02	$2.100^{+0.684}_{-0.513}$	1.45 ± 0.02	0.37 ± 0.05	64 (74)	0.79
	MW	$1.64^{+0.93}_{-0.89}$	$0.79^{+0.02}_{-0.01}$	$1.347^{+0.526}_{-0.150}$	$1.29^{+0.02}_{-0.01}$	< 0.03	145 (74)	$2e^{-6}$
060512	SMC	< 0.47	$0.54^{+0.05}_{-0.01}$	0.003 ± 0.001	$1.04^{+0.05}_{-0.01}$	$0.58^{+0.06}_{-0.03}$	32 (19)	0.04
	LMC	< 0.42	0.53 ± 0.01	0.003 ± 0.001	1.03 ± 0.01	$0.57^{+0.06}_{-0.03}$	35 (19)	0.01
	MW	< 0.32	0.51 ± 0.01	< 0.001	1.010 ± 0.01	$0.49^{+0.04}_{-0.003}$	44 (19)	0.001

[1] At the redshift of the GRB
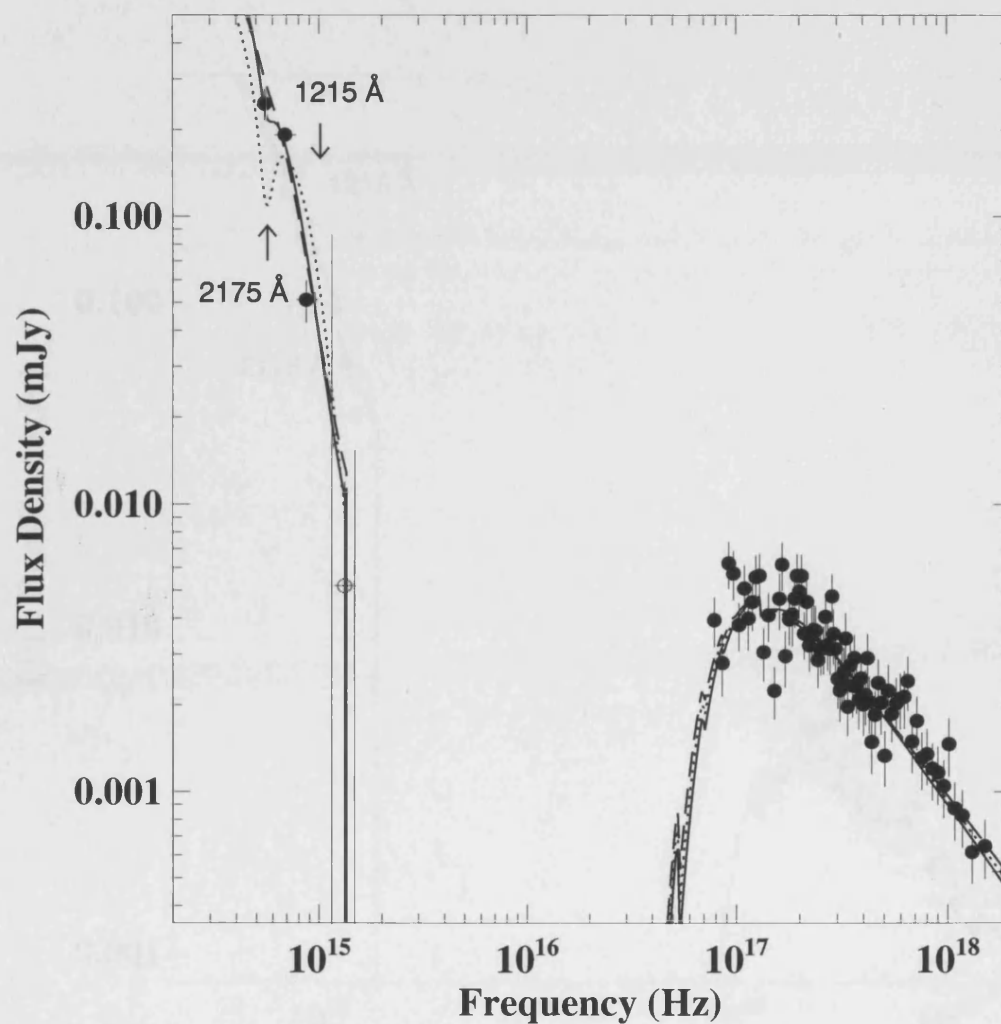
Figure 4.3: SED for GRB 050318 at 1 hour after the prompt emission with best-fit models for each corresponding dust extinction curve shown; SMC (dashed), LMC (solid) and Galactic (dotted). Open circles are data points at wavelength $\lambda < 1215$ Å in the rest frame, and therefore not used in the spectral fitting. The positions of 2175 Å and 1215 Å in the rest frame are indicated.

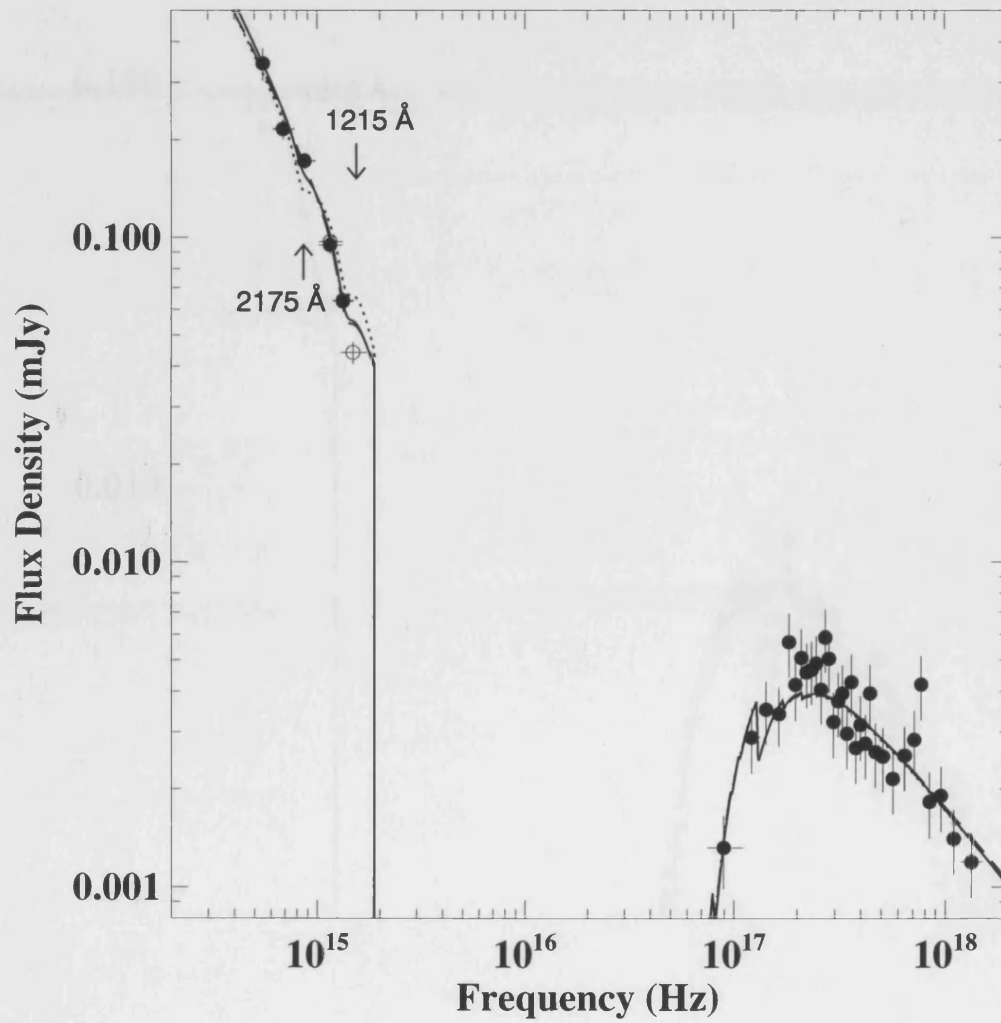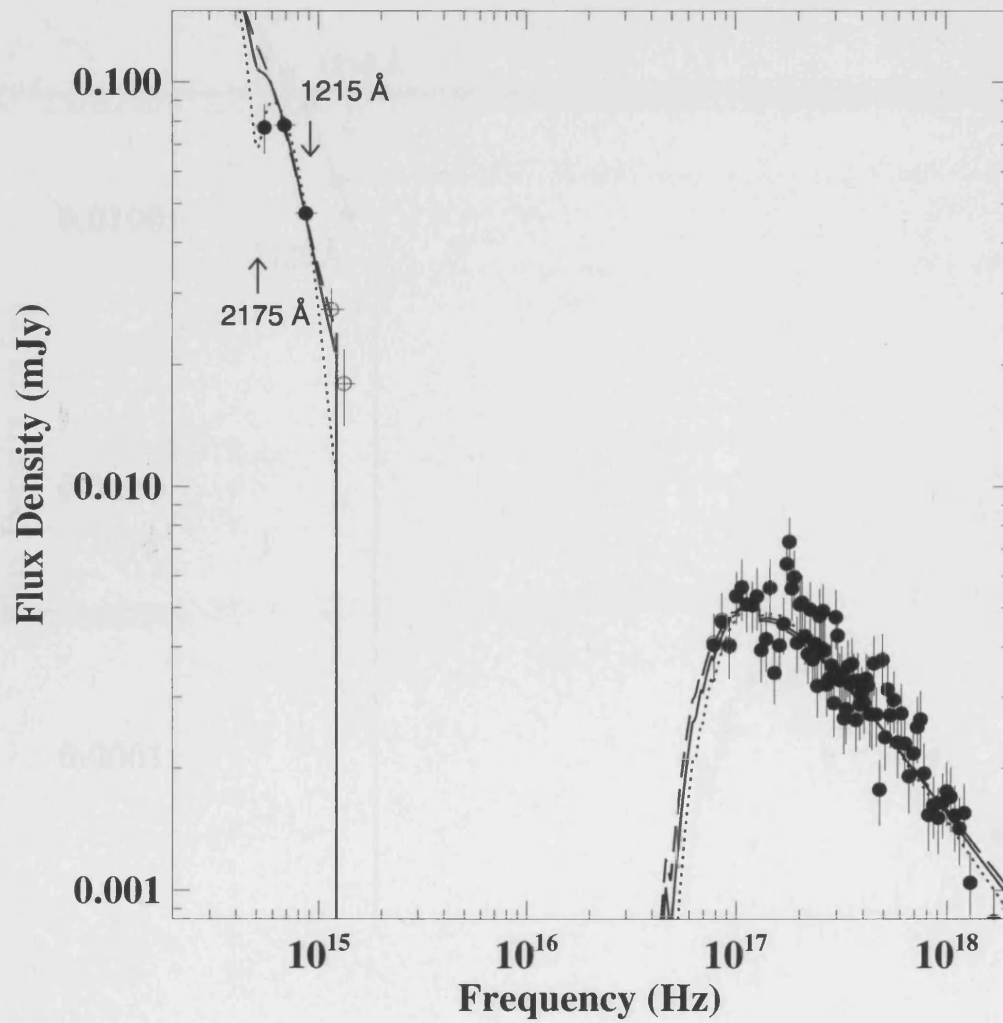Figure 4.4: SED for GRB 0500525 at 1 hour after the prompt emission

Figure 4.5: SED for GRB 050802 at 1 hour after the prompt emission
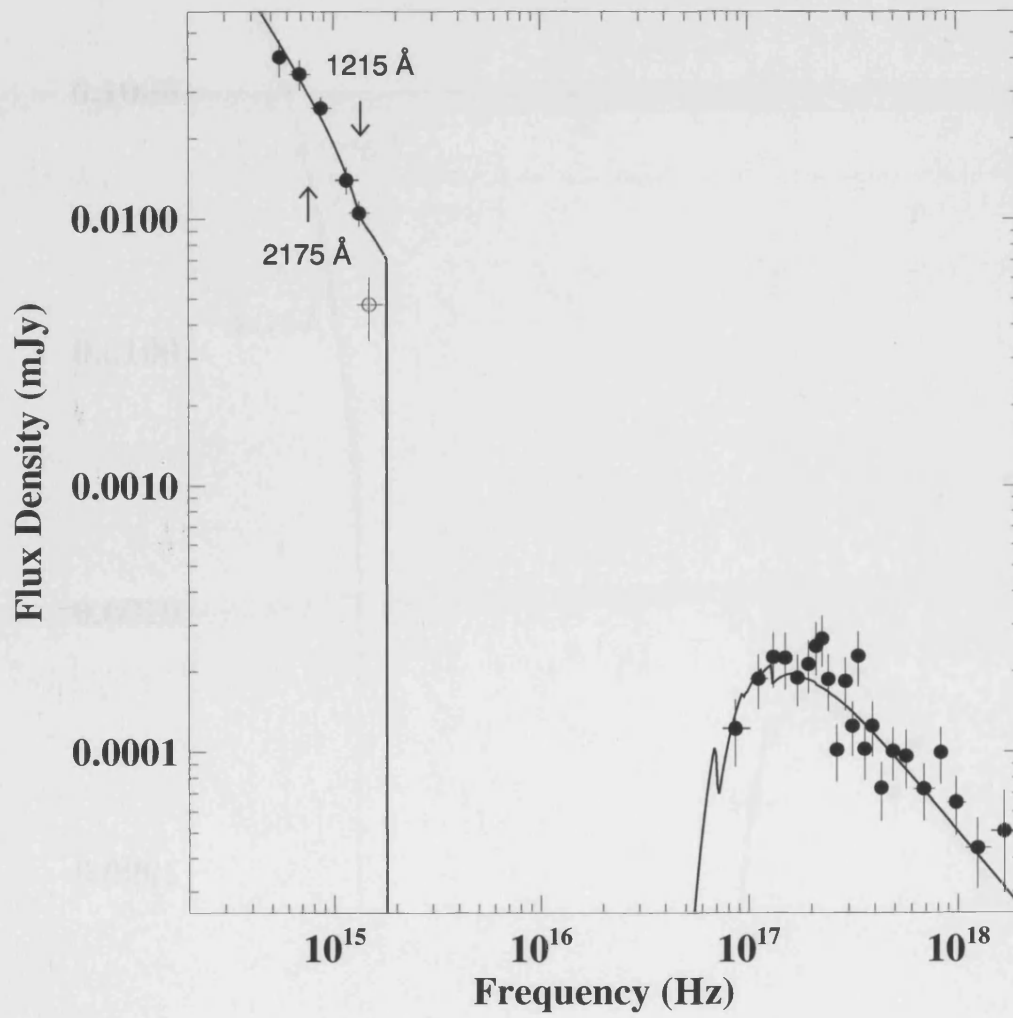
Figure 4.6: SED for GRB 050824 at 2 hours after the prompt emission
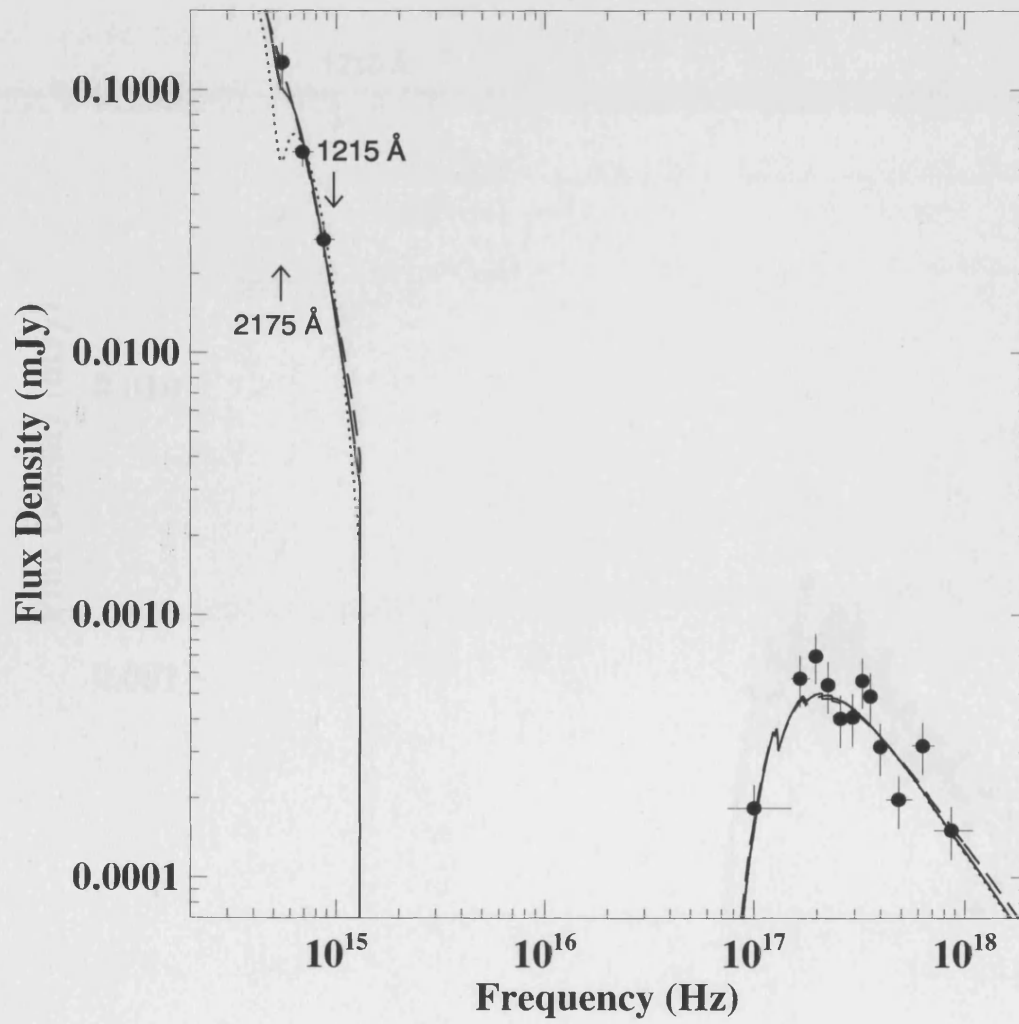
Figure 4.7: SED for GRB 051111 at 2 hours after the prompt emission
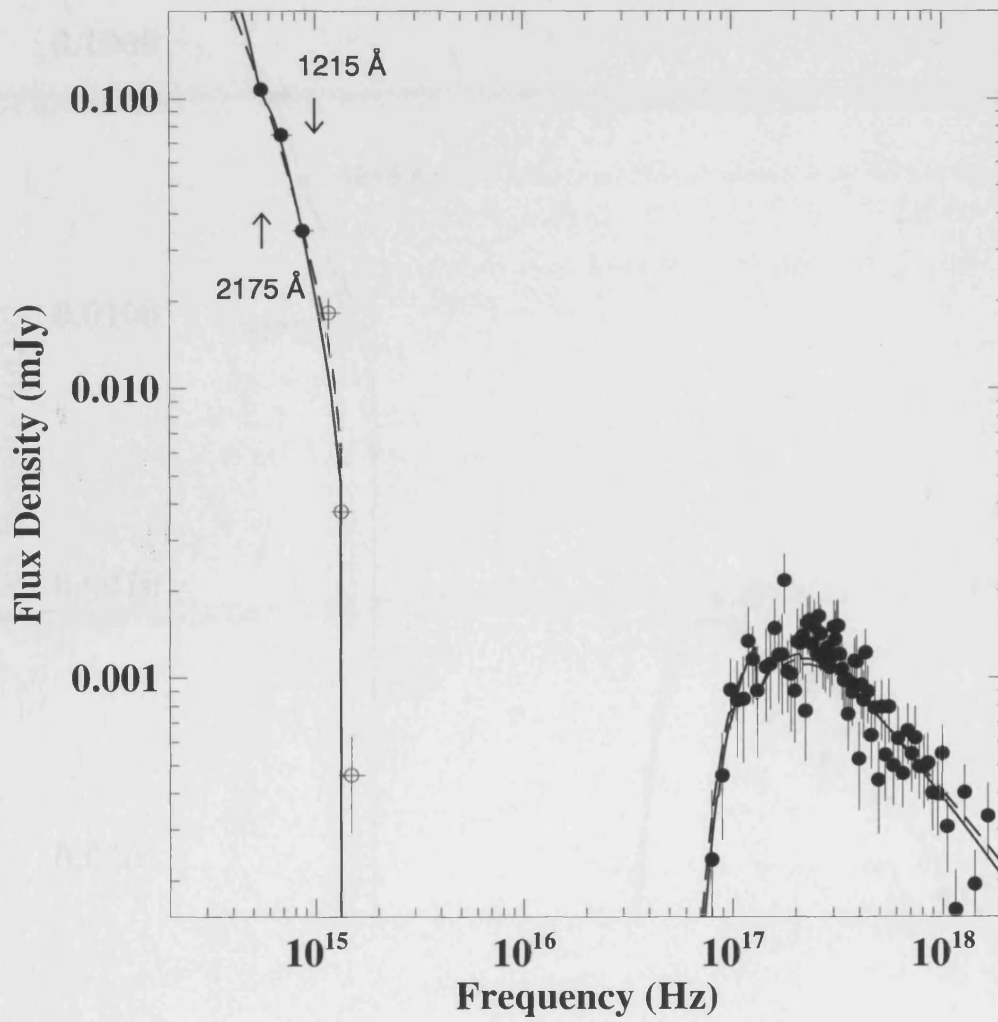
Figure 4.8: SED for GRB 060418 at 2 hours after the prompt emission
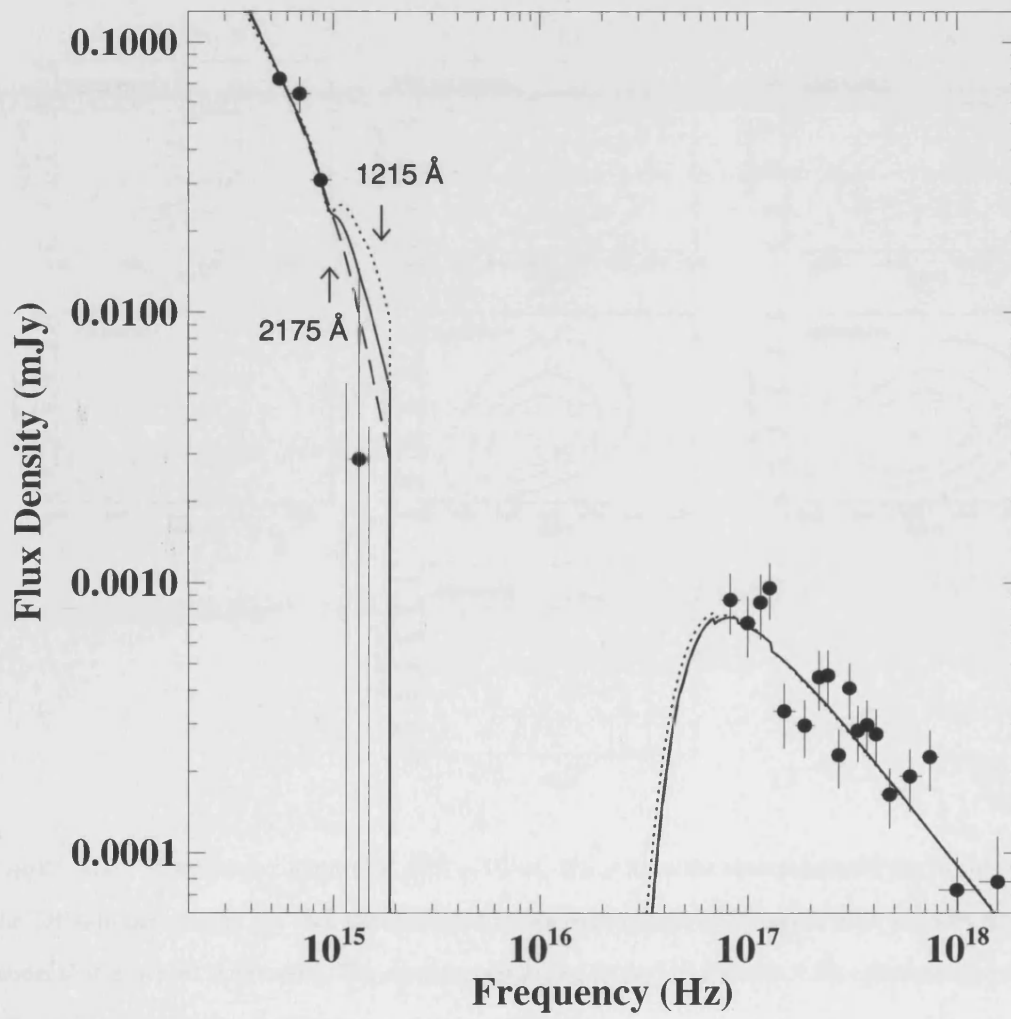
Figure 4.9: SED for GRB 060512 at 1 hour after the prompt emission
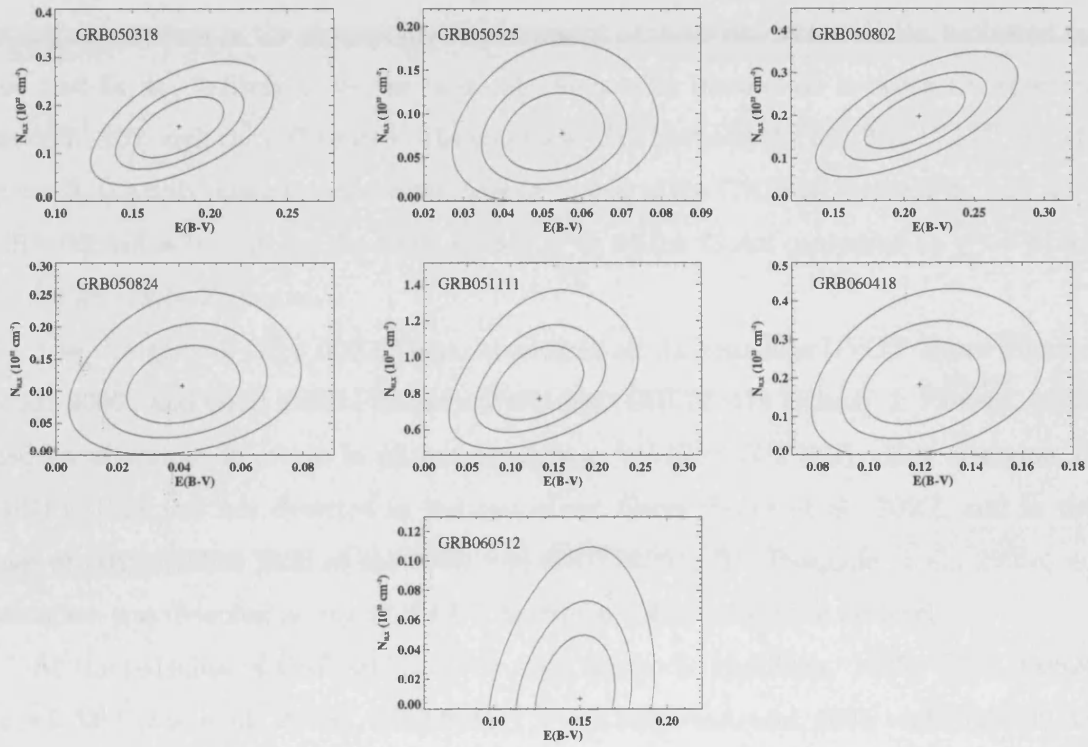
Figure 4.10: Confidence contours for $E(B-V)$ vs. $N_{H,X}$ from the spectral model fits to the SEDs of the GRBs in the sample. For each GRB, the confidence contours shown are taken from the dust extinction model that provided the best fit. The contours are drawn at $\Delta\chi^2 = 2.3, 4.61, 9.21$, corresponding to 68%, 90% and 99% confidence for two interesting parameters.

4.5.1 GRB Host Extinction Laws

Six of the seven GRBs in the sample were best fit by the SMC or LMC model, with the MW model rejected with at least 97% confidence for four of these (GRB 050318, 050525, 051111 and GRB 060512). For GRB 050824 and GRB 060418 the MW model is rejected with 84% and 87% confidence, respectively. The relatively small amount of extinguishing dust in the circumburst environment of those two latter GRBs, indicated by the best-fit A_V, is likely to be the cause for the smaller distinction between the spectral models. Although the difference in the goodness of fit between the SMC and LMC models is small, the SMC model provides the best fit to five of the GRBs in the sample, and only GRB 060418 is best fit by the LMC model; $\chi^2 = 68$ for 75 dof compared to $\chi^2 = 79$ for 75 dof for the SMC model.

The afterglow of GRB 050525 was detected in all six lenticular UVOT filters [Blustin et al., 2006], and GRB 050824 [Schady, 2005] and GRB 060418 [Schady & Falcone, 2006] had an afterglow detection in all but the bluest UV filter ($UVW2$). The afterglow of GRB 051111 was not detected in the two bluest filters [Poole et al., 2005], and in the case of GRB 050318 [Still et al., 2005] and GRB 060512 [De Pasquale et al., 2006a] no afterglow was detected in any of the UV lenticular filters above the 3σ level.

At the redshifts of GRB 050318 [$z = 1.44$; Berger & Mulchaey, 2005], GRB 050824 [$z = 0.83$; Fynbo et al., 2005a], GRB 051111 [$z = 1.549$; Prochaska, 2005] and GRB 060418 [$z = 1.49$; Dupree et al., 2006], the lack of an optical afterglow detection in the bluest filters could either be the result of Ly-α blanketing or high levels of dust extinction blueward of ~ 3800 Å. GRB 050318 and GRB 051111 have A_V values that lie at the higher end of the distribution observed in the sample, with best-fit parameters $A_V = 0.53 \pm 0.06$ mag and $A_V = 0.39^{+0.11}_{-0.10}$ mag, respectively, if the SMC model is used. GRB 050824 and GRB 060418, on the other hand, have at least half this amount of rest frame extinction if the SMC model is used ($A_V = 0.12 \pm 0.04$ mag and $A_V = 0.17 \pm 0.02$ mag, respectively). The comparable redshifts for three of the four GRBs considered here make it unlikely that a redshift effect can account for the difference in the number of filters in which the

GRB afterglow was detected. Instead, the correlation between A_V and the number of filters in which the afterglow is detected could indicate that it is dust present in the local environment of these GRBs that contributes to the observed dimness of their UV afterglow.

GRB 060512 was a low redshift burst [z=0.4428; Bloom et al., 2006a], eliminating neutral hydrogen absorption as the cause for the lack of a UV afterglow detection. The best fit is provided by the SMC model ($\chi^2 = 33$ for 20 dof) yielding a host galaxy extinction of $A_V = 0.44^{+0.04}_{-0.05}$ mag, which is comparable to those observed in GRB 050318 and GRB 051111. This, therefore, provides further support to the hypothesis whereby dust in the local environment of the GRB blocks a large fraction of the UV flux emitted.

In contrast to the other bursts discussed in this section, GRB 050525 had very small amounts of local absorption and extinction. However, good quality data resulting from the proximity [z=0.606; Blustin et al., 2006] and brightness of this burst in the UV and optical bands constrain well the spectral fits, and provide a distinction between them. The afterglow SED was best fit by the SMC model ($\chi^2 = 29$ for 33 dof).

GRB 050802 is the only burst in the sample where the goodness of the spectral fit is improved with the MW model, ($\chi^2 = 88$ for 81 dof). The SED of GRB 050802 flattens out at longer wavelengths (Fig. 4.5) and this is well fit by a model with a dust extinction curve that contains the 2175 Å absorption feature (i.e. LMC and MW models). The χ^2 of the LMC model fit is still acceptable, with $\chi^2 = 98$ for 81 dof, although it is rejected at the 90% confidence level in contrast to the MW model, which is only rejected at the 71% confidence level.

4.6 Discussion

4.6.1 The 2175 Å Absorption Feature

The redshift range of the GRB sample in this chapter places the 2175 Å Milky Way absorption feature in the UVOT wavelength range, and its degree of prominence in the
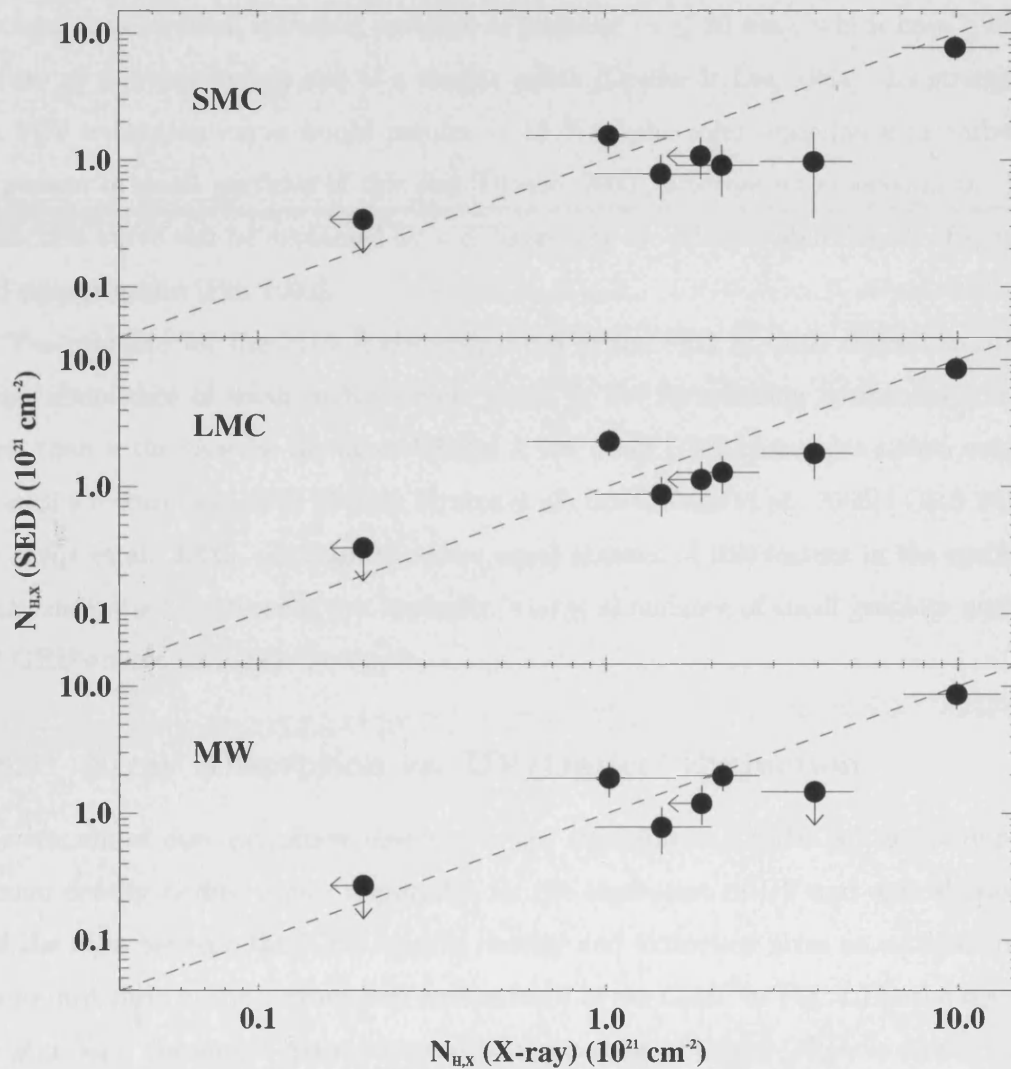
Figure 4.11: Best-fit $N_{H,X}$ from SED spectral analysis vs. best-fit $N_{H,X}$ from spectral analysis to X-ray data alone. Top, middle and bottom panel correspond to the results from the SED spectral analysis using an SMC, LMC and MW model, respectively. In each panel the dashed line corresponds to $N_{H,X}$(X-ray) = $N_{H,X}$(SED). All data points lie on or very close to this line, illustrating the robustness of the spectral analysis.

GRB SEDs provides information on the graphite content of small grains in the surrounding circumburst material. The origin of the 2175 Å feature is most likely to be carbonaceous material such as small spherical particles of graphite ($a \leq 30$ nm), which have a strong feature at this wavelength and of a similar width [Draine & Lee, 1984]. Its strength in the MW extinction curve would require ~ 15 % of the solar abundance in carbon to be present in small particles of this size [Draine, 2003], whereas its absence in the SMC extinction curve can be explained by a difference in the relative abundances of graphite and silicate grains [Pei, 1992].

The evidence for the 2175 Å absorption dip in the SED of GRB 050802 suggests a larger abundance of small carbonaceous grains in the surrounding environment of this burst than is the case for the other GRBs. A few other GRBs have also shown evidence for such a feature [e.g. GRB 970508; Stratta et al., 2004, Kann et al., 2006] [GRB 991216; Vreeswijk et al., 2006], although the more usual absence of this feature in the spectra of GRBs indicates that there is not, typically, a large abundance of small graphite grains in the GRB's surrounding environment.

4.6.2   X-ray Absorption vs. UV/Optical Extinction

The amount of dust extinction observed in the afterglow of a GRB is a measure of the column density of dust grains responsible for the absorption of UV and optical photons, and the ratio between the X-ray column density and extinction gives an estimate of the gas-to-dust ratio in the surrounding environment of the GRB. In Fig. 4.12a the region of A_V and $N_{H,X}$ parameter space occupied by the sample of bright GRBs is shown for the best-fit A_V and $N_{H,X}$ values determined from the spectral analysis when the data are fit with the SMC (top panel), the LMC (middle panel), and the MW models (bottom panel).

The dashed lines in the figure are plotted as a point of reference and correspond to the empirical relation observed between A_V and $N_{H,X}$ in the SMC, LMC and MW. These are determined from the N_H/A_V values reported in the literature for each of these environments, which are then converted to an $N_{H,X}/A_V$ ratio relating to the column density

that would be measured from X-ray observations of the galaxy if solar abundances were assumed. The parameterisation of these lines differs between each panel, and correspond to

$$\frac{N_{H,X}}{A_V}(\text{SMC}) = \tfrac{1}{8}\frac{N_H}{A_V}(\text{SMC}) = \tfrac{1}{8}(1.6 \times 10^{22}) \text{ cm}^{-2} \qquad (4.2)$$

$$\frac{N_{H,X}}{A_V}(\text{LMC}) = \tfrac{1}{3}\frac{N_H}{A_V}(\text{LMC}) = \tfrac{1}{3}(0.7 \times 10^{22}) \text{ cm}^{-2} \qquad (4.3)$$

$$\frac{N_{H,X}}{A_V}(\text{MW}) = \frac{N_H}{A_V}(\text{MW}) = 0.18 \times 10^{22} \text{ cm}^{-2} \qquad (4.4)$$

where the factors of $\tfrac{1}{8}$ and $\tfrac{1}{3}$ account for the lower metallicities observed in the SMC and LMC [Pei, 1992]. The N_H/A_V relations are taken from Weingartner & Draine [2000] and Predehl & Schmitt [1995] for the SMC and MW, respectively, and the average of the ratios found by Koornneef [1982] and Fitzpatrick [1985] are used for the LMC.

The data points in Fig. 4.12 primarily lie to the right of the lines of constant $N_{H,X}/A_V$. However, they are confined to an area of the $N_{H,X}$–A_V parameter space much closer to the dust-to-gas ratio observed in the MW and Magellanic Clouds than the region of space occupied by previous data. This is illustrated in Fig. 4.12b, where the host galaxy $N_{H,X}$ and A_V for two pre-*Swift* GRB samples taken from Stratta et al. [2004] (SFA sample) and Kann et al. [2006] (KKZ sample) are included, represented by open triangles and open squares, respectively. Stratta et al. [2004] did not use the LMC extinction law to model the afterglow spectrum, and consequently there are no triangles shown in the centre panel of Fig. 4.12b.

Despite the apparent differences between the *Swift* sample and previous samples, the distribution in A_V and $N_{H,X}$ between samples remain consistent within errors. Considering only the KKZ sample, which has smaller errors, the mean of the logarithmic visual extinction is -0.83 ± 0.30 mag, and in the *Swift* sample it is $-0.59^{+0.08}_{-0.07}$ mag, respectively. The mean of the logarithmic column density is $21.4^{+0.6}_{-0.4}$ cm^{-2} and 21.1 ± 0.3 cm^{-2} for the KKZ and *Swift* sample, respectively.

The X-ray data in the SFA sample are from *BeppoSAX* and were taken hours to days after the prompt outburst, with the earliest observation beginning at $\sim T + 4$ hours. In
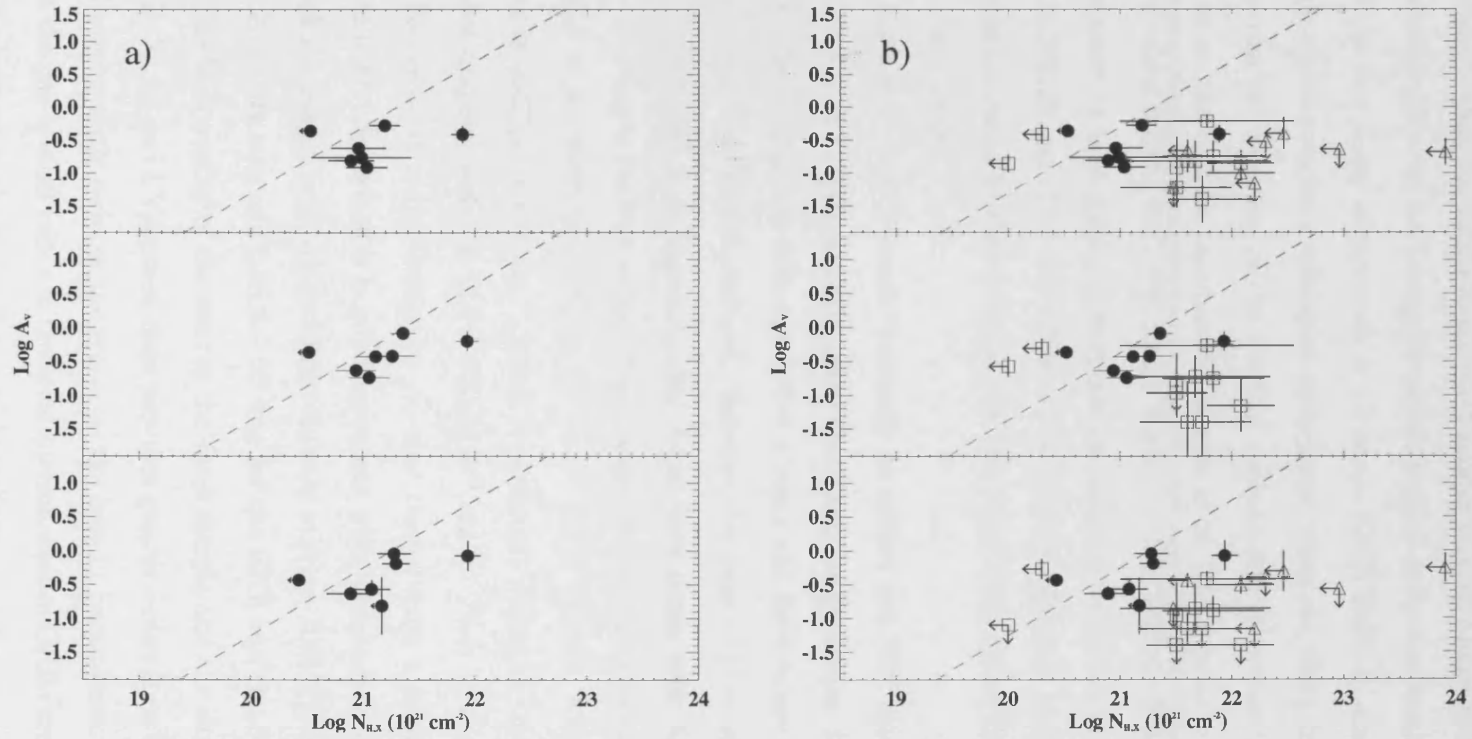
Figure 4.12: Host galaxy A_V vs. $N_{H,X}$. In both plots solid circles represent the host galaxy A_V and $N_{H,X}$ determined from the spectral analysis using the SMC model (top panel), the LMC model (middle panel) and the MW model (bottom panel). The dashed curves are the $N_{H,X}/A_V$ ratios for each corresponding environment. This was determined using the N_H/A_V ratios reported in the literature, where N_H is converted to the X-ray equivalent $N_{H,X}$ value assuming a metallicity 1/8 and 1/3 solar for the SMC and LMC, respectively (see text for details). In the right panel the open triangles and open squares are GRBs taken from the SFA and KKZ sample, respectively.

contrast to this, the GRBs in the *Swift* sample typically have X-ray data starting hundreds of seconds after the BAT trigger, and the longest delay between the GRB prompt emission and the first X-ray observation is 1.7 hours [GRB 050824; Campana et al., 2005]. The larger signal-to-noise available at early times, when the afterglow is significantly brighter, improves the accuracy of the spectral analysis and consequently reduces the systematic errors on the best-fit parameters. Stratta et al. [2004] point out that the quality of the X-ray data for the majority of the bursts in their sample does not allow for significant detections of host galaxy absorption in addition to Galactic, and in only the cases of GRB 990123 and GRB 010222 were the presence of excess absorption robustly detected. This is indicated in Fig. 4.12b, where the $N_{H,X}$ value for all but two of the SFA sample are upper limits.

Kann et al. [2006] focused primarily on optical and NIR data, while the X-ray column densities used in their analysis were taken from the literature. In their sample the earliest X-ray observation was still only $\sim T + 4$ hours and the average delay was nearly 50 hours from the time of initial outburst. However, for most of their sample the column density was determined from higher quality X-ray data taken with XMM-Newton or *Chandra*. For this sample the host galaxy $N_{H,X}$ ranged from an undetectable amount [GRB 021004; Möller et al., 2002] to $(12^{+7}_{-6}) \times 10^{21}$ cm^{-2} [GRB 010222; Stratta et al., 2004], and the mean is $(4.6^{+1.7}_{-1.0}) \times 10^{21}$ cm^{-2}, which is consistent within 2σ of the *Swift* sample analysed in this chapter, which is $(2.2 \pm 0.3) \times 10^{21}$ cm^{-2}. Their optical and NIR analysis of 19 GRBs provided a distribution in A_V that ranged from a negligible amount up to $A_V = 0.80 \pm 0.29$ mag , which is in good agreement with the results presented in this chapter, for which A_V ranges from $A_V = 0.12 \pm 0.04$ mag to $A_V = 0.65^{+0.08}_{-0.07}$ mag. The mean extinction is 0.21 ± 0.04 mag and 0.38 ± 0.02 mag for the KKZ and the *Swift* sample, respectively.

The high quality of the data in the *Swift* sample and the simultaneous spectral fitting of the X-ray and UV/optical data provides greater constraints on the spectral modelling, and consequently reduces the errors on the best-fit parameters. The results from this are that the gas-to-dust ratios in the local environment of GRBs are in better agreement with those observed in the Milky Way and Magellanic Clouds than previous data suggest. The

relatively large gas-to-dust ratios in GRB local environments indicated by previous data were interpreted as evidence of dust destruction by the GRB, which would cause the value of A_V to decrease. However, the results from the *Swift* data analysis show little evidence of this.

Moreover, when interpreting the $N_{H,X}$ to A_V ratio in the GRB local environment compared with that of other environments, it is necessary to consider more than just the effect of the GRB emission on A_V. Photoionisation of the gas in the surrounding environment by the GRB X-ray radiation causes $N_{H,X}$ to decrease with time, and the extent to which the GRB affects the measured value of A_V and $N_{H,X}$ will depend on the properties of the GRB and its local environment, such as the prompt and afterglow spectral and temporal indices, and the density and density profile of the absorbing and extinguishing material.

4.6.3 Effect of GRBs on Surrounding Environmental

The intense radiation emitted by a GRB is expected to both photoionise the gas and destroy the dusts grains in the circumburst environment, although it is not clear out to what distance the GRB should affect its environment. For example, both Prochaska et al. [200] and Vreeswijk et al. [2007] used the detection of absorption lines from elements such as Mg II, Fe II and Ni II at the redshift of the GRB to estimate the distance of this absorbing material from the source and, between them, came up with a range from $\gtrsim 50$ pc up to 1.7 kpc.

Heating and Sublimation

Dust grains that are excited and heated up by the absorption of photons can cool through radiative cooling. However, if the absorption rate of photons is greater than the cooling rate, the build up of energy within the grain will break the bonds between the atoms at the surface of the grains and lead to the destruction of the dust when a critical temperature is reached. This temperature is dependant on the density and size of the grain material,

and on its composition, where grains made of atoms with larger binding energies and a smaller mean atomic mass require a larger temperature for sublimation to occur. This process is dominated by photons with energies 1 eV$< h\nu < 7.5$ ev, in the UV to NIR energy range, which have the largest dust absorption cross section. At energies larger than this, in the far UV range, radiation is primarily absorbed by molecular and neutral hydrogen.

Charging and Electrostatic Shattering

Dust destruction can also occur through the build up of Coulomb charges within the grain. If the absorption of a photon results in the release of an electron from the dust grain, a positive charge is left on the dust grain, and the buildup of electrostatic stress from the repeated release of electrons can cause the grain to shatter. To remove an electron from the dust grain the absorbed photon needs to have an energy at least equal to the electron binding energy plus the minimum energy required for the electron to then escape the dust grain. The rate of electrostatic shattering of dust grains is, therefore, determined by the fluence of the soft X-ray energy band.

The lack of evidence for any colour evolution in the UV/optical data (see section 4.3.1), provides an upper limit on the time by which the GRB is no longer destroying significant amounts of dust. i.e. the time at which colour information is available with UVOT, which is typically within $\sim 10^3$ s. A limit on the time after which the GRB no longer photoionises the surrounding environment can also be determined by investigating the change in $N_{H,X}$ over time during the early stages of the X-ray afterglow. For this purpose, I performed a spectral analysis of the early time X-ray data on the five GRBs in the sample for which there were data within the first few 100 seconds of the BAT trigger. Of these GRBs only GRB 060418 shows evidence for evolution in the column density at greater than the 3σ level. For GRB 060418 the column density measured from T+84 s to T+114 s was $(1.6 \pm 0.10) \times 10^{22}$ cm^{-2}, whereas beyond T+400 s this was $(3.9^{+1.3}_{-1.2}) \times 10^{21}$ cm^{-2}. GRB 060418 had a very large X-ray flare that peaked at T+135 s [Falcone et al., 2006b] and increased the X-ray flux by about an order of magnitude in ~ 15 s, which could

have caused photoionisation of the circumburst environment at later times, and out to greater radii from the source. However, it is possible to misinterpret intrinsic spectral evolution as a change in the column density [Butler & Kocevski, 2007]. The spectral index indeed changed from $\Gamma = 2.75 \pm 0.05$ to $\Gamma = 2.15 \pm 0.08$ between the two spectral epochs analysed, and the apparently larger $N_{H,X}$ could be due to intrinsic curvature of the flare spectrum. The column density measured in GRB 060418 no longer evolves beyond T+300 s, by which time the flare is over and, therefore, a typical upper limit of a few hundred seconds can be put on the time interval over which the GRB photoionises its surrounding environment.

Perna & Lazzati [2002] simulated the effect of the GRB X-ray and UV emission on $N_{H,X}$ and A_V over time, where they assumed the same initial hydrogen column density $N_H = 10^{22}$ cm^{-2} and optical extinction $A_V = 4.5$ mag in all cases, but varied the compactness of the absorbing medium and, therefore, also the number density, n_H. Their simulations indicate that the intense radiation emitted by a GRB is capable of photoionising and destroying all gas and dust out to a radius of ~ 3 pc within a few tens of seconds. Further evolution in the gas and dust column resulting from this is, therefore, not expected more than a few hundreds of seconds after the peak of the emission, consistent with the observations presented in this chapter.

This, therefore, places a lower limit of a few parsecs on the scale of the absorbing and extinguishing system detected local to the GRB for six of the seven in the sample. If the dust and gas were any closer it would have been fully destroyed and photoionised. Furthermore, Perna & Lazzati [2002] showed in their simulations that if the dust and gas extends out to a few tens of parsecs, the A_V and $N_{H,X}$ measured local to the GRB will not change significantly. This would suggest that the host galaxy dust and gas systems probed by the sample in this chapter lie a few tens of parsecs from the source. This suggests that the dust-to-gas ratios measured are effectively unaltered by the GRB and a fair representation of their local environment. It is, therefore, not so surprising that there is no significant deviation in the GRB local environment $N_{H,X}/A_V$ ratio when compared to the Milky Way or Magellanic Clouds.

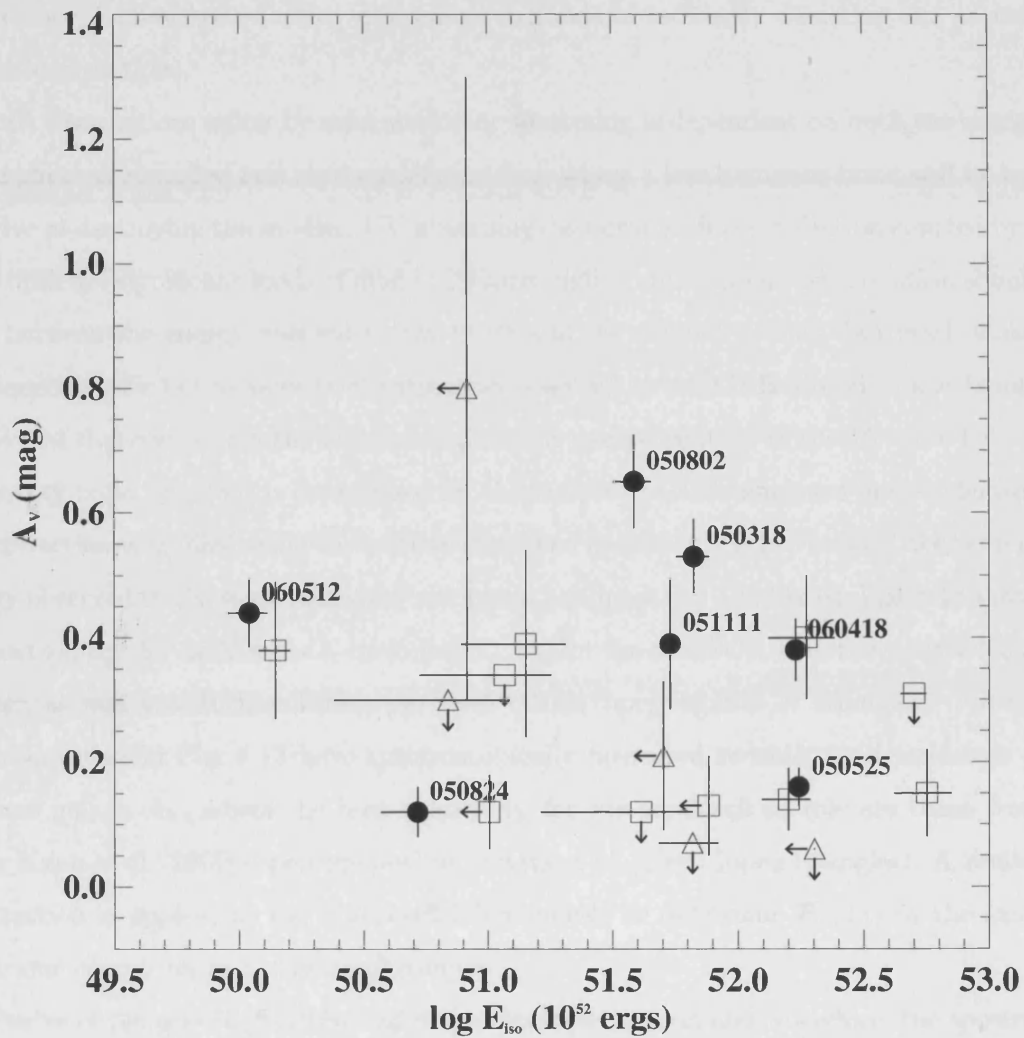Figure 4.13: Host galaxy visual extinction against isotropic equivalent energy in γ-rays for a sample of 16 bursts. Solid data points correspond to the GRBs studied in this chapter. Open data points are GRBs from a pre-*Swift* sample of GRBs where the E_{iso} values are taken from Bloom et al. [2001] and the A_V values are from Kann et al. [2006] (square) and Stratta et al. [2004] (triangle).

4.6.4 Alternative Indicators Of Dust Destruction

To verify that the effect of the GRB on the dust and gas in its local environment is of little significance, I investigate further alternative methods of indirectly detecting the process of dust destruction.

Dust destruction, either by sublimation or shattering is dependent on both the energy of the photons absorbed and on the radiation flux, where a less-luminous burst will be less effective at destroying the smaller, UV-absorbing dust grains. If the radiation emitted by a GRB destroys significant levels of dust in its surrounding environment a correlation should exist between the energy released by the burst and the amount of dust destroyed, which consequently affects the amount of extinction observed in the GRB afterglow spectrum.

To test this correlation the isotropic equivalent energy emitted in the 15 – 150 keV γ-ray energy band ($E_{iso}(\gamma)$) is determined for the sample of GRBs analysed in this chapter. A k-correction is applied using the method described in section 1.2.1 to convert the prompt energy observed to the same comoving rest frame bandpass (15 – 150 keV). Fig. 4.13 shows the host galaxy A_V against the k-corrected $E_{iso}(\gamma)$ for the seven GRBs in the sample (solid circles), as well as a further fifteen pre-*Swift* GRBs (open squares or triangles). All the GRBs included in Fig. 4.13 have spectroscopically measured redshifts and estimates of the host galaxy A_V, where the host galaxy A_V for the pre-*Swift* sample are taken from either Kann et al. [2006] (open squares) or Stratta et al. [2004] (open triangles). A similar k-correction is applied to the non-*Swift* GRB sample to determine $E_{iso}(\gamma)$ in the same rest frame energy range as the *Swift* sample.

Twelve of the pre-*Swift* GRBs had no spectral information and, therefore, the spectral shape had to be assumed. Band et al. [1993] found the GRB prompt emission to be well modelled by a smoothed, broken, power law with a soft and hard spectral index, β_1 and β_2, respectively, and spectral break E_0 (see section 1.2.1). Those GRBs with no spectral information are assumed to have a Band spectrum, and their $E_{iso}(\gamma)$ is taken from the average of 54 values, each computed with a different set of (β_1, β_2, E_0). The set of 54 (β_1, β_2, E_0) combinations are taken from fits to 54 BATSE GRBs done by Band et

al. [1993].

To test the presence of any correlation between the log of E_{iso} and A_V, a Spearman rank test is used, which assesses how well the relationship between two variables can be described by a monotonic function, which is not required to be linear. To remove the functional form of any correlation linking two sets of data, the variables are assigned a rank value within their set. The rank correlation, R, is given by

$$R = \sum_{i=1}^{n} (x_i - y_i)^2,$$ (4.5)

where x_i and y_i are the rank values assigned to the variables in each data set. Based on the Spearman rank test the set of log E_{iso} and log A_V values shown in Fig. 4.13 have a correlation coefficient of only $r_s = -0.21$ with a null-hypothesis probability of P=0.60, which indicates that there is no significant correlation between E_{iso} and A_V. This is consistent with the findings of Nardini et al. [2006], whose analysis showed a sample of 23 pre-*Swift* GRBs to show no correlation between the isotropic γ-ray emitted energies and the optical luminosities. This, therefore, suggests that any dust-destruction caused by the GRB intense radiation is not significant enough to affect greatly their observed extinction properties, as already indicated in Fig. 4.12 and discussed in section 4.6.2.

4.7 Summary

In this chapter I used the SEDs of seven optically bright GRBs, covering the optical, UV and X-ray energy bands, to determine the amount of dust extinction and soft X-ray absorption present in the local environments of the GRB. The Milky Way (MW) and the Large and Small Magellanic Cloud (LMC and SMC) extinction laws were used to model the host galaxy dust extinction dependence on wavelength. These show a decreasing prominence in the strength of the 2175 Å feature, and increasing levels of far-ultraviolet extinction, respectively.

All GRBs but one were best fit by an SMC extinction law, with the LMC law being only slightly inferior in some cases. Only in the case of GRB 050802 did a model with a

Milky Way extinction law provide a better fit, although SMC and LMC extinction laws were rejected with only 97% and 90% confidence, respectively. This, therefore, suggests that small graphite grains responsible for the 2175 Å feature are not generally predominant in the local environments of GRBs.

For six of the seven GRBs in the sample an absorption and extinction system was detected at the redshift of the GRB, which must be located at least several parsecs or more from the source to have survived the intense radiation emitted by the GRB. However, the gas-to-dust ratios measured in the host galaxies of the sample of bursts are lower than previously suggested from analysis of pre-*Swift* GRBs, and consistent with those observed in the Milky Way and Magellanic Clouds. There is, therefore no evidence of dust destruction by the GRB in its circumburst environment provided by the spectral analysis alone. However, this does not rule out the destruction and photoionisation of dust and gas within several parsecs of the GRB, which is likely to occur in the first few tens of seconds of the GRB outburst, before the beginning of the X-ray and UV/optical afterglow observations. Indeed, the expectation that the GRB intense radiation will photoionise and destroy the gas and dust has important implications for the distance of the absorption and extinction systems detected at the host galaxy of six out of the seven GRBs. Based on the work done by Perna & Lazzati [2002], the distance of this material must be a few parsecs from the source.

Chapter 5

GRB 061007: an extreme GRB

Swift's fast slewing capabilities allow GRB afterglow light curves to be measured from ~ 60 s after the trigger. The well-sampled X-ray and optical light curves from *Swift* have revealed far fewer achromatic breaks than had been expected prior to launch (Ghirlanda, Ghisellini & Lazzati 2004; O'Brien et al. 2006). This may be an indication that many jet breaks don't occur until after the afterglow has fallen below the level of detectability. In the X-ray band this is at around 10^6 s after the prompt emission for a typical GRB. The time of the jet break, t_j, increases with the jet opening-angle, θ_j, as $t_j \propto \theta_j^{8/3}(n/E_k)^{-1/3}$ erg, for a constant density circumburst medium with density n and GRB kinetic energy E_k. Large average jet opening-angles, small circumburst densities or large GRB kinetic energies may, therefore, all contribute to delaying the time of the jet-break to when the afterglow is no longer detectable by *Swift*, although t_j is only weakly dependent on the circumburst density and the GRB kinetic energy.

GRB 061007 is an example of a burst that showed no evidence of a break in the X-ray or UV/optical afterglow from 80 s after the prompt emission, until it was no longer detected above background, at $\sim 10^6$ s. A particularly unusual feature of the afterglow of this GRB was the similarity in the temporal evolution between the X-ray and the UV/optical bands, which decayed at the same, rapid rate and had no structure, such as flaring behaviour or plateau's in any band. Both the X-ray and UV/optical afterglows decayed as a steep power law with decay index $\alpha \sim 1.65$, which in the UV and optical

bands is a particularly steep GRB afterglow decay, and in the X-ray is not usually observed until $\sim T + 10^3$ s.

Prompt observations by ground based observatories measured the redshift of this burst to be z=1.26 (Osip, Chen & Prochaska 2006; Jakobsson et al. 2006a). At this redshift, GRB 061007 had one of the highest isotropic equivalent energies ever seen, releasing $\sim 10^{54}$ erg in γ-radiation alone, with an optical afterglow comparable to that of GRB 990123 [Akerlof et al., 1999], with $V < 11.1$ mag at 71.7 s after the BAT trigger.

In this chapter I present the work from Schady et al. [2007b], which describes in detail the γ-ray, X-ray and optical observations taken by *Swift*. From the high resolution early time data I constrain the type of environment in which the burst occurred and determine the conditions that distinguish this burst from others. In section 5.1 I describe the data reduction and analysis techniques used, followed by an analysis of the possible physical parameters and emission mechanisms that could explain the observations in section 5.3.1-5.3.3. In these subsections I investigate both a wind and ISM circumburst environment, as well as spherical-equivalent emission and collimated emission. I also use the afterglow spectral energy distribution (SED) to analyse the properties of the circumburst medium of GRB 061007 in section 5.2. The results are discussed in section 5.3.5, and a summary is given in section 5.4.

5.1 Observations and Analysis

5.1.1 BAT

The BAT on-board *Swift* triggered on GRB 061007 on 7th October, 2006 at 10:08:08 UT, resulting in an immediate slew to point the narrow field instruments in the direction of the burst. The refined BAT position for GRB 061007 is RA $= 03^h05^m11.8^s$, Dec $= -50°29'$ $47.4''$ (J2000) with an uncertainty (systematic and statistical) of 0.9' at 90% containment [Markwardt et al., 2006].

The BAT light curve consists of three large and distinct peaks and is shown in Fig. 5.1.

The time-interval over which 90% of the 15–150 keV γ-radiation was emitted was $T_{90}=$ 75 $\pm$ 5 s, although emission above the background level was detected out to $\sim$T+500 s. The light curves for the four BAT energy channels are shown in Fig. 5.1, and although they are only shown out to T+150 s, the continual emission above background beyond T+75 s is most pronounced in the soft energy band (top panel of Fig. 5.1). The time lag in the prompt emission, which is the time interval between the peak structure in the light curves of two different energy channels [Norris & Bonnell, 2006], was 16^{+8}_{-6} ms between the 50–100 keV and the 15–25 keV energy bands, and 21^{+7}_{-5} ms between the 100–350 keV and 25–50 keV bands.

5.1.2 XRT

The first XRT observation was a centroiding image taken 80.4 s after the BAT trigger, and a bright uncatalogued source was found at RA = $03^h05^m19.5^s$, Dec = $-50°30'\ 01.9''$, with a 90% containment radius of 3.5" [Vetere et al., 2006].

At 86.6 s after the BAT trigger the XRT began taking data in WT mode. At T+2000 s the count rate fell to below $\sim$ 1 count s^{-1} and the automated sequence switched to PC mode. The X-ray afterglow was detected for 10^6 s after the BAT trigger before it fell below the detection threshold. During the first 2200 s of observations the count rate of the burst was high enough to cause pile-up in both WT and PC mode data. To account for this effect, the WT data were extracted in a rectangular 40×20-pixel region with a 9×20-pixel region excluded from its centre. Due to a large amount of pile-up in the first 30 s of WT observations, these data were not used in the spectral analysis.

The 0.3–10 keV light curve is well fit by a power law with decay index $\alpha = 1.66 \pm 0.01$ from T+80 s until at least T+10^6 s, when it reached the detectability threshold of XRT (see Fig. 5.2). I constrained the presence of a break in the light curve that might result from either the edge of the jet coming into the line of sight, or the migration of the cooling frequency, ν_c, through the observing energy bands. To determine the 3σ lower limit on the time at which such a jet or cooling break could have occurred, I applied a broken power
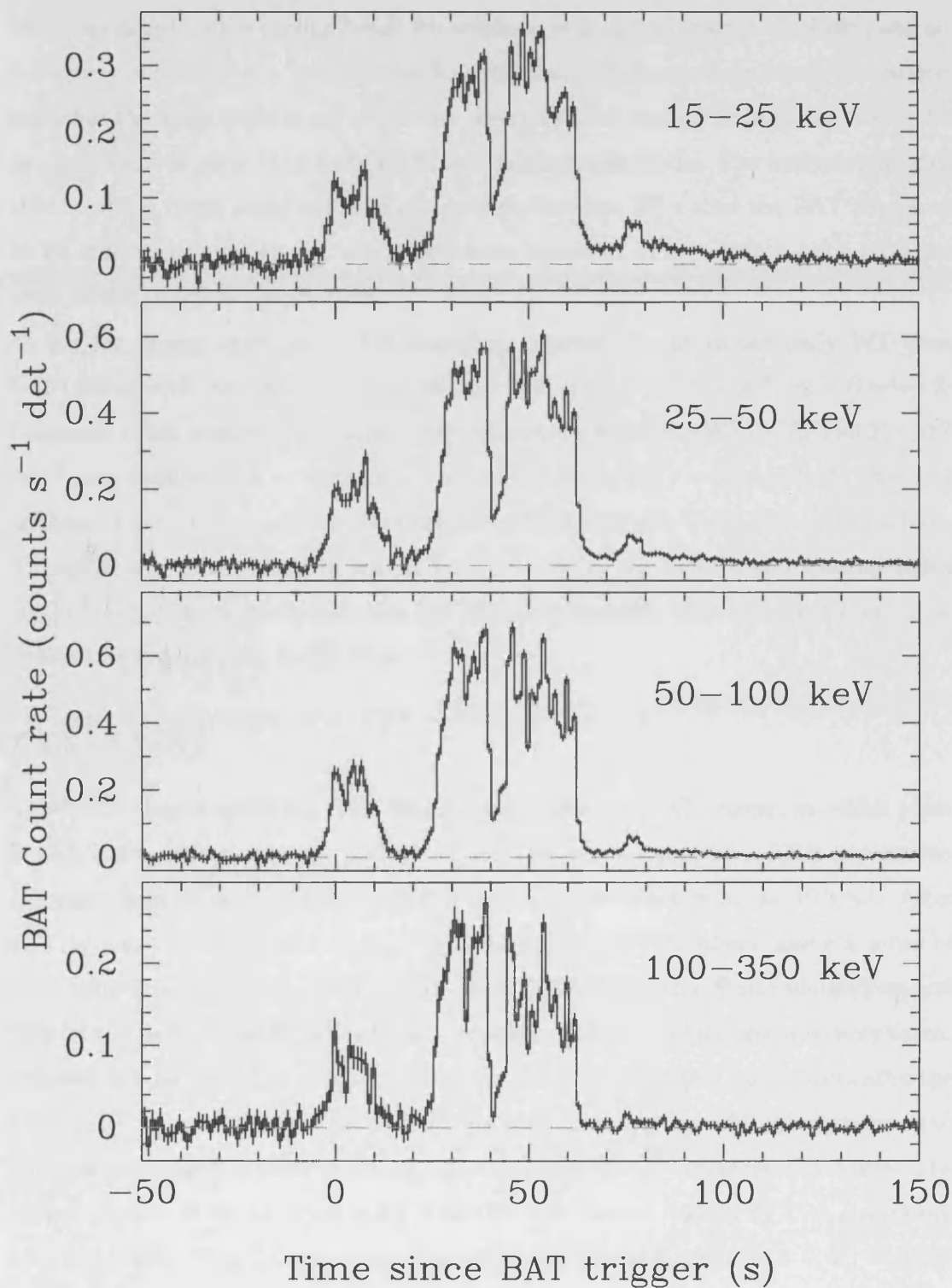
Figure 5.1: Prompt emission light curve of GRB 061007 shown in the four BAT energy bands.

law fit modelled on the cooling break, for which $\alpha_2 = \alpha_1 + 0.25$ [Sari et al., 1998], and on a jet break, where $\alpha_2 = \alpha_1 + 0.75$ [Rhoads, 1999], and in each case determined the earliest time that the break could occur within the observing time interval without disturbing the goodness of fit by more than 3σ from the best-fit power law model. The analysis indicates that a cooling break could not have occurred earlier than 10^5 s after the BAT trigger to 99.7% confidence, and any jet break must have happened at $t_j > 2.65 \times 10^5$ s after the onset of the afterglow observations.

For the energy spectrum of the afterglow, a power law fit to the early WT data (<T+600 s) with the Galactic column density fixed at $N_H = 2.13 \times 10^{20}$ cm^{-2} [Dickey & Lockman, 1990], gives a best-fit host galaxy column density of $N_H(\text{WT}) = (5.3\pm0.2)\times10^{21}$ cm^{-2} at a redshift of $z = 1.26$ for a spectral index $\beta_X(\text{WT}) = 0.96 \pm 0.01$. Spectral analysis of the PC data during the time interval T+5000 s to T+25,000 s gives a best-fit host galaxy column density $N_H(\text{PC}) = (5.1 \pm 0.6) \times 10^{21}$ cm^{-2}, and spectral index $\beta_X(\text{PC}) = 0.92 \pm 0.5$, consistent with the WT data, therefore indicating that there is no spectral evolution in the X-ray data.

5.1.3 UVOT

The UVOT began observing GRB 061007 71.7 s after the BAT trigger, at which point it took a 9 s settling exposure in the V-filter. This was followed by a 100 s exposure in the white light filter ($\lambda \sim 1600 - 6500$ Å) and a 400 s exposure in the V-band. After this the automated sequence rotated twice through the UVOT filters taking a series of short exposures ($V, UVM2, UVW1, U, B$, white, $UVW2$) (10 s for B and white filters and 20 s for the rest). A further 400 s V-band exposure and 100 s white exposure were taken, followed by a further series of rapid rotations around the filter wheel up to 2260 s after the trigger. With the exception of the second 100 s white band exposure, all observations up to this time were taken in event mode, and after this image mode exposures were taken. The refined position of the afterglow is RA $= 03^h05^m19.6^s$, Dec $= -50°30'\,02.4''$ to a certainty of 0.5" (J2000). The Galactic extinction along this line of sight is $E(B - V) = 0.021$
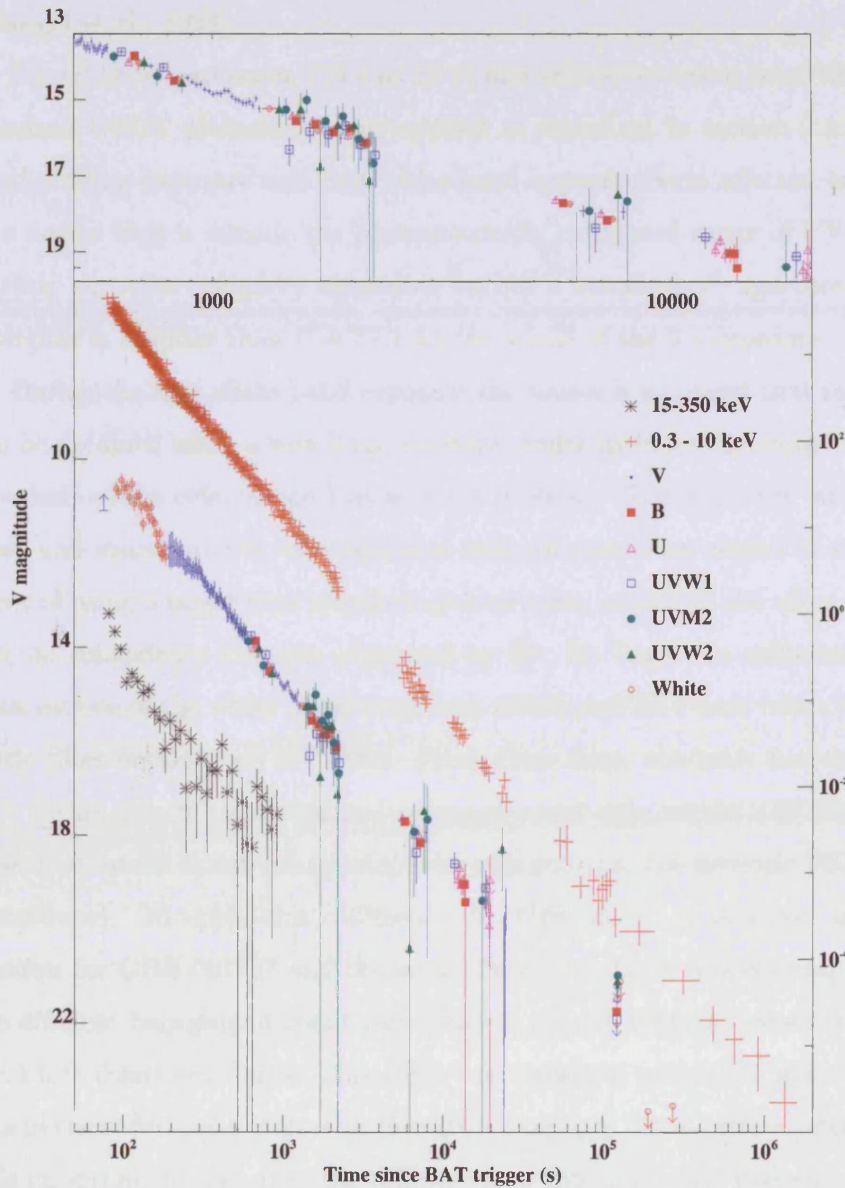
Figure 5.2: GRB afterglow light curve shown in all six UVOT lenticular filters, in the X-ray (0.3–10 keV) and in the γ-ray (15–350 keV). All light curves have been shifted vertically with respect to the UV/optical light curve for clarity, and the B, U, $UVW1$, $UVM2$, $UVW2$ and white filter have all been normalised to the V band light curve. A close up of the UV/optical light curve from $\sim \mathrm{T} + 500\,\mathrm{s} - \mathrm{T} + 20,000\,\mathrm{s}$ is shown in the top panel. The left hand axis corresponds to the V-band light curve, and the count rate axis on the right applies to the X-ray and γ-ray light curves. The best-fit decay indices to the combined UVOT light curve, the X-ray light curve and the BAT light curve are $\alpha_{UVOT} = 1.64 \pm 0.01$, $\alpha_{XRT} = 1.66 \pm 0.01$ and $\alpha_{BAT} = 1.61 \pm 0.14$, respectively. Error bars are smaller than the symbol size if not visible.

[Schlegel et al., 1998].

For all short exposures (10 s or 20 s) and exposures taken later than T+2260 s, the standard UVOT photometry was applied as described in section 2.3.3. The first V-band settling exposure and first white-band exposure were affected by coincidence loss to a degree that is outside the photometrically calibrated range of UVOT; for a V-band settling exposure complete saturation within a standard 6" aperture implies that this afterglow is brighter than $V = 11.1$ for the whole of the 9 s exposure.

During the first white band exposure the source is so bright that relative photometry can be obtained using a very large aperture, which includes the wings of the point spread function, where coincidence loss is not a problem. The exposure was divided into 5 s bins, and source counts were obtained from an extraction region of radius $\sim 26''$. The effect of using a larger than standard aperture size, as well as the effect of the background rate on coincidence loss was calibrated by Dr. M. Page. To calibrate this photometry, observations of the white dwarf standards GD50 and HZ2 were taken with UVOT in the white filter on October 18th 2006. From these data, the ratio between observed count rate within the 26" aperture and expected count rate within a 6" source aperture was measured, and a linear relationship was assumed (i.e. the intrinsic PSF is constant with count rate). To apply this calibration to GRB 061007, a constant offset between this relation for GRB 061007 and the white dwarf standards was determined to account for the different background count rate between the GRB 061007 observations and those of the white dwarf standards. This offset was chosen to match the mean white-band count rate in the saturated exposure to the white filter light curve extrapolated from later times. It is important to note that the calibration of this first white exposure is crude and thus the apparent steepening of the light curve towards the end of the exposure may not be real. However, the overall behaviour of a steadily decreasing count rate over the course of the exposure is not in doubt. For the first 400 s V-band exposure a higher resolution light curve was created by splitting it into 4 s bins, and the second V-band exposure was split into 20 s bins to make it consistent with the majority of the exposures around this

---

[1]http://heasarc.gsfc.nasa.gov/docs/heasarc/caldb/swift/docs/uvot/

time.

In order to get the best measurement of the optical temporal decay, a single UV/optical light curve was created from all the UVOT filters. To do this the light curve in each filter was individually fitted to find the corresponding normalisation, and this was then used to re-normalise each light curve to the V-band. The combined UV and optical light curve, from T+85 s up to T+2.5 × 10^4 s, shows no apparent colour evolution, and is best fit with a power law decay with temporal index $\alpha_{opt} = 1.64 \pm 0.01$. This is consistent with $BVRi'$ observations taken with the Faulkes Telescope South, which had a best-fit decay index of $\alpha_{BVRi'} = 1.72 \pm 0.10$ [Mundell et al., 2007]. A main difference between the UVOT observations and those presented in Mundell et al. [2007] is the presence of an additional broad, multicolour bump detected in the $BVRi'$ data between 40 mins and 350 mins after the BAT trigger. This bump is not detected in the UVOT observations, and this is likely due to the slightly shallower best-fit decay index fit to the UVOT data.

The combined UVOT light curve is shown alongside the 0.3–10 keV and 15–350 keV light curve in the lower panel of Fig. 5.2, and a close up of the UVOT light curve from T+500 s to T+20,000 s is shown in the top panel. The log-log scale in this figure shows the decaying light curve in the 15-350 keV energy band from 80–500 s much better than the linear scale in Fig 5.1. The magnitude along the left axis corresponds to the V-band, and the count rate along the right axis applies to the X-ray and γ-ray light curves.

5.1.4 Observations By Other Facilities

The prompt emission from GRB 061007 also triggered Konus-Wind and Suzaku, and the afterglow was monitored by ground based telescopes, which carried out both spectroscopic and photometric observations. GRB 061007 was measured to be at z=1.26 [Osip et al., 2006, Jakobsson et al., 2006a], for which the rest-frame isotropic energy release and maximum luminosity in the 20 keV–10 MeV are $E_{iso} \sim 1.0 \times 10^{54}$ erg, and $L_{iso} \sim 1.8 \times 10^{53}$ erg s^{-1} [Golenetskii et al., 2006]. The optical afterglow was also detected by ROTSE at 26.4 s after the BAT trigger at a magnitude of 13.6 mag in an unfiltered exposure [Rykoff

& Rujopakarn, 2006], and the Faulkes Telescope South measured an R-band magnitude of $R = 10.15 \pm 0.34$, 142 s after the trigger [Bersier et al., 2006], consistent with the UVOT observations. The ROTSE measurement is indicative of a significant brightening during the first 90 s. The *Swift* observations from T+80 s show that by this time the afterglow had entered a constant power law decay phase (see Fig. 5.2). Radio observations were also performed 1–1.24 days and 5.03–5.28 days after the prompt emission, none of which resulted in the detection of a radio source. The flux limit for the first set of observations were -25 ± 45 μJy at 4.8 GHz, -13 ± 47 μJy at 8.6 GHz and -1 ± 37 μJy at 19 GHz [van der Horst & Rol, 2006].

5.1.5 Multi-Wavelength Light Curve Analysis

After the last flare in the BAT light curve (Fig. 5.1), at $\sim$ T + 100 s, the light curve in the 15–350 keV band appears to decay smoothly and monotonically out to $\sim$T+500 s, after which the flux becomes indistinguishable from the background in the BAT energy range. A power law fit to the BAT light curve from T+100 s to T+500 s provides an acceptable fit ($\chi^2 = 32$ for 29 dof) with a best-fit decay index of $\alpha_{BAT} = 1.61 \pm 0.14$, which is consistent with the decay observed in both the UV/optical and X-ray light curves. Furthermore, a power law spectral fit to this last part of the BAT light curve, beyond $\sim$T+100 s, gives a best-fit energy spectral index $\beta_{BAT}(> \mathrm{T}+100 \text{ s}) = 0.80 \pm 0.09$, in fairly good agreement with the spectral indices determined for the X-ray and optical afterglows. This supports a scenario in which the γ-emission at this epoch is generated by the same radiation mechanism as the X-ray and UV/optical afterglow.

5.1.6 The Spectral Energy Distribution

Using the full range of data available with *Swift*, a SED of the afterglow was produced using optical, X-ray and γ-ray data, which were normalised to an instantaneous epoch at 600 s after the BAT trigger. This assumes that the 15–350 keV BAT light curve continues to decay at the same rate of $\alpha_{BAT} = 1.61 \pm 0.14$ from T+500 s to T+600 s,
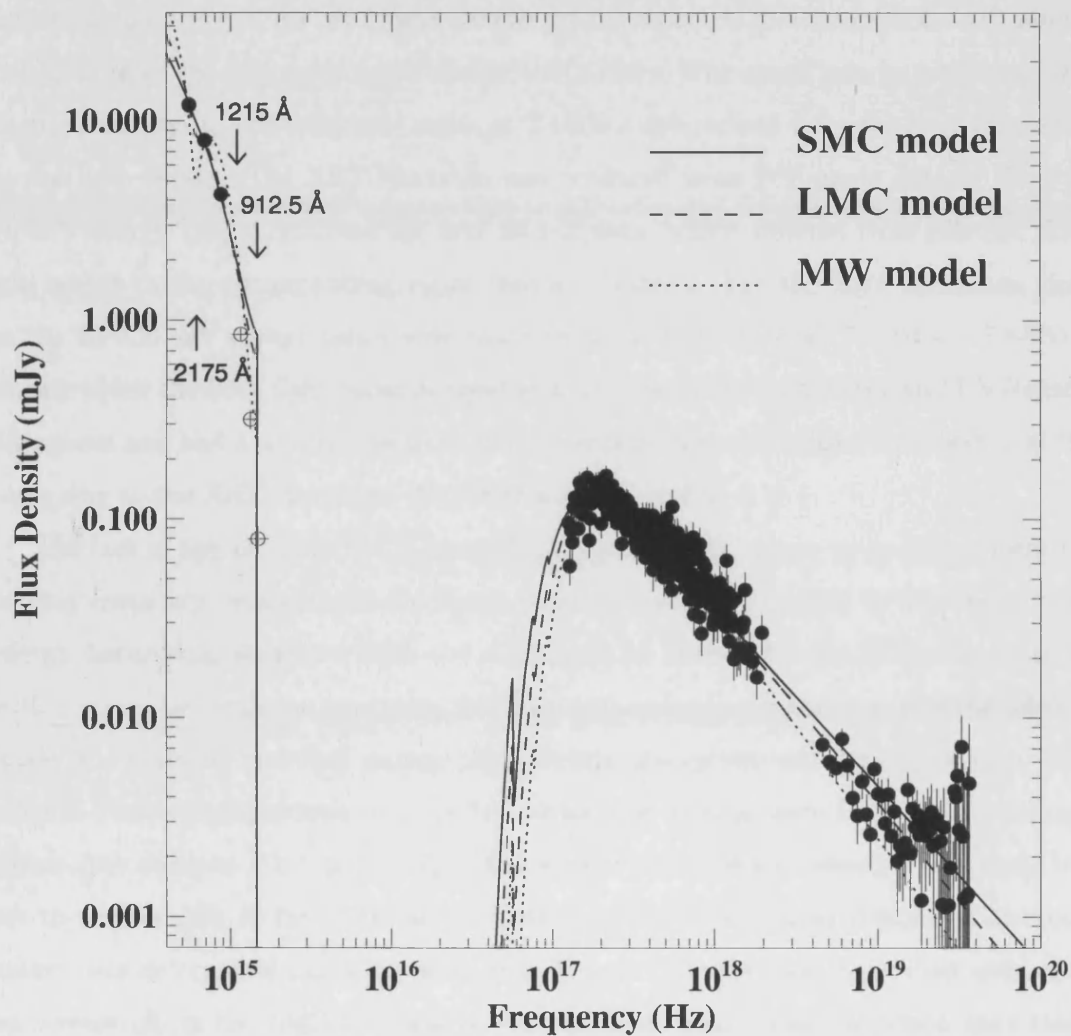
Figure 5.3: The combined γ-ray, X-ray and UV/optical spectral energy distribution of GRB 061007 at T+600 s with best-fit models for each corresponding dust extinction curve shown; SMC (dashed), LMC (solid) and Galactic (dotted). Open circles are data points at wavelength $\lambda < 1215$ Å in the rest frame, and therefore not used in the spectral fitting. The rest-frame positions of the Galactic absorption feature at 2175 Å, the beginning of the Ly-α forest at 1215 Å, and the Ly-α break at 912.5 Å, are indicated.

and without any spectral evolution. At this time there are data available from all three instruments, and good colour information from UVOT. For each of the UVOT lenticular filters the tool UVOT2PHA (v1.1) was used to produce spectral files compatible with XSPEC (v12.2.1) from the exposures taken closest to T+600 s. The count rate in each band was then normalised to the estimated value at T+600 s determined from the best-fit models to the light curves. The XRT spectrum was produced from WT mode data in the 0.5–10 keV energy range, omitting the first 30 s of data, which suffered from pile-up. This was scaled to the corresponding count rate at T+600 s. For the BAT spectrum, data in the 15–150 keV energy range were taken from the time interval T+100 s – T+500 s, during which the BAT light curve decayed at a rate consistent with X-ray and UV/optical afterglows and had a similar spectrum. This spectrum was normalised to T+600 s in the same way as the XRT spectrum. The SED is shown in Fig. 5.3.

The lack of any break in the X-ray and UV/optical light curves up to 10^5 s places the cooling frequency either above the X-ray band or below the optical at T+600 s. Both energy bands will, therefore, have the same spectral index, and the SED was, thus, fit with a power law emission spectrum, and two dust and gas components were included to model the Galactic and host galaxy photoelectric absorption and dust extinction. The column density and reddening in the first absorption system were fixed at the Galactic values (see sections 5.1.2 and 5.1.3). The second photoelectric absorption system was set to the redshift of the GRB and the neutral hydrogen column density in the host galaxy was determined assuming solar abundances. The dependence of dust extinction on wavelength in the GRB host galaxy was modelled using three extinction laws taken from observations of the Milky Way (MW), the Large Magellanic Cloud (LMC) and the Small Magellanic Cloud (SMC) (see section 4.1.1).

As was the case in chapter 4, the assumed metallicity of the GRB host galaxy will affect the determined neutral hydrogen column density when this is measured by using the amount of soft X-ray absorption in the spectrum. The effect that the difference in average metallicity between the Magellanic Clouds and the Milky Way has on the equivalent N_H is taken into account when discussing the results from the spectral analysis in section 5.2.

Table 5.1: Power law spectral fit results to the spectral energy distribution of GRB 061007

Spectral Model	Host galaxy $N_H{}^1$ (10^{21} cm^{-2})	Rest-Frame visual extinction, A_V	$\beta_{o,X}$	χ^2 (dof)	Null-hypothesis probability
SMC	$3.66^{+0.29}_{-0.28}$	0.39 ± 0.01	0.90 ± 0.005	398 (308)	4×10^{-4}
LMC	$5.30^{+0.33}_{-0.32}$	0.66 ± 0.02	0.98 ± 0.007	347 (308)	0.063
MW	$7.62^{+0.81}_{-0.77}$	1.13 ± 0.10	$1.13^{+0.04}_{-0.03}$	1042 (308)	0.000

^{1} Equivalent hydrogen column density assuming solar abundances at the GRB host galaxy.

At a redshift of $z = 1.26$ the beginning of the Ly-α forest is redshifted to an observer-frame wavelength of ~ 2580 Å, which falls squarely on the $UVW1$ filter, the reddest of the UV filters. The unknown equivalent width of Ly-α absorption from the host galaxy of the GRB and the variation of the Ly-α forest along different lines of sight makes it difficult to model this additional source of absorption in the SED. Therefore, as in chapter 4, the three data points affected by Ly-α are left out from the spectral analysis. The results from the spectral analysis are summarised in Table 5.1.

In all three cases an absorption and extinction system is measured at the GRB host galaxy, which has the smallest optical depth in an SMC model and largest in a MW model. The optical, X-ray and γ-ray spectrum is best fit by a model that assumes the GRB host galaxy to have an LMC extinction law, which gives a $\chi^2 = 347$ for 308 dof with a null-hypothesis probability of $p = 0.063$. This model also provides best-fit parameters consistent with Mundell et al. [2007], who found a best-fit spectral index of $\beta = 1.02 \pm 0.05$, rest-frame optical extinction of $A_V = 0.48 \pm 0.19$, and host galaxy column density $N_H = (5.8 \pm 0.4) \times 10^{21}$ cm^{-2}. In my analysis, models with an SMC and MW extinction law at the host galaxy were rejected with 99.96% confidence and 100% confidence, respectively.

5.2 The Circumburst Medium

From the spectral analysis the dust extinction in the circumburst medium is determined to be most consistent with a wavelength dependence similar to that of the LMC. This is consistent with previous studies of GRB environments (e.g. Fruchter et al. 2006, Kann et al. 2006; Chapter 4), which also find GRB hosts to be irregular galaxies. This result is also in agreement with the collapsar model, which requires a sub-solar metallicity progenitor star, with an upper limit of $Z_\odot \lesssim 0.3$ [e.g. Hirschi et al., 2005, Woosley & Heger, 2006].

The best-fit parameters for the X-ray column density and dust extinction local to the GRB are $N_H = (5.3 \pm 0.3) \times 10^{21}$ cm^{-2} and $A_V = 0.66 \pm 0.02$, and this gives a gas-to-dust ratio of $N_H/A_V = (8.0 \pm 0.5) \times 10^{21}$ cm^{-2}. However, A_V was determined assuming an LMC dust extinction law, whereas N_H was determined assuming solar abundances, which are unlikely to be correct for an irregular, Magellanic-type galaxy. Correcting the X-ray column measurement to a metallicity of 1/3 solar, which is appropriate for an ISM similar to that of the LMC, gives a gas-to-dust ratio that is a factor of more than three larger than that measured in the LMC. It should be noted that an environment's metallicity affects the amount of dust present as well as the equivalent N_H measured. The assumptions made on the metallicity, therefore, do not change the A_V/N_H ratio as measured here since, to first order, both A_V and equivalent N_H scale directly with metallicity. It is, therefore, valid to compare the dust-to-gas ratio derived in this way with different environments, independent of their metallicity. Although not consistent with the LMC, the dust-to-gas ratio measured in the local environment of GRB 061007 is consistent with the average gas-to-dust measured in the local environment of the sample of *Swift* GRBs in chapter 4, which was $\langle N_H/A_V \rangle = (6.7 \pm 1.1) \times 10^{21}$ cm^{-2}. For comparison GRB 061007 is shown on a $\log N_{H,X}$- $\log A_V$ plot in Fig. 5.4, alongside the GRB sample from chapter 4.

The lack of evolution in the soft X-ray absorption from ~ 80 s after the prompt emission suggests that the burst must have completely ionised the gas in its immediate environment within this time scale. The absorbing medium observed must, therefore, be far enough from the burst that it was not completely ionised in the first few hundreds of
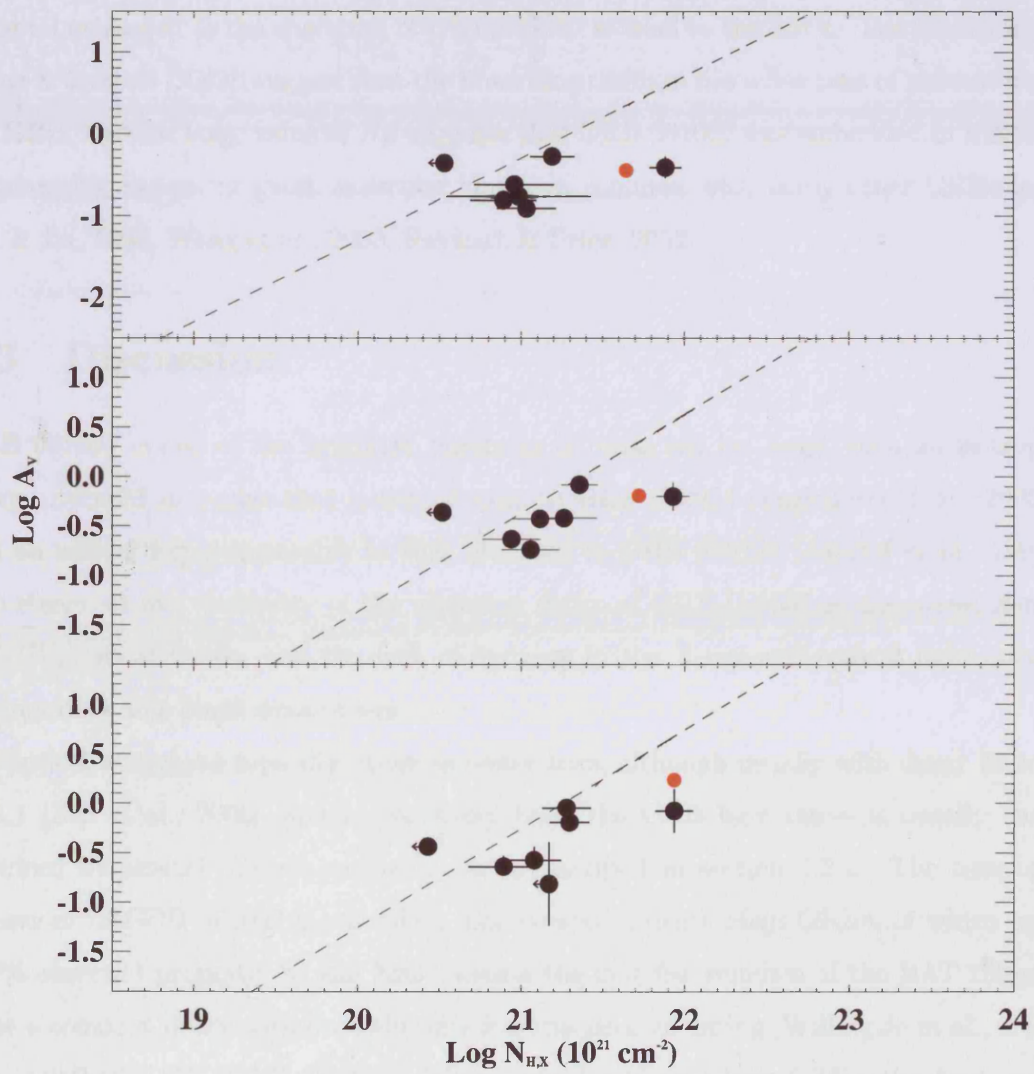
Figure 5.4: Same plot as Fig. 4.12 with the inclusion of GRB 061007, shown in red.

seconds after the initial explosion. The probability of there being an absorption system in the line of sight from an unrelated, intervening galaxy that is of sufficient optical depth to contribute a measurable amount of soft X-ray absorption is very small [O'Flaherty & Jakobsen, 1997, Campana et al., 2006b], leading us to conclude that the absorbing material measured in the spectrum of GRB 061007 is local to the burst. The results from Perna & Lazzati [2002], suggest that the absorbing medium lies a few tens of parsecs from the GRB, and the large value of N_H suggests that GRB 061007 was embedded in a dense, star-forming region, or giant molecular cloud, in common with many other GRBs [e.g. Dai & Lu, 1999, Wang et al., 2000, Reichart & Price, 2002].

5.3 Discussion

GRB 061007 is one of the brightest bursts to be observed by *Swift*, with an isotropic energy released in γ-rays that is second only to GRB 050904 [Tagliaferri et al., 2005a] and an optical flux comparable to that observed in GRB 990123 [Akerlof et al., 1999]. The steepness and similarity of the afterglow decay of GRB 061007 in the γ-ray, X-ray and UV/optical bands, and the lack of features in the X-ray and optical light curves distinguishes this burst from others.

Optical afterglows typically decay as power laws, although usually with decay indices $\sim$ 1.1 [Zeh et al., 2006], and in the X-ray band the GRB light curve is usually characterised by several discrete segments, as is described in section 1.2.2. The temporal behaviour of GRB 061007 is, therefore, not typical of other *Swift* GRBs, of which only $\sim$ 7% observed promptly by the XRT (within the first few minutes of the BAT trigger) show a constant decay with no additional features such as flaring [Willingale et al., 2007] (e.g. GRB 051117B, GRB 060403). When only considering long GRBs, the fraction of smooth decaying, featureless X-ray afterglows is even more infrequent, amounting to only $\sim$ 4% of the long GRB population, of which only GRB 051117B has a comparably steep decay index [$\alpha_X = 1.60^{+0.16}_{-0.14}$; Willingale et al., 2007]. GRB 051210 also had a very steep decay throughout the XRT observations [$\alpha_X = 2.07^{+0.16}_{-0.15}$; Willingale et al., 2007], but,

unlike GRB 061007, the X-ray afterglow also had early time flaring activity.

According to the fireball model, the temporal and spectral indices of the afterglow depend on the properties of both the GRB ejecta and the circumburst environment, which determine the location of the characteristic synchrotron frequency, ν_m and the cooling frequency, ν_c, with respect to the observing band [Zhang et al., 2007]. At any one time the location of these frequencies are dependent on the energy distribution of electrons in the circumburst environment, defined by the energy index p, the density and density profile of the circumburst medium, the amount of kinetic energy in the outflow, and on the fraction of energy in electrons and in the magnetic field, ϵ_e and ϵ_B, respectively. ϵ_e and ϵ_B are typically assumed to remain constant with time, and therefore the evolution of ν_m and ν_c, and thus the afterglow decay and spectral indices, depend on the density and density profile of the circumburst medium and on the amount of kinetic energy released by the GRB.

The lack of a break in the light curves provide constraints on the spectral regime that the X-ray and UV/optical afterglow are in, and on the frequency of ν_m and ν_c, neither of which could have crossed the observing window from T+80 s to T+10^5 s. Based on the white band effective area curve (see Fig. 2.1), around half the counts detected in the white band observations must correspond to the V and B filter. The lack of a break in the first white filter exposure, therefore, indicates that at T+80 s, ν_m was no bluer than the B-band filter. This corresponds to an upper limit on the characteristic synchrotron frequency $\nu_m < 7.5 \times 10^{14}$ Hz. From the UV/optical data it is also determined that at T+80 s the flux density in the U-band, corresponding to $\nu = 8.7 \times 10^{14}$ Hz, is $F_\nu = 460$ mJy, after correcting for absorption at the host galaxy.

With these constraints in place I investigate the various conditions that can explain the temporal and spectral properties of GRB 061007, all of which can be categorised into two parent models that differ fundamentally in the effect of collimation on the observations. In the first model I assume no jet break to have occurred before T+2.65×10^5 s based on the constraints obtained in section 5.1.2, and the observed emission is, therefore, indistinguishable from isotropic emission. Secondly, I investigate a model in which the

jet break occurs before the first X-ray and UV/optical observations, at T+80 s, such that the assumption of isotropic emission no longer applies.

5.3.1 Spherical Expansion Model

The simplest model to consider is one in which the observed afterglow emission follows the flux decay and spectral evolution as would be expected from synchrotron radiation emitted from an isotropic outflow. As already mentioned, one of the important factors that determines the evolution of the defining synchrotron frequencies is the density profile in the surrounding circumburst material, and both a wind-like circumburst environment, such as would be expected in the vicinity of a massive star, and a constant density profile, such as in the ISM are, thus, considered. For simplicity, the density profile of the circumburst medium is assumed to have the form $\rho \propto r^{-s}$, where $s = 0$ and $s = 2$ correspond to an ISM and wind-like profile, respectively.

Assuming spherically equivalent emission, the standard closure relations (see table 1.1) do not fully satisfy the observed spectral and temporal indices of GRB 061007 for either an ISM or a wind-like circumburst medium, where $\alpha_{o,X} = 1.65 \pm 0.01$ and $\beta_{o,X} = 0.99 \pm 0.02$. This could be the result of additional components unaccounted for in the closure relations, or an oversimplification of the assumptions in the closure relations, e.g. the density profile may not be distributed as r^{-s}.

For both a wind and an ISM circumburst density profile the observations are in closest agreement with a model in which the observed synchrotron emission is in the slow cooling phase ($\nu_m < \nu_c$), and where the UV/optical and X-ray bands are in the same slow-cooling regime ($\nu_m < \nu < \nu_c$). The decay index is steeper than expected for a constant circumburst density profile by $\Delta\alpha \sim 0.17$, and requires a fairly soft electron distribution index $p \sim 3$. In the case of a wind circumburst environment the decay index is shallower than predicted by this model, by a difference $\Delta\alpha \sim 0.33$. It is possible that the density profile in the environment surrounding GRB 061007 lies somewhere between the two scenarios considered here, where $0 < s < 2$. Alternatively, the shallowness of the decay

index for a wind case could be explained if energy injection is involved. This would require a late-time source of energy into the forward shock that would slow down the cooling rate of the excited electrons and, thus, slow down the afterglow decay. Either way, the lack of a cooling break for the duration of *Swift* observations out to 10^6 s requires consideration, and the conditions necessary to maintain ν_c above or below the observing frequency range need to be investigated.

The evolution of ν_c with time is dependent on the density profile of the circumburst medium, whereby for $s > \frac{4}{3}$ ν_c will increase with time, whereas for $s < \frac{4}{3}$ it will decrease [Panaitescu, 2007a]. The conditions needed for the cooling frequency to not have crossed the observing window, therefore, differ for an ISM and wind circumburst density profile. For an ISM medium the cooling frequency has to be maintained above the X-ray band for up to T+10^5 s, whereas in a wind scenario the cooling frequency needs to be above the X-ray band at the start of the X-ray observations, at T+80 s. Either way the cooling frequency must lie above the peak X-ray frequency out to at least T+10^5 s for a cooling break not to occur in the X-ray observations (see section 5.1.2). This corresponds to the requirement that $\nu_c > 6 \times 10^{17}$ Hz at T+10^5 s. In the next section I investigate the consistency of a spherical emission model with the data for both an ISM and wind medium where $\nu_m < \nu < \nu_c$.

ISM Case

For an ISM-like circumburst environment, the temporal and spectral flux decay indices are related as $\alpha = 3\beta/2$. For a value of $\beta_X = 0.99 \pm 0.02$, the decay index is expected to be $\alpha = 1.49 \pm 0.03$, which is shallower than the observed decay rate of $\alpha = 1.65 \pm 0.01$. However, this deviation from the relation is small, and could be accommodated if the density profile is slightly different from the uniform density assumed. In this regime $\beta = (p-1)/2$, where p is the electron energy index. Thus, for $\beta_X = 0.99 \pm 0.02$ the electron energy index is in the range $2.94 < p < 3.02$. I therefore take $p = 3.0$. These relations hold as long as the characteristic synchrotron frequency, ν_m, lies below the optical band, i.e. $\nu_m < 7.5 \times 10^{14}$ Hz, at T+80 s, as discussed previously.

For a constant density medium in which synchrotron radiation is the dominating emission mechanism, the characteristic synchrotron frequency, the cooling frequency and the peak density flux are given by the following equations

$$\nu_m = 3.3 \times 10^{15} \left(\frac{p-2}{p-1}\right)^2 (1+z)^{1/2} \epsilon_B^{1/2} \epsilon_e^2 E_{k,52}^{1/2} t_d^{-3/2} \text{ Hz} \tag{5.1}$$

$$\nu_c = 6.3 \times 10^{12} (1+z)^{-1/2} (1+Y)^{-2} \epsilon_B^{-3/2} E_{k,52}^{-1/2} n^{-1} t_d^{-1/2} \text{ Hz} \tag{5.2}$$

$$F_{\nu,\text{max}} = 16(1+z) D_{28}^{-2} \epsilon_B^{1/2} E_{k,52} n^{1/2} \text{ mJy} \tag{5.3}$$

[Zhang et al., 2007], where ϵ_B is the fraction of energy in the circumburst magnetic field, ϵ_e is the fraction of energy in electrons, $E_{k,52}$ is the kinetic energy in the GRB in units of 10^{52}, t_d is the time since the prompt emission in units of days, n is the density of the surrounding circumburst medium, Y is the Compton parameter, and D_{28} is the luminosity distance in units of 10^{28} cm. Typical values for the fraction of energy in the circumburst magnetic field and in the electrons are $\epsilon_B = 0.01$ and $\epsilon_e = 0.1$, respectively.

For a spectral index $\beta = 1$, νF_ν is constant for $\nu_m < \nu < \nu_c$, and since at T+80 s $F_\nu = 460$ mJy for $\nu = 8.7 \times 10^{14}$ Hz, $\nu_m F_{\nu,\text{max}} = 460 \times (8.7 \times 10^{14})$ erg cm^{-2} s^{-1}. By using this together with Eq. 5.1 and 5.3, the circumburst medium density can be expressed by:

$$n = \frac{3.36 \times 10^{-6}}{\epsilon_B^2 \epsilon_e^4 E_{k,52}^3} \tag{5.4}$$

In Eq. 5.2 I apply the condition that at 10^5 s after the prompt emission ν_c must still be greater than 6×10^{17} Hz, and substituting in Eq. 5.4 gives

$$(1+Y)^{-2} \epsilon_B^{1/2} \epsilon_e^4 E_{k,52}^{5/2} > 0.52 \tag{5.5}$$

Considering now the characteristic synchrotron frequency, it is known that $\nu_m < 7.5 \times 10^{14}$ Hz, and this reduces Eq. 5.1 to

$$\epsilon_B^{1/2} \epsilon_e^2 E_{k,52}^{1/2} < 1.70 \times 10^{-5} \tag{5.6}$$

This, and the inequality given in Eq. 5.5 provide an upper limit to the value of ϵ_B in terms of $E_{k,52}^3$, such that

$$\epsilon_B < 3.15 \times 10^{-19} (1+Y)^{-4} E_{k,52}^3 \tag{5.7}$$

The above equation bounds us to extreme values of $E_{k,52}$ and ϵ_B. For $E_{k,52} = 10^3$ erg, $\epsilon_B < 3.1 \times 10^{-10}(1 + Y)^{-4}$, which is an unrealistically low value of ϵ_B. Even a value as small as $\epsilon_B = 10^{-6}$ requires a huge amount of kinetic energy to meet the condition that $E_{k,52} > 1.5 \times 10^4(1 + Y)^{4/3}$ erg. Nevertheless, the values $E_{k,52} = 1.5 \times 10^4(1 + Y)^{4/3}$ erg, $\epsilon_B = 10^{-6}$, $\epsilon_e = 0.012(1 + Y)^{-1/3}$ and $n = 54(1 + Y)^{-8/3}$ would satisfy the conditions laid down by the observations.

The amount of kinetic energy assumed is an isotropic equivalent value that would, thus, be smaller if it were corrected for collimation. The earliest time that a jet break could have occurred at the 3σ level is $t_j > 2.65 \times 10^5$ s, where t_j is the time of the jet break measured from the onset of the afterglow, which is taken to be equal to T. From this a lower limit on the jet opening-angle can be determined using

$$\theta_j = 0.17\left(\frac{t_j}{1 + z}\right)^{3/8}\left(\frac{n}{E_{k,52}}\right)^{1/8}, \tag{5.8}$$

where t_j is in units of days (see section 1.7). The equation for the IC parameter is as follows:

$$Y = [-1 + (1 + 4\eta_1\eta_2\epsilon_e/\epsilon_B)^{1/2}]/2 \tag{5.9}$$

[Zhang et al., 2007], where $\eta_1 = \min[1, (\nu_c/\nu_m)^{(2-p)/2}]$ [Sari & Esin, 2001], and $\eta_2 \leq 1$ accounts for the Klein-Nishina correction. At the minimum time of jet break, $t_j = 26500$ s, and for the physical parameters assumed, Eq. 5.9 reduces to $Y(1 + Y)^{2/3} = 1.4$, which is satisfied by $Y \sim 3$. In this case, a jet opening-angle for GRB 061007 would need to be $\theta_j > 3.2°$ to produce a jet break later than T+2.65 $\times 10^5$ s. The estimated jet opening-angle assumes the hydrodynamics as described by Panaitescu & Kumar [2000], and variations on the hydrodynamics, such as that discussed in Sari et al. [1999], result in a different coefficient in Eq. 5.8. However, these differences are of order unity, and do not affect the implications of the model discussed. A jet half opening-angle of $\theta_j > 3.2°$ would provide a beam-corrected kinetic energy of $E_k^{corr} > 1.4 \times 10^{54}$ erg, which is more than half a solar mass, and is three orders of magnitude greater than more typical GRBs [Freedman & Waxman, 2001]. Furthermore, the beam-corrected γ-ray energy would be

$E_\gamma^{corr} = 5.7 \times 10^{51}$ erg, which would imply a GRB efficiency of $\eta \approx 0.004$, which is two orders of magnitude smaller than is typically inferred [Zhang et al., 2007]. The energetics required by this model are unreasonably large and the inferred γ-ray efficiency is extremely low for a long GRB, resulting in this model being an unlikely solution to explain the properties of GRB 061007.

Wind Case

In the slow cooling regime where $\nu_m < \nu < \nu_c$, the spectral and temporal indices for a wind-like circumburst environment are related such that $\alpha = (3\beta + 1)/2$, which can be rejected by the observations at more than 10 σ confidence. In order for this model to be compatible with the data an additional source of energy is required to slow down the decay rate of the afterglow. A continual source of energy injection could come from either the central engine itself, or late time refreshed shocks that slow down the decay of the afterglow. The shallow decay phase observed in many XRT light curves has been interpreted as being due to energy injection, and although this phase typically lasts for 10^4 s, there are examples of GRBs with evidence of energy injection for prolonged periods of time, and with very smooth decay slopes [e.g. Romano et al., 2006b, Huang et al., 2006]. Taking this into account, an explanation whereby continual energy injection maintains the afterglow and slows down its decay over a long period of time is not unreasonable. For the purpose of this analysis the source of this additional energy is not considered and the energy injection is simply quantified by the expression $L \propto t^{-q}$, where L is luminosity in units of erg s^{-1} [Rees & Mészáros, 1998]. A wind circumburst environment may then be compatible with the observations if $\nu_m < \nu < \nu_c$, with $q = 0.66 \pm 0.02$ and $p = 2.98 \pm 0.02$. Using these best-fit parameters and the known constraints provided by the data it is possible to determine the parameter space of the GRB kinetic energy and the circumburst medium microphysical parameters that could reproduce the observations.

For a wind environment the characteristic synchrotron frequency, ν_m, and flux at this

frequency are given by

$$\nu_m = 4.0 \times 10^{15} \left(\tfrac{p-2}{p-1}\right)^2 (p - 0.69)(1 + z)^{1/2} \epsilon_B^{1/2} \epsilon_e^2 E_{k,52}^{1/2} t_d^{-3/2} \text{ Hz}$$
$$F_{\nu,\text{max}} = 77(p + 0.12)(1 + z)^{3/2} D_{28}^{-2} \epsilon_B^{1/2} E_{k,52}^{1/2} A_* t_d^{-1/2} \text{ mJy} \tag{5.10}$$

where $A_* = A/(5 \times 10^{11})$ g cm^{-1} is the density scaling such that $\rho = Ar^{-2}$ [Chevalier & Li, 2000]. As before the flux at $\nu = 8.7 \times 10^{14}$ Hz is $F_\nu = 460$ mJy at T+80 s, and since $\nu F_\nu = \nu_m F_{\nu,\text{max}}$, the density scaling is

$$A_* = \frac{8.82 \times 10^{-7}}{\epsilon_B \epsilon_e^2 E_{k,52}} \tag{5.11}$$

The dependencies on the cooling frequency also vary from Eq. 5.2 for a wind medium, where it is now defined by

$$\nu_c = 4.4 \times 10^{10} (3.45 - p) e^{0.45p} (1 + z)^{-3/2} (1 + Y)^{-2} \epsilon_B^{-3/2} E_{k,52}^{1/2} A_*^{-2} t_d^{1/2} \text{ Hz} \tag{5.12}$$

[Chevalier & Li, 2000]. A new expression, therefore, needs to be defined regarding the conditions on the cooling frequency. Since ν_c increases with time, the only useful constraint is a lower limit on ν_c at early times. This constraint can be determined through spectral modelling of the afterglow SED at an epoch of T+300 s, which is the weighted mid-time of the time interval over which the BAT spectrum shown in Fig. 5.3 was accumulated. This SED was fit with a broken power law with a spectral break above the BAT energy range, and the change in spectral index at the break was fixed to $\Delta\beta = 0.5$, to correspond to a cooling break. Taking the χ^2 from this fit into account, the ν_c upper limit was then determined by shifting the spectral break to lower energies until the goodness of fit deviated by $\Delta\chi^2 = 9$ (3σ confidence for one interesting parameter). This gave a lower limit on the cooling frequency of $\nu_c > 1.2 \times 10^{19}$ Hz at T+300 s. Applying this, Eq. 5.12 combined with Eq. 5.11 reduces to

$$(1 + Y)^{-2} \epsilon_B^{1/2} \epsilon_e^4 E_{k,52}^{5/2} > 0.0071 \tag{5.13}$$

As for an ISM circumburst environment, $\nu_m < 7.5 \times 10^{14}$, which if applied to Eq. 5.10 gives

$$\epsilon_B^{1/2} \epsilon_e^2 E_{k,52}^{1/2} < 6.08 \times 10^{-6}, \tag{5.14}$$

and combining this expression with Eq. 5.13 gives

$$\epsilon_B < 2.76 \times 10^{-17} (1+Y)^{-4} E_{k,52}^3 \qquad (5.15)$$

For $\epsilon_B = 10^{-6}$ the kinetic energy in the forward shock needs to be $E_{k,52} > 3.3 \times 10^3 (1 + Y)^{4/3}$ erg, in which case $\epsilon_e < 0.010(1+Y)^{-1/3}$, $A_* = 2.5(1+Y)^{-2/3}$ g cm^{-1}, and $Y \sim 4$. When taking into account the possible jet collimation, the kinetic energy needed reduces to $E_K^{corr} > 1.2 \times 10^{54}$ erg. However, it is also necessary to include the energy injected into the fireball, which increases the total energy in the forward shock with time as $E_k \propto t^{1-q}$. For $q = 0.66$ the total energy in the forward shock at T+10^5 s increases by an order of magnitude to $E_K^{corr} > 1.2 \times 10^{55}$ erg, which is even more that the amount of kinetic energy required for an ISM-like circumburst environment, and the equivalent of over twelve solar masses. A wind environment, therefore, faces the same energy budget problem as present for an ISM environment

In the spherical emission model discussed above the primary assumptions made in both the ISM and wind scenarios are that both the X-ray and UV/optical afterglow observed are produced by the same radiation mechanism, and that the decay rate is equivalent to spherical emission. The difficulty in accommodating the observations with a standard fireball model indicate that in the case of GRB 061007 either synchrotron emission is not the dominant radiation mechanism throughout the observing energy range, or that the GRB outflow is collimated, whereby the observed emission is no longer equivalent to isotropic emission. With this in mind I investigate how additional radiation mechanisms and various collimation effects would alter the observed afterglow from that produced by synchrotron emission from an isotropic outflow.

5.3.2 Highly Collimated Models

The emission observed from a collimated outflow is distinguishable from isotropically emitted radiation, provided that the bulk Lorentz factor, Γ, is greater that the inverse of the half-jet opening-angle i.e. $\Gamma > 1/\theta$. However, once Γ drops such that $\Gamma\theta = 1$, the change in energy density at the jet edge will result in a different evolution between α and

β to that observed for spherical emission. How these two parameters vary is dependent on the structure of the collimated outflow and distribution in energy density ε across the jet (see section 1.7). However, in all cases the afterglow decay rate will steepen from that prior to the jet break.

The large amount of energy required to power a model with isotropic emission leads me to investigate a scenario in which the emission from the GRB is highly collimated, where the circumburst environment is assumed to be of constant density. A very narrow jet opening-angle could reduce the energy required to explain the observations by several orders of magnitude, where t_j must be prior to the first afterglow observations in order to account for the lack of a break in the X-ray and UV/optical light curves at later times. If the afterglow is assumed to begin no earlier than the time of trigger, this corresponds to a time $t_j < 80$ s. Within the premise that the outflow is highly collimated I consider two cases in which the cooling frequency is either above or below the observing frequencies. In these two regimes p and β are related by $\beta = (p - 1)/2$ and $\beta = p/2$, respectively, corresponding to $p \sim 3.0$ or $p \sim 2.0$. For a uniform jet, the flux decays as $F_t \propto t^{-p}$ after the jet break [Sari et al., 1999], where p is either 2 or 3, which is steeper than the observed decay rate of $\alpha \sim 1.65$. However, this does not account for continual energy injection, which would reduce the afterglow decay rate.

Case in which $\nu_m < \nu < \nu_c$

For a laterally expanding jet with constant density circumburst medium and $\nu_m < \nu < \nu_c$, the relation between the temporal decay of the GRB afterglow, α, and the spectral index, β, post jet-break is given by

$$\alpha = (1 + 2\beta) - \frac{2}{3}(1 - q)(\beta + 2), \tag{5.16}$$

[Panaitescu et al., 2006] where q is the energy injection parameter such that $L = L_0(t/t_0)^{-q}$ [Zhang & Mészáros, 2001], and since the time of the jet break is taken to be at $t_j = 80$ s, $t_0 = t_j$, and therefore, $L = L_0(t/t_j)^{-q}$. As already mentioned, if the afterglow observations of GRB 061007 are post jet-break and in the slow cooling phase, $p = 3$, and for the

observed temporal and spectral indices, Eq. 5.16 gives an energy injection of $q = 0.3$.

Prior to the jet break Eq. 5.1-5.3 still apply, but in order to take into account the effect of energy injection, the kinetic energy requires an additional factor of $(t/t_j)^{(1-q)}$. The time of jet break and the jet opening-angle are related as $\theta_j \propto t_j^{3/8}$, and in order to determine the largest half-jet opening-angle that such a model would allow, the time of the jet break, t_j, is taken to be as large as possible, which is $t_j = 80$ s. At T+80 s the additional factor of $(t/t_j)^{(1-q)}$ is unity and there is no change in Eq. 5.1-5.3. Thus at T+80 s, Eq. 5.4 and Eq. 5.6 stand. For Eq. 5.2 the constraint that $\nu_c > 6 \times 10^{17}$ at T+10^5 s means that the evolution of ν_c post jet-break has to be taken into account. If ν_{c_j} is the frequency of ν_c at the time of the jet break, $t_j = 80$ s,

$$\nu_{c_j} = 4.07 \times 10^{19} (1 + Y)^{-2} \epsilon_B^{1/2} \epsilon_e^4 E_{k,52}^{5/2} \tag{5.17}$$

However, it is the location of ν_c at T+10^5 s that is of concern. After a jet break, $\nu_c \propto \gamma^{-4} t^{-2}$ where $\gamma \propto t^{-(2+q)/6}$ is the Lorentz factor of the electrons in the circumburst environment [Sari et al., 1999]. The cooling frequency after T+80 s is given by

$$\nu_c = \nu_{c_j} \left(\frac{\gamma}{\gamma_j}\right)^{-4} \left(\frac{t}{t_j}\right)^{-2} = \nu_{c_j} \left(\frac{t}{t_j}\right)^{\frac{2}{3}(q-1)}, \tag{5.18}$$

where γ_j is the electron Lorentz factor at T+80 s. Using the condition that $\nu_c > 6 \times 10^{17}$ Hz at T+10^5 s, for $q = 0.3$ Eq. 5.18 reduces to

$$(1 + Y)^{-2} \epsilon_B^{1/2} \epsilon_e^4 E_{k,52}^{5/2} > 0.41 \tag{5.19}$$

In the same way that the inequality given in Eq. 5.7 was determined, the above is combined with Eq. 5.6, which reduces to

$$\epsilon_B < 4.94 \times 10^{-19} (1 + Y)^{-4} E_{k,52}^3 \tag{5.20}$$

For $E_{k,52} = 5 \times 10^4$ erg, $\epsilon_B < 6.2 \times 10^{-5} (1 + Y)^{-4}$, and taking this upper limit as the value of ϵ_B gives $\epsilon_e = 3.1 \times 10^{-3} (1 + Y)$. These set of values give an IC parameter value of $Y \sim 0.5$. However, the assumed kinetic energy is again large, and when taking energy injection into account increases by a further three orders of magnitude. However,

this corresponds to the isotropic equivalent value, and the beam-corrected kinetic energy is a few orders of magnitude smaller than this. For values, of $E_{k,52} = 5 \times 10^4$ erg, $\epsilon_B = 6.2 \times 10^{-5}(1 + Y)^{-4} = 2.2. \times 10^{-5}$, and $\epsilon_e = 3.1 \times 10^{-3}(1 + Y) = 0.004$, which assumes $Y = 0.5$, the particle density in the circumburst environment is $n = 0.07$ cm^{-3}. Using Eq. 5.8, this gives an opening-angle of $\theta_j = 2.0 \times 10^{-3}$ rad, which corresponds to $\theta_j = 0.1°$. The beam-corrected kinetic energy is then $E_k^{corr} = 1.5 \times 10^{51}$ erg and γ-ray energy $E_\gamma^{corr} = 2 \times 10^{48}$ erg. This would imply an efficiency of $\eta \approx 0.002$, which is two orders of magnitude smaller than is typically inferred [Zhang et al., 2007].

This model is, therefore, able to satisfy our observations without the requirement of an excessively large kinetic energy. However, the opening angle is a factor of at least 30 narrower than previously observed [Bloom et al., 2003] and the inferred γ-ray energy is extremely low for a long GRB, prompting other options to be considered.

Case in which $\nu > \nu_c$

Keeping in place the condition that $t_j < 80$ s, I investigate a model in which the X-ray and UV/optical bands are above ν_m and ν_c. In this model the observational constraints on the values of ν_m, ν_c and $F_{\nu,max}$ are most stringent at the start of the afterglow observations at T+80 s.

In the slow cooling phase, where $\nu > \nu_c$, and a jet break has already occurred,

$$\alpha = 2\beta - \frac{2}{3}(1 - q)(\beta + 1) \tag{5.21}$$

[Panaitescu et al., 2006], which gives a value of $q = 0.75$ for the energy injection parameter. However, since a jet break is assumed to occur at $t_j = 80$ s, the factor of $(t/t_j)^{(1-q)}$ in the kinetic energy is unity, and q is therefore not of importance in the calculations. For ν_c above the observing band, $\beta = p/2$ and, therefore, $p = 2$, in which case the dependence on the minimum Lorentz factor of the shock accelerated electrons γ_m changes from

$$\gamma_m = \frac{(p-2)}{(p-1)}\epsilon_e \frac{m_p}{m_e}\Gamma \tag{5.22}$$

to

$$\gamma_m = \ln\left(\frac{\varepsilon_m}{\varepsilon_M}\right)\epsilon_e \frac{m_p}{m_e}\Gamma, \tag{5.23}$$

where ε_m and ε_M are the minimum and maximum energy of the shock accelerated electrons, and Γ is the bulk Lorentz factor in the shocked medium [Pe'er & Zhang, 2006]. $\nu_m \propto \gamma_m$, and therefore the expression for ν_m given in Eq. 5.1 has to be modified such that $[(p-2)/(p-1)]^2$ is replaced by $[\ln(\varepsilon_m/\varepsilon_M)]^2$. The value of $\ln(\varepsilon_M/\varepsilon_m)$ is not well determined due to the unknown magnetic field in the upstream of the GRB shock, although it generally ranges between 5 and 10 [Li & Waxman, 2006]. A mid-value between this range is, therefore, used with $\ln(\varepsilon_M/\varepsilon_m) = 7$, such that Eq. 5.1 becomes

$$\nu_m = 6.7 \times 10^{13}(1+z)^{1/2}\epsilon_B^{1/2} \; \mathrm{Hz}\epsilon_e^2 \mathrm{E}_{k,52}^{1/2} \mathrm{t}_d^{-3/2} \tag{5.24}$$

The same jet break time as before is assumed ($t_j = 80$ s), and the condition $\nu_m < 7.5 \times 10^{14}$ Hz still applies. However, the cooling frequency must, now, lie below the observing band, and therefore $\nu_c < 7.5 \times 10^{14}$ Hz. Applying these conditions reduces Eqs. 5.2 and 5.24 to

$$\epsilon_B^{-3/2} E_{k,52}^{-1/2} n^{-1} (1+Y)^{-2} < 5.45 \tag{5.25}$$

and

$$\epsilon_B^{1/2} \epsilon_e^2 E_{k,52}^{1/2} < 2.10 \times 10^{-4} \tag{5.26}$$

In the slow cooling regime, where $\nu_m < \nu_c$,

$$\begin{aligned} F_\nu &= F_{\nu,\mathrm{max}}\left(\frac{\nu_c}{\nu_m}\right)^{-(p-1)/2}\left(\frac{\nu}{\nu_c}\right)^{-p/2} \\ &= F_{\nu,\mathrm{max}}\nu_c^{1/2}\nu_m^{(p-1)/2}\nu^{-p/2} \end{aligned} \tag{5.27}$$

By taking the measured value of $F_\nu = 460$ at $\nu = 8.7 \times 10^{14}$ Hz, and using Eq. 5.2, 5.3 and 5.24, the expression for F_ν reduces to

$$\epsilon_e E_{k,52}(1+Y)^{-1} = 3.64 \tag{5.28}$$

Using these equalities, a kinetic energy of $E_{k,52} = 10^3$ erg would require $\epsilon_e = 3.6 \times 10^{-3}(1+Y)$, $\epsilon_B < 0.25(1+Y)^{-4}$ and $n > 0.05(1+Y)^4$. For these values, the IC parameter is very small, with $Y \sim 0.1$. Furthermore, although the kinetic energy is increased by around an order of magnitude when energy injection is taken into account, this is still less than the amount of energy required in the previous models investigated. For a GRB local

environment with a particle density of $n = 10^4$ cm^{-3}, which is a typical density for a molecular cloud [Reichart & Price, 2002], the jet opening-angle would be $\theta_j = 0.8°$, a factor of a few smaller than that determined for other GRBs [e.g. GRB 980519; Nicastro et al., 1999]. This gives a beam-corrected kinetic energy of $E_k^{corr} = 10^{51}$ erg. This model is, therefore, able to satisfy the observations without the requirement of an excessively large amount of kinetic energy.

5.3.3 Synchrotron Self-Compton Emission

For completeness we look into a scenario in which synchrotron self-Compton (SSC) radiation contributes to the observed emission. For a dense ISM circumburst medium, photons are upscattered into the X-ray band by electrons that are accelerated by the magnetic field, causing SSC radiation to be the dominant component in the X-ray band, whereas synchrotron radiation remains dominant in the UV/optical bands. In a scenario where the X-ray and UV/optical emission processes differ, where the former is predominantly due to SSC radiation and the latter is due to synchrotron radiation, it is possible for the temporal and spectral indices to be consistent if both observed bands are above the cooling frequency such that, $\nu_{opt} > \nu_c > \nu_m$ and $\nu_X^{IC} > \nu_c^{IC} > \nu_m^{IC}$. In this case the spectral index is given by $\beta = p/2$, which gives a value of $p = 2.0$. However, the decay rate of the synchrotron optical afterglow should be $(3p - 2)/4$, which for $p = 2.0$ implies $\alpha = 1.0$, and this is inconsistent with the observed decay index of $\alpha = 1.65 \pm 0.01$. A dominant SSC component in the X-ray band is, therefore, not compatible with the data.

5.3.4 Implications For Radio Afterglow

To put further constraint on the models investigated, radio observations of GRB 061007 at T+1 day are considered (see section 5.1.4). In this case, the location of the self-absorption frequency is of importance, and to account for the lack of a radio afterglow detection at $T + 1$ day at a frequency of 19 GHz, the radio emission from GRB 061007 at this time must have either been less than 37 μJy at 19 GHz, or the self-absorption frequency, ν_a,

must have been greater than 19 GHz.

In the first two models investigated, where spherical expansion was assumed and $\nu_m <$ $\nu < \nu_c$, a possible set of GRB and microphysical values that could satisfy the observations were $E_{k,52} = \times 10^4 (1 + Y)^{4/3}$ erg, $\epsilon_B = 10^{-6}$, $\epsilon_e = 0.012(1 + Y)^{-1/3}$ and $n = 54(1 +$ $Y)^{-8/3}$ cm^{-3} for a constant density circumburst medium, and $E_{k,52} = 3.3 \times 10^3 (1 +$ $Y)^{4/3}$ erg, $\epsilon_B = 10^{-6}$, $\epsilon_e = 0.010(1 + Y)^{-1/3}$ and $A_* = 2.5(1 + Y)^{-2/3}$ g cm^{-1} for a wind density profile. Adopting these values, the inverse compton parameter must have been $Y \sim 0.9$ and $Y \sim 4.0$ at the time of the radio observations, for the first two models, respectively, to satisfy the conditions laid out in the ISM and Wind cases in section 5.3.1. For $\nu_m < \nu < \nu_c$, the absorption frequency for an ISM circumburst medium is

$$\nu_a = 1.05 \times 10^9 \left(\frac{(p+2)(p-1)}{(3p+2)} \right)^{3/5} \left(\frac{p-1}{p-2} \right) (1+z)^{-1} \epsilon_e^{-1} \epsilon_B^{1/5} E_{k,52}^{1/5} n^{3/5} \text{ Hz}, \qquad (5.29)$$

and for a wind environment is

$$\nu_a = 8.3 \times 10^9 \left(\frac{p-1}{3p+2} \right)^{3/5} \left(\frac{p-1}{p-2} \right) (1+z)^{-2/5} \epsilon_e^{-1} \epsilon_B^{1/5} E_{k,52}^{-2/5} A_*^{6/5} t_d^{-3/2} \text{ Hz}, \qquad (5.30)$$

For the microphysical values given above, the absorption frequency at one day after the prompt emission would, therefore, have been $\nu_a = 1.8 \times 10^{11}$ Hz for model 1 and $\nu_a =$ 2.4×10^8 Hz for model 2. A spherical expansion model with a constant circumburst profile is, therefore, in agreement with the radio observations, since $\nu_a = 1.8 \times 10^{11}$ Hz > 19 GHz. However, in the case of a wind circumburst environment, the absorption frequency would have been below 19 GHz at one day. In this model the injection frequency is $\nu_m = 8.4 \times 10^{10}$ Hz at one day after the prompt emission, and therefore $\nu_a < 19$ GHz $<$ $\nu_m < \nu < \nu_c$. In this case the flux a day after the prompt emission at 19 GHz is

$$
\begin{aligned}
F_{19 \text{ GHz}}(1 \text{ day }) &= F_\nu(1 \text{ day}) \left(\frac{\nu_m}{\nu} \right)^{-1} \left(\frac{19 \text{ GHz}}{\nu_m} \right)^{1/3} \text{ Hz} \\
&= 5.4 \text{ Jy},
\end{aligned}
\qquad (5.31)
$$

which is also not in agreement with the radio observations, which placed an upper limit on the 19 GHz flux of 37 μJy at T+1 day. A spherical expansion model with a wind-like circumburst density profile is therefore ruled out by the radio observations.

In the first highly collimated jet model, where $\nu_m < \nu < \nu_c$, for $E_{k,52} = 5 \times 10^4$ erg, $\epsilon_B = 6.2 \times 10^{-5}(1+Y)^{-4}$, $\epsilon_e = 0.031(1+Y)$ and $n = 0.07(1+Y)^{-4}$ cm^{-3}, IC parameter at T+1 day is $Y \sim 0.5$, for which $\nu_a = 2.3 \times 10^{10}$ Hz, which is above the 19 GHz radio frequency observation, and therefore consistent with the lack of a radio afterglow detection at this frequency.

A highly collimated jet model with $\nu > \nu_c > \nu_m$ is satisfied by the values $E_{k,52} = 10^3$ erg, $\epsilon_e = 3.6 \times 10^{-3}(1+Y)$, $\epsilon_B = 0.25(1+Y)^{-4}$ and $n = 0.05(1+Y)^4$, and $Y \sim 0.1$ at T+1 day. For these values, $\nu_a = 7.4 \times 10^{10}$ Hz, which is, again, above 19 GHz, and consistent with the radio observations.

5.3.5 Comparing Models

It is interesting to note that with $E_{\gamma,iso} = 10^{54}$ erg in the 10 keV–20 MeV energy range, and a rest-frame peak energy of $E_p = 902$ keV, GRB 061007 satisfies the Amati relation, given by $E_p \propto E_{\gamma,iso}^{1/2}$ [Amati et al., 2002b]. It also satisfies a correlation between the peak isotropic luminosity, $L_{p,iso}$, and spectral lag in the prompt emission, τ_{lag}, whereby $L_{p,iso} \propto \tau_{lag}^{-1.1}$. Both these correlations are satisfied by a large fraction of long GRBs [e.g. Amati, 2006, Gehrels et al., 2006], suggesting that GRB 061007 has the same class of progenitor as other long GRBs.

The consistency observed in the spectral and temporal afterglow behaviour in the X-ray and UV/optical bands, and in the late time γ-ray band, implies that the emission observed comes from the same spectral segment. If the afterglow is assumed to be in the slow cooling regime and a jet break is assumed to occur at $t_j > 2.65 \times 10^5$ s, a large amount of kinetic energy of at least $E_k^{corr} = 1.4 \times 10^{54}$ erg is required for a constant density and a wind-like circumburst medium, which is the equivalent to more that half a solar mass. Simulations of the gravitational collapse of massive stars indicate that a progenitor star with a total mass of $\sim 35 M_\odot$ and iron core of $\sim 2 M_\odot$ can produce a maximum collimated energy of $\sim 10^{52}$ erg [MacFadyen & Woosley, 1999], around 2 orders of magnitude smaller than that estimated for GRB 061007 in a spherically equivalent expansion model. Larger

energies may be produced by more massive progenitors. However, to account for a kinetic energy of $E_k = 1.4 \times 10^{54}$ erg requires a progenitor of several hundred or more solar masses. The implausibly large amount of energy required by both these scenario makes them unsatisfactory models to explain the properties of GRB 061007.

I also investigated a second scenario in which a highly collimated outflow produces a jet break before T+80 s. This requires a jet angle no larger than 0.8°, which satisfies the observational requirements with a lower energy budget and more reasonable set of parameters. The upper limit on the jet opening-angle of 0.8° is a factor of 4 smaller than that previously determined in GRBs [Berger et al., 2003], although still physically possible. Highly collimated ejecta is seen in other astrophysical phenomena, such as radio galaxies, micro-quasars and AGN, and although the mechanism by which the ejecta are accelerated and collimated into narrow jets is still poorly understood, two possibilities are a coiled magnetic field, which would produce a poynting flux dominated jet [e.g. GRB 990123; Zhang & Mészáros (2002), GRB 021211; Kumar & Panaitescu (2003)], or pressure from the surrounding stellar material. Furthermore, the need to observe the jet break in order to measure θ_j introduce selection effects, and the smaller and larger end of the current jet opening-angle distribution will, thus, be underestimated. For the very smallest of jet opening-angles to be measured, very early time data of the afterglow are needed, preferentially covering several energy bands.

For a jet break earlier than T+80 s the observations are valid for a spectral regime in which $\nu_m < \nu < \nu_c$, and $\nu_c < \nu$, where in the latter a larger jet opening-angle is obtained by assuming a density $n = 10^4$ cm^{-3}, consistent with that observed in molecular clouds. The dependence of the circumstellar particle density on ϵ_B, ϵ_e and $E_{k,52}$ in the former of these models does not allow for such high densities, for which the circumburst number density is estimated to be $n = 0.08$ cm^{-3}. The spectral analysis on the afterglow resulted in a large column density, which supports a scenario in which the GRB is embedded within a dense molecular cloud or active star-forming region. This, therefore, favours a model in which $\nu_c < \nu$, where the number density is inferred to be larger.

I note here that Mundell et al. [2007] favour a model in which the jet break does

not occur until after the optical and X-ray observations, rejecting a highly collimated, early jet-break model due to the very small electron index required in such a case. In the analysis presented here, a small electron index is not required due to the presence of energy injection in the model. For there to be smooth injection of energy over a period of 10^5 s, the black hole accretion rate and Lorentz distribution within the jet need to have specific properties. However, this option seems easier to account for than a model that requires a kinetic energy of $E_k \sim 10^{54}$ erg.

In the case of a uniform jet, where the energy and Lorentz factor are constant across the jet, the afterglow after a jet break should decay as t^{-p}. In both the post jet-break models considered in this chapter, the predicted decay slope is steeper than the observed value of $\alpha = 1.65 \pm 0.01$. A possible explanation is continual energy injection, which would maintain the energy in the afterglow and slow down the rate of decay. The requirement for steady energy injection over the entire light curve is of some concern, but seems plausible on the basis of many other examples of energy injection in *Swift* afterglow observations [e.g. GRB 050406, GRB 050714B, GRB 070518, GRB 070520A]. One indication of late time engine activity is in observations of late time X-ray flares out to $10^4 - 10^5$ s. The steepness of the decay of these flares suggest an internal shock origin, which provides a short lived surge of energy that is rapidly radiated away. Further evidence of prolonged energy injection is in the form of plateaus in X-ray light curves, which is observed in a large fraction of *Swift* GRBs, although typically up to 10^3-10^4 s after the prompt emission. In the case of GRB 061007 a steady energy injection is needed for at least an order of magnitude longer than this, during which no break is observed in the light curve. This is not to say that the central engine needs to be active for this length of time, but simply that it is active for the duration of the prompt emission and ejects shells with a large distribution in the Lorentz factor, as discussed in section 1.5. Nevertheless, an energy injection mechanism that remains extremely constant for such a long time requires specific conditions to be in place, such as a central engine luminosity that varies smoothly with time in the case of a long-lasting engine, or a smooth distribution of Lorentz factors in the case of refreshed shocks [Zhang et al., 2006]. This may be particularly problematic

to explain when one considers the chaotic nature of the GRB outburst.

Alternatively, the slow decay rate of the afterglow in the context of post jet-break could also be the result of a jet-edge effect in which there is no sideways expansion. In such a case, at $\Gamma = 1/\theta_j$, the afterglow decay index would steepen by 3/4, and would continue to decay at this rate due to the lack of lateral expansion [Mészáros & Rees, 1999]. In such a scenario there is no need for energy injection, although additional conditions would be required to prevent the jet from expanding further, such as a high magnetic field within the jet.

A possibly more natural form of non-laterally expanding jet is a structured jet or outflow with an energy distribution that is a decreasing function of angular distance from the jet axis, θ_0. In such a jet, emission from the inner core and along the line-of-sight will dominate over that produced at the outer edges of the jet due to the distribution in energy per unit solid angle. A jet break is, therefore, observed when the bulk Lorentz factor at the core of the jet, Γ_c, is equal to the inverse of the viewing angle, θ_v, and it is, therefore, the viewing angle rather than the half-jet opening-angle that determines the time of the jet break (see section 1.7). In order for a jet break to occur before T+80 s the viewing angle needs to be close to the jet axis, which is not that unreasonable given the brightness of GRB 061007. At the time of the jet break, the smoother distribution in energy, ϵ, between $\theta < \Gamma^{-1}$ and $\theta > \Gamma^{-1}$ compared to a uniform jet results in a smaller change in the decay slope, which will be shallower than the 3/4 increase in decay index observed in a uniform jet break. For a power law distribution of ϵ, where $\epsilon \propto \theta^{-k}$, the smaller the value of k the shallower the afterglow light curve will be after the jet-break. In the case of $\nu_m < \nu_{obs} < \nu_c$, where $p = 3$, a decay rate after a jet break with index $\alpha = 1.65$ will occur in structured jet with an ϵ distribution index $k = 0.3$, and for $\nu_c < \nu_{obs}$, where $p = 2$, the energy distribution is $k = 1.4$ [Panaitescu, 2005].

A consequence of a very early jet break time is the faster evolution of Γ into a non-relativistic phase (i.e. $\Gamma \lesssim 1$), which will produce an additional break in the light curve as the decay rate slows down. For a uniform jet with no energy injection $\Gamma \propto t^{-1/2}$ post-jet break, and therefore, the transition of the jet into a non-relativistic phase would occur at

$t_{nr} = t_j \theta_j^{-2}$ [Livio & Waxman, 2000]. For $t_j = 80$ s and $\theta_j < 0.8°$, the jet would, therefore, not enter the non-relativistic phase until more than 4×10^5 s after the prompt emission, which is not in conflict with the observations, and in the presence of energy injection or for structured jets t_{nr} would only get larger.

In the context of post-jet break emission, a decay slope of $\alpha = 1.65$ can, therefore, be accounted for by a non-laterally expanding jet as well as continual energy injection through refreshed shocks. An early jet break before T+80 s can, therefore, satisfy the conditions imposed by the observations without requiring a large energy budget and with a reasonable set of physical parameters.

5.4 Summary

GRB 061007 was the brightest gamma-ray burst to be detected by *Swift* and was accompanied by an exceptionally luminous afterglow that had a V-band magnitude brighter than 11.1 mag at 80 s after the prompt emission. It had an unusually smooth and steep panchromatic temporal decay, which, from the start of the *Swift* observations, decayed as a power law with a slope that is identical in the X-ray and UV/optical bands within the errors ($\alpha_X = 1.66 \pm 0.01$ in the X-ray and $\alpha_{opt} = 1.64 \pm 0.01$ in the UV/optical). This decay slope was maintained up to the point that the source was no longer detected above background in the optical or X-ray bands. In the 15–350 keV energy band, the emission after T+100 s had similar temporal and spectral properties to the X-ray and UV/optical, suggesting the γ-ray emission at >T+100 s originated from the same region as the X-ray and UV/optical emission, in the forward shock. It is difficult to reconcile the brightness of this GRB with the steep, constant decay rate observed in the X-ray, optical and γ-ray emission, which places stringent constraints on the location of the cooling frequency. The exceptional properties of this GRB, therefore, present a challenge to the fireball model.

On many levels GRB 061007 appears to be typical of other GRBs, suggesting that the same progenitor model that explains most long GRBs is also applicable to GRB 061007. The surrounding dust has properties most consistent with an LMC-like environment,

and the relatively large column density measured local to the GRB suggests that it is embedded in a large molecular cloud or a region of active star formation. The absorption and extinction system measured at the redshift of the GRB host suggests a gas-to-dust ratio that is consistent with the mean host galaxy gas-to-dust ratio determined in chapter 4 from a sample of 7 *Swift* GRBs. Furthermore, the burst properties are consistent with both the Amati and timelag-luminosity relations, which apply to a large fraction of long GRBs, suggesting that the source of energy in GRB 061007 is no different from that of most other long GRBs. The large apparent brightness of GRB 061007 is, therefore, unlikely to be due to a different type of progenitor, but the result of extreme values for a few defining characteristics.

The lack of a cooling or jet break in the afterglow up to $\sim 10^5$ s after the burst trigger constrains any model that can produce the large luminosity observed in GRB 061007. I found that either an excessively large kinetic energy is required or a highly collimated outflow. Analysis of the multi-wavelength spectral and high-resolution temporal data taken with *Swift* suggests an early time jet-break to be a more plausible scenario. A model in which a jet break did not occur until after the *Swift* observations requires an excessively large kinetic energy due to the wide emitting region required in this model. In such a case the GRB fireball would need to have a kinetic energy of at least $E_k^{corr} > 1.4 \times 10^{54}$ erg, and this is with collimation of the ejecta taken into account.

If instead, the time of jet break was within 80 s of the prompt emission, the jet opening-angle would have to be, at most, $\theta_j = 0.8°$. Such a highly collimated outflow would resolve the energy budget problem presented in a spherical emission model, reducing the isotropic equivalent energy of this burst to $E_\gamma^{corr} = 10^{51}$ erg, consistent with other GRBs. Though steep, the decay of the afterglow is nevertheless somewhat slower than that typically expected from post jet-break decay indices in a simple model. However, the slower decay can be accounted for if long term energy injection is considered, or if the jet has a structured outflow.

The brightness of GRB 061007 across the electromagnetic spectrum makes it ideal to explore the conditions surrounding the production of GRBs, and its uniqueness provides

further insight into the range in properties that GRBs have. In particular, the small opening-angle that is determined for GRB 061007 has important implications on the true range in jet opening-angles.

Chapter 6

Long GRBs in the *Swift* era

The previously unexplored time-domain that is now accessible with the launch of *Swift* is providing crucial information that can address key areas in understanding the underlying mechanism that powers a GRB, and the conditions required for its formation. Whilst providing greater insight into the phenomenon of GRBs, *Swift* observations have also revealed the complexities of the internal engine, the GRB collimation, and the emission regions involved, and as a result many areas in GRB science that were previously believed to be understood need to be reconsidered and revised accordingly.

One of the underlying problems in GRB science that has been highlighted by *Swift* observations is that of collimation. This is of vital importance in our current understanding of the energetics of GRBs. However, *Swift* has detected far fewer jet breaks than expected, on the order of 10%–30% of GRBs observed. The sparsity of jet breaks has opened many questions on the structure of GRB jets, on the differences in emitting regions across the spectrum, and on the degree of collimation.

Critical to determining the total energy of a GRB is also the amount of energy injected into the jet and the way in which is is injected. Understanding the effect that this has on the GRB afterglow is not only important for determining the total kinetic energy of the GRB, but also to identify the origin of certain features in the light curve, such as plateau phases and breaks.

Both the role of energy injection and the collimation of GRBs have been material to

the results presented in chapters 3 and 5 of this thesis, and in this chapter I shall address further the implications that *Swift* observations have as a whole on these issues.

Another unexpected and significant result from *Swift* observations has been the large fraction of GRBs observed promptly by UVOT, but that have no afterglow detected blueward of 5500 Å. This could either be due to the afterglow being intrinsically dim at these wavelengths, the result of absorption by dust, or absorption by neutral hydrogen if the GRB is at high redshift. Which of these is the dominant cause for the low UVOT detection rate has important implications for GRB progenitors and their environments, and needs to be addressed in order to understand the selection effects present in our observations. In this chapter I, therefore, also review briefly our current observations of long GRB host galaxies, and in light of the work presented in chapter 4, I investigate the role that dust may play in the case of those GRBs that have no UV/optical afterglow detected by UVOT.

6.1 Energy Injection

The presence and effect of energy injection in GRBs, from both a long lasting engine and refreshed shocks, had been studied prior to the launch of *Swift* [e.g. Rees & Mészáros, 1998, Zhang & Mészáros, 2001, MacFadyen et al., 2001]. However, this work had primarily been theoretical, and *Swift* data have provided the first opportunity to measure the importance of energy injection on a large, homogeneous sample of GRBs.

The afterglows of both XRF 050406 (chapter 3) and GRB 061007 (chapter 5) are well described by a model that has an energy injection component. In the case of XRF 050406, the best-fit energy injection parameter is $q = 0.3$, and for GRB 061007, a post-jet break model requires $q = 0.3$ or $q = 0.7$, depending on whether the cooling frequency is above or below the observing band, respectively. For $q = 0.7$ the rate of energy injected into the forward shock is only $\dot{E} \propto t^{0.3}$, so that its effect on the afterglow is fairly small. The need for a smooth and continuous energy injection is, therefore, not as imperative as for $q = 0.3$. For $q = 0.3$, any variations in the rate of energy injection would be more easily

detected in the afterglow decay rate, and in this case the source of the energy injection would need to be continuous and smooth for the duration of the observations to produce the afterglow light curves of XRF 050406 and GRB 061007.

It is possible for a long lasting engine to inject energy at a smooth rate. However, the duration of the central engine is related to the accretion timescale, which cannot last much longer than 10^3–10^4 s [MacFadyen et al., 2001]. A long-lasting engine may, therefore, explain the plateau phase observed in many X-ray afterglows up to $\sim 10^3$–10^4 s, but it cannot produce the afterglows of XRF 050406 and GRB 061007, which continued on the same power law decay rate for up to 10^6 s after the BAT trigger. There are other examples of GRBs that showed evidence of energy injection out to T+10^6 s, such as GRB 050714B [Willingale et al., 2007] and GRB 070520B [Romano et al., 2007], and the UV, optical and NIR afterglows frequently maintain a shallow decay rate, with $\alpha < 1$, out to at least T+10^5 s [Oates et al., 2007b]. If these long, shallow decay phases are caused by energy injection, an alternative source of energy injection to a long-lasting engine is, therefore, needed to maintain the afterglow shallow decay for over 10^4 s.

The release of shells from the central engine with a distribution in Lorentz factor may produce long lasting energy injection out to T+$10^5 - 10^6$ s without the need for the central engine to be continually active for the duration of the energy injection. The forward shock is re-energised or refreshed as slower shells catch up with the forward shock. In this case the duration of the energy injection is determined by the amount of mass accreted onto the black hole, and on the Lorentz factor distribution index. For the injection of energy into the forward shock to be smooth, the mass ejected from the accreting disk would need to have a power law distribution in Lorentz factor, where the fraction of mass with Lorentz factor Γ_{sh} is inversely proportional to Γ_{sh} [Rees & Mészáros, 1998]. Such a smooth distribution in Lorentz factor within the ejecta may seem counter-intuitive, given the chaotic nature of the ejecta indicated by the prompt emission. However, the simulations in MacFadyen et al. [2001] indicate that after ~ 400 s the accretion rate begins to decline roughly as $t^{-5/3}$, which may, also, provide a smooth distribution in Γ_{sh}. Furthermore, in an internal shock model, the dissipation of kinetic energy resulting

from the collision of individual shells reduces the Lorentz factor of these shells, and thus increases the fraction of mass within the ejecta with a Lorentz factor at the low end of the distribution. Only the fastest of shells released at earlier times will maintain a large Lorentz factor. The distribution of mass within the ejecta with Lorentz factor Γ_{sh} may, therefore, approximate an inverse power law during the prompt emission phase, where the slowest moving shells will trail behind. It is also possible that, provided that the shells are close to each other, the energy injected through refreshed shocks would be near continuous, and discrete components of energy injection would then be smoothed out and produce a uniformly decaying afterglow light curve.

The cessation of energy injection from both a long-lasting engine and from late-time shocks produced by slow shells will produce a break in the afterglow light curve, as is observed at the end of the X-ray afterglow plateau phase at 10^3–10^4 s. However, such a break is not observed in the UV to NIR energy bands, which typically have breaks during the third phase of the X-ray canonical light curve, at epochs later than T+10^4 s, and which are usually accredited to jet breaks rather than the cessation of energy injection [e.g. GRB 050525; Blustin et al., 2006, GRB 060206; Curran et al., 2007, GRB 060526; Dai et al., 2007]. The fact that this is purely an X-ray phenomenon and that a simultaneous break is not observed in the UV and lower energy bands, suggests that there are different emission regions producing the X-ray and optical/NIR GRB afterglow. This would implicitly imply a two-component jet. A narrow component with larger bulk Lorentz factor, Γ_{nr}, would travel further into the circumburst medium than a wider jet component that had a bulk Lorentz factor $\Gamma_{wd} < \Gamma_{nr}$. The narrow and wide jet components would, therefore, produce two separate forward shocks at radii R_{nr} and R_{wd}, respectively, where $R_{nr} > R_{wd}$, and the emission produced at R_{nr} would primarily be in the X-ray energy band due to the larger Lorentz factor of the narrow jet component. A two-component jet of this kind could form from electro-magnetic forces that collimate and accelerate protons into a narrow, baryon-poor jet, whilst the decoupled neutrons would form a wider, slower jet [Vlahakis et al., 2003]. Alternatively, an initially single component jet could form into two components during its propagation through the stellar envelope. Beyond a certain

radius, r, the external stellar pressure may no longer be enough to confine the shocked jet material, causing the material at the head of the jet to spread laterally and trail behind the collimated ejecta, thus forming a second jet component [Mészáros & Rees, 2001].

Whether afterglow plateau phases are short lived (i.e. finished by 10^3–10^4 s) or last for more than 10^5 s will depend on which of the two jet components dominates the observed emission. In the case of a short-lived, X-ray plateau phase, the narrow jet would be the dominant component, and the cessation of this phase may then arise when the Lorentz factor of the narrow jet component, Γ_{nr}, were no longer large enough for the shells within the narrow jet to reach R_{nr}. Another possibility is that the end of the plateau phase is, in fact, a jet-break caused when $\theta_{nr} \sim \Gamma_{nr}^{-1}$ [e.g. Oates et al., 2007a]. A longer lived plateau phase could then be explained by a two-component jet with a dominant wide jet component. In such a case, shells would continue to plough into the wide component jet forward shock, R_{wd}, for longer, and a jet-break would then arise at later times than would be the case for the narrow jet component.

The afterglow of GRB 061007 decayed at the same rate in both the X-ray and the UV/optical energy bands, which would indicate that the emission region was the same for all energy bands. GRB 061007 is, therefore, likely to have had a single component jet, although the jet morphology could have changed at the time of the jet break. The analysis on GRB 061007 described in chapter 5 indicates that its afterglow emission is post jet-break, and both narrow and wide jet components may, therefore, have merged by the onset of the UVOT and XRT observations if the narrow component was a laterally expanding jet.

In the case of XRF 050406, the X-ray light curve did not have a short lived plateau phase. However, for a large viewing angle, as believed to be the case in XRF 050406, the emission produced at the narrow component forward shock would be beamed out of the line-of-sight, and it would, therefore, not dominate over the emission produced at the wide component forward shock. In fact, in this model the duration of the plateau phase should be anti-correlated with the viewing angle, and observations of XRF and XRR GRB X-ray afterglows should, therefore, provide a means to test whether there is a source of

energy injection that dominates the central region of the GRB jet. In a comparison of the properties of XRFs, XRR GRBs and standard GRBs, Sakamoto et al. [2007] find that GRBs have larger plateau phases than XRFs, and that the duration of the plateau phase in XRR GRBs is somewhere in between. This, therefore, is consistent with the predictions of a two component jet, where detection of emission from regions more concentrated along the core of the jet are strongly dependent on viewing angle.

Although energy injection is currently the most favoured model to account for the short-lived X-ray plateau phase, in the case of long-term shallow decay rates, as in XRF 050406, the afterglow light curves could also be well explained by a structured jet model. The decay rate observed from a structured jet model when the viewing angle is large is smaller than for a uniform jet viewed on-axis. A structured jet model was mentioned in both chapter 3 and chapter 5 to explain the afterglow of XRF 050406 and GRB 061007, respectively, and the appeal of this model is that it removes the fine-tuned conditions needed in long term energy injection to explain the smoothness of the decay. Furthermore, analysis of the prompt and afterglow properties of XRF 050406 already indicates that the jet does not have a uniform energy density profile. This does not exclude the presence of a narrow jet component, which may be embedded within a structured jet and produce a forward shock independent to the rest of the jet. However, the long term shallow afterglow decay would now be caused by the slower decay rate of a wide structured jet, rather than by energy injection of the wide component forward shock.

The large fraction of GRBs observed with a plateau phase in their X-ray light curves indicates that energy injection is a common phenomenon. However, it is not yet clear to what degree energy injection plays a role at 10^5–10^6 s after the prompt emission. Although a power law distribution in the Lorentz factor of shells within the ejecta could produce smooth, late-time energy injection, a structured jet could naturally produce a smooth decaying afterglow where the shallowness of the decay would depend on the energy density profile. The soft nature of the prompt emission spectrum of XRF 050406, and the decaying nature of the afterglow light curve from the onset of the X-ray and optical observations were best explained by a jet that was structured, so in this case at least, the

slow decay rate is likely to the result of a non-uniform energy density jet profile.

The flexibility in the possible values for both the energy injection parameter, q, and the energy density index, k, make it possible to account for a broad range of afterglow decay indices by incorporating either energy injection or a structured jet into the standard fireball afterglow model. It is, therefore, difficult to distinguish between the two, and observations of a temporal break are needed to determine the origin of long-term shallow afterglow decay phases. The relation between the temporal and spectral indices before and after a break in the afterglow light curve differ for a break caused by the cessation of energy injection, and one accredited to a jet-break. In the case of the cessation of energy injection, the closure relations satisfied by the observations should have a value of $q < 1$ pre-break, and $q = 1$ post-break. A jet-break, on the other hand, should have the same value of q before and after the break, and the change in decay index should be consistent with jet-break model predictions. Deep, multi-wavelength, late-time observations are, therefore, important to maximise the chance of detecting breaks, and thus determine whether these are caused by the cessation of energy, or due to the edge of the jet coming into view.

6.2 Collimation

Some of the most crucial questions surrounding the mechanisms involved in GRBs are related to the collimation of the ejecta, and the structure of any jet that is produced. The collimation of GRBs can significantly reduce the energy budget problem associated with some GRBs [e.g. GRB 990123; Frail et al., 2001, GRB 061007; chapter 5], and, as a consequence, the degree of collimation and jet structure of GRBs cannot be neglected when determining their energetics and other related properties, and is of critical importance in any GRB model. The degree of collimation and energy density profile is also important when interpreting the observed properties of the prompt emission and the broadband afterglow, in particular when considered in terms of the viewing angle.

6.2.1 Off-Axis GRBs

Due to the collimation of GRBs and the effects of relativistic beaming, the viewing angle to a GRB and the jet model needs to be considered when interpreting the observed GRB properties. In particular, it is important to know where the viewing angle lies with respect to the dominant emission region.

As discussed in chapter 3, a large viewing angle, θ_v, that is outside a uniform jet's half opening-angle, or at large angles from the core of a structured jet will have a softer prompt emission and dimmer afterglow. This is due to the reduced Doppler boosting factor at larger viewing angles, and the decrease in flux observed at larger viewing angles with respect to an on-axis observer. XRF 050406 is one example of an X-Ray Flash that is most likely the result of an off-axis GRB, and there are several other XRFs that are, similarly, best described as off-axis GRBs, such as XRF 050215B [Levan et al., 2006], XRF 050408 [de Ugarte Postigo et al., 2007], and XRF 050416A [Mangano et al., 2007]. The large number of similar properties between XRFs, XRR GRBs, and standard GRBs suggest that all three classes of bursts are produced by the same phenomenon, and a geometrical interpretation of X-ray flashes was also favoured by Lamb et al. [2005] and Gendre et al. [2007], who used a large sample of XRFs to determine the model that was most consistent with the observations.

The X-ray afterglows of XRF 050215B and XRF 050408 decayed as power laws with decay indices $\alpha_X = 0.82 \pm 0.08$ [Levan et al., 2006] and $\alpha_X = 0.99 \pm 0.21$ [de Ugarte Postigo et al., 2007], respectively, whereas the X-ray afterglow of XRF 050416A was better fit with a single or double break in the light curve, with a final decay index of $\alpha_{X,2} = 0.81 \pm 0.02$ or $\alpha_{X,3} = 0.88 \pm 0.02$, depending on the model. In the case of XRF 050215B and XRF 050416A, the final decay index of the light curve is shallower than the typical decay rate of X-ray afterglows at late times [e.g. $1 \lesssim \alpha \lesssim 1.5$ Nousek et al., 2006], and XRF 050408 is at the shallow end of the distribution. Furthermore, in the analysis done by Sakamoto et al. [2007], standard GRBs were found to have steeper temporal indices at T+10 hrs than XRFs, and the decay rates of XRR GRBs at the same

epoch were in the intermediate range. This was also the case for the X-ray afterglow of XRF 050406, and is consistent with the observations expected from an off-axis jet.

Another similarity between the four XRFs discussed above is that they all had afterglow light curves that decayed from the start of the afterglow observations, which was at most 45 minutes after the prompt emission, and this behaviour is similarly true of a further two XRFs and three XRR GRBs studied by Sakamoto et al. [2007]. However, for a jet half opening-angle, $\theta_j = 1°$, a uniform jet observed at viewing angles $\theta_v > \theta_j$ should have a rising light curve out to at least 10^4 s after the prompt emission, and the duration of the brightening phase will become larger for greater θ_v and θ_j [Rossi et al., 2002, Granot et al., 2002]. This indicates that either XRFs are not uniform jets observed at angles $\theta_v > \theta_j$, or that their jet half opening-angles are smaller than 1°. Only for $\theta_j < 1°$ could the bulk Lorentz factor have slowed down sufficiently by the onset of the afterglow observations such that $\Gamma < \theta_v^{-1}$, at which point the afterglow would be observed to decay. In this case radiation from the centre of the jet would be seen by the observer from the start, and the rising behaviour produced by the centre of the jet coming into view would have already taken place.

Around 1/3 of GRBs observed by BeppoSAX and HETE-2 are XRFs, and around 1/3 are XRR GRBs [Lamb et al., 2005], and the indication that XRFs and XRR GRBs decay as power laws from a few thousand, if not hundred, of seconds after the prompt emission implies that, in the context of a uniform XRF model where $\theta_v > \theta_j$, the majority of GRBs have jet half opening-angles $\theta_j < 1°$, which is in contradiction with observations. Pre-*Swift*, the median jet opening-angle of GRBs was $\theta_j \sim 5°–10°$ [Bloom et al., 2003, Ghirlanda et al., 2004, Soderberg et al., 2006], and this average is based on only those GRBs which had a detected jet break. Those GRBs with large jet opening-angles and, hence, late-time jet-breaks that occur outside of the observing window, will not have been taken into account, and the median jet opening-angle is, therefore, likely to be more than 10°. XRFs are, therefore, unlikely to have jet half opening-angles that are $\theta_j < 1°$, in which case a uniform jet observed at angles $\theta_v > \theta_j$ cannot be the origin of XRFs.

XRF 050215b, XRF 050406, XRF 050408 and XRF 050416A were all detected in the

X-ray band for at least 3×10^5 s after the the BAT trigger, and in the case of XRF 050416A, the X-ray afterglow was detected for up to 42 days after the BAT trigger [Mangano et al., 2007]. However, none of these afterglow observations showed evidence of a jet break. To explain this, both Levan et al. [2006] and Mangano et al. [2007] suggested that a GRB with a very wide jet half-opening angle, θ_j, and viewing angle $\theta_v < \theta_j$, could account for the lack of jet breaks, as well as the soft nature of the XRFs. However, the distribution of XRFs, XRR GRBs and standard GRBs is also not consistent with an XRF model where XRFs have jet opening angles that are on average larger than the jet opening angles of GRBs. The probability of detecting a GRB increases with jet opening-angle, and this model therefore over-estimates the fraction of XRFs that should be observed unless the distribution in jet opening angles is skewed towards smaller angles. However, there are, also, examples of GRBs that have a hard prompt emission spectra, and are therefore not XRFs or XRR GRBs, but which show no sign of jet breaks out to T+10^6 s or more [e.g. GRB 050822, GRB 051109A, GRB 051117A, GRB 060202; Burrows & Racusin, 2007]. This, therefore, suggests that it is not the size of the jet opening-angle alone that produces an XRF.

In a structured jet model, the functional dependence of the energy density on the angle from the jet-axis can be modelled on the observed distribution in XRFs, XRR GRBs and standard GRBs, and in this way, Zhang et al. [2004a] found that a Gaussian energy density profile provides a good solution. A structured jet viewed at a large angle from the jet-axis can, therefore, produce an afterglow light curve that decays from the start at a decay rate that is shallower than if observed on axis, as well as reproduce the distribution of observed XRFs, XRR GRBs and standard GRBs. This was found to be the best model to describe the observations of XRF 050406 (chapter 3), and is consistent with the observations of XRF 050215b, XRF 050408 and XRF 050416A, as well as those XRFs and XRR GRBs analysed by Sakamoto et al. [2007].

The current data on XRFs and GRBs, as well as the indication that there is more than a single emission region producing the GRB afterglow, therefore, suggests that the energy density distribution within the jet is not uniform, but that GRB jets have a structured

energy density profile with a uniform core component. The differences in the afterglow light curves produced by different jet models are most prominent at large viewing angles and at early times, when the emission is still narrowly beamed [e.g. Rossi et al., 2002, Granot et al., 2002, Donaghy, 2006], and further multi-wavelength observations of XRFs and XRR GRBs can, therefore, continue to provide better constraints on the morphology of GRB jets. Not only will these data discriminate between jet models from the early time light curves of XRFs and XRR GRBs, as was done in chapter 3, but the relative number distribution observed between these classes of GRBs may also constrain the jet model.

6.2.2 On-Axis GRBs

Prior to the launch of *Swift*, jet-breaks were detected in $\sim$ 75% of well sampled GRB optical afterglows [Panaitescu, 2007b], with a mean jet break time of $\sim$ 2 days [Zeh et al., 2006]. *Swift* observations were, therefore, expected to detect achromatic breaks caused by the edge of the jet coming into view in the large fraction of GRBs. Instead, UV and optical afterglows, when detected by UVOT, have typically decayed as power laws, and breaks observed in the X-ray light curves have not been observed in the optical bands, nor have they satisfied the closure relations described by a standard, uniform jet break. This is despite the near complete detection rate of X-ray afterglows by XRT, lasting for at least several days and often for several weeks after the prompt emission.

In a sample of 99 GRBs that *Swift* slewed to in the first few minutes of the BAT trigger, the X-ray afterglow for $\sim$ 15% show a constant power law decay in the range $\alpha = 0.79 - 2.07$ during the entire period of observations (a few hundred seconds after the bursts to T+10^5 – T+10^6 s) [Willingale et al., 2007]. A further 25% have an initial short-lived steep decay (phase I in section 1.2.2) followed by a break to a shallower decay $(0.5 < \alpha < 1.25)$ for the continuation of the observations. Any jet breaks in this 40% of the sample must have, therefore, occurred either before or after the XRT observations. Assuming a uniform jet with lateral expansion and no energy injection, Willingale et al.

[2007] found only $\sim 20\%$ of the remaining GRBs in the sample to have breaks that were well fit by a jet break. The fraction of GRBs well fit by a jet break, therefore, corresponds to only 12% of the complete sample.

Panaitescu [2007b] modelled the X-ray afterglow light curves of 94 well-sampled *Swift* GRBs and found that when both a jet model with and without lateral expansion was tried, 32% of the sample were well fit by a jet break at 0.1–10 days after the prompt emission.

One likely explanation for the drop in jet-break detection rates in the *Swift* sample of GRBs is the result of selection effects. The increased sensitivity of BAT compared to *Beppo*SAX and HETE-2 has increased the fraction of dim GRBs that are detected, and this, combined with the speed of the observations taken by *Swift* and ground based observations triggered by *Swift*, is providing a sample of GRB afterglows that are, on average, fainter than those observed prior to *Swift* [Berger et al., 2005a]. To make a fair comparison between the fraction of jet-breaks detected in GRBs observed prior to *Swift* and those from the *Swift* era, I apply a cutoff to the 15–350 keV fluence of those GRBs considered in the *Swift* sample. This cutoff is set at $S_{15-350\ keV} = 5 \times 10^{-7}$ erg cm^{-2}, which corresponds to the lower sensitivity threshold of *Beppo*SAX [Berger et al., 2005a]. When this is applied on the sample of *Swift* GRBs used by Panaitescu [2007b], the fraction of GRBs with good evidence of a jet-break in the X-ray afterglow light curve goes up to 48%. However, this cutoff only takes into account the selection effects present in the instruments' sensitivity to the GRB prompt emission, and not the selection effects related to the afterglow detection. A cutoff is, therefore, also introduced in the brightness of *Swift* GRB afterglows. In the sample of pre-*Swift* GRBs listed in Panaitescu [2007b], all those with good evidence of a jet-break had an *R*-band magnitude of at least 20.5 magnitude at 12 hours after the prompt emission. To account for the brightness bias in the pre-*Swift* sample I, therefore, impose a further condition and consider only those GRBs (pre-*Swift* and *Swift*) with an *R*-band magnitude of $R = 20.5$ or brighter at 12 hours after the prompt emission. In this case, two pre-*Swift* GRBs in Panaitescu [2007b] are no longer included in the sample, and there remain 18 GRBs in the pre-*Swift* sample, and 76 GRBs

in the *Swift* sample. To take into account the low number statistics of the pre-*Swift* and *Swift* samples, binomial statistics for small numbers [Gehrels, 1986] are used to determine the fraction and statistical errors of the number of GRB jet-breaks observed in these two samples. Applying this, prior to *Swift* 80^{+17}_{-27} % of well sampled GRB afterglows had a jet-break at 99% confidence, and of the *Swift* GRBs considered by Panaitescu [2007b], 75^{+11}_{-37} % showed good evidence of having a jet break, also at 99% confidence.

When the selection effects present in the *Swift* and pre-*Swift* samples of GRBs are taken into account as well as the low number statistics involved, the jet-break detection rate in the two samples becomes much more comparable, although the fraction of pre-*Swift* GRBs with observed jet-breaks is still slightly larger. Reasons for this could be the length of time after the prompt emission that the afterglow was observed for, and differences in the prominence and time of a jet break between observing bands. Pre-*Swift* GRB jet-breaks were purely based on optical and NIR observations, whereas analysis of *Swift* jet-breaks is typically carried out on X-ray data, which provides a more complete afterglow sample. In the NIR and optical energy bands, the afterglows of *Swift* GRBs are not as well sampled as pre-*Swift* GRBs. One reason for this is that the GRB detection rate was smaller prior to *Swift* which meant that ground-based observatories dedicated more time to individual GRBs. Given the improvement in the quality of X-ray data made available, XRT observations should make a good substitute for the lack in optical and NIR data, and provided that the afterglow is detected, the band in which the afterglow observations are made should not matter. However, this assumes that jet-breaks occur achromatically in the X-ray and optical bands, which may not always be the case. There have been a few examples of GRBs with good evidence for the presence of jet breaks in the X-ray but not the optical energy bands [e.g. GRB 050802; Oates et al., 2007a, Panaitescu, 2007a], which could result from a two component jet. The possibility of two sources of energy injection, as proposed in section 6.1, would also suggest that there were two components to the jet. However, only a handful of *Swift* GRBs have had sufficient optical and NIR data to determine whether jet breaks in the X-ray and optical bands are typically achromatic across the spectrum [e.g. GRB 0505025; Blustin et al. (2006),

GRB 060526; Dai et al. (2007)], which highlights all the more the need for long-term, multi-wavelength observations.

Nevertheless, the increased sensitivity and rapid response of *Swift* is providing a more complete sample of GRBs, and the small fraction of jet-breaks detected in the full *Swift* sample indicates that the range in jet-break times is larger than previous GRB observations suggested.

The work presented in chapter 5 shows that for at least one GRB (GRB 061007) the jet break may have occurred at very early times, before the start of the X-ray and UV/optical observations, which would require a jet opening-angle of $\theta_j < 0.8°$. GRB 051210 is another possible example of a very early jet break that may have occurred prior to the first XRT observation, at T+93 s. It had an X-ray afterglow decay index of $\alpha = 2.07 \pm 0.16$, and a spectral index that is compatible with a uniform, laterally expanding jet [Willingale et al., 2007]. However, GRB 061007 was an exceptional GRB on the basis of its large early time optical flux and because of its X-ray and UV/optical steep and uniform temporal behaviour. More importantly, the chance of detecting a GRB that is highly collimated is small, and it is, therefore, likely that very early time jet breaks of this kind are not typically observed, and do not account for the large fraction of *Swift* GRBs with no detected jet break. A more reasonable assumption is that the jet break occurs once the afterglow has decreased below the XRT and UVOT sensitivity levels. For 19 GRBs in the Panaitescu [2007b] sample this corresponds to 3–10 days after the prompt emission, for 13 GRBs this would be at 10–30 days after the prompt emission, and for 6 GRBs the jet break would have had to take place more than 30 days after the prompt emission.

However, it is important to note that in both Willingale et al. [2007] and Panaitescu [2007b], analysis was carried out on X-ray data alone, and the jet was assumed to be uniform. The analysis presented in chapter 3 and the discussion in section 6.2.1 indicates that for at least some GRBs, the jet structure is likely to be more complex than a uniform distribution in energy density, for example. The closure relations that correspond to the fireball model are not satisfied by $\sim 50\%$ of the XRT GRB sample in Willingale et al. [2007], either in the pre or post jet-break case, which suggests that additional, unaccounted

for processes are present, such as energy injection, and that the GRB jet may have a more complex morphology than that assumed. The consequent change in the decay index at the jet-break, and over which energy range the break is achromatic, will depend on the jet model, and if the wrong model is fit to the GRB afterglow, a jet-break in the light curve may not be identified.

There is at least one GRB in the Swift sample used by Panaitescu [2007b] which showed evidence of a jet-break in the optical afterglow [GRB 060206; Curran et al., 2007], but that was not detected in the X-ray afterglow. The X-ray afterglow of GRB 060206 is well fit by a power law ($\chi^2 = 65$ for 65 dof), and although a broken power law did improve the quality of the fit ($\chi^2 = 50$ for 63 dof), the best-fit decay indices to a broken power law fit were not consistent with a uniform jet break ($\alpha_1 = 1.04 \pm 0.10$, $\alpha_2 = 1.40 \pm 0.07$) [Curran et al., 2007], which should steepen by $\Delta\alpha = 0.75$. Both Willingale et al. [2007] and Panaitescu [2007b], therefore, concluded that this GRB did not show good evidence for a jet break. However, when the optical data is used to constrain the fit to the afterglow light curve, the X-ray data is adequately fit by a broken power law model with a change in decay index that is more consistent with a jet break ($\chi^2 = 62$ for 66 dof, with $\Delta\alpha = 0.55 \pm 0.06$) [Curran et al., 2007]. A steepening in decay index of $\Delta\alpha = 0.55$ at the break to $\alpha_2 = 1.7$, is still less than predicted for a uniform jet-break. However, such a break can by modelled with a structured jet. The afterglow of GRB 060206, therefore, illustrates that more complex jet models than the uniform jet need to be used when modelling jet-breaks in GRB afterglow light curves. It is also important that afterglow data across the spectrum are used when possible to model the shape of the afterglow light curve, which may have a smaller change in decay index or more gradual steepening in the afterglow decay than predicted by the uniform jet model that is better constrained by multi-wavelength data.

The increase in detection rate of GRBs and rapid, arcsecond localisations since the launch of Swift has meant that few GRBs are followed-up for periods longer than a day, and it is, therefore, highly likely that many jet breaks in the optical bands are missed. This problem is further exacerbated by the relative dimness of Swift GRB optical afterglows compared to the optical afterglows of pre-Swift GRBs, which are usually below

the detection threshold of UVOT, and also below the detection threshold of many ground based telescopes by around 10^5 s after the prompt emission. Furthermore, the detection of jet breaks in X-rays that are not present in the optical afterglows, as well as the evidence presented in section 6.2.1, indicates that GRB jet breaks are much more complex than a simple uniform model suggests. Detailed and simultaneous fitting of the X-ray and optical afterglow light curves with a jet model that can vary in structure is, therefore, required before an accurate determination can be made of the range of jet models that GRBs may have, and thus of the fraction of GRBs with jet breaks.

6.3 GRB Environments

As well as the early time afterglow observations provided by *Swift*, the rapid, arcsecond localisation of GRBs are also allowing follow-up observations of the host galaxy to be made on a large, homogeneous sample of GRBs [e.g. Jakobsson et al., 2006b]. Understanding the conditions required for a galaxy to host a GRB is not only important for progenitor models, but also if GRBs are to be used as cosmological tools. The detectability of GRBs out to high redshifts and the association between long GRBs and massive stars makes GRBs, potentially, very powerful candidates for tracing the star formation rate. The GRB luminosity function and redshift distribution could provide information on the star formation rate history, and high-resolution spectroscopic observations of afterglows would provide a wealth of information on the cosmic chemical evolution. However, the indication that other factors, such as the rotational speed of the progenitor and the metallicity and chemical composition of the environment, are important in the production of a GRB, complicate the relation between the GRB rate and the star formation rate. Understanding this relation is further hampered by the effect that the collimation of GRBs has on the detection rate and, thus, the determined GRB rate. Therefore, if GRBs are to be accurate and unbiased tracers of the star formation history and the chemical evolution of galaxies, a clear understanding is needed of the progenitors of GRBs, of the GRB formation rate, of the fine-tuned environments required for a galaxy to host a GRB, and how these evolve

with redshift.

Around three quarters of the star formation in the high redshift Universe is believed to have occurred in starburst, submillimetre-bright galaxies [Ramirez-Ruiz et al., 2002]. If GRBs trace star formation, three quarters of the population should, therefore, have dusty, red hosts observable in the submillimetre band in contrast to current observations [Fruchter et al., 2006, Le Floc'h et al., 2006], which indicate that they are UV bright, and weak emitters at submillimetre wavelengths [e.g Barnard et al., 2003, Le Floc'h et al., 2006]. In a combined sample of 11 GRBs from Smith et al. [1999, 2001] and Barnard et al. [2003], the detection of submillimetre emission at 850 μ with flux density greater than 2 mJy was ruled out in 9 cases at the 3σ level, and in the remaining 2 cases it was ruled out at the 2σ level [Barnard et al., 2003]. In a larger sample of 26 GRBs with spectroscopically measured redshifts and < 1.4 mJy flux uncertainties, the 850 μm flux density distribution of GRB hosts showed a shortage of GRBs with fluxes greater than 4 mJy when compared to the expected flux distribution of submillimetre galaxy populations [Tanvir et al., 2004]. *Spitzer* observations in the mid-IR of 11 pre-*Swift* GRBs similarly revealed a smaller detection rate than expected when compared to IR galaxy evolution models, which indicate $\gtrsim$ 50% of GRB hosts should have a flux greater than 100μJy at 24μm [Le Floc'h et al., 2006]. The lack of mid-IR and submillimetre detections in the large fraction of observations at the locations of GRBs suggest that other factors apart from high star formation rates, are important in the formation of a GRB.

UV-luminous galaxies have low metallicities compared to submillimetre bright galaxies [Sanders & Mirabel, 1996], and long GRB host galaxy observations could, therefore, be indicative of the preference for GRB progenitors to form in sub-solar metallicity environments [Fruchter et al., 2006]. This would be in agreement with the predictions of the collapsar model, and with the analysis presented in chapter 4, whereby an extinction law suitable for irregular, sub-solar metallicity environments is, in the majority of cases, in closest agreement with the extinction properties of the environments local to long GRBs.

However, in both the sample of GRBs selected for spectral analysis in chapter 4, and in the sample of GRBs with host galaxy detections used by Fruchter et al. [2006] and

Le Floc'h et al. [2003], for example, selection effects are present. In order to produce a multi-wavelength spectrum, the GRB optical or NIR afterglow needs to have been detected, and this is typically also the case for the identification of the host galaxy. GRBs that are heavily enshrouded by dust, and thus have their UV and optical afterglow obscured are, therefore, more likely to be omitted from the sample. Although the intense radiation emitted by the GRB may destroy much of the surrounding absorbing medium and photoionise the gas in the circumburst environment, simulations [e.g. Perna & Lazzati, 2002] indicate that this will only apply out to a few tens of parsecs. GRB 061007 had the brightest optical afterglow detected by UVOT, and one of the brightest afterglows detected by the XRT. Nevertheless, a dust and gas system was still detected within the GRB host galaxy, and it had an absorbing column density $N_H = (5.30^{+0.33}_{-0.32}) \times 10^{20}$ cm^{-2}, and an extinction of $A_V = 0.66 \pm 0.02$ mag. This, therefore, suggests that for the majority of GRBs, an absorption system local to the GRB will survive the intense radiation emitted at early times, and that GRBs embedded deep enough in their stellar nursery environments will not be able to destroy enough dust to allow the optical and UV afterglow to escape.

A further indication that selection effects are present and that the conditions in host galaxies of GRBs with optical afterglow detections differ from the hosts of dark GRBs is in the gas-to-dust ratio observed in the sample of GRBs analysed in chapter 4. Although the distribution in the gas-to-dust ratio was found to be consistent within errors with that of the Milky Way and the Magellanic Clouds, there was a systematic offset towards larger gas-to-dust ratios with a 4σ significance. The implication of this is that the amount of absorbing dust in the vicinity of the GRB is less than that of other environments relative to the abundance of neutral gas. It is not clear why GRBs should have a preference for such environments, and these observations are more easily understood when selection effects are considered. UV, optical and NIR observations are required to determine the value of A_V in the local environment of the GRB, but circumburst environments with very large A_V values are more likely to block out the UV to NIR afterglow. The low end of the $N_{H,X}/A_V$ ratio distribution at the circumburst environment of GRBs will, therefore, be under-represented, due to the selection bias against those GRBs with large A_V.

As already discussed in chapter 4, the effect of the GRB radiation on both the dust column density and the metal column density make it unlikely for differences in the $N_{H,X}/A_V$ ratio to be the result of the GRB itself. Variations in the $N_{H,X}/A_V$ ratio could, instead, be the result of the grain size distribution and the amount of dust destruction that has taken place in the environment prior to the GRB explosion. The efficiency with which dust is destroyed in an environment will depend on the rate of supernova explosions in the environment [e.g Lisenfeld & Ferrara, 1998, Hirashita et al., 2002], which destroy small dust grains that are primarily responsible for the absorption of the dust and optical photons. A decrease in the column of small dust grains may also be present in very dense environments, where dust may coagulate and thus skew the dust distribution to larger grains.

The ongoing uncertainty in the selection effects present are interlinked with the precise conditions required for a galaxy to host a GRB, and a more complete sample of long GRB host galaxy identifications is required. The ability to acquire this sample is now stronger than ever, with $\sim 95\%$ of GRBs observed by XRT localised to within 5". A dedicated campaign to obtain deep observations in the submillimetre at these arcsecond positions would provide significantly improved constraints on the types of galaxies that host long GRBs, such as is currently being carried out by Jakobsson et al. [2006b]. This would also greatly improve our understanding of the origin of dark GRBs, and, subsequently, provide a much more accurate representation of the luminosity function of GRBs.

6.4 UVOT Dark GRBs

The promptness with which X-ray and optical/UV data are available with *Swift* has increased the number of GRB afterglow detections. Many would previously have been missed as a result of their dim afterglow (e.g. XRF 050406). However, *Swift* observations have shown that optical flashes on the order of GRB 990123 [Akerlof et al., 1999] are rare, and that a large fraction of GRBs observed by UVOT ($\sim 70\%$) have no optical or UV afterglow down to 3σ upper limits of $V \gtrsim 19.5$ mag within the first few hundred

seconds after the prompt emission. This is despite $\sim 86\%$ of UVOT observations being made within the first hour and $\sim 76\%$ within the first 5 minutes. In stark contrast to this, $\sim 98\%$ of *Swift* GRBs have had an X-ray counterpart detected by the XRT. The promptness of the observations provides stringent constraints on any model that accounts for the lack of a UV/optical counterpart through rapid decay and/or the outburst having been weak. Similarly, the current mean redshift of the *Swift* sample of $\langle z \rangle = 2.8$ [Jakobsson et al., 2006d] rules out high redshifts as the sole reason for their 'darkness'. These factors together with the information provided in chapter 4 on the local environment of GRBs can help identify the primary causes for the lack of an optical afterglow in the large fraction of GRBs observed by *Swift*.

6.4.1 Rapid Decaying Afterglow

It is now clear that a rapid decay of the UV and optical afterglow cannot account for the bulk of the GRBs not detected by UVOT, which would require the afterglow to decay below the background level within a few hundred seconds. Such a scenario is unsubstantiated by X-ray and NIR observations, which show no evidence for a systematically faster decay rate in those GRBs that are not detected by UVOT. Around 95 % of GRBs observed in under 5 mins by the XRT have X-ray afterglow detections, and in the case where the optical afterglow is detected, the optical decay rate is comparable to, or shallower than that in the X-ray band [e.g. GRB 050802; Oates et al., 2007b]. A steep UV/optical decay is, therefore, unlikely. Moreover, from a comparison of ~ 25 UVOT GRBs with UV and/or optical afterglow detections, there is evidence to suggest that the faster decaying afterglows are the brightest at early times, which should make them easier to detect at early times [Oates et al., 2007b].

6.4.2 High-z origin

At redshifts $z \gtrsim 5$ the Lyman-edge is redshifted to wavelengths greater than the UVOT bandpass, causing any GRBs at such redshifts to appear dark to UVOT. The detection

of three GRBs at redshifts $z > 5$ [GRB 050814; Jakobsson et al., 2006c, GRB 050904; Kawai et al. 2005, GRB 060522; Cenko et al. 2006] is clear evidence that GRBs do occur at high redshifts, and therefore a fraction of the population should not be detected by UVOT for this reason.

Of the current 66% of *Swift* GRBs which are dark to UVOT (up to GRB070517), only 23% have a spectroscopically measured redshift. This is illustrated in Fig. 6.1, which shows that the majority of *Swift* GRBs with redshifts were detected by UVOT. For the remaining 77% it is, therefore, not possible to directly determine whether the lack of an UV/optical afterglow is the result of neutral hydrogen absorption in the interstellar medium. 4% of *Swift* GRBs with spectroscopically measured redshifts are at redshifts $z > 5$, and 6% are at redshifts $z > 4$. However, the need for an optical/NIR detection of the GRB afterglow or host galaxy to determine the GRB redshift introduces a selection bias, where it is harder to acquire spectra for those GRBs at higher redshift.

Based on evolutionary models of GRB progenitors, estimates of the GRB redshift distribution have been made. Using a model in which GRBs trace the SFR, and one in which GRBs are tracers of the average metallicity in the Universe, Natarajan et al. [2005] determined the fraction of GRBs at redshifts $z > 4$ to be $\sim 25\%$ and $\sim 40\%$ for these two models, respectively. In a model where the progenitor star is limited to metallicities $Z < 0.004Z_\odot$, Yoon et al. [2006] estimated a faction of 50 % of GRBs to be at $z > 4$, and 20 % to lie at $z > 6$, and Salvaterra et al. [2007] estimated between 10% and 30% of *Swift* GRBs to lie at redshifts $z > 5$, depending on the adopted metallicity threshold for GRB formation.

Although a certain fraction of those GRBs not detected by UVOT are likely to be the result of being at high redshift, a high-z origin for the complete population of UVOT dark GRBs is incompatible with predictions. Furthermore, there is a now a large population of GRBs with no afterglow detected by UVOT but with spectroscopically measured redshifts at $z \ll 5$ (e.g. GRB 050724; Prochaska et al., 2005, and GRB 051227; Foley et al., 2005b), and there is also no evidence of time dilation in the γ-ray light curves of dark GRBs, which would be expected if all those bursts that were dark were at high redshift.
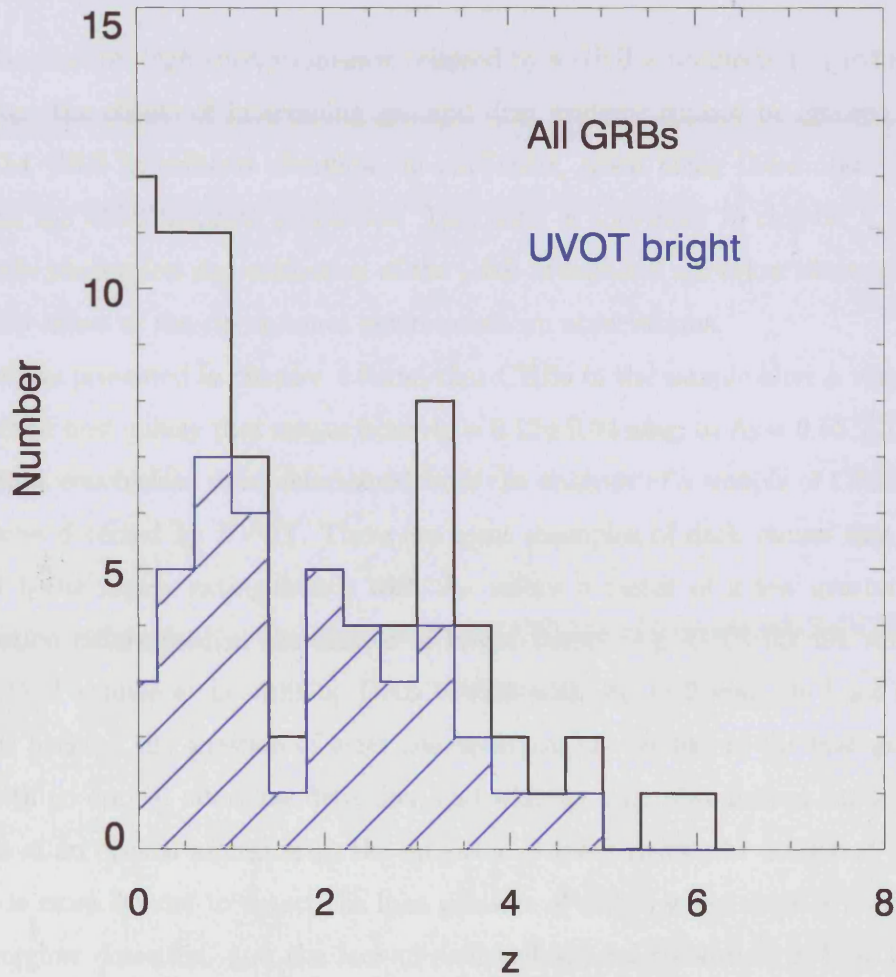
Figure 6.1: *Swift* GRB redshift distribution for a sample of 75 GRBs. The black histogram represents the redshift distribution for 75 *Swift* GRBs with a spectroscopic redshift, and the blue histogram represents the redshift distribution for a subset of 43 *Swift* GRBs with an afterglow detected by UVOT.

High-z bursts can therefore not be the sole reason for the large fraction of the GRB population that have no associated optical counterpart.

6.4.3   Dust Obscuration

Although the prompt, high-energy emission released by a GRB is unaffected by extinction or absorption, the effects of intervening gas and dust systems cannot be ignored when analysing the GRB broadband afterglow, in particular, when using these observations to determine the GRB intrinsic properties. This issue is addressed in chapter 4, where analysis of the absorption and extinction of the GRB broadband afterglow illustrates the non-negligible effect of the circumburst environment on observations.

The analysis presented in chapter 4 found that GRBs in the sample have a visual extinction in their host galaxy that ranges from $A_V = 0.12 \pm 0.04$ mag, to $A_V = 0.65^{+0.08}_{-0.07}$ mag. However, these conclusions were determined from the analysis of a sample of GRBs that had afterglows detected by UVOT. There are some examples of dark bursts that show evidence of being highly extinguished, with A_V values a factor of a few greater than the distribution determined in the sample of bright bursts (e.g. GRB 050401 with $A_V \approx 3$ mag; [De Pasquale et al., 2006b], GRB 030528 with $A_V \approx 2$ mag [de Luca et al., 2005]). This beckons the question of what the environments are like in the host galaxies of GRBs with no optical afterglow detection, and whether dust obscuration can account for the lack of an optical afterglow in the majority of these cases. As described in section 6.3, it is much harder to detect the host galaxies of GRBs when there is no optical or NIR afterglow detection, and the lack of sufficient spatial resolution in host galaxy observations may also not identify localised areas of high dust density in the vicinity of the GRB. Alternate methods of probing the extinction in the local environments of GRBs are, therefore, needed.

Of those GRBs detected by UVOT, the mean V-band magnitude during the first few hundred seconds is $\langle V \rangle = 17.7$ mag. For a typical host galaxy rest frame extinction of $A_V \sim 0.4$, which is the mean extinction for the sample of seven GRBs presented in

chapter 4, the mean unabsorbed V-band magnitude would be $\langle V \rangle = 17.3$ mag. Assuming this to be a typical V-band magnitude at early times, there would only have to be 3–4 magnitudes of extinction at the host galaxy for the GRB afterglow to not be detected by UVOT, which is easily satisfied if the GRB resides in an active star-forming region (e.g. the internal extinction in lines of sight to the ULIG Arp 220 is > 30 mag [Genzel et al., 1998, Scoville et al., 1998, Shioya et al., 2001]).

For a more detailed analysis on the role of dust in the environment of GRBs not detected by UVOT, it is necessary to determine the amount of visual extinction that there is at the GRB host galaxy. Due to the lack of optical data for dark GRBs, spectral modelling cannot be applied to determine the amount of visual extinction in the local environment of these GRBs. However, the relation between the metallicity of an environment and the dust column density should make it possible to use the amount of host galaxy X-ray absorption as an indicator of the amount of visual extinction undergone in the GRB local environment. By assuming the relation between $N_{H,X}$ and A_V at the GRB host galaxy to be linear, as is the case within the Magellanic Cloud and the Milky Way, the X-ray column density measured at the GRB host galaxy, $N_{H,X}$, can be used to trace the amount of host galaxy dust-extinction affecting the GRB UV and optical afterglow. All parameters of interest must be in the rest frame and this analysis can, therefore, only be applied to GRBs with a measured redshift.

There are fifteen *Swift* GRBs, up until GRB 070521, that were observed but were not detected by UVOT within 1 hour of the BAT trigger, and with spectroscopically measured redshifts $z < 5$. At higher redshifts than this a GRB would always appear dark to UVOT due to the shift of the Lyman break below the UVOT energy band. A total of 42 *Swift* GRBs makes up the sample of bright GRBs, which includes all GRBs up until GRB 070521 that have a UV/optical afterglow detected by UVOT and a corresponding spectroscopic redshift. All data were taken from epochs where no spectral evolution is observed, and were reduced in the same way as described in section 4.3.2. The intrinsic column density was then determined from a single power law fit with two absorbers; one at $z = 0$ with the column density fixed at the Galactic value, and a second one at the

redshift of the burst with the column density and X-ray spectral slope, β_X, left as free parameters. The resulting distribution in $N_{H,X}$ within the two populations of bursts is shown in Fig. 6.2, where the solid histogram corresponds to the dark bursts, and the UVOT bright bursts are represented by the dashed histogram. Fourteen bright GRBs had negligible absorption at the host galaxy, represented in the smallest bin of $N_{H,X}$. The mean logarithm of the X-ray column density in cm^{-2} over and above the Galactic column is < 20.8 and 21.9 ± 0.1 for the bright and dark population of GRBs, respectively, and a KS test finds that the two datasets differ with 99.99% confidence. Although this does suggest that dark GRBs reside in denser environments, the smaller mean column density in the host galaxy of the bright sample of GRBs is primarily due to the fourteen GRBs that have negligible X-ray absorption at the host galaxy. In this case, a more representative average of the logarithm of the column density is the median, which for the bright and dark population of GRBs is 21.5 and 22.1, respectively. When measured in this way, the host galaxy X-ray absorption measured in UVOT dark GRBs is still a factor of 4 larger than the host galaxy X-ray absorption measured in bright GRBs, suggesting that dark GRBs reside in denser environments.

To have a better handle on the amount of dust present in the local environment of those GRBs not detected by UVOT, I assume GRB host galaxies to have an $N_{H,X}$ and A_V relation similar to that observed in the SMC (Eq. 4.2), and determine A_V from the column density, $N_{H,X}$, measured from the GRB X-ray spectra. This provides an estimated mean visual extinction of $\langle A_V(\text{dark}) \rangle = 7.4$ mags for the dark population of bursts shown in Fig. 6.2. The most absorbed GRB in the sample of dark GRBs was GRB 061222B, which had a rest frame column density $N_{H,X} = (4.1^{+1.1}_{-0.9}) \times 10^{22}$ cm^{-2} and, therefore, an estimated rest frame visual extinction of $A_V \approx 20.7$ mags. However, GRB 061222B had an R-band detection of R $\sim 17.7 \pm 0.5$ at around 8 minutes after the prompt emission, making the inferred extinction unrealistic. This suggests that the $N_{H,X}/A_V$ ratio of 2×10^{21} cm^{-2} is likely too small for the most absorbed GRBs.

Instead, A_V is estimated using the mean value of $N_{H,X}/A_V$ acquired from the SMC

model spectral fits described in chapter 4, which corresponds to:

$$\langle\frac{N_{H,X}}{A_V}\rangle = 6.7 \times 10^{21} \text{ cm}^{-2}. \tag{6.1}$$

Using this relation the visual extinction local to the UVOT dark GRBs is estimated to be in the range $0.1 < A_V < 6.2$, with a mean of $\langle A_V \rangle = 2.2$ mags and median $\langle A_V \rangle = 1.9$ mags. In the case of the bright GRBs, the mean and median A_V values are 0.7 mags and 0.4 mags, respectively, with a range in A_V from 0 to 4.3 mags. Therefore, although the mean and median extinction in bright GRBs is smaller than in dark GRBs by a factor of a few, there is still a lot of overlap, as would be expected from the distribution in $N_{H,X}$ between the two populations of GRBs.

It is possible that $N_{H,X}$ does not scale linearly with A_V, as already discussed in section 6.3, and that those GRBs not detected by UVOT have smaller $N_{H,X}/A_V$ ratios than the average $N_{H,X}/A_V$ ratio of those GRBs with a detected optical afterglow. However, the luminosity, redshift and viewing angle to the GRB will also certainly affect the observed optical flux, and are, therefore, factors that also need to be considered when determining the origin of dark GRBs. The additional factors could account for the overlap in the host galaxy extinction in GRBs with and without UVOT detected afterglows. However, the fact that those GRBs with negligible host galaxy absorption were all detected by UVOT strongly indicates that dust obscuration is a prime cause for the lack of afterglow detections by UVOT.

6.5 Future

The rapid arcsecond localisations and multi-wavelength capabilities of *Swift* have meant a great enhancement in our understanding of Gamma-Ray Bursts, and in this thesis I have made use of the early-time data (first few hours of the GRB) from all three instruments on-board *Swift* to investigate how the properties of the fireball model, the GRB local environment, and the line of sight to the GRB may affect our observations of both the prompt and afterglow emission. The early-time, panchromatic observations available
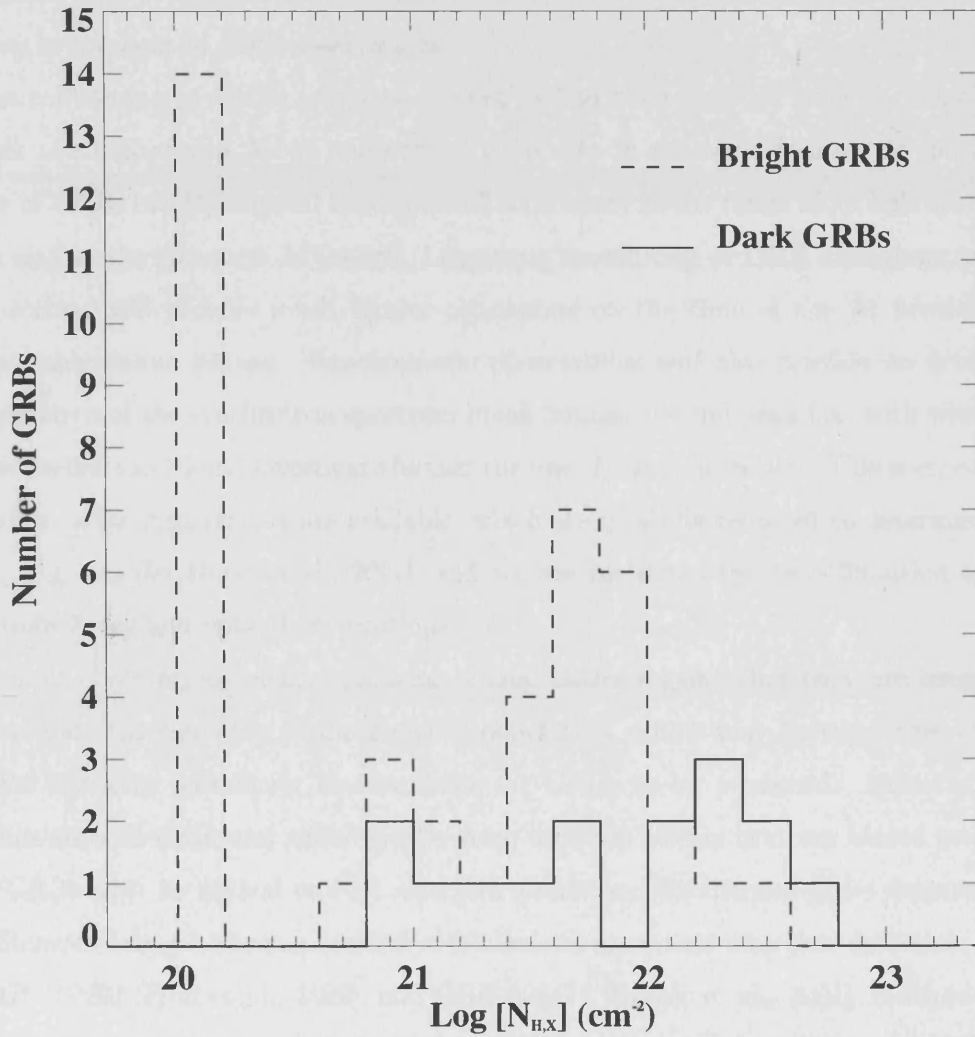
Figure 6.2: Distribution of the X-ray column density at the redshift of the GRB for a sample of GRBs with (dashed), and without (solid) a UVOT detected afterglow, where all GRBs have a spectroscopically measured redshift. The smallest $N_{H,X}$ bin represents those GRBs with no measurable X-ray column density above the Galactic absorption.

with *Swift* have allowed the GRB internal engine and the surrounding environment to be modelled with much greater accuracy than ever before. However, in this chapter I have highlighted some of the more critical areas of GRB research that have become much more complex in the light of *Swift* observations.

The collimation of GRBs is not as evident as had been believed prior to *Swift*, and the lack of simultaneous X-ray and optical jet breaks in the large fraction of the *Swift* sample of GRBs has highlighted the degree of uncertainty in the range of jet half opening-angles and in the structure of the jet. Long term monitoring of GRB afterglows across the spectrum will provide much tighter constraints on the time of the jet breaks and on their achromatic nature. Panchromatic observations will also provide an accurate determination of the synchrotron spectrum break frequencies and peak flux with which to test the fireball model and investigate further the role of energy injection. This is especially true when radio observations are available, which are typically required to determine ν_m and ν_a [e.g. van der Horst et al., 2007], and are less restricted by the collimation of the GRB than X-ray and optical observations.

Current observations of host galaxies of long GRBs suggest that they are irregular, sub-luminous galaxies with a young stellar population, which may be suggestive of the need for sub-solar metallicity environments for GRBs to be produced. However, the statistics are still small and suffer greatly from selection affects that are biased towards those GRBs with an optical or NIR afterglow detection. Furthermore, the detection of submillimetre-bright hosts in a handful of GRBs with an optical afterglow detection, such as GRB 010222 [Frail et al., 2002], and GRB 000418 [Berger et al., 2001], indicate that GRB host galaxies are not solely UV-bright. Due to dust obscuration in submillimetre galaxies, GRBs with no NIR and optical afterglow detection would be the most favourable candidates to have such hosts. However, submillimetre observations indicate that this is not the case [e.g Barnard et al., 2003], at least not in the majority of cases. The lack of a full sample of GRB host galaxy observations, therefore, limits our understanding of the principle properties of GRB host galaxies, which would also provide important insight into the differences between GRBs with and without optical and NIR afterglow detections. In

order to address the topic of dark GRBs, a complete sample of GRB redshifts and host galaxy properties is required, which will provide an accurate measure of the fraction of GRBs that are absorbed in the UV up to the NIR by neutral hydrogen or by dust.

The determination of GRB redshifts is limited by the detection of the optical/NIR afterglow or host galaxy. IR observations into the far IR could significantly improve the current redshift determination rate by finding the photometric redshift, and XRT observations, which provide arcsecond positional accuracy to within 5" for ~ 95% of GRBs observed, could lead to the detection of the host galaxy in deep observations for many GRBs. Even if these observations do not provide a host galaxy detection, a complete sample of multi-wavelength and deep upper limits of the GRB field will provide the constraints required to determine whether dark GRB host galaxies are submillimetre dusty galaxies.

Potential future missions such as EDGE [Piro et al., 2007] and the Pharos GRB afterglow mission[1] will have a significant impact on determining both the GRB redshift distribution and properties of the surrounding circumburst environment. Both will have a very high X-ray spectral resolution of around 3 eV at < 2 keV, and will, thus, be able to make direct measurements of the X-ray metal edges in the GRB X-ray afterglow spectra from which spectroscopic redshift measurements can be made. These spectra will also allow the determination of metal abundances, depletion patterns, velocity structures of the surrounding medium, and thus the metallicity and column densities in the local environment of the GRB, and the distance of absorbing material from the source.

Swift has defined a new era in GRB research, and the rapid, arcsecond localisations and prompt, multi-wavelength observations have significantly opened up the field of GRBs, and are bringing to light the level of complexity of this phenomenon. In many cases *Swift* data have provided the first opportunity to test theoretical models, such as the properties of the afterglow at early times, and unexpected observations, such as the X-ray plateau phase and flaring activity, have presented challenges to the current theory.

Swift is, therefore, providing the early time panchromatic data needed to progress in

---

[1]http://hea-www.harvard.edu/~elvis/Pharos_GSFC_Aug06.pdf

our understanding of GRBs. Further analysis is yet required before these data are fully understood, and a combined dataset built from *Swift* observations as well as ground based observations and future missions, such as EDGE and Pharos, promises to continue the advances being made towards understanding GRBs.

Acknowledgements

I would like to thank many people both in and out of work and from the UK and abroad for their help, support and patience during my thesis.

First of all I would like to thank my supervisor, Keith Mason, for having given me the opportunity to do this PhD, and for his continual support and advice, despite his growing commitment with PPARC. I would also like to thank him for recommending that I go to the *Swift* Missions Operation Centre in Penn State in my second year, where I experienced genuine excitement towards GRB science for the first time and where my thesis began.

I would also like to thank Mat Page for his continuous patience and time, for his ability to read through my papers ten times over, for coming into work on a weekend on the day before Oscar was born, for his insight, and rigorous comments and questions, without which I would not have gained the same depth and understanding during this thesis.

I also thank Pete Roming for his complete support during my time in Penn State, for his positive attitude, and for the opportunities that he gave me, not only by inviting me to stay at Penn State University for a year, but also for including me in all areas of GRB science going on at that time.

I must also thank my contemporaries and peers who put up with complaints, frustrations and frequent questions. Thanks to my friends and family, who saw increasingly less of me towards the end but who remained patient, and a thank you to Tom, for putting up with my last few months of grumpiness, and without whom working weekends would have been doubly depressing.

I would also like to gratefully acknowledge the contribution and help of all members of the *Swift* team and the support of a PPARC Studentship.

Appendix A

UVOT AT sequences

Table A.1: AT sequence release10, release11, release11_1

T+	Exposure	Filter	Image	Event	Binning
	100 s	V FC	8 × 8	17 × 17	
For 981 s	10 s	*UVW2*		17 × 17	
	10 s	*V*		12 × 12	
	10 s	*UVM2*		17 × 17	
	10 s	*UVW1*		17 × 17	
	10 s	*U*		12 × 12	
	10 s	*B*		12 × 12	
For 4096 s	100 s	*UVW2*	17 × 17		
	100 s	*V*	12 × 12		
	100 s	*UVM2*	17 × 17		
	100 s	*UVW1*	17 × 17		
	100 s	*U*	12 × 12		
	100 s	*B*	12 × 12		
up to 10*365*86400 s	900 s	*UVW2*		12 × 12	
	900 s	*V*	12 × 12		2 × 2
	900 s	*UVM2*		12 × 12	
	900 s	*UVW1*		12 × 12	
	900 s	*U*	12 × 12		2 × 2
	900 s	*B*	12 × 12		2 × 2

Table A.2: AT sequence release11_2

T+	Exposure	Filter	Image	Event	Binning
	200 s	V FC	8 × 8	17 × 17	
For 981 s	50 s	*UVW*2		17 × 17	
	50 s	*V*		12 × 12	
	50 s	*UVM*2		17 × 17	
	50 s	*UVW*1		17 × 17	
	50 s	*U*		12 × 12	
	50 s	*B*		12 × 12	
	50 s	white		12 × 12	
For 4096 s	100 s	*UVW*2	17 × 17		
	100 s	*V*	12 × 12		
	100 s	*UVM*2	17 × 17		
	100 s	*UVW*1	17 × 17		
	100 s	*U*	12 × 12		
	100 s	*B*	12 × 12		
up to 10*365*86400 s	900 s	*UVW*2		12 × 12	
	900 s	*V*	12 × 12		2 × 2
	900 s	*UVM*2		12 × 12	
	900 s	*UVW*1		12 × 12	
	900 s	*U*	12 × 12		2 × 2
	900 s	*B*	12 × 12		2 × 2

Table A.3: AT sequence release12

T+	Exposure	Filter	Image	Event	Binning
	200 s	V FC	8 × 8	17 × 17	
	200 s	B FC	8 × 8	17 × 17	
For 820 s	20 s	*UVW2*		17 × 17	
	20 s	*V*		12 × 12	
	20 s	*UVM2*		17 × 17	
	20 s	*UVW1*		17 × 17	
	20 s	*U*		12 × 12	
	20 s	*B*		12 × 12	
	20 s	white		12 × 12	
For 1200 s	200 s	V FC	8 × 8	17 × 17	
	200 s	B FC	8 × 8	17 × 17	
For 5400 s	20 s	*UVW2*	17 × 17		
	20 s	*V*	12 × 12		
	20 s	*UVM2*	17 × 17		
	20 s	*UVW1*	17 × 17		
	20 s	*U*	12 × 12		
	20 s	*B*	12 × 12		
	20 s	white	12 × 12		
For 11000 s	200 s	*UVW2*	17 × 17		
	200 s	*V*	12 × 12		
	200 s	*UVM2*	17 × 17		
	200 s	*UVW1*	17 × 17		
	200 s	*U*	12 × 12		
	200 s	*B*	12 × 12		
	200 s	white	12 × 12		
up to 10*365*86400 s	4 × 225 s	*UVW2*	17 × 17		
	4 × 225 s	*V*	12 × 12		2 × 2
	4 × 225 s	*UVM2*	17 × 12		
	4 × 225 s	*UVW1*	17 × 17		
	4 × 225 s	*U*	12 × 12		2 × 2
	4 × 225 s	*B*	12 × 12		2 × 2
	4 × 225 s	white	12 × 12		2 × 2

Table A.4: AT sequence release12_1

T+	Exposure	Filter	Image	Event	Binning
	200 s	V FC	8 × 8	17 × 17	
For 981 s	50 s	$UVW2$		17 × 17	
	50 s	V		12 × 12	
	50 s	$UVM2$		17 × 17	
	50 s	$UVW1$		17 × 17	
	50 s	U		12 × 12	
	50 s	B		12 × 12	
	50 s	white		12 × 12	
For 4096 s	100 s	$UVW2$	17 × 17		
	100 s	V	12 × 12		
	100 s	$UVM2$	17 × 17		
	100 s	$UVW1$	17 × 17		
	100 s	U	12 × 12		
	100 s	B	12 × 12		
up to 10*365*86400 s	900 s	$UVW2$		12 × 12	
	900 s	V	12 × 12		2 × 2
	900 s	$UVM2$		12 × 12	
	900 s	$UVW1$		12 × 12	
	900 s	U	12 × 12		2 × 2
	900 s	B	12 × 12		2 × 2

Table A.5: AT sequence release12_2, release12_3

T+	Exposure	Filter	Image	Event	Binning
	100 s	white FC	8 × 8	8 × 8	
	400 s	V FC	8 × 8	8 × 8	
For 850 s	20 s	$UVW2$		12 × 12	
	20 s	V		8 × 8	
	20 s	$UVM2$		12 × 12	
	20 s	$UVW1$		12 × 12	
	20 s	U		8 × 8	
	20 s	B		8 × 8	
	20 s	white		8 × 8	
	100 s	white FC	8 × 8		
	400 s	V FC	8 × 8	8 × 8	
For 2700 s	20 s	$UVW2$		12 × 12	
	20 s	V		8 × 8	
	20 s	$UVM2$		12 × 12	
	20 s	$UVW1$		12 × 12	
	20 s	U		8 × 8	
	10 s	B		8 × 8	
	10 s	white		12 × 12	
For 8400 s	200 s	$UVW2$	12 × 12		2 × 2
	200 s	V	8 × 8		2 × 2
	200 s	$UVM2$	12 × 12		2 × 2
	200 s	$UVW1$	12 × 12		2 × 2
	200 s	U	8 × 8		2 × 2
	200 s	B	8 × 8		2 × 2
up to 10*365*86400 s	900 s	$UVW2$	12 × 12		2 × 2
	3 × 300 s	V	12 × 12		2 × 2
	900 s	$UVM2$	12 × 12		2 × 2
	900 s	$UVW1$	12 × 12		2 × 2
	3 × 300 s	U	12 × 12		2 × 2
	3 × 300 s	B	12 × 12		2 × 2
	3 × 300 s	white	12 × 12		2 × 2

Bibliography

Akerlof, C., et al. 1999, Nature, 398, 400

Amati, L., Capalbi, M., Frontera, F., Gandolfi, G., Piro, L., in't Zand, J. J. M., Granata, S., & Reali, F. 2002a, GCN, 1386

Amati, L., et al. 2002b, A&A, 390, 81

Amati, L. 2006, *Mon. Not. R. astr. Soc.*, 372, 233

Arnaud, K. A. 1996, ASP Conf. Ser. 101: Astronomical Data Analysis Software and Systems V, 101, 17

Band, D., et al. 1993, *Astrophys. J.*, 413, 281

Barnard, V. E., et al. 2003, *Mon. Not. R. astr. Soc.*, 338, 1

Barraud, C., Daigne, F., Mochkovitch, R., & Atteia, J. L. 2005, A&A, 440, 809

Barthelmy, S. D., et al. 2005a, Space Sci. Rev., 120, 143

Barthelmy, S. D., et al. 2005b, *Astrophys. J.*, 635, L133

Berger, E., Kulkarni, S. R., & Frail, D. A. 2001, *Astrophys. J.*, 560, 652

Berger, E., Kulkarni, S. R., & Frail, D. A. 2003, *Astrophys. J.*, 590, 379

Berger, E., & Mulchaey, J. 2005, GCN, 3122

Berger, E., et al. 2005a, *Astrophys. J.*, 634, 501

Berger, E., Oemler, G., & Gladders, M. 2005b, GCN, 3185

Berger, E., et al. 2005c, Nature, 438, 988

Bersier, D., et al. 2006, GCN, 5709

Blake, C. H., et al. 2005, Nature, 435, 181

Blandford, R. D., & McKee, C. F. 1976, Bulletin of the American Astronomical Society, 8, 539

Bloom, J. S., Frail, D. A., & Sari, R. 2001, AJ, 121, 2879

Bloom, J. S., Kulkarni, S. R., & Djorgovski, S. G. 2002, Aj, 123, 1111

Bloom, J. S., Frail, D. A., & Kulkarni, S. R. 2003, *Astrophys. J.*, 594, 674

Bloom, J. S., et al. 2006a, GCN, 5217

Bloom, J. S., et al. 2007, *Astrophys. J.*, 654, 878

Blustin, A. J., et al. 2006, *Astrophys. J.*, 637, 901

Boër, M., Atteia, J. L., Damerdji, Y., Gendre, B., Klotz, A., & Stratta, G. 2006, ApJ, 638, L71

Burrows, D. N., et al. 2005a, Space Sci. Rev., 120, 165

Burrows, D. N., et al. 2005b, Science, 309, 1833

Burrows, D. N., & Racusin, J. 2007, "Swift and GRBs: Unveiling the Relativistic Universe" meeting,Venice, June 5-9 2006 (astro-ph/0702633)

Butler, N. R., et al. 2006, *Astrophys. J.*, 652, 1390

Butler, N. R., & Kocevski, D. 2007, *Astrophys. J.*, 663, 407

Campana, S., Mangano, V., Chincarini, G., Tagliaferri, G., Burrows, D. N., Cominsky, L., & Norris, J. 2005, GCN, 3872

Campana, S., et al. 2006a, Nature, 442, 1008

Campana, S., et al. 2006b, A&A, 449, 61

Campana, S., et al. 2007, *Astrophys. J.*, 654, L17

Capalbi, M., et al. 2005, GCN, 3184

Cardelli, J. A., Clayton, G. C., & Mathis, J. S. 1989, *Astrophys. J.*, 345, 245

Cash, W. 1979, *Astrophys. J.*, 228, 939

Cenko, S. B., Berger, E., Djorgovski, S. G., Mahabal, A. A., & Fox, D. B. 2006, GCN, 5155

Christensen, L., Hjorth, J., & Gorosabel, J. 2004, A&A, 425, 913

Chevalier, R. A., & Li, Z.-Y. 2000, *Astrophys. J.*, 536, 195

Costa, E., et al. 1997, Nature, 387, 783

Covino, S., et al. 2006, A&A, 447, L5

Curran, P. A., et al. 2007, *Mon. Not. R. astr. Soc.*, L90

D'Alessio, V., Piro, L., & Rossi, E. M. 2006, A&A, 460, 653

Dai, Z. G., & Lu, T. 1998, *Mon. Not. R. astr. Soc.*, 298, 87

Dai, Z. G., & Lu, T. 1999, *Astrophys. J.*, 519, L155

Dai, X., et al. 2007, *Astrophys. J.*, 658, 509

de Luca, A., et al. 2005, A&A, 440, 85

De Pasquale, M., et al. 2003, *Astrophys. J.*, 592, 1018

De Pasquale, M., & Cummings, J. 2006a, GCN, 5130

De Pasquale, M., al. 2006b, *Mon. Not. R. astr. Soc.*, 365, 1031

Dermer, C. D., Chiang, J., Böttcher, M. 1999, *Astrophys. J.*, 513, 656

Dermer, C. D. 2004, *Astrophys. J.*, 614, 284

Dickey, J. M., & Lockman, F. J. 1990, ARA&A, 28, 215

Donaghy, T. Q. 2006, *Astrophys. J.*, 645, 436

Draine, B. T. 2003, Annual Rev. of A&A, 41, 241

Draine, B. T., & Lee, H. M. 1984, *Astrophys. J.*, 285, 89

Dupree, A. K.., et al., 2006, GCN, 4969

Eichler, D., Livio, M., Piran, T., & Schramm, D. N. 1989, Nature, 340, 126

Falcone, A. D., et al. 2006a, *Astrophys. J.*, 641, 1010

Falcone, A. D., et al. 2006b, GCN, 5009

Fireman, E. L. 1974, *Astrophys. J.*, 187, 57

Fitzpatrick, E. L. 1985, *Astrophys. J.*, 299, 219

Foley, R. J., Chen, H.-W., Bloom, J., & Prochaska, J. X. 2005a, GCN, 3483

Foley, R. J., Bloom, J. S., Prochaska, J. X., Illingworth, G. D., Holden, B. P., Magee, D., Challis, P., & Garg, A. 2005b, GCN, 4409

Fox, D. B., et al. 2005, Nature, 437, 845

Frail, D. A., Kulkarni, S. R., Nicastro, S.R̃., Feroci, M., & Taylor, G. B. 1997, Nature, 389, 261

Frail, D. A., et al. 1999, *Astrophys. J.*, 525, L81

Frail, D. A., et al. 2001, *Astrophys. J.*, 562, L55

Frail, D. A., et al. 2002, *Astrophys. J.*, 565, 829

Freedman, D. L., & Waxman, E. 2001, *Astrophys. J.*, 547, 922

Fruchter, A., Krolik, J. H., & Rhoads, J. E. 2001, *Astrophys. J.*, 563, 597

Fruchter, A. S., et al. 2006, Nature, 441, 463

Fryer, C. L., & Mészáros, P. 2003, *Astrophys. J.*, 588, L25

Fryer, C. L. 1999, *Astrophys. J.*, 522, 413

Fynbo, J. P. U., et al. 2004, *Astrophys. J.*, 609, 962

Fynbo, J. P. U., et al. 2005a, GCN, 3874

Fynbo, J. P. U., et al. 2005b, GCN, 3749

Galama, T., et al. 1997, Nature, 387, 479

Galama, T. J., & Wijers, R. A. M. J. 2001, *Astrophys. J.*, 549, L209

Gehrels, N. 1986, *Astrophys. J.*, 303, 336

Gehrels, N., et al. 2004, *Astrophys. J.*, 611, 1005

Gehrels, N., et al. 2005, Nature, 437, 851

Gehrels, N., et al. 2006, Nautre, 444, 1044

Gendre, B., Galli, & Piro, L. 2007, A&A, 465, L13

Genzel, R., et al. 1998, *Astrophys. J.*, 498, 579

Ghirlanda, G., Ghisellini, G., & Lazzati, D. 2004, *Astrophys. J.*, 616, 331

Golenetskii, S., Aptekar, R., Mazets, E., Pal'Shin, V., Frederiks, D., & Cline, T. 2006, GCN, 5722

Gorosabel, J., et al. 2006, A&A, 450, 87

Granot, J., Panaitescu, A., Kumar, P., & Woosley, S. E. 2002, *Astrophys. J.*, 570, L61

Granot, J. 2005, *Astrophys. J.*, 631, 1022

Granot, J. 2007, Revista Mexicana de Astronomia y Astrofisica Conference Series, 27, 140

Granot, J., & Kumar, P. 2006, *Mon. Not. R. astr. Soc.*, 366, L13

Groot, P. J., et al. 1998a, *Astrophys. J.*, 493, L27

Groot, P. J., et al. 1998b, *Astrophys. J.*, 502, L123

Halpern, J. P., & Mirabal, N. 2005, GCN, 3907

Heger, A., Fryer, C. L., Woosley, S. E., Langer, N., & Hartmann, D. H. 2003, *Astrophys. J.*, 591, 288

Heise, J. 2003, AIP Conf. Proc. 662: Gamma-Ray Burst and Afterglow Astronomy 2001: A Workshop Celebrating the First Year of the HETE Mission, 662, 229

Heise, J., in't Zand, J., Kippen, R. M., & Woods, P. M. 2001, Gamma-ray Bursts in the Afterglow Era, 16

Hill, J. E., et al. 2004, Proceedings of the SPIE, 5165, 217

Hirashita, H., Tajiri, Y. Y., & Kamaya, H. 2002, A&A, 388, 439

Hirschi, R., Meynet, G., & Maeder, A. 2005, A&A, 443, 581

Hjorth, J., et al. 2003, Nature, 423, 847

Hjorth, J., et al. 2005, Nature, 437, 859

van der Horst, A J., & Rol. E. 2006, GCN, 5720

van der Horst, A. J., et al. 2007, submitted to A&A,(astro-ph/0706.1321)

Huang, Y. F., Wu, X. F., Dai, Z. G., Ma, H. T., & Lu, T. 2004, *Astrophys. J.*, 605, 300

Huang, Y. F., Cheng, K. S., & Gao, T. T. 2006, *Astrophys. J.*, 637, 873

Jakobsson, P., Fynbo, J. P. U., Tanvir, N., & Rol, E. 2006a, GCN, 5716

Jakobsson, P., Hjorth, J., Fynbo, J. P. U., Gorosabel, J., & Jaunsen, A. O. 2006b, "Eleventh Marcel Grossmann Meeting on General Relativity" proceedings (arXiv:astro-ph/0611561)

Jakobsson, P., et al. 2006c, Gamma-Ray Bursts in the Swift Era, 836, 552

Jakobsson, P., et al. 2006d, A&A, 447, 897

Kann, D. A., Klose, S., & Zeh, A. (KKZ) 2006, *Astrophys. J.*, 641, 993

Kawai, N., Yamada, T., Kosugi, G., Hattori, T., & Aoki, K. 2005, GCN, 3937

Klebesadel, R. W., Strong, I. B., & Olson, R. A. 1973, *Astrophys. J.*, 182, L85

Klotz, A., Gendre, B., Stratta, G., Atteia, J. L., Boër, M., Malacrino, F., Damerdji, Y., & Behrend, R. 2006, A&A, 451, L39

Koornneef, J. 1982, A&A, 107, 247

Kouveliotou, C., et al. 1993, *Astrophys. J.*, 413, L101

Krimm, H., et al. 2005, GCN, 3183

Kulkarni, S. R., et al. 1998, Nature, 395, 663

Kumar, P., & Panaitescu, A. 2000, *Astrophys. J.*, 541, L51

Kumar, P., & Granot, J. 2003, *Astrophys. J.*, 591, 1075

Kumar, P., & Panaitescu, A. 2003, *Mon. Not. R. astr. Soc.*, 346, 905

Lamb, D. Q., & Reichart, D. E. 2000, *Astrophys. J.*, 536, 1

Lamb, D. Q., & Graziani, C. 2003, American Astronomical Society Meeting Abstracts, 202,

Lamb, D. Q., Donaghy, T. Q., & Graziani, C. 2005, *Astrophys. J.*, 620, 355

Landsman, W., et al. 2005, GCN, 3182

Langer, N., & Norman, C. A. 2006, *Astrophys. J.*, 638, L63

Lazzati, D., Covino, S., & Ghisellini, G. 2002, *Mon. Not. R. astr. Soc.*, 330, 583

Le Floc'h, E., et al. 2003, A&A, 400, 499

Le Floc'h, E., Charmandaris, V., Forrest, W. J., Mirabel, I. F., Armus, L., & Devost, D. 2006, *Astrophys. J.*, 642, 636

Levan, A. J., et al. 2006, *Astrophys. J.*, 648, 1132

Li, L.-X., & Paczyński, B. 2006, *Mon. Not. R. astr. Soc.*, 366, 219

Li, Z., & Waxman, E. 2006, *Astrophys. J.*, 651, 328

Lipunov, V. M., Postnov, K. A., & Prokhorov, M. E. 2001, Astronomy Reports, 45, 236

Lisenfeld, U., & Ferrara, A. 1998, *Astrophys. J.*, 496, 145

Livio, M., & Waxman, E. 2000, *Astrophys. J.*, 538, 187

MacFadyen, A. I., & Woosley, S. E. 1999, *Astrophys. J.*, 524, 262

MacFadyen, A. I., Woosley, S. E., & Heger, A. 2001, *Astrophys. J.*, 550, 410

Madau, P. 1995, *Astrophys. J.*, 441, 18

Mangano, V., et al. 2007, *Astrophys. J.*, 654, 403

Markwardt, C., et al., 2006, GCN, 5713

Mason, K. O., et al. 2001, A&A, 365, L36

Mason, K. O., et al. 2006, *Astrophys. J.*, 639, 311

Mathis, J. S., Rumpl, W., & Nordsieck, K. H. 1977, *Astrophys. J.*, 217, 425

Meszaros, P., & Rees, M. J. 1997, *Astrophys. J.*, 476, 232

Mészáros, P., & Rees, M. J. 1999, *Mon. Not. R. astr. Soc.*, 306, L39

Mészáros, P., & Rees, M. J. 2001, *Astrophys. J.*, 556, L37

Mészáros, P., Ramirez-Ruiz, E., Rees, M. J., & Zhang, B. 2002, *Astrophys. J.*, 578, 812

Möller, P., et al. 2002, A&A, 396, L21

Monfardini, A., et al. 2006, ApJ, 648, 1125

Moretti, A., et al. 2005, Proceedings of the SPIE, 5898, 360

Morrison, R., & McCammon, D. 1983, *Astrophys. J.*, 270, 119

Mundell, C. G., et al. 2007, ApJ, 660, 489

Natarajan, P., Albanna, B., Hjorth, J., Ramirez-Ruiz, E., Tanvir, N., & Wijers, R. 2005, *Mon. Not. R. astr. Soc.*, 364, L8

Nardini, M., Ghisellini, G., Ghirlanda, G., Tavecchio, F., Firmani, C., & Lazzati, D. 2006, A&A, 451, 821

Nicastro, L., et al. 1999, A&A, supp., 138, 437

Norris, J. P., Marani, G. F., & Bonnell, J. T. 2000, *Astrophys. J.*, 534, 248

Norris, J. P., & Bonnell, J. T. 2004, Gamma-Ray Bursts: 30 Years of Discovery, 727, 412

Norris, J. P., & Bonnell, J. T. 2006, *Astrophys. J.*, 643, 266

Nousek, J. A., et al. 2006, *Astrophys. J.*, 642, 389

O'Brien, P. T., et al. 2006, *Astrophys. J.*, 647, 1213

Oates, S. R., et al. 2007a, *Mon. Not. R. astr. Soc.*, 380, 270

Oates, S. R., et al. 2007b, Amsterdam Conf. Proc.: 070228: The Next Decade of GRB Afterglows

O'Flaherty, K. S., & Jakobsen, P. 1997, *Astrophys. J.*, 479, 673

Osip, D., Chen, H. W., & Prochaska, J. X. 2006, GCN, 5715

Paczynski, B. 1986, *Astrophys. J.*, 308, L43

Page, K. L., et al. 2007, *Astrophys. J.*, 663, 1125

Panaitescu, A., & Mészáros, P. 1999, *Astrophys. J.*, 526, 707

Panaitescu, A., & Kumar, P. 2000, *Astrophys. J.*, 543, 66

Panaitescu, A. 2005, *Mon. Not. R. astr. Soc.*, 363, 1409

Panaitescu, A., Mészáros, P., Gehrels, N., Burrows, D., & Nousek, J. 2006, *Mon. Not. R. astr. Soc.*, 366, 1357

Panaitescu, A. 2007a, *Mon. Not. R. astr. Soc.*, 379, 331

Panaitescu, A. 2007b, astro-ph/0705.1015

van Paradijs, J., et al. 1997, Nature, 386, 686

Parsons, A., et al. 2005, GCN, 3180

Pe'er, A., & Zhang, B. 2006, *Astrophys. J.*, 653, 454

Pei, Y. C. 1992, *Astrophys. J.*, 395, 130

Perna, R., & Lazzati, D. 2002, *Astrophys. J.*, 580, 261

Perna, R., Lazzati, D., & Fiore, F. 2003, *Astrophys. J.*, 585, 775

Piran, T. 1996, General Relativity and Gravitation, 28, 1421

Piro, L., den Herder, J. W., Ohashi, T., 2007, astro-ph/0707.4103

Poole, T. S., et al. 2005, GCN, 4263

Poole, T. S., et al. 2007, astro-ph/0708.2259

Predehl, P., & Schmitt, J. H. M. M. 1995, A&A, 293, 889

Prochaska, J. X. 2005, GCN, 4271

Prochaska, J. X., Bloom, J. S., Chen, H.-W., Hansen, B., Kalirai, J., Rich, M., & Richer, H. 2005, GCN, 3700

Prochaska, J. X., Chen, H.-W., & Bloom, J. S. 2006, *Astrophys. J.*, 648, 95

Ramirez-Ruiz, E., & Lloyd-Ronning, N. M. 2002, New Astronomy, 7, 197

Ramirez-Ruiz, E., Trentham, N., & Blain, A. W. 2002, *Mon. Not. R. astr. Soc.*, 329, 465

Rees, M. J., & Meszaros, P. 1992, *Mon. Not. R. astr. Soc.*, 258, 41P

Rees, M. J., & Meszaros, P. 1998, *Astrophys. J.*, 496, L1

Reichart, D. E. 1998, *Astrophys. J.*, 495, L99

Reichart, D. E., Lamb, D. Q., Fenimore, E. E., Ramirez-Ruiz, E., Cline, T. L., & Hurley, K. 2001, *Astrophys. J.*, 552, 57

Reichart, D. E., & Price, P. A. 2002, *Astrophys. J.*, 565, 174

Rhoads, J. E. 1997, *Astrophys. J.*, 487, L1

Rhoads, J. E. 1999, *Astrophys. J.*, 525, 737

Ricker, G. R., & HETE Science Team 2000, Bulletin of the American Astronomical Society, 32, 1441

Ricker, G. R., Vanderspek, R. K., & HETE Science Team 2003, Bulletin of the American Astronomical Society, 35, 1308

Romano, P., et al. 2006a, A&A, 456, 917

Romano, P., et al. 2006b, A&A, 450, 59

Romano, P., et al. 2007, GCNR, 58, 2 (2007), 58, 2

Roming, P. W. A., et al., 2005, Space Sci. Rev, 120, 95

Roming, P. W. A., et al. 2006, *Astrophys. J.*, 652, 1416

Rykoff, E. S., et al. 2005, *Astrophys. J.*, 631, L121

Rykoff, E. S., & Rujopakarn, W., 2006, GCN, 5706

Rossi, E., Lazzati, D., & Rees, M. J. 2002, *Mon. Not. R. astr. Soc.*, 332, 945

Ryde, F., & Svensson, R. 1999, *Astrophys. J.*, 512, 693

Sakamoto, T., et al. 2003, AIP Conf. Proc. 662: Gamma-Ray Burst and Afterglow Astronomy 2001: A Workshop Celebrating the First Year of the HETE Mission, 662, 94

Sakamoto, T., et al. 2004, AIP Conf. Proc. 727: Gamma-Ray Bursts: 30 Years of Discovery, 727, 106

Sakamoto, T., et al. 2006, *Astrophys. J.*, 636, L73

Sakamoto, T., et al. 2007, American Astronomical Society Meeting Abstracts, 210, #10.04

Salvaterra, R., Campana, S., Chincarini, G., Tagliaferri, G., & Covino, S. 2007, *Mon. Not. R. astr. Soc.*, 380, L45

Sanders, D. B., & Mirabel, I. F. 1996, Ann. Rev. A&A, 34, 749

Sari, R., Piran, T., & Narayan, R. 1998, *Astrophys. J.*, 497, L17

Sari, R., Piran, T., & Halpern, J. P. 1999, *Astrophys. J.*, 519, L17

Sari, R., & Mészáros, P. 2000, *Astrophys. J.*, 535, L33

Sari, R., & Esin, A. A. 2001, *Astrophys. J.*, 548, 78

Schady, P. 2005, GRB GCN, 3878

Schady, P., & Falcone, A. D. 2006, GCN, 4978

Schady, P., et al. 2006, *Astrophys. J.*, 643, 276

Schady, P., et al. 2007a, *Mon. Not. R. astr. Soc.*, 377, 273

Schady, P., et al. 2007b, *Mon. Not. R. astr. Soc.*, 704

Schlegel, D. J., Finkbeiner, D. P., & Davis, M. 1998, *Astrophys. J.*, 500, 525

Scoville, N. Z., et al. 1998, *Astrophys. J.*, 492, L107

Shi, F., Kong, X., Li, C., & Cheng, F. Z. 2005, A&A, 437, 849

Shioya, Y., Trentham, N., & Taniguchi, Y. 2001, *Astrophys. J.*, 548, L29

Smith, I. A., et al. 1999, A&A, 347, 92

Smith, I. A., Tilanus, R. P. J., Wijers, R. A. M. J., Tanvir, N., Vreeswijk, P., Rol, E., & Kouveliotou, C. 2001, A&A, 380, 81

Soderberg, A. M., et al. 2004, *Astrophys. J.*, 606, 994

Soderberg, A. M., et al. 2005, *Astrophys. J.*, 627, 877

Soderberg, A. M., et al. 2006, *Astrophys. J.*, 650, 261

Still, M., et al. 2005, *Astrophys. J.*, 635, 1187

Stratta, G., Fiore, F., Antonelli, L. A., Piro, L., & De Pasquale, M. (SFA) 2004, *Astrophys. J.*, 608, 846

Tagliaferri, G., et al. 2005a, A&A, 443, L1

Tagliaferri, G., et al. 2005b, Nature, 436, 985

Tanvir, N. R., et al. 2004, *Mon. Not. R. astr. Soc.*, 352, 1073

Taylor, G. B., Frail, D. A., Kulkarni, S. R., Shepherd, D. S., Feroci, M., & Frontera, F. 1998, *Astrophys. J.*, 502, L115

Taylor, G. B., Bloom, J. S., Frail, D. A., Kulkarni, S. R., Djorgovski, S. G., & Jacoby, B. A. 2000, *Astrophys. J.*, 537, L17

Thompson, T. A. 2005, Nuovo Cimento C Geophysics Space Physics C, 28, 583

Turner, M. J. L., et al. 2001, A&A, 365, L27

Ubertini, P., & INTEGRAL Team 2000, Bulletin of the American Astronomical Society, 32, 1210

de Ugarte Postigo, A., et al. 2007, A&A, 462, L57

Vaughan, S., et al. 2006, *Astrophys. J.*, 638, 920

Vestrand, W. T., et al. 2005, Nature, 435, 178

Vetere, L., Pagani, C., Burrows, D. N., & Schady, P. 2006, GCN, 5714

Villasenor, J. S., et al. 2005, Nature, 437, 855

Vlahakis, N., Peng, F., Köumlnigl, A. 2003, *Astrophys. J.*, 594, L23

Vreeswijk, P. M., et al. 2006, A&A, 447, 145

Vreeswijk, P. M., et al. 2007, A&A, 468, 83

Wang, X. Y., Dai, Z. G., & Lu, T. 2000, *Mon. Not. R. astr. Soc.*, 317, 170

Weingartner, J. C., & Draine, B. T. 2000, Bulletin of the American Astronomical Society, 32, 1466

Willingale, R., et al. 2007, *Astrophys. J.*, 662, 1093

Woods, E., & Loeb, A. 1999, *Astrophys. J.*, 523, 187

Woosley, S. E. 1993, *Astrophys. J.*, 405, 273

Woosley, S. E., & Heger, A. 2006, *Astrophys. J.*, 637, 914

Wu, Y., Charmandaris, V., Hao, L., Brandl, B. R., Bernard-Salas, J., Spoon, H. W. W., & Houck, J. R. 2006, *Astrophys. J.*, 639, 157

Yamazaki, R., Ioka, K., & Nakamura, T. 2002, *Astrophys. J.*, 571, L31

Yoon, S.-C., Langer, N., & Norman, C. 2006, A&A, 460, 199

Zeh, A., Klose, S., & Hartmann, D. H. 2004, *Astrophys. J.*, 609, 952

Zeh, A., Klose, S., & Kann, D. A. 2006, *Astrophys. J.*, 637, 889

Zhang, B., & Mészáros, P. 2001, *Astrophys. J.*, 552, L35

Zhang, B., & Mészáros, P. 2002, *Astrophys. J.*, 581, 1236

Zhang, B., & Mészáros, P. 2004, International Journal of Modern Physics A, 19, 2385

Zhang, B., Dai, X., Lloyd-Ronning, N. M., & Mészáros, P. 2004a, *Astrophys. J.*, 601, L119

Zhang, W., Woosley, S. E., & Heger, A. 2004b, *Astrophys. J.*, 608, 365

Zhang, B., Fan, Y. Z., Dyks, J., Kobayashi, S., Mészáros, P., Burrows, D. N., Nousek, J. A., & Gehrels, N. 2006, *Astrophys. J.*, 642, 354

Zhang, B., et al. 2007, *Astrophys. J.*, 655, 989